Spin Current Propagation in Metallic Heterostructure: Pt, Pt/Au and Ta

by

Pavlo Omelchenko

B.Sc., Simon Fraser University, 2014

Thesis Submitted in Partial Fulfillment of the
Requirements for the Degree of
Doctor of Philosophy

in the
Department of Physics
Faculty of Science

SIMON FRASER UNIVERSITY
Spring 2021

Declaration of Committee

Name:	**Pavlo Omelchenko**
Degree:	**Doctor of Philosophy (Physics)**
Title:	**Spin Current Propagation in Metallic Heterostructure: Pt, Pt/Au and Ta**
Examining Committee:	**Chair: Karen Kavanagh** Professor, Physics

Bret Heinrich
Co-Supervisor
Professor Emeritus, Physics

Erol Girt
Co-Supervisor
Professor, Physics

Malcolm Kennett
Supervisor
Associate Professor, Physics

Simon Watkins
Examiner
Professor, Physics

Can-Ming Hu
External Examiner
Professor, Physics and Astronomy
University of Manitoba

Abstract

Magnetic and structural studies of sputter deposited Py(an alloys, $Ni_{80}Fe_{20}$) and [Py/Fe] thin films allowed for the characterization of their magnetization dynamics properties relevant for subsequent studies. Spin transport and structural studies of Ta in Py/Ta (single magnetic layer) and Py/Ta/[Py/Fe] (double magnetic layer) structures were performed by spin-pumping. It was found that in order to extract self-consistent spin-pumping parameters it is important to study both the single and double magnetic layer structures.

Ferromagnetic resonance studies of Py/Pt/[Py/Fe] multilayers reveal interlayer exchange coupling of ferromagnetic nature. The coupling strength is interpreted by the proximity polarization of the Pt due to the neighboring ferromagnets. The coupled layers exhibit optical and acoustic modes of resonance which provide a very stringent test for the spin-pumping model. The induced magnetic damping of the two modes is found to be very well described by the spin-pumping model suggesting a communication of spin-current between the two magnetic layers. No significant spin memory loss contribution is observed.

Lastly, the spin-pumping model is studied in a system in which the coupling is interrupted by a Au spacer layer: Py/Au/Pt/Co. It is found that spin-transport across the Au/Pt interface cannot be modeled by the continuity of chemical potential or the continuity of spin accumulation boundary conditions. A new model is presented which treats Pt as a partial spin-sink and results in good fit to all the data sets. Importantly, both the model and data suggest a large asymmetry in spin transport across the Au/Pt interface.

Keywords: ferromagnetic resonance; spin-pumping; spin transport; proximity polarization; Pt; Ta; spin diode

Dedication

To my parents.

Table of Contents

List of Tables

List of Figures

Chapter 1

Introduction

Perhaps one of the most important discoveries in the field of spintronics is the magnetic coupling of two metallic magnetic layers across a non-magnetic metallic spacer layer [1]. This effect instantly attracted attention and led to the discovery of the giant magnetoresistance effect (GMR) and then subsequently tunneling magnetroresistance (TMR). These discoveries revolutionized information storage technology by allowing for a much larger density of recording media in modern hard drives. Spin transfer torque (STT) has also gained popularity due to its application in non-volatile magneto random access memory.

More recently, a new approach to spintronics has gained a lot of attention in the scientific community, one that separates charge and spin-currents. Pure spin-currents are more advantageous than spin-polarized currents since they do not carry any net charge and therefore avoid the issues present in conventional electronics such as Joule heating or electromigration. A powerful technique which allows one to study the transport of pure spin-current is the spin-pumping effect. Early spin-pumping studies focused on simple ferromagnet (FM)/normal-metal (NM) structures, where changes in magnetic damping in ultrathin FMs were used to determine the efficiency of spin-pumping at various FM/NM interfaces as governed by the (renormalized) spin mixing conductance ($\tilde{g}_{\uparrow\downarrow}$) $g_{\uparrow\downarrow}$ and the spin diffusion length in the adjacent NM λ_{sd}. First spin-pumping/spin transport studies focused on NMs with relatively low spin-orbit interactions (Ag [2, 3], Au [4, 3], Cu [5, 6]) finding that the experimental observations could be consistently descrbied by the spin-pumping/spin-diffusion models[7]. These metals were found to have spin-diffusion lengths on the order of dozens on nm ($\lambda_{\mathrm{sd,Ag}}$ = 80 nm, $\lambda_{\mathrm{sd,Au}}$ = 31 nm) [3]. Since then, spin-pumping and spin-transport has been studied in a variety of materials; spin-pumping driven by insulating ferrimagnets [8, 9, 10] and antiferromagnets [11] and spin-pumping into non-metallic materials such as antiferromagnetic insulators [12, 13, 14] and organic semiconductors [15, 16] has been demonstrated.

Significant attention has been devoted to the understanding of spin-transport in heavy metals with large spin-orbit interaction such as Pt, Ta, and W. In particular, Pt is a material of choice for many spin-transport studies due to its ease of deposition and low resistivity.

However, in the literature there is disagreement regarding the mechanism of spin-transport into Pt. Inverse spin Hall effect studies observe a spin-diffusion length in Pt of ~6 nm as compared to ~1 nm as measured from conventional spin-pumping studies. In fact it is not clear that spin-transport in Pt can still be described by the conventional spin diffusion model. Furthermore, Pt has strong electron-electron interactions resulting in an induced magnetic moment at the ferromagnet/Pt interface. Additionally, it has been argued that there is an additional spin-memory loss at the ferromagnet/Pt interface which can impact pure spin-current generation and transport [17, 18, 19, 20]. Experimental spin-pumping studies which avoid the direct contact of Pt (or Pd) with a ferromagnet by the addition of a spacer layer (Cu or Au) observe an oscillatory spin-pumping induced damping dependence as a function of Pt thickness [21, 22].

This thesis is mainly dedicated to the study spin-dynamics and spin-transport through Pt, Pt/Au and Ta. It is found that spin-pumping into Ta saturates on a diffusion length of 1 nm. The enhancement in damping of a ferromagnet adjacent to Ta is a consequence of spin-pumping as determined by the spin-sink magnetic structures [23]. Similarly, the enhancement in damping due to Pt is also very well described by the spin-pumping/spin-diffusion models. This is unambiguously observed in a phase-dependent spin-pumping experiment. The spin-diffusion length in Pt is also 1 nm. Importantly, the proximity polarization of Pt, due to interfacing a ferromagnet, appears to enhance the efficiency of spin-pumping (as predicted for spin-pumping into electron correlated system [24, 25]) but does not influence the spin-diffusion length. The difference in the spin-diffusion length as measure by the spin-pumping experiment (1 nm) and those determined from ISHE experiments (~ 6 nm) is explained to originate from a different type of measurement. A spin-pumping experiment measures the rf, transverse component of the spin-accumulation, where as the ISHE measures the dc, longitudinal component; i.e. spin-pumping measures the dephasing length scale. Finally, the spin-pumping model is tested for a heterostructure involving two materials with very different spin-transport properties Au/Pt (spin diffusion length in Pt vs Au is 1 nm vs. 30 nm). It is found that all the data sets can be self consistently described by the spin-pumping/spin-diffusion models assuming a boundary condition of reflection and transmission of spin-current proportional to the spin chemical potentials established on either side of the interface. The spin-transport across the Pt/Au is found to be non-reciprocal with a four times larger reflection if spin-current is injected from the Pt side as compare to the Au side.

1.0.1 Thesis Outline

Chapter 2 provides an overview of magnetic interactions which are relevant to the work presented in this thesis. The second part of this chapter focuses on the dynamics of a magnetic moment under the influence of a constant external field and a radio-frequency (rf) driving field. The equations derived in this section are relevant for the interpretation of the

ferromagnetic resonance data. The last part introduces the spin-pumping and spin-diffusion effects in ferromagnet/non-magnetic metal structures.

Chapter 3 provides an overview of the deposition and structure characterization tools employed in the studies presented in this thesis. These include sputter deposition, SQUID magnetometry, ferromagnetic resonance, x-ray diffraction, x-ray reflection and Van der Pauw method resistivity measurements.

Chapter 4 presents an experimental study of the magnetic properties of Py/Fe bilayer structures (Py=$Ni_{80}Fe_{20}$) for various relative thicknesses of Py and Fe. This study is fundamental for the rest of the thesis since most subsequent work utilizes the properties of the Py and [Py/Fe] structures to study the spin-pumping and spin-transport into Ta and Pt.

Chapter 5 presents an experimental study of spin-transport in Ta by utilizing the spin-pumping of Py in Py/Ta (single magnetic layer) and Py/Ta/[Py/Fe] (double magnetic layer). This work highlights the important of using the results of the single magnetic layer (SL) and double magnetic layers (DL) for a unique interpretation of the data.

Chapter 6 presents an experimental study of interlayer exchange coupling mediated by Pt due to proximity polarization from adjacent magnetic layers. By utilizing broadband ferromagnetic resonance (FMR) is it shown that very large ferromagnetic interlayer exchange coupling can be measured in a Py/Pt/[Py/Fe] system. An attempt is made to interpret the magnetic damping data in order to extract the spin-pumping into Pt, however it is found that the interpretation is quite convoluted as a consequence of two-magnon scattering and the averaging of the dampings of the two magnetic layers due to interlayer exchange coupling.

Chapter 7 presents an experimental study of spin-pumping in a Py/Pt/Py structure due to the in-phase and out-of-phase precession modes of the two magnetic layers. In this study the two magnetic layers are nearly identical in their magnetic properties which results in a much more well defined interpretation of the magnetic damping data as compared to the attempt made in ***Chapter 6***. This study uses interlayer exchange coupling measurements as determined in ***Chapter 6*** and the concepts of the SL and DL to uniquely interpret the spin-pumping and spin-diffusion through Pt. The main conclusion of this study is that the magnetic damping induced by Pt is indeed due to spin-pumping.

Chapter 8 presents an experimental study of spin-pumping through a Au/Pt bilayer by utilizing the SL and DL structures. It is observed that there is a large asymmetry in spin-transport across the Au/Pt interface which depends on the direction of the spin-current. Interpretation of the data by the continuity of spin accumulation and continuity of chemical potential fail to describe the observed data. A new model is proposed which treats Pt as a partial spin-sink and is consistent with the idea of an asymmetric transport of spin-current across the Au/Pt interface. Finally, the spin-memory loss model is tested against the data and yields unrealistic fitting parameters.

Chapter 2

Theoretical Considerations

This chapter presents the theoretical background necessary to understand the experimental ferromagnetic resonance (FMR) results presented throughout this thesis. The first part of the chapter (section 2.1) describes the magnetic energy terms relevant in thin film magnetic heterostructures. Sections 2.2 describes the dynamics of a magnetic moment as determined by the Landau-Lifshitz-Gilbert (LLG) equation of motion. Section 2.3 extends this to the case of FMR in two typical geometries, in-plane and out-of-plane FMR. Many of the studied structures in this thesis consist of two ferromagnetic layers which experience a form of coupling through a spacer layer. Section 2.4 extends on section 2.3 to present a description of such a coupled structure in the framework of the LLG. Section 2.5 introduces spin-pumping in two approaches: *i*) as a time retarded response of the static interlayer exchange coupling and *ii*) as derived from scattering theory. Finally, section 2.6 briefly presents two scattering mechanisms which lead to the attenuation of spin-current. It is useful for the reader to be aware that all of the structures studied in this thesis consist of either one or two ferromagnetic layers (see fig. 2.1). In the case of two ferromagnetic layer structure, (see fig. 2.1 a)), the metallic spacer layer can mediate magnetic coupling between the two ferromagnetic layer, referred to as interlayer exchange coupling.

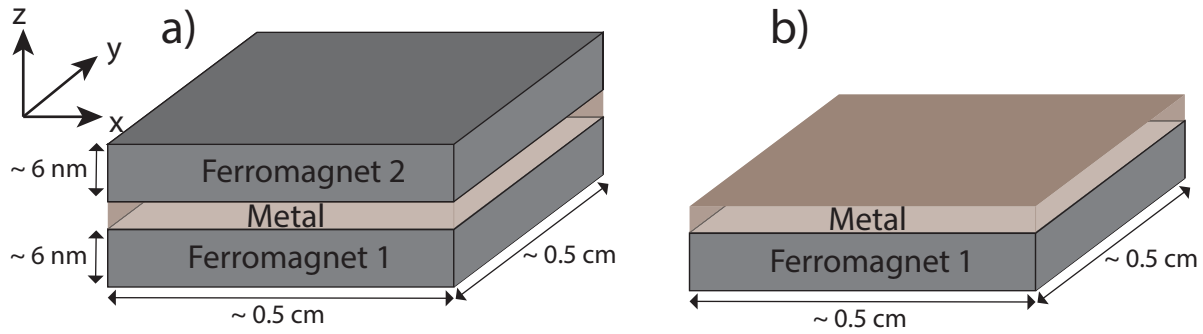

Figure 2.1: Schematic of the magnetic structures studied throughout this thesis.

2.1 Magnetic Free Energy

The net magnetic free energy density of a magnetic multilayer system under the influence of an external field is given by [26]

$$U_{\mathrm{Tot}} = U_{\mathrm{ex}} + U_{\mathrm{Z}} + U_{\mathrm{an}} + U_{\mathrm{D}} + U_{\mathrm{J}}, \tag{2.1}$$

where U_{ex} is the exchange energy due to exchange interaction between atoms, U_{Z} is the Zeeman energy which results from the interaction between the magnetic moments and the external magnetic field, U_{J} is the energy due to interlayer exchange coupling between two magnetic materials through a non-magnetic spacer, U_{an} is the crystallographic anisotropy energy and U_{D} is the demagnetization energy arising from the dipole-dipole interactions.

2.1.1 Exchange energy

The exchange interaction is a quantum mechanical phenomenon which is a consequence of the Coulomb interaction and the indistinguishably of electrons. In a ferromagnetic system the exchange energy favors parallel alignment of electron spins. For homogeneous materials one can define a characteristic length scale over which the exchange energy dominates the dipole-dipole interactions,

$$\delta_{ex} = \sqrt{\frac{A_{\mathrm{ex}}}{2\pi M_s^2}}, \tag{2.2}$$

where M_s is the magnetization of the ferromagnetic material at saturation and A_{ex} is the exchange constant. Typical values of A_{ex} are $\sim 10^{-6}$ erg/cm and $\delta_{ex} \sim 2-3$ nm for metallic ferromagnets (Co, Fe) [27]. Magnetic structures whose thickness is comparable to the exchange thickness have all their magnetic moments locked together in one direction. In this thesis the thicknesses of all deposited films are considered to be in this limit.

2.1.2 Zeeman energy

The Zeeman energy is the result of the interaction between the magnetic moments of a system and an external magnetic field. In general the Zeeman energy is expressed as,

$$E_{\mathrm{Z}} = -\int_V \boldsymbol{M} \cdot H_{\mathrm{DC}}\, dV, \tag{2.3}$$

where $\boldsymbol{M}$ is the magnetization, H_{DC} is the external magnetic field and the integral is performed over the entire volume V of the magnetic material. Assuming that the magnetic field and the magnetic material are both uniform over the volume V, one can simply write:

$$E_{\mathrm{Z}} = -\boldsymbol{M} \cdot H_{\mathrm{DC}} V. \tag{2.4}$$

Therefore the energy density associated with the Zeeman energy is

$$U_{\mathrm{Z}} = -\boldsymbol{M} \cdot H_{\mathrm{DC}}. \tag{2.5}$$

2.1.3 Magnetic Anisotropy Energy

In crystalline magnetic films the magnetization has preferential directions determined by the lattice symmetry and the shape of the magnetic material. This results in a dependence of the energy on the direction of magnetization referred to as the magnetic anisotropy energy (MAE). The MAE relevant for the studies performed in this thesis are magnetocrystalline anisotropy, surface anisotropy and the demagnetization (shape anisotropy) energy .

Demagnetization Energy

Any realistic magnetic film will always have finite size, which results in an uncompensated magnetic charge at the boundaries. Consequently, a magnetic field is established by the surface charge, $\mathbf{H}_{\mathrm{D}}$, which is oriented opposite to the direction of magnetization of the film. The dipole-dipole interaction of the charge results in a demagnetizing energy density is given by

$$U_{\mathrm{D}} = \boldsymbol{M} \cdot \boldsymbol{H}_{\mathrm{D}}. \tag{2.6}$$

$\boldsymbol{H}_{\mathrm{D}}$ will depend on the dimensions of the magnetic structure and is therefore not intrinsic to the magnetic material. In this thesis the studied structures are magnetic thin films in which the lateral dimensions (length ~ cm and width ~ cm) are much greater than the thickness of the films, ~ nm. Therefore the film can be approximated as an infinite sheet. For this structure when the magnetization of the film is oriented in the plane of the film then there is no surface charge. If the magnetization is tilted away from the surface of the film, this results in a surface charge on two faces of the film which leads to a demagnetizing energy given by,

$$U_{\mathrm{D}} = 2\pi D M_s^2 \cos(\theta_M), \tag{2.7}$$

where θ_M is the angle the magnetization makes with respect to the film surface normal. For thin films thicker than a few atomic layers, $D \approx 1$. Therefore the effect of the demagnetization energy is to act as a restoring force to bring the magnetization back into the plane of the film.

Magnetocrystalline and Interface/Surface Anisotropy Energy

Magnetocrystalline anisotropy arises from the energy dependence of the orientation of the magnetic moment with respect to the crystal lattice. The lattice symmetry dictates the electric charge distribution in the crystal and the electron orbits are coupled to the lattice due to the Coulomb interaction. The spin-orbit interaction then couples the electron spin to the crystal lattice. All the structures deposited and studied in this thesis are polycrystalline

and therefore all in-plane anisotropies are averaged out due to random orientation of the crystal grains in the plane of the film. However, since the films are textured there can be an anisotropy contribution along the film normal. The phenomenological anisotropy energy density is given by,

$$U_{\mathrm{D}} = -\frac{K_U}{M_s^2}(\boldsymbol{M}\cdot\boldsymbol{n}_\perp)^2, \tag{2.8}$$

where K_U is the uniaxial anisotropy constant and $\boldsymbol{n}_\perp$ is a unit vector along the film normal. K_U can have a bulk and interface contributions and is therefore described by

$$K_U = K_c + \frac{K_s}{d}, \tag{2.9}$$

where d is the thickness of the ferromagnetic film, K_c is the bulk anisotropy constant and K_s is the interface anisotropy constant.

2.2 Landau–Lifshitz–Gilbert: LLG

The mechanical torque exerted on a magnetic object with magnetization $\boldsymbol{M}$ by an external field, $\boldsymbol{H}_{DC}$, is given by,

$$\mathcal{T}_{\mathrm{M}} = \boldsymbol{M}\times\boldsymbol{H}_{DC}. \tag{2.10}$$

Due to the cross-product, this torque is always perpendicular to the instantaneous direction of magnetization, which causes a precession of magnetization around the component of magnetization parallel to $\boldsymbol{H}_{DC}$. Additionally, it is known that the spin of an electron $\boldsymbol{S}$ is related to the magnetic moment by the gyromagnetic ratio,

$$\boldsymbol{M} = -\frac{g\mu_B}{\hbar}\boldsymbol{S}, \tag{2.11}$$

where g is the Landé g–factor of the electron ($\approx$2.002319 for a free electron), μ_B is the Bohr magneton and $\hbar$ is the reduced Planck's constant; their product is called the gyromagnetic ratio $\gamma = \frac{g\mu_B}{\hbar}$. Since torque can be defined as the rate of change of angular momentum, the above can be rewritten as,

$$\mathcal{T}_{\mathrm{M}} = \frac{\partial\boldsymbol{S}}{\partial t} = \frac{1}{-\gamma}\frac{\partial\boldsymbol{M}}{\partial t}, \tag{2.12}$$

Putting this into eq. (2.10) results in

$$\frac{\partial\boldsymbol{M}}{\partial t} = -\gamma\boldsymbol{M}\times\boldsymbol{H}_{DC}, \tag{2.13}$$

Since the right hand side of eq. (2.13) is a cross product, it cannot result in any change in the magnitude of $\boldsymbol{M}$. Instead, the solution describes the precession of $\boldsymbol{M}$ around $\boldsymbol{H}_{DC}$ (see

fig. 2.2(a)). This equation would suggest that the magnetization can never align itself with the external magnetic field, this is a clear contradiction to what is observed experimentally. To remedy this, L. Landau and E. Lifshitz introduced a dissipative term into eq. (2.13) leading to the Landau-Lifshitz (LL) equation,

$$\frac{\partial \boldsymbol{M}}{\partial t} = -\gamma \boldsymbol{M} \times \boldsymbol{H}_{DC} - \frac{\lambda}{M_s^2} \left(\boldsymbol{M} \times \left(\boldsymbol{M} \times \boldsymbol{H}_{DC} \right) \right), \tag{2.14}$$

where the second term on the right hand side corresponds to the magnetic damping with a phenomenological parameter $\lambda > 0$ in units of inverse time.

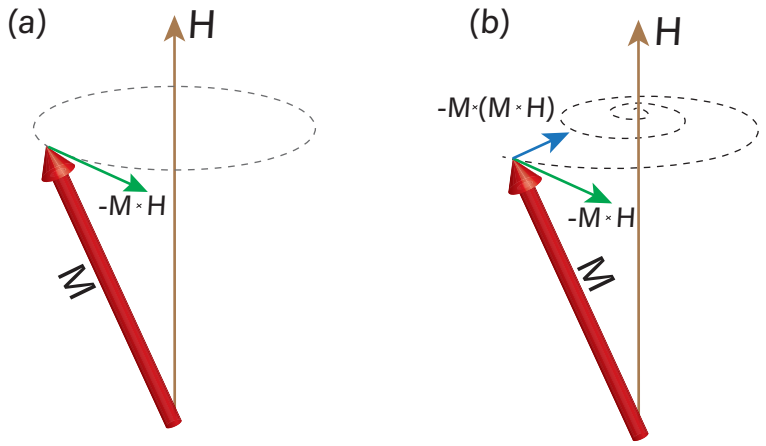

Figure 2.2: Precessional motion of the magnetic moment $\boldsymbol{M}$ under the influence of an external field $\mathbf{H}$ without magnetic damping (a) and with magnetic damping (b).

It is convenient to define a dimensionless parameter to describe the damping,

$$\alpha = \frac{\lambda}{\gamma M_s}. \tag{2.15}$$

Using this definition of damping, Gilbert, T. L [28] rewrote eq. (2.14) with the damping term as dependent on the time derivative of the magnetization,

$$\frac{\partial \boldsymbol{M}}{\partial t} = -\gamma \left[\boldsymbol{M} \times \boldsymbol{H}_{DC} \right] + \alpha \left[\boldsymbol{M} \times \frac{\partial \boldsymbol{n}}{\partial t} \right], \tag{2.16}$$

where $\boldsymbol{n}$ is the unit vector in the direction of $\boldsymbol{M}$. The two equations eq. (2.16) and eq. (2.14) lead to equivalent dynamics in the limit of $\alpha << 1$. This limit is satisfied in all the studied presented in this thesis.

2.3 Ferromagnetic Resonance

As can be observed from eq. (2.16), the magnetic moment of a ferromagnetic sample will eventually reorient itself along the effective field due to magnetic damping. Applying a small

rf magnetic field, perpendicular to the magnetic moment, can induce precessional motion of the magnetic moment. The magnetic moment will undergo a resonant absorption of energy when the precessional frequency coincides with the rf field. At resonances the microwave losses are increased, this is the key principle behind the technique used to measure ferromagnetic resonance (FMR) in this thesis. Described below are the two typical geometries of FMR and the derivation of the equations used for interpreting the data from the FMR experiment.

The dynamics of the magnetic moment of the ferromagnet can be determined by solving eq. (2.16) with all the appropriate magnetic fields included. Other than the external fields, a real magnetic system will have additional effective fields originating from the energies discussed in section 2.1,

$$\boldsymbol{H}_{\text{eff}} = -\frac{\partial U_{\text{tot}}}{\partial \boldsymbol{M}}, \tag{2.17}$$

where U_{tot} is the sum of all the energy terms introduced in the previous section. For a textured crystal, thin film one can identify the three contributions to the free energy: *i*) the Zeeman energy $U_Z = -\boldsymbol{M} \cdot \boldsymbol{H}_{DC}$ coming from the applied external fields, *ii*) the shape anisotropy energy, $U_D = 2\pi(\boldsymbol{M} \cdot \boldsymbol{n}_\perp)^2/M_s^2$, which gives rise to the demagnetizing field, and *iii*) the perpendicular anisotropy energy $U_a = -\boldsymbol{K_u}(\boldsymbol{M} \cdot \boldsymbol{n}_\perp)^2/M_s^2$ which give rise to internal anisotropy fields, where $\boldsymbol{K_u}$ is the perpendicular anisotropy constant and $\boldsymbol{n}_\perp$ is a unit vector perpendicular to the film surface. This thesis focuses on sputter deposited, textured, polycrystalline samples; the in-plane anisotropies are not detectable by FMR which measures the average properties of the structure.

2.3.1 In-plane FMR

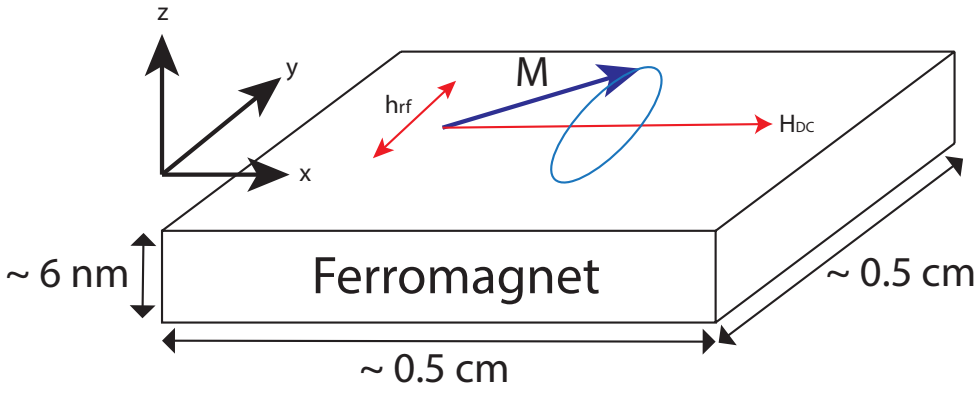

Figure 2.3: Illustration of the magnetic precession for the in-plane geometry. The $\boldsymbol{H}_{DC}$ field is applied in the plane of the sample and the rf driving field is perpendicular to $\boldsymbol{H}_{DC}$ but still in the plane of the sample.

The in-plane FMR geometry refers to the fact that the external $\boldsymbol{H}_{DC}$ is applied in the plane of the magnetic structure. The plane of the film refers to the surface of the thin film

(see fig. 2.3). The coordinate system is chosen such that the $\boldsymbol{H}_{DC}$ is along the x-axis and the $\boldsymbol{h}_{\mathrm{rf}}$ is in the y-axis.

In this thesis the FMR was operated in the limit of small perturbation (weak rf-field), therefore the dynamics of $\boldsymbol{M}$ can be well described by,

$$\boldsymbol{M}(\boldsymbol{x},t) = M_s\hat{\boldsymbol{x}} + m_y e^{i\omega t}\hat{\boldsymbol{y}} + m_z e^{i\omega t}\hat{\boldsymbol{z}}, \tag{2.18}$$

which assumes a small angle of precession with frequency ω around the direction of the applied dc-field $\boldsymbol{H}_{DC} = H_{DC}\hat{\mathbf{x}}$. The net effective field is expressed as,

$$\boldsymbol{H}_{\mathrm{eff}} = \boldsymbol{H}_{DC} + \boldsymbol{h}_{\mathrm{rf}} - 4\pi M_s\hat{\boldsymbol{z}} + 2\frac{K_u^{\perp}}{M_s}\hat{\boldsymbol{z}}, \tag{2.19}$$

where $\boldsymbol{h}_{\mathrm{rf}} = h_{\mathrm{rf}}e^{i\omega t}\hat{\boldsymbol{y}}$. Note, the demagnetizing field and the perpendicular anisotropy term are both oriented perpendicular to the surface, along the $\hat{\boldsymbol{z}}$ direction, see fig. 2.3.

Including eq. (2.19) and eq. (2.18) into the eq. (2.16) yields two coupled equations for the $\hat{\boldsymbol{y}}$ and the $\hat{\boldsymbol{z}}$ components,

$$\begin{aligned} 0 &= i\frac{\omega}{\gamma}m_y + \left(H_{DC} + 4\pi M_{\mathrm{eff}} + i\alpha\frac{\omega}{\gamma}\right)m_z \\ M_s h_{\mathrm{rf}} &= \left(H_{DC} + i\alpha\frac{\omega}{\gamma}\right)m_y - i\frac{\omega}{\gamma}m_z, \end{aligned} \tag{2.20}$$

where $4\pi M_{\mathrm{eff}} = 4\pi M_s - 2K_u^{\perp}/M_s$.

The magnetic transverse susceptibility can be obtained by solving the above for m_y resulting in,

$$\chi_y = \chi_y' + i\chi_y'' = \frac{m_y}{h_{\mathrm{rf}}} = \frac{M_s\left(H_{DC} + 4\pi M_{\mathrm{eff}} + i\alpha\frac{\omega}{\gamma}\right)}{\left(H_{DC} + i\alpha\frac{\omega}{\gamma}\right)\left(H_{DC} + 4\pi M_{\mathrm{eff}} + i\alpha\frac{\omega}{\gamma}\right) - \left(\frac{\omega}{\gamma}\right)^2}, \tag{2.21}$$

where χ_y' and χ_y'' are the dispersive and absorptive parts of the transverse susceptibility, respectively. FMR occurs when the denominator of eq. (2.21) is minimized. Neglecting the small contribution from the damping term, it is easy to see that the in-plane FMR will occur at,

$$\left(\frac{\omega}{\gamma}\right)^2 = H_{DC}\left(H_{DC} + 4\pi M_{\mathrm{eff}}\right)|_{H_{DC}=H_{\mathrm{res}}}. \tag{2.22}$$

Recall $4\pi M_{\mathrm{eff}} = 4\pi M_s - 2\frac{K_u^{\perp}}{M_s}$. It can be shown that in the linear precession regime (dropping second order terms, i.e. $m_y m_z$), the real and imaginary parts of the transverse susceptibility are well described by [29],

$$\mathrm{Re}(\chi_y) = \chi_y' \approx AM_s\left(\frac{1}{B_{\mathrm{res}}} + \frac{H_{DC} - H_{\mathrm{res}}}{(H_{DC} - H_{\mathrm{res}})^2 + \Delta H^2}\right), \tag{2.23}$$

$$\mathrm{Im}(\chi_y) = \chi_y'' \approx AM_s \left(\frac{\Delta H}{(H_{DC} - H_{\mathrm{res}})^2 + \Delta H^2} \right), \tag{2.24}$$

where $\Delta H = \alpha\omega/\gamma$ is the half width at half maximum of the signal linewidth and H_{res} is the resonance field. The parameter $A = B_{\mathrm{res}}/(B_{\mathrm{res}} + H_{\mathrm{res}})$ is called the ellipticity factor and $B_{\mathrm{res}} = H_{\mathrm{res}} + 4\pi M_{\mathrm{eff}}$.

For inhomogeneous samples the signal linewidth is well described by,

$$\Delta H = \alpha \frac{\omega}{\gamma} + \Delta H(0), \tag{2.25}$$

where the parameter $\Delta H(0)$ is the zero-frequency linewidth broadening due to long range inhomogeneities.

2.3.2 Perpendicular-to-plane FMR

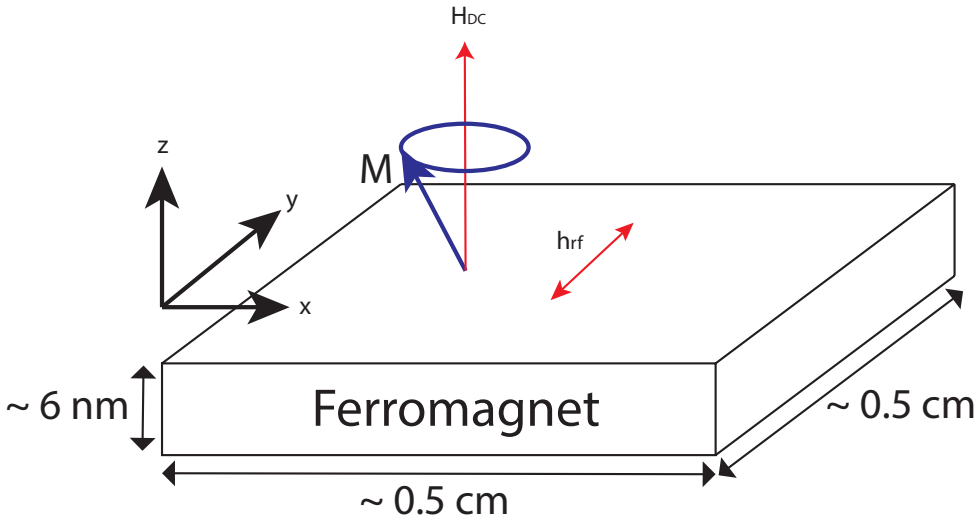

Figure 2.4: Illustration of the magnetic precession for the perpendicular-to-plane geometry. The $\boldsymbol{H}_{DC}$ field is applied perpendicular to the plane of the sample and the rf driving field is in the plane of the sample.

The perpendicular-to-plane geometry refers to the structure in which both the external DC magnetic field and the magnetic moment of the sample are perpendicular to the plane of the sample, see fig. 2.4. In this situation the magnetic moment is described by,

$$\boldsymbol{M}(\boldsymbol{x}, t) = m_x e^{-i\omega t}\hat{\boldsymbol{x}} + m_y e^{-i\omega t}\hat{\boldsymbol{y}} + M_s\hat{\boldsymbol{z}} \tag{2.26}$$

The effective field has a simpler form,

$$\boldsymbol{H}_{\mathrm{eff}} = \boldsymbol{H}_{DC} + \boldsymbol{h}_{\mathrm{rf}} - \left(4\pi M_s - 2\frac{K_u^{\perp}}{M_s} \right)\hat{\boldsymbol{z}}. \tag{2.27}$$

Substituting eq. (2.26) and eq. (2.27) in eq. (2.16) results in two coupled equations

$$\begin{aligned} 0 &= i\frac{\omega}{\gamma}m_y - \left(H_{DC} - 4\pi M_{\text{eff}}^{\perp} + i\alpha\frac{\omega}{\gamma}\right)m_x, \\ M_s h_{\text{rf}} &= \left(H_{DC} - 4\pi M_{\text{eff}}^{\perp} + i\alpha\frac{\omega}{\gamma}\right)m_x + i\frac{\omega}{\gamma}m_y. \end{aligned} \tag{2.28}$$

The magnetic transverse susceptibility can be obtained by solving the above for m_y resulting in,

$$\chi_y = \chi_y' + i\chi_y'' = \frac{m_y}{h_{\text{rf}}} = \frac{M_s\left(H_{DC} - 4\pi M_{\text{eff}}^{\perp} + i\alpha\frac{\omega}{\gamma}\right)}{\left(H_{DC} - 4\pi M_{\text{eff}}^{\perp} + i\alpha\frac{\omega}{\gamma}\right)\left(H_{DC} - 4\pi M_{\text{eff}}^{\perp} + i\alpha\frac{\omega}{\gamma}\right) - \left(\frac{\omega}{\gamma}\right)^2}. \tag{2.29}$$

As before, the FMR occurs when the denominator of eq. (2.29) is minimum. Neglecting the damping term, this occurs at,

$$\frac{\omega}{\gamma} = H_{DC} - 4\pi M_{\text{eff}}^{\perp}|_{H_{DC}=H_{\text{res}}}. \tag{2.30}$$

As was the case for the in-plane geometry, in the perpendicular-to-plane geometry, the real and imaginary parts of the transverse susceptibility (assuming linear precession regime) are well described by

$$\text{Re}(\chi_y) = \chi_y' \approx \frac{M_s}{2}\left(\frac{1}{H_{res} - 4\pi M_{\text{eff}}^{\perp}} + \frac{H_{DC} - H_{\text{res}}}{(H_{DC} - H_{\text{res}})^2 + \Delta H}\right), \tag{2.31}$$

$$\text{Im}(\chi_y) = \chi_y'' \approx \frac{M_s}{2}\left(\frac{\Delta H}{(H_{DC} - H_{\text{res}})^2 + \Delta H}\right). \tag{2.32}$$

Apart from the constant term (first term on the right hand side of eq. (2.31)), the transverse susceptibility dependence on ΔH and H_{res} of the in-plane and perpendicular-to-plane cases are the same. Note, our FMR measurements employ field modulation with the lock-in technique, which results in measuring the field derivative of the susceptibility described above. Therefore, the first term on the right hand side of eq. (2.31) does not contribute to the measured response, see section 3.7 for more details.

2.4 FMR and Interlayer Exchange Coupling

For two magnetic thin films separated by a non-magnetic film can undergoing bilinear interlayer exchange coupling. The three most common origins of type of coupling are; interface roughness [30, 31], proximity polarization [32] and difference of spin-polarized reflections at the FM interface [33]. one can introduce an additional interface energy term (E_J) and its corresponding energy densities for FM1 ($U_{J,1}$) and FM2 ($U_{J,2}$) [26],

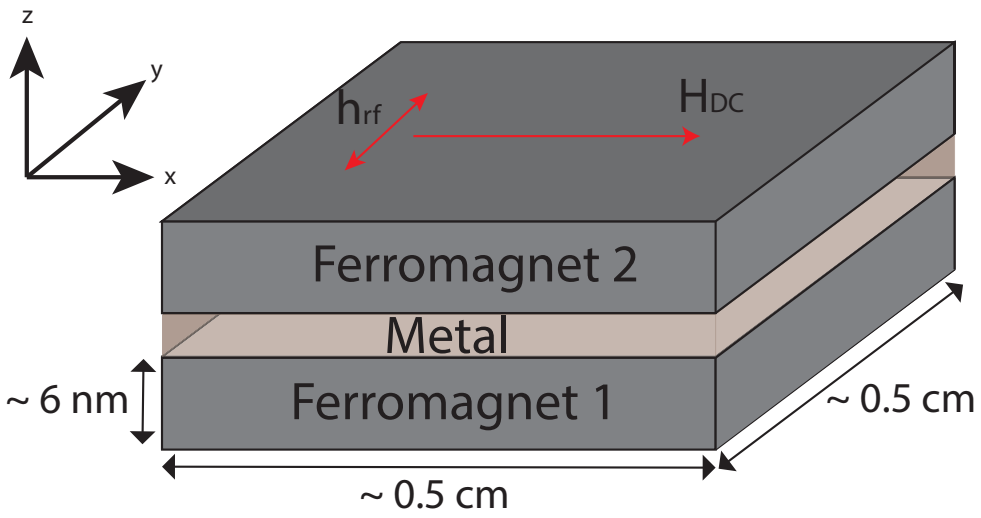

Figure 2.5: Schematic of a FM1/NM/FM2 structure. The external DC field is in the plane of the structure and the rf driving field is perpendicular to the DC field but also in the plane. The thicknesses of both ferromagnets are on the order of several nanometers.

$$\begin{aligned} E_J &= -J\frac{\boldsymbol{M}_1 \cdot \boldsymbol{M}_2}{M_{s1}M_{s2}}, \\ U_{J,i} &= -J\frac{\boldsymbol{M}_1 \cdot \boldsymbol{M}_2}{d_i M_{s1}M_{s2}}, \end{aligned} \tag{2.33}$$

where J is the interlayer exchange coupling strength and $\boldsymbol{M}_1$ and $\boldsymbol{M}_2$ are the magnetization vectors of FM1 and FM2, respectively.

In this thesis the coupling strength J was measured only for the in-plane geometry, therefore the discussion is limited to the in-plane configuration with the external dc and rf fields as shown in fig. 2.5. As before, for the in-plane geometry, the instantaneous magnetization of each layer is given by $\boldsymbol{M}_i(\boldsymbol{x},t) = M_{s,i}\hat{\boldsymbol{x}} + m_{y,i}e^{i\omega t}\hat{\boldsymbol{y}} + m_{z,i}e^{i\omega t}\hat{\boldsymbol{z}}$, which assumes a small angle of precession with frequency ω around the direction of the applied dc-field $\boldsymbol{H}_{DC} = H_{DC}\hat{\boldsymbol{x}}$. The rf driving field $\boldsymbol{h}_{rf} = h_{rf}e^{i\omega t}\hat{\boldsymbol{y}}$ is oriented in the plane of the film, perpendicular to the dc-field. Finally, the effective field term for the two layers can be written as

$$\begin{aligned} \boldsymbol{H}_{\text{eff},1} &= \boldsymbol{H}_{DC} + \boldsymbol{h}_{rf} + J\frac{\boldsymbol{M}_2}{d_{\text{FM1}}M_{s,1}M_{s,2}} - 4\pi M_{\text{eff},1}\hat{\boldsymbol{z}}, \\ \boldsymbol{H}_{\text{eff},2} &= \boldsymbol{H}_{DC} + \boldsymbol{h}_{rf} + J\frac{\boldsymbol{M}_1}{d_{\text{FM2}}M_{s,2}M_{s,1}} - 4\pi M_{\text{eff},2}\hat{\boldsymbol{z}}, \end{aligned} \tag{2.34}$$

where $4\pi M_{\text{eff,i}} = 4\pi M_{s,i} - 2K_{u,i}/M_{s,i}$, $d_{\text{FM}i}$ is the thickness of the i_{th} magnetic layer. Note that the exchange coupling term in eq. (2.34) is inversely proportional to the thickness of magnetic film. Substituting eq. (2.34) into LLG equation of motion, eq. (2.16), one can solve

for the rf components of $\boldsymbol{M}_1$ and $\boldsymbol{M}_2$. The averaged rf magnetization of a structure with FM1 and FM2 is then given by,

$$m_y = \frac{\hat{y}}{d_{\mathrm{FM1}} + d_{\mathrm{FM2}}} \cdot \left(d_{\mathrm{FM1}} \boldsymbol{M}_1 + d_{\mathrm{FM2}} \boldsymbol{M}_2 \right). \tag{2.35}$$

The full explicit solution of m_y is too large to include in this thesis. The H_{DC} fields at which the resonances occur, H_{res}, has a more manageable form. The resonance condition can be extracted by finding a solution such that the denominator of $m_y|_{\alpha=0}$ goes to zero. It can be shown that these solutions need to satisfy,

$$\begin{aligned} 0 = {} & \mathrm{H}_1^2 \mathrm{H}_2^2 + J^2 \mathrm{H}_2^2 + J^2 \mathrm{H}_1^2 + 2J^2 \mathrm{H}_{12}^2 \\ & + 2J \mathrm{H}_2^2 \left(H_{res} + 2\pi M_{\mathrm{eff},1} \right) \left(M_{s,1} d_1 \right) \\ & + 2J \mathrm{H}_1^2 \left(H_{res} + 2\pi M_{\mathrm{eff},2} \right) \left(M_{s,2} d_2 \right) \end{aligned} \tag{2.36}$$

where

$$\begin{aligned} \mathrm{H}_1 &= M_{s,1} d_{\mathrm{FM1}} \sqrt{H_{res}^2 + 4\pi M_{\mathrm{eff},1} H_{res} - \left(\frac{\omega}{\gamma} \right)^2}, \\ \mathrm{H}_2 &= M_{s,2} d_{\mathrm{FM2}} \sqrt{H_{res}^2 + 4\pi M_{\mathrm{eff},2} H_{res} - \left(\frac{\omega}{\gamma} \right)^2}, \\ \mathrm{H}_{12} &= \sqrt{H_{res}^2 + 2\pi \left(M_{\mathrm{eff},1} + M_{\mathrm{eff},2} \right) H_{res} - \left(\frac{\omega}{\gamma} \right)^2} \\ &\quad \times \sqrt{M_{s,1} d_{\mathrm{FM1}} M_{s,2} d_{\mathrm{FM2}}}, \end{aligned} \tag{2.37}$$

where d_{FM1} and d_{FM2} are the thicknesses of FM1 and FM2. There are four H_{res} solutions to eq. (2.36), two are non-physical and the other two correspond to the acoustic and optical modes as discussed below. It is easy to see that for $J = 0$ eq. (2.36) reduces to the resonance condition for uncoupled films, eq. (2.22).

For $J \neq 0$, the solution becomes a lot more complicated; its explicit form will not be included in this thesis. The qualitative effect of $J \neq 0$ is to shift the FMR spectra of both resonances of FM1 and FM2 either up or down in field [34], depending on the coupling type (ferromagnetic or antiferromagnetic), see fig. 2.6. With $J > 0$ the measured resonances, previous for FM1 and FM2, are no longer independent precessions of each magnetic layer and are now referred to as the acoustic and optical modes, respectively. The acoustic mode is the in-phase precession of the two magnetic films. In a typical FMR experiment the external magnetic field will align the two magnetic moments nearly parallel to each other (assume relatively small anisotropy contributions). For $J > 0$, the parallel magnetic moment configuration is already the lowest energy state. Increasing the external field brings the magnetic moments closer to the parallel orientation. For $J > 0$ the interlayer exchange energy contribution, eq. (2.33), will depend on the degree of misalignment from parallel and since the moments are already nearly aligned by the external field, this contribution

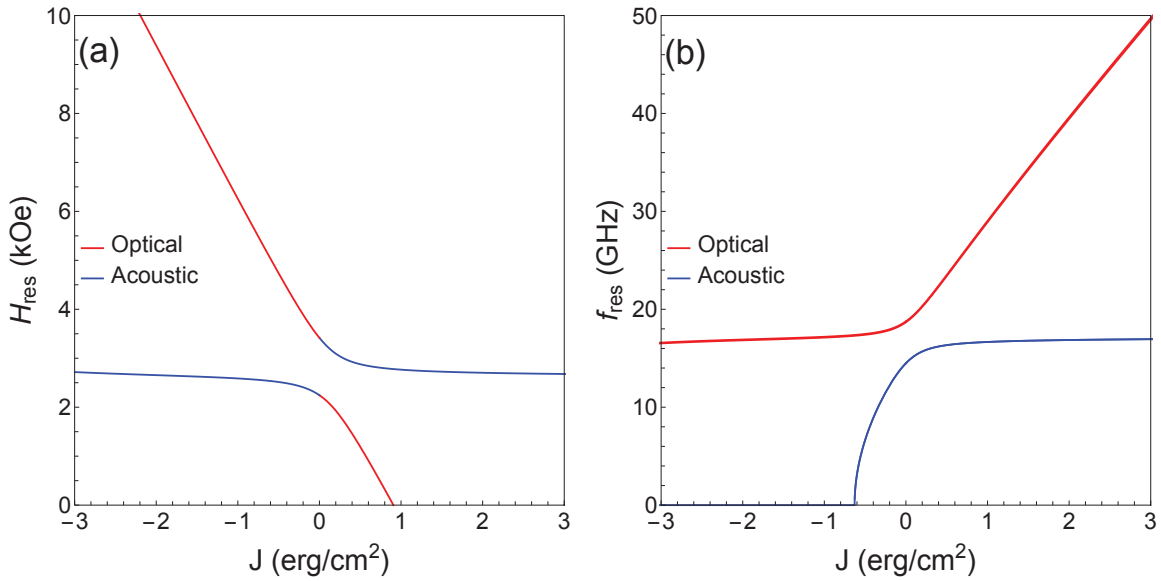

Figure 2.6: (a) the resonance fields corresponding to the FMR at f = 20 GHz of the acoustic (blue) and optical (red) modes for two coupled ferromagnetic layers with coupling strength J. (a) the resonance frequencies corresponding to the FMR at H_{DC} = 2.0 kOe of the acoustic (blue) and optical (red) modes for two coupled ferromagnetic layers with coupling strength J. Plots were determined from solutions to eq. (2.36) assuming M_{s1} = 817 emu/cm^3 and M_{s2} = 1463 emu/cm^3 and assuming K_U = 0. For $J < 0$ it is possible that the external field is not large enough to align the two magnetic moments parallel to each other, this is not captured by eq. (2.36).

will be small. In the FMR measurements this contribution is observed as a shift in the acoustic mode; for very large J the shift due to coupling reaches a stationary point and any further increase in J does not show any measurable shift in the resonance position[34].

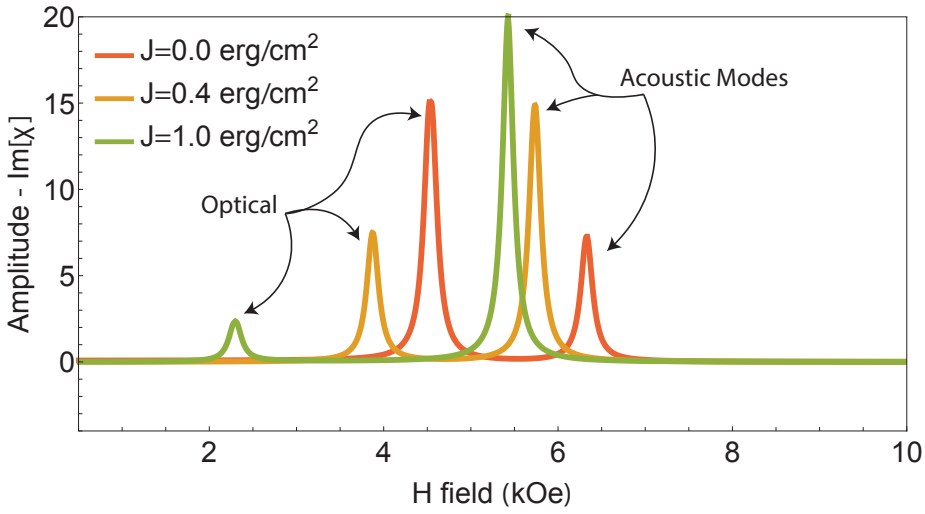

Figure 2.7: Simulation of the imaginary components of the rf susceptibility of a system of two magnetic layers undergoing various levels of interlayer exchange coupling. The layer parameters are $\alpha_1 = \alpha_2 = 8 \times 10^{-3}$, $g_1 = g_2 = 2.1$, $K_{U,1} = K_{U,2} = 0$, $d_{\mathrm{FM1}} = d_{\mathrm{FM2}} = 6$ nm $M_{s1} = 817$ emu/cm^3 and $M_{s2} = 1463$ emu/cm^3.

The optical mode is the out-of-phase precession frequency of the magnetic moments of FM1 and FM2. It is the higher energy mode for ferromagnetic coupling and starts at the lower-field resonance position, see the red line in fig. 2.6. With increasing J the energy required to excite the optical mode increases, as FM1 and FM2 become less parallel. As a result, the optical mode rapidly shifts to lower fields eventually moving below zero field becoming unmeasurable for a given frequency. In this regard, to be able to detect the resonance of the optical mode for large coupling strength, one requires a FMR setup which is able to achieve high frequencies [34]. Note, for $J < 0$ it is possible that the external DC field is not large enough to align the magnetic moments of the two layers parallel to each other. This would further limit the external field for which one can measure the antiferromagnetic coupling strength. Equation (2.36) does not capture this possibility, however in the study presented in this thesis, only ferromagnetic coupling is observed.

It is possible to model the full response of eq. (2.35) for $J > 0$, see fig. 2.7. As mentioned, both modes shift to lower field, however the optical mode shifts more quickly. It can be observed that the amplitude of the modes is dependent on the coupling strength. This is also observed experimentally and is a consequence of the in-phase and out-of-phase precession of the two magnetic layers. Since the acoustic mode is the in-phase precession, the magnetic susceptibilities of both layers add up, see fig. 2.8(b). However for the out-of-phase resonance, the susceptibilities subtract and the total response is weaker, see fig. 2.8(b). The experiment

is sensitive to the total susceptibility, therefore the response of the acoustic mode appears weaker and is more difficult to measure for larger J.

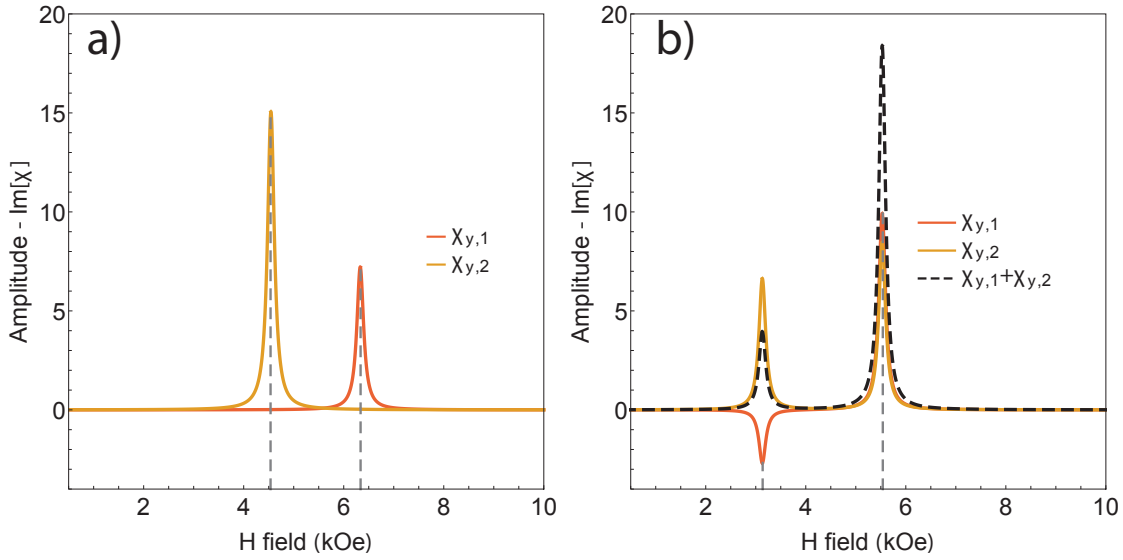

Figure 2.8: Imaginary components of the rf susceptibility of a system of two magnetic layers undergoing (a) $J = 0$ erg/cm^2 and (b) $J = 0.7$ erg/cm^2 interlayer exchange coupling strengths. The layer parameters used for this simulation are $\alpha_1 = \alpha_2 = 8\times10^{-3}$, $g_1 = g_2 = 2.1$, $K_{U,1} = K_{U,2} = 0$, $d_{\mathrm{FM1}} = d_{\mathrm{FM2}} = 6$ nm $M_{s1} = 817$ emu/cm^3 and $M_{s2} = 1463$ emu/cm^3.

2.5 Spin-Pumping

As discussed in the previous section, the magnetic moment of an out-of-equilibrium FM (its moment is not parallel with the effective field) will result in precessional and damping-like torques. The damping-like torque will eventually bring the FM into equilibrium. In a metallic FM the main source of Gilbert damping is due to the spin-orbit interactions. Without the spin-orbit coupling there would be no damping-like torque for a uniform precession mode of the FM [35]. However, even for a FM without any intrinsic damping, in contact with a NM, the interface between the two provides an opportunity to transfer the spin angular momentum from the FM to the conduction electrons of the NM. Since the total angular momentum is conserved, then the loss of the spin angular momentum of the FM results in a transfer of spin momentum to the NM. Assuming diffuse scattering, this leads to a pure-spin-current due to a thickness dependent spin accumulated density in the NM. This process was first demonstrated in Tserkovnyak *et al.*[36] where it was shown that a precessing magnetic moment of a FM resulted in a spin-current into NM. The NM reservoir was assumed to act as an ideal spin sink (perfectly absorbing all incoming spins). The spin-current was calculated by using the time dependent Brouwer's scattering matrix [37]. The

pumped spin-current from the FM into the NM at the FM/NM interface is given by [36]

$$\boldsymbol{I}_{\mathrm{sp}} = \frac{\hbar}{4\pi} g^r_{\uparrow\downarrow} \left[\boldsymbol{n} \times \frac{\partial \boldsymbol{n}}{\partial t} \right], \tag{2.38}$$

where $\boldsymbol{n}$ is the instantaneous direction of the magnetization of the FM and $g^r_{\uparrow\downarrow}$ determines the efficiency of the spin-pumping process and is referred to as the real part of mixing conductance; see eq. (2.52) below for a more precise mathematical definition.

This section presents the main concepts necessary for interpreting the experimental results presented later in the thesis. The first section introduces spin-pumping as a time-retarded extension of static interlayer exchange coupling. The second section presents spin-pumping in the more modern form as derived from scattering theory. The advantage of this treatment is that it explicitly introduces spin-pumping parameters allowing one to extend this concept to spin tranpsort by spin-diffusion in a NM. Spin-diffusion is discussed in the third section. The last section covers the full treatment of spin-pumping and spin-diffusion in a system which also experiences static interlayer exchange coupling.

2.5.1 Šimánek model

Šimánek and Heinrich [24] recognized that the spin-mixing conductance ($g_{\uparrow\downarrow}$) also enters in the derivation of the static, interlayer exchange coupling [38]. They pursued the idea that spin-pumping could be described as a form of interlayer exchange coupling (coupling between two FM through a NM). Their model takes a one atom thick FM sheet, embedded between two semi-infinite NM layers and includes the s-d interaction of the localized spin moments in the FM sheet, $\mathbf{S}$, and the electron spin density in NM layer, $\mathbf{s}(\mathbf{r}, t)$. The resulting interface energy term is given by,

$$E_{\mathrm{sd}} = -J \sum_{i}^{sheet} \int \mathbf{S}^i(t) \cdot \mathbf{s}(\mathbf{r}, t) \delta(\mathbf{r} - \mathbf{r}_i), \tag{2.39}$$

where J is the s-d exchange interaction parameter and the sum is over all the localized moments in the FM sheet given by $\mathbf{S}^i$. J is related to the interatomic exchange interaction by

$$J = 2 J_{\mathrm{sd}} \frac{\Delta V}{\hbar^2}, \tag{2.40}$$

where ΔV is the volume per atom in the NM, and J_{sd} conventional, atomic, s-d exchange interaction in erg. $\mathbf{S}(t)$ is related to the average magnetization by

$$\mathbf{S}(t) = \frac{\mathbf{M}(t) \Delta V}{\gamma}, \tag{2.41}$$

where γ is the gyromagnetic ratio.

For a FM layer of finite thickness d, with interatomic spacing a, and assuming the limit of ultrathin films (interface torque is shared by a whole FM layer) one can express a reaction field as

$$\mathbf{H}_{\mathrm{r}}(t) = \frac{2Ja}{\gamma d}\mathbf{s}(x=0,t), \tag{2.42}$$

resulting in a torque on the magnetic moment of the FM. Using linear response theory [39] and eq. (2.39) allows one to evaluate components of $\mathbf{s}(\mathbf{r},t) = s_\mu(\mathbf{r},t)$. This introduces advanced Green's functions which describe transverse spin electron correlations (transverse susceptibility) in time and space in the NM,

$$\chi_{\mu,\nu}(\mathbf{r},\mathbf{r}',t,t') = \frac{i}{\hbar}\Theta(t-t')\left[s_\mu(\mathbf{r},t), s_\nu(\mathbf{r}',t')\right], \tag{2.43}$$

where $\Theta(t-t')$ is the unit step function. $s_\mu(\mathbf{r},t)$ is then given by using the driving term $J\mathbf{S}^i(t)$ and susceptibility $\chi_{\mu,\nu}(\mathbf{r},\mathbf{r}',t,t')$ [39]

$$s_\mu(\mathbf{r},t) = J\sum_i^{sheet}\int_{-\infty}^{\infty} dt' S_\nu^i(t-t')\chi_{\mu,\nu}(\mathbf{r},\mathbf{r}_i,t,t'). \tag{2.44}$$

It is useful to Taylor expand S_ν^i in t' leading to

$$S_\nu^i(t-t') = S_\nu^i(t) - t'\frac{dS_\nu^i(t)}{dt}. \tag{2.45}$$

Note that $\chi_{\mu,\nu}(\mathbf{r},\mathbf{r}_i,t,t')$ will only depend on the differences, $\mathbf{r}_i-\mathbf{r}$ and $t-t'$, and therefore can be expressed in Fourier components as $\chi_{\mu,\nu}(\mathbf{q},\omega)$, where $\mathbf{q}$ is the space component and ω is the time component. For a planar interface (depends only the x coordinate perpendicular to the interface), eq. (2.44) can be written as

$$s_\mu(x,t) = \frac{J\Delta V}{\gamma}\left[X_{\mu,\nu}(x,\omega)M_\nu(t) - \frac{\partial X_{\mu,\nu}}{\partial\omega}\frac{dM_\nu(t)}{dt}\right]\Bigg|_{\omega\to 0}, \tag{2.46}$$

where

$$X_{\mu,\nu}(x,\omega) = n_{\mathrm{s}}\int\frac{dq_\perp}{2\pi}\exp(iq_\perp x)\chi_{\mu,\nu}(q_\perp,\omega). \tag{2.47}$$

n_{s} is the density of spins in FM, and for planner symmetry the accumulated density $s_\mu(\mathbf{r},t)$ is only dependent on the coordinate perpendicular to the interface and therefore $\mathbf{q}\to q_\perp$.

The first term in eq. (2.46) leads to accumulated spin density and was obtained by Yafet for the Ruderman–Kittel–Kasuya–Yosida (RKKY) interaction [40]. RKKY theory has had success in explaining the oscillatory ferromagnetic/antiferromagnetic dependence of interlayer exchange coupling in a system of two ferromagnets separated by a normal metal. The second term on the right hand side of eq. (2.47) is a dissipative term which represents the spin-pumping contribution to interface damping. For isotropic susceptibility the RKKY spin density at the interface is parallel to the magnetic moment and therefore

exerts no torque. The reaction field acting on FM is given by the second term in eq. (2.46),

$$H_{\mathrm{r},\mu} \simeq \frac{2J^2\Delta V a n_{\mathrm{s}}}{\gamma^2 d}\frac{\partial}{\partial\omega}\mathrm{Im}\chi_{\mu,\nu}(q,\omega)\frac{dM_\nu(t)}{dt}\bigg|_{\omega\to 0}. \tag{2.48}$$

The dissipative reaction field is proportional to the rate of change of the magnetization of FM, $dM_\nu(t)/dt$, similar to that derived by Tserkovnyak *et al.* [36] see eq. (2.55).

Using linear response theory allows one to include electron spin correlations. Assuming on-site Hubbard interactions leads to renormalization of the transverse susceptibility:

$$\chi_{\mathrm{T}}(q,\omega) = \frac{\chi^0_{\mathrm{T}}(q,\omega)}{1-\widetilde{U}\chi^0(q,\omega)} \tag{2.49}$$

where $\widetilde{U} = 4\Omega U/\hbar^2$ and U is the screened intra-atomic Coulomb energy. This modifies Equation (2.48),

$$\frac{\partial}{\partial\omega}\left[\mathrm{Im}\chi_{\mathrm{T}}(q,\omega)\right] = \left[1-\widetilde{U}\chi^0_{\mathrm{T}}\right]^{-2}\frac{\partial}{\partial\omega}\left[\mathrm{Im}\chi^0_{\mathrm{T}}(q,\omega)\right], \tag{2.50}$$

enhancing the spin-pumping strength by the Stoner factor S^2_{E},

$$S_E = \left[1-UN(E_{\mathrm{F}})\right]^{-1}, \tag{2.51}$$

where $N(E_{\mathrm{F}})$ is the density of states at the Fermi level.

In a subsequent work Šimánek showed that with increasing J the spin-pumping enhancement due to the Stoner factor, S^2_{E}, is appreciably smaller [25]. In fact for the interatomic exchange energy $J\to\infty$ the spin-pumping contribution goes to zero. This is expected since the increasing s-d atomic energy J increases the dc exchange bias effective field in the longitudinal spin direction resulting in partial suppression of transverse spin moment fluctuations making the Stoner parameter less effective.

2.5.2 Spin-pumping in spin diffusive NM

The efficienty of transfereing spin momentum from the ferromagnet (FM) to the adjacent non-magnetic metal (NM) during the spin-pumping process in a FM/NM structure is determined by the spin mixing conductance [7],

$$g_{\uparrow\downarrow} = \frac{1}{2}\sum_n\left[|r_{\uparrow,n}-r_{\downarrow,n}|^2+|t_{\uparrow,n}-t_{\downarrow,n}|^2\right], \tag{2.52}$$

where $r_{\uparrow(\downarrow),n}$ and $t_{\uparrow(\downarrow),n}$ are the spin majority (minority) reflection and transmission parameters of a NM electron in the n_{th} conduction channel impinging on the FM/NM interface. In the case of a metallic, FM that is thicker than the transverse spin coherence length, the terms $\left(t_\uparrow t^*_\downarrow\right)$ vanish and the mixing conductance does not depend on the thickness of the

FM [7]. In this case it has been shown that the real part of the spin mixing conductance dominates the spin momentum transfer, and can be expressed as [41]

$$g^r_{\uparrow\downarrow} = \mathrm{Re}\left[g_{\uparrow\downarrow}\right] = \sum_n \left[1 - \mathrm{Re}\left(r_{\uparrow,n} r^*_{\downarrow,n}\right)\right]. \tag{2.53}$$

The majority and minority reflection coefficients have independently varying phases resulting in a negligible magnitude of the cross terms ($r_\uparrow r^*_\downarrow$) for the metallic FM/NM interface [41]. Varying phases result in phase cancellation when summed over all electrons impinging at the FM/NM interface. Equation (2.53) then reduces to counting the number of single spin conduction channels at the FM/NM interface. It is useful to look at the free electron model to get a better feel for the important parameters. For a free electron model the Fermi surface is in the shape of a sphere. Therefore $g^r_{\uparrow\downarrow}$ can be determined by counting all electrons at the Fermi level which are impinging on the FM interface, resulting in

$$g^r_{\uparrow\downarrow} \approx \frac{k^2_{\mathrm{F}}}{4\pi} A, \tag{2.54}$$

where k_F is the magnitude of the Fermi wavevector and A is cross-sectional area of the sample. Since the area of all our films is the same, it is possible and convenient to set it to $A = 1$ (it divides out of all equations). The pumped spin-current from the FM into the NM at the FM/NM interface is given by [7]

$$\boldsymbol{I}'_{\mathrm{sp}} = \frac{\hbar}{4\pi} g^r_{\uparrow\downarrow} \left[\boldsymbol{n} \times \frac{\partial \boldsymbol{n}}{\partial t}\right], \tag{2.55}$$

where $\boldsymbol{n}$ is a unit vector in the direction of the instantaneous magnetic moment of the FM. Spin-pumping into a diffusive medium must be modified by replacing the spin mixing conductance $g^r_{\uparrow\downarrow}$ with $\tilde{g}_{\uparrow\downarrow}$ [7]. Therefore spin-current into a diffusive medium results in a spin-current given by

$$\boldsymbol{I}_{\mathrm{sp}} = \frac{\hbar}{4\pi} \tilde{g}_{\uparrow\downarrow} \left[\boldsymbol{n} \times \frac{\partial \boldsymbol{n}}{\partial t}\right]. \tag{2.56}$$

$\tilde{g}_{\uparrow\downarrow}$ is referred to as the renormalized spin mixing conductance (a correction for diffusive medium), which is obtained by the subtraction of a spurious Sharvin conductance g_{Sh}[42],

$$\frac{1}{\tilde{g}_{\uparrow\downarrow}} = \frac{1}{g^r_{\uparrow\downarrow}} - \frac{1}{2g_{\mathrm{Sh}}}. \tag{2.57}$$

Since the Sharvin conductance is calculated by counting the number of conduction channels and for intermetallic interfaces $g^r_{\uparrow\downarrow}$ is also mainly determined by counting the number of single spin conduction channels [41], then

$$g^r_{\uparrow\downarrow} \approx g_{\mathrm{Sh}}. \tag{2.58}$$

This approximation leads to the renormalized spin mixing conductance

$$\tilde{g}_{\uparrow\downarrow} \approx 2g^r_{\uparrow\downarrow}. \tag{2.59}$$

We will use this approximation for the remainder of this chapter. Note, from the point of view of the experiment, this is a free fitting parameter.

Diffuse electron momentum scattering at the FM/NM interface allows one to introduce the chemical potential for the majority ($\boldsymbol{\mu}_{major}$) and minority ($\boldsymbol{\mu}_{minor}$) spins in the NM which results in an accumulated spin density $\boldsymbol{S}$ in the NM. Note, $\boldsymbol{\mu}_{major}$ is defined here as a vector since the direction of the spins is always changing in time. The accumulated spin density $\boldsymbol{S}$ propagates across the NM spacer by a spin diffusion current. The accumulated spin density is given by

$$\boldsymbol{S} = \frac{\hbar}{2}\mathcal{N}(E_{\mathrm{F}})\,\Delta\boldsymbol{\mu}, \tag{2.60}$$

where $\Delta\boldsymbol{\mu} = \boldsymbol{\mu}_{major} - \boldsymbol{\mu}_{minor}$ is the chemical potential difference of the majority and minority electrons. $\mathcal{N}(E_{\mathrm{F}})$ is the single spin density of states at the Fermi level in the NM, assuming the free electron model it can shown that

$$\mathcal{N}(E_F) = \frac{k_{\mathrm{F}}^2}{4\pi^2\hbar v_{\mathrm{F}}}, \tag{2.61}$$

where v_{F} is the Fermi velocity in the NM.

Spin current injected into a diffusive medium will partially return back to the ferromagnet, this returning current is referred to as the backflow spin-current [43]. The backflow current is assumed to be perfectly absorbed by the FM and is given by [7]

$$\boldsymbol{I}_{\mathrm{bf}} = -\frac{1}{4\pi}\tilde{g}_{\uparrow\downarrow}\boldsymbol{n}\times\Delta\boldsymbol{\mu}\times\boldsymbol{n}. \tag{2.62}$$

From eqs. (2.60) and (2.62) it follows that the spin-current backflow $\boldsymbol{I}_{\mathrm{bf}}$ is proportional to the accumulated spin density $\boldsymbol{S}$ at the FM/NM interface.

For small angle of precession magnetic moment in FM is nearly perpendicular to the saturation magnetic moment and consequently the rf accumulated spin density, in the linear approximation, is also perpendicular to the saturation magnetization and will be described by $\boldsymbol{s}$. The expression $\boldsymbol{n}\times\boldsymbol{S}\times\boldsymbol{n}$ can be then replaced by $\boldsymbol{s}$ at the FM/NM interface.

Using eqs. (2.54), (2.59), (2.60), (2.62) and (2.81) one can show that the spin backflow at the FM/NM interface is given by

$$\boldsymbol{I}_{\mathrm{bf}} = -\frac{1}{2}v_{\mathrm{F}}\boldsymbol{s}(x)\Big|_{x=0}, \tag{2.63}$$

where $\boldsymbol{s}(0)$ is the rf accumulated spin density in the plane of rf magnetization precession and at the FM/NM interface and v_{F} is the Fermi velocity in the NM layer adjacent to FM layer.

The Fermi surface in zero electric field must be symmetric about the origin. Equation (2.63) states that the accumulated spin density associated with transverse rf spin-current is perfectly absorbed by the FM.

To relate the pumped spin-current to the magnetic damping of the ferromagnet we need to recall Slozewski torque,

$$\frac{d\boldsymbol{n}}{dt} = \frac{\gamma}{M_s d_{\mathrm{FM}} A} \boldsymbol{n} \times \boldsymbol{I}_{\mathrm{sp}} \times \boldsymbol{n} \tag{2.64}$$

where A is the area and d_{FM} is the thickness of the ferromagnetic material. For clarity we will rewrite the above in dot-product form

$$\frac{d\boldsymbol{n}}{dt} = \frac{\gamma}{M_s d_{\mathrm{FM}} A} \left(\boldsymbol{I}_{\mathrm{sp}} (\boldsymbol{n} \cdot \ \boldsymbol{n}) - \boldsymbol{n} (\boldsymbol{I}_{\mathrm{sp}} \cdot \boldsymbol{n}) \right), \tag{2.65}$$

and since $\boldsymbol{n}$ is a unit vector, this expression can be further simplified to

$$\frac{d\boldsymbol{n}}{dt} = \frac{\gamma}{M_s d_{\mathrm{FM}} A} \left(\boldsymbol{I}_{\mathrm{sp}} - \boldsymbol{n} (\boldsymbol{I}_{\mathrm{sp}} \cdot \boldsymbol{n}) \right). \tag{2.66}$$

From the above equation it is easy to see that if the direction of the spin-current $\boldsymbol{I}_{\mathrm{sp}}$ is perpendicular to the magnetic moment of the ferromagnet $\boldsymbol{n}$, then the torque on the ferromagnet due to spin-pumping is,

$$\frac{d\boldsymbol{n}}{dt} = \frac{\gamma}{M_s d_{\mathrm{FM}} A} \boldsymbol{I}_{\mathrm{sp}}. \tag{2.67}$$

For the case of small angle of precession the above is a very good approximation.

2.5.3 Spin diffusion theory

Spin-pumping establishes an accumulated spin density in the NM at the FM/NM interface, however, its propagation is governed by the spin diffusion equation theory. Similarly to the standard diffusion, spin diffusion is driven by the gradient of the accumulated spin density with an additional modification to allow the relaxation of spin density on time scales of τ_{sf}, leading to the spin diffusion equation

$$\frac{\partial \boldsymbol{s}_i}{\partial t} = D_i \frac{\partial^2 \boldsymbol{s}_i}{\partial x^2} - \frac{\boldsymbol{s}_i}{\tau_{\mathrm{sf},i}}, \tag{2.68}$$

where $\boldsymbol{s}_i$ is the accumulated spin density, $D_i = v_{\mathrm{F},i}^2 \tau_{\mathrm{m},i}/3$ is the spin diffusion constant, $v_{\mathrm{F},i}$ is the Fermi velocity, $\tau_{\mathrm{m},i}$ is the electron momentum scattering time, and $\tau_{\mathrm{sf},i}$ is the spin flip scattering time, all in the i_{th} layer. Since the magnetization precession times at our

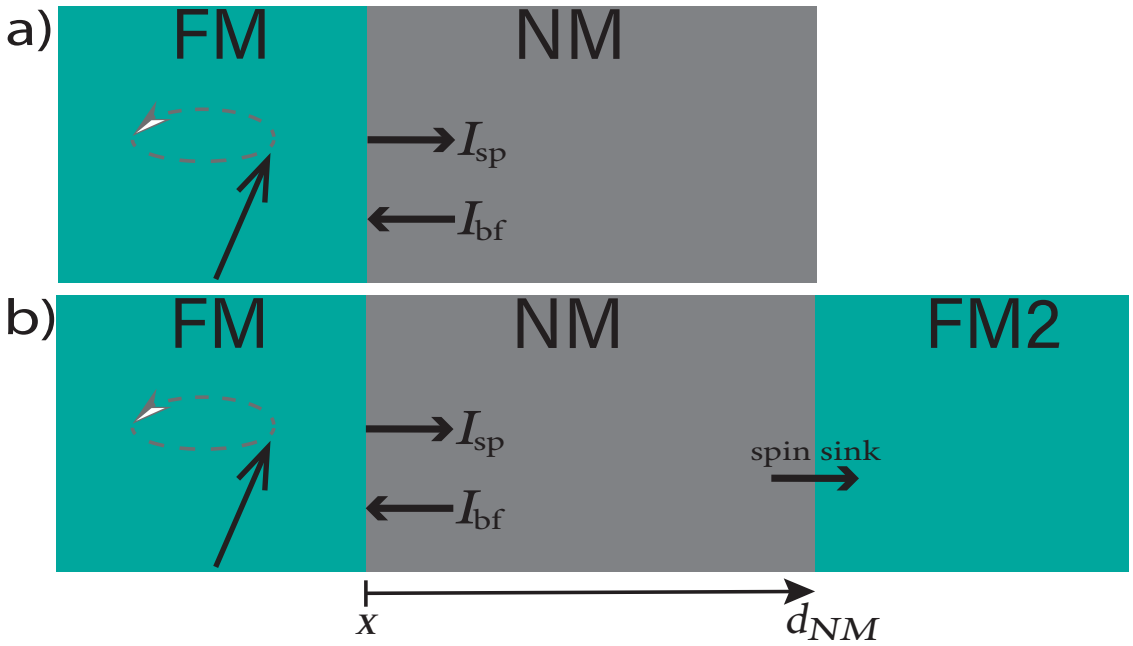

Figure 2.9: A precessing magnetization in the FM layer leads to a spin-current $\boldsymbol{I}_{\rm sp}$ in the adjacent NM layer. The net pumped spin-current it $\boldsymbol{I}_{\rm sp}^{\rm net} = \boldsymbol{I}_{\rm sp} + \boldsymbol{I}_{\rm bf}$. The boundary condition on the other side of NM is given by eq. (2.74) for the structure in a), by eq. (2.76) for the structure in b).

microwave frequencies are much longer than the spin flip relaxation times, eq. (2.68) can be approximated as time independent. The general solution takes the form of

$$\boldsymbol{s}_i(x) = A_i e^{\kappa_i x} + B_i e^{-\kappa_i x}, \tag{2.69}$$

where the coefficients A_i and B_i are determined by appropriate boundary conditions given by the magneto-electronic equations and $\kappa_i = \lambda_{\rm sd}^{-1} = 1/v_{{\rm F}i}\sqrt{\tau_{{\rm m},i}\tau_{{\rm sf},i}/3}$ is the inverse spin diffusion length. These ideas can be extended for a heterostructure of multiple NM interfaces i.e.
FM/NM1/NM2/NM3... In these cases one needs to introduce two boundary conditions at each NMi/NM$(i+1)$ interface to dictate the transport of chemical potential across each interface. The two boundary conditions solve for the two coefficients in eq. (2.69). Typically, these are the continuity of chemical potential and continuity of spin-current. However, as it is shown in chapter 9, there are other possible boundary conditions used within the literature. The remainder of this section deals with a structures consisting of only one NM, either FM/NM or FM/NM/FM2.

At the FM/NM interface the boundary conditions is given by the conservation of spin-current at the interface and states that the net spin current is sum the pumped spin current

($\boldsymbol{I}_{\rm sp}$) and the backflow current ($\frac{1}{2}v_{\rm F}\boldsymbol{s}(x)$), see fig. 2.9

$$-D\frac{\partial}{\partial x}\boldsymbol{s}(x) = \boldsymbol{I}_{\rm sp} - \frac{1}{2}v_{\rm F}\boldsymbol{s}(x).\Big|_{x=0}, \tag{2.70}$$

Note that $\boldsymbol{I}_{\rm bf}$ is defined as negative. This relationship can be rewritten as

$$\boldsymbol{I}_{\rm sp}^{\rm net} = \boldsymbol{I}_{\rm sp} + \boldsymbol{I}_{\rm bf}, \tag{2.71}$$

where $\boldsymbol{I}_{\rm sp}^{\rm net} = -D\frac{\partial}{\partial_x}\boldsymbol{s}\,(0)$ is the net spin current. The net spin-current pumped into the NM is equal to the net spin momentum lost by the FM, i.e. the induced damping in the FM layer. For ultrathin FM

$$\left(\frac{\partial \boldsymbol{M}}{\partial t}\right)_{\rm sp} = \alpha_{\rm sp}\left[\boldsymbol{M}\times\frac{\partial \boldsymbol{n}}{\partial t}\right] = \frac{\gamma}{d_{\rm FM}}\left(\boldsymbol{I}_{\rm sp} - \frac{1}{2}v_{\rm F}\boldsymbol{s}(0)\right). \tag{2.72}$$

The term before the round brackets on the RHS of eq. (2.72) takes into account the conversion from spin dynamics to magnetization dynamics and the fact that, for ultrathin FM, the interface transfer of moment is shared equally throughout the volume of FM by the exchange interaction. This equation is connects the idea of spin-pumping to an experimentally measurable quantity, the magnetic damping α. Therefore, one can introduce a spin-pumping induced damping in the FM,

$$\alpha_{\rm sp} = \frac{g\mu_{\rm B}}{4\pi M_s}\tilde{g}_{\uparrow\downarrow}\frac{1}{d_{\rm FM}}\left[\frac{1}{1+\Upsilon}\right], \tag{2.73}$$

where the form of Υ determined by the material parameters and boundary conditions of the adjacent system.

In the case of a single NM layer, FM/NM structure, (as in fig. 2.9 (a)) there is a perfect reflection of spin current at the NM/ambient interface, which is expressed as

$$-D\frac{\partial}{\partial x}\boldsymbol{s}(x) = 0\Big|_{x=d_{\rm NM}}. \tag{2.74}$$

One can show that results in a Υ in eq. (2.73) taking the form

$$\Upsilon_1 = \frac{v_{\rm F}}{2}\frac{1}{D\kappa\tanh\left(d_{\rm NM}\kappa\right)}. \tag{2.75}$$

In the ballistic limit, $d_{\rm NM}\kappa \ll 1$, and $\Upsilon_1 \to \infty$ then $\alpha_{\rm sp} \to 0$ in eq. (2.73) and there is no damping induced spin-pumping. Everything that is pumped out is perfectly returned back to the ferromagnet.

Another important boundary condition is for the FM/NM/FM2 structure where FM is the source of the spin current and FM2 is off resonances (not spin-pumping), see fig. 2.9 b)). In this case the boundary condition at $x = d_{\rm NM}$ changes to that of perfect absorption

of all the spin-current impinging on the NM/FM2 interface (perfect spin sink),

$$-D\frac{\partial}{\partial x}\boldsymbol{s}(x) = \frac{1}{2}v_{\mathrm{F}}\boldsymbol{s}(x)\Big|_{x=d_{\mathrm{NM}}}. \tag{2.76}$$

This leads to α_{sp} of the FM/NM/FM2 structure having dependence on the thickness of NM with Υ in eq. (2.73) taking the form

$$\Upsilon_2 = \frac{\frac{v_{\mathrm{F}}}{2}D\kappa + \left(\frac{v_{\mathrm{F}}}{2}\right)^2 \tanh\left(d_{\mathrm{NM}}\kappa\right)}{\frac{v_{\mathrm{F}}}{2}D\kappa + \left(D\kappa\right)^2 \tanh\left(d_{\mathrm{NM}}\kappa\right)}. \tag{2.77}$$

It is worth expanding on the consequences of using spin diffusion theory outside of its derivation. The first derivation of spin-pumping theory was assuming that the spin-current from FM is pumped into a NM reservoir, which was modeled as a perfect spin sink [36]. In a perfect spin sink implies no there is no backflow spin-current; it is assumed that the spin-current leaves the interface or decays fast enough that spin accumulation does not build up. In the diffusive NM system, one has to include the accumulated spin density, backflow spin-currents, and the renormalized spin mixing conductance, see eqs. (2.56) and (2.63). The ratio $\epsilon = \tau_{\mathrm{sf}}/\tau_{\mathrm{m}}$ is an important parameter for determining whether a particular material can be treated as a simple diffusive NM with respect to spin-currents. To illustrate this fact, it is useful to first consider the FM/NM1/FM2 system, with FM as the source of spin current (at resonance), NM1 as a diffuse spin scatterer, and FM2 as a perfect spin sink (off resonance). Allowing the NM1 layer thickness to approach 0 leads to $\lim_{d_{\mathrm{NM}}\to 0}\Upsilon_2 = 1$. In this limit, the term $[1/(1+\Upsilon_2)]$ in eq. (2.73) reduces to 1/2. Multiplying this term by the renormalized spin mixing conductance $\tilde{g}_{\uparrow\downarrow}\left(\approx 2g^r_{\uparrow\downarrow}\right)$ we recover the bare spin mixing conductance $g^r_{\uparrow\downarrow}$. This is the original result of spin-pumping as derived for pumping directly into a perfect spin sink. This is the maximum spin-pumping one can achieve.

2.5.4 Reformulation using the Einstein relation

More recently in the literature it has become more common to parameterize the spin-pumping induced damping in terms of single spin resistivity $\rho_\uparrow$ and spin diffusion length λ_{sd}. The advantage of this approach is that $\rho_\uparrow$ can be easily measured with a separate technique and used as an established parameter when fitting the spin-pumping data. It is convenient to start with the spin-pumping induced damping for the FM/NM structure (using eq. (2.73) and eq. (2.75)),

$$\alpha^{\mathrm{SL}} = \frac{g\mu_{\mathrm{B}}}{4\pi M_s}\tilde{g}_{\uparrow\downarrow}\frac{1}{d_{\mathrm{FM}}}\left[1 + \frac{v_{\mathrm{F}}}{2}\frac{1}{\frac{D}{\lambda_{\mathrm{sd}}}\tanh\left(\frac{d}{\lambda_{\mathrm{sd}}}\right)}\right]^{-1}. \tag{2.78}$$

The required equations to make the conversion are the Einstein relation,

$$\frac{1}{\rho} = D\mathcal{N}e^2, \tag{2.79}$$

where e is the fundamental charge and $\mathcal{N}$ is the density of states. The definition of the diffusion constant is

$$D = \frac{v_{\mathrm{F}}^2 \tau_{\mathrm{m}}}{3}. \tag{2.80}$$

Also, the single spin density of states for a free electron model,

$$\mathcal{N}(E_F) = \frac{k_{\mathrm{F}}^2}{4\pi^2 \hbar v_{\mathrm{F}}}, \tag{2.81}$$

and the enhanced spin-mixing conductance is

$$\tilde{g}_{\uparrow\downarrow} \approx 2g_{\uparrow\downarrow}^r \approx \frac{k_{\mathrm{F}}^2}{2\pi}. \tag{2.82}$$

Using eqs. (2.79) to (2.82) one can show that eq. (2.78) can be rewritten as,

$$\alpha_{\mathrm{sp}}^{\mathrm{SL}} = \frac{g\mu_{\mathrm{B}}}{4\pi M_s} \frac{\tilde{g}_{\uparrow\downarrow}}{d_{\mathrm{FM}}} \left[1 + \frac{\tilde{g}_{\uparrow\downarrow}\mathcal{R}}{\tanh\left(\frac{d_{\mathrm{NM}}}{\lambda_{\mathrm{sd}}}\right)} \right]^{-1}, \tag{2.83}$$

where

$$\mathcal{R} = \frac{\rho_{\uparrow} e^2}{2\pi\hbar} \lambda_{\mathrm{sd}}, \tag{2.84}$$

and $\rho_{\uparrow}$ is the single spin resistivity.

Similarly, spin-pumping induced damping for the FM/NM/FM2 structure (using eq. (2.73) and eq. (2.77)) can be rewritten as,

$$\alpha_{\mathrm{sp}}^{\mathrm{DL}} = \frac{g\mu_{\mathrm{B}}}{4\pi M_s} \frac{\tilde{g}_{\uparrow\downarrow}}{d_{\mathrm{Py}}} \left[1 + \tilde{g}_{\uparrow\downarrow}\mathcal{R} \left(\frac{1 + \tilde{g}_{\uparrow\downarrow}\mathcal{R} \tanh\left(\frac{d_{\mathrm{NM}}}{\lambda_{\mathrm{sd}}}\right)}{\tanh\left(\frac{d_{\mathrm{NM}}}{\lambda_{\mathrm{sd}}}\right) + \tilde{g}_{\uparrow\downarrow}\mathcal{R}} \right) \right]^{-1}. \tag{2.85}$$

Equations eq. (2.85) and eq. (2.83) will be heavily used throughout this thesis for the interpretation of the damping data.

2.6 Relaxation Mechanisms

There are two spin-orbit mechanisms used to interpret spin relaxation inside metals. First is the Elliott-Yafet spin scattering model, [44, 45]. In this model spin relaxation is caused by the scattering of spin on phonons and impurities in the presence of spin-orbit coupling, resulting in a linear proportionality between spin-flip and momentum scattering, $\tau_{sf}^{EY} \propto$

τ_m^{EY}. More electron scattering leads to more rapid dephasing of the spin-current. The second is Dyakonov-Perel [46] model, spin precession around an effective spin-orbit field due to broken inversion symmetry, resulting in $\tau_{sf}^{DP} \propto \left(\tau_m^{DP}\right)^{-1}$. For monatomic metals, this type of relaxation can occur due to scattering at interfaces. This is only possible if the τ_{sf}^{EY} is long enough to allow for the spin to probe the interfaces. Dyakonov-Perel becomes more dominant for low temperature measurements since τ_m^{EY} increases and therefore τ_{sf}^{EY} decreases.

The Dyakonov-Perel relaxation mechanism was originally derived for semiconductors and originates from lack of inversion symmetry (either at the interfaces or with the crystal itself). Crystals without inversion symmetry have spin splitting of the electron energies; the electron energy depends on the component of the k-vector in the direction of the spin. This energy can be expressed as $\hbar\Omega$ where Ω is the frequency of precession of the spin in the presence of an effective magnetic field which depends on the k-vector.

To get an intuitive model for the Dyakonov-Perel relaxation it is first useful to look at the limit in which the electron momentum scattering time (τ_m) is very long in comparison to the period of its precession ($\Omega\tau_m >> 1$). In this case the electron spin gets reoriented as a consequence of simple precession around an effective field. The component of spin perpendicular to H_{eff} is lost before any momentum scattering events occur. Note, this is never the case for the systems studied in this thesis. The spin precession rates are much slower than the average time it takes for the electron to traverse the film thickness.

The second limit is for low energy electrons, $\Omega\tau_m << 1$. In this case the electron precesses only a small angle before a momentum scattering event occurs. The scattering leads to a rotation of the axis of precession resulting in a new cone of precession. If the scattering rate is very high in comparison the to the precessional rate, then the electron has no time to precess and is effectively jiggling around a multitude of randomly varying effective fields. This process can be described by a random walk where the step size is Ωt_m and the time between scattering events is τ_m. The average of the square of the change in angle of the spin is then given by

$$\langle\phi^2\rangle = \frac{t}{\tau_m}(\Omega\tau_m)^2. \tag{2.86}$$

The spin-flip time is defined as the period of time over which the angle of rotation of the spin is sufficiently large, such that the spin is considered to be scattered, $\langle\phi^2\rangle \sim 1$. This results in the inverse relationship,

$$\frac{1}{\tau_s} = a\Omega^2\tau_m \tag{2.87}$$

where a is a constant to be determined experimentally [47].

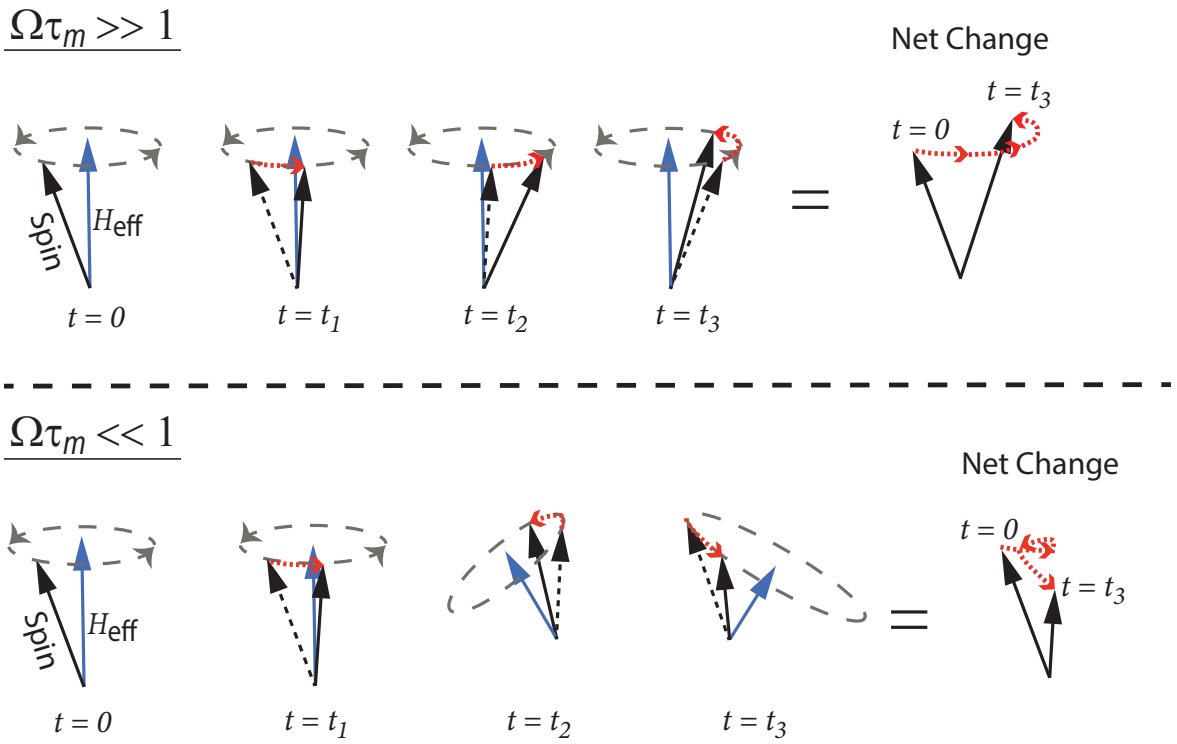

Figure 2.10: Illustration of the Dyakonov-Perel relaxation process. In the case of the Elliot-Yafet process the external field is constant and the spin gets reoriented due to a scattering event (not shown here). In the Dyakonov-Perel process the external field and therefore the torque is rapidly changing and consequently the spin gets reoriented without any scattering events. The top figure shows limit of no scattering events, the spin is precessing under the influence of a constant effective field for all time steps, t_1, t_2 and t_3. The bottom figure illustrates the Dyakonov-Perel relaxation process, the spin is continuously reoriented by a rapidly changing effective field for each time step.

Chapter 3

Sample Deposition and Characterization

3.1 RF Magnetron Sputter Deposition

Sputter deposition is a mechanism by which material is removed from one location (the target) and deposited to a different location (the substrate). It is a popular technique for creation of thin film structures. This section describes the mechanisms of rf sputter deposition.

Sputter deposition occurs inside of a vacuum chamber which is also equipped with a variety of other tools for controlling the deposition rate, see fig. 3.2. The first step is to load the chamber with the desired target and substrate and evacuate the chamber to pressures below 5×10^{-8} Torr. This is done in order to minimize impurity contamination during the film deposition. Next, a flow of Ar is established into the chamber and kept below 2.2 mTorr (see below for the purpose of the Ar gas). A rf voltage is applied to the target which initiates the sputtering process, see fig. 3.1.

Sputtering is a process by which atoms are physically ejected from a solid target due to bombardment of high-energy particles. Generally, ionized Ar atoms are used as the high-energy particles due to Argon being a noble gas and unlikely to react with the target material. A large electrical potential accelerates stray electrons which collide with neutral Ar atoms and convert them to charged particles

$$\mathrm{Ar} + e^- = \mathrm{Ar}^+ + 2e^-. \tag{3.1}$$

The ionized Ar^+ atoms are accelerated inside in the electric field and collide with the target. If the energy of the Ar^+ ion is greater than the binding energy of the target then an atom gets ejected, see fig. 3.1. This collision also causes secondary electrons to be ejected from the surface. The magnetic field, due to the permanent magnets underneath the target, confines the electrons to the region just above the target. This region of increased electron density increases the probability of another electron-Ar collision to form more ions, result-

ing in a cascading process which results in the formation of plasma above the target. A sufficiently high pressure of Ar is required to sustain this cascading process and therefore the plasma (typically < 1 mTorr). At too high of an Ar pressure there will be too many collisions and therefore the electrons will not have enough time to build up enough energy to ionize the Ar atoms (typically > 30 mTorr). During a sustained plasma there will be a continuous set of collisions of Ar^+ with the target resulting in the ejected neutral target atoms. These atoms are deposited all over the chamber, including the substrate.

During rf sputtering the alternating electric field results in a self-bias on the target. This is a result of the alternating field changing too rapidly to impart enough energy onto the Ar^+ for sputtering to occur. The electrons, however, are accelerated much more easily resulting in an abundance of electrons on the target during the positive phase of the rf cycle. The consequence is a build up of negative charge on the target which is enough to provide additional energy to the Ar^+ for sputtering to occur. For conductive targets a blocking capacitor is placed in series with the target to establish self-bias on the target.

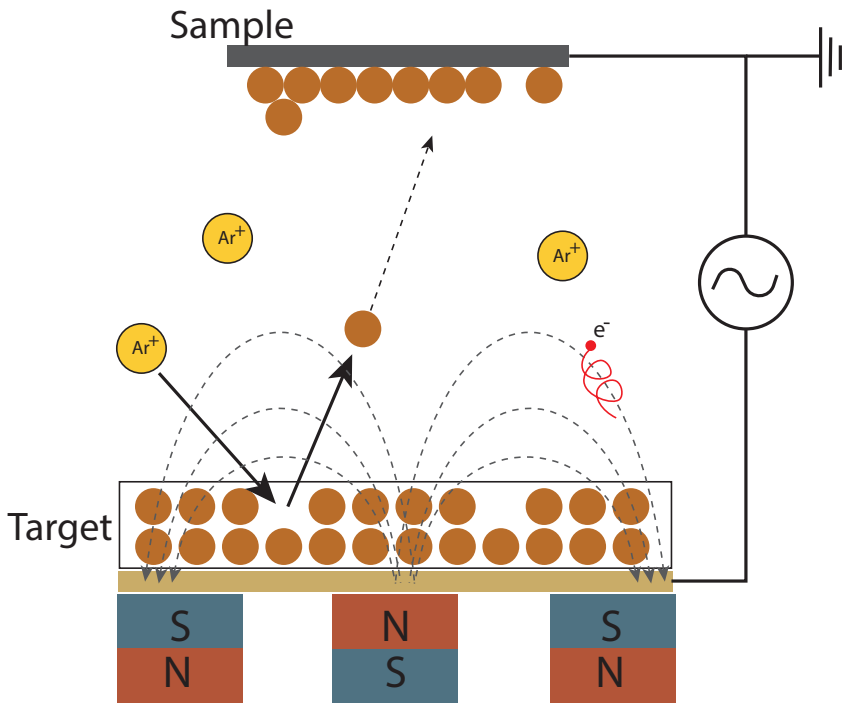

Figure 3.1: Illustration of the sputter deposition process from a single sputter gun.

3.2 Experimental Setup

The sputter deposition system (Kurt J. Lesker Company) used for the deposited films studied in this thesis is composed of a loadlock and two process chambers. The loadlock chamber can support up to 6 substrates each up to 6" in diameter. Each substrate can be

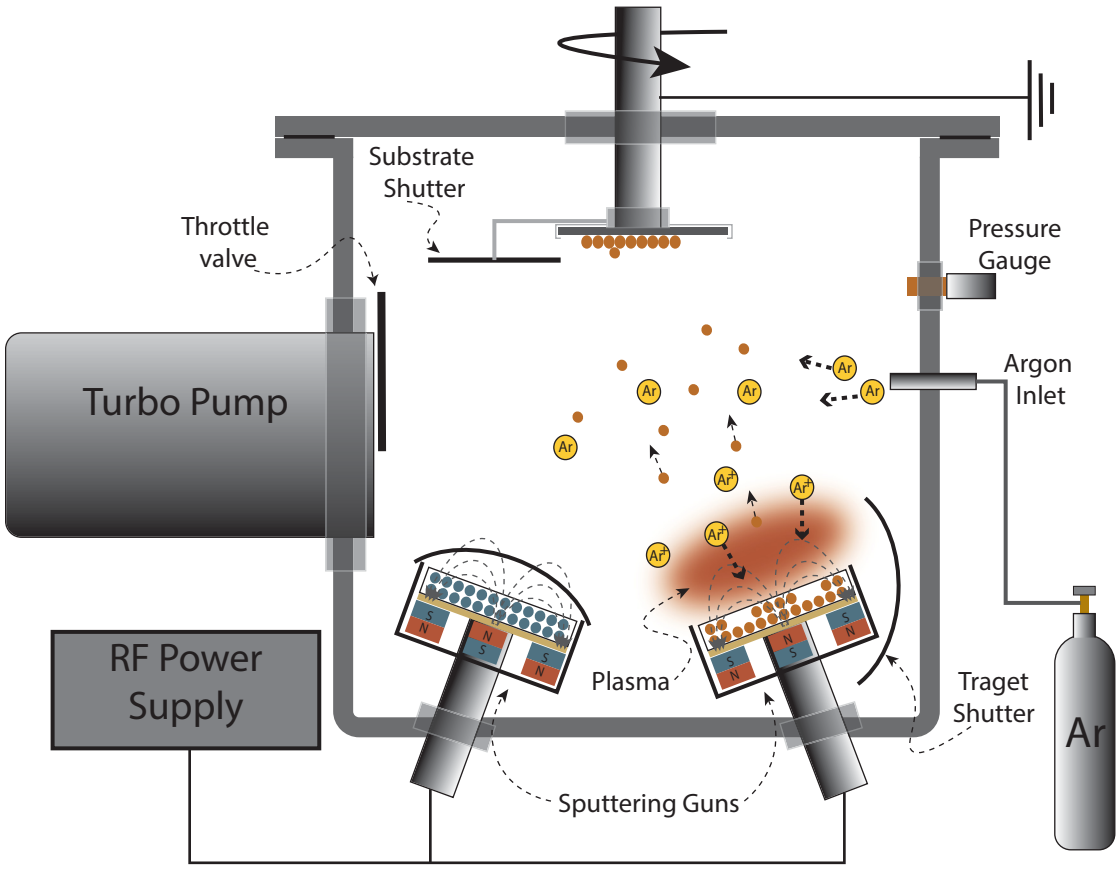

Figure 3.2: Illustration of the sputter deposition machine during deposition from one of the sputter guns. The pressure inlet, turbo pump shutter and RF power are all controlled automatically by the computer during deposition (not displayed here).

transferred to one of the two process chambers with an automated transfer arm. The first process chamber (PC1) was devoted to metallic targets and used extensively for the research in this thesis. The second process chamber was devoted to oxides. PC1 was equipped with six 2" sputter guns angled to face the substrate at a distance of approximately 30 cm from the target to the substrate. Each gun was equipped with a pneumatic shutter to prevent cross-contamination of material during the deposition of each target, which also allows for precise control of the start and stop of the deposition process. The substrate holder is also equipped with a shutter to prevent any unnecessary deposition during the cleaning of the sputter guns.

3.2.1 Substrate Preparation

Prior the start of the sputtering process, the first step is the cleaning procedure of the substrate which is done outside the sputter machine. For all samples the Si substrate cleaning was based on RCA-1 cleaning procedure. First the 6" Si(001) wafer is cut into 25×25 mm pieces. A load of 10 pieces is first cleaned in acetone in an ultrasonic cleaner at 50 °C for 10 minutes. This is repeated in an ethanol bath for another 10 minutes at 50 °C. Next, the substrates are from of the bath, one at a time, and blow dried with nitrogen. Next, the pieces are submerged in a solution of 5 parts water, 1 part 27% NH_4OH, 1 part 30% H_2O_2 at 70 °C for 15 minutes. The substrate pieces are then thoroughly rinsed in de-ionized water. Finally, the substrates are removed from the DI water bath and again blow dried with nitrogen.

After cleaning, the substrate pieces are placed into the substrate holder in the loadlock, typically 2 pieces per holder. The first holder is always loaded with glass, these samples serve as a test run for the sputter to come for the rest of the samples. The first holder is moved from the loadlock to the process chamber by the transfer arm. Sputter deposition is initiated one at a time for 5 minutes for each sputter gun. This serves two purposes, first this cleans off the native oxide layer which may have developed on the targets over night. Second, this serves as a test run for each gun to confirm that it operates within the desired Ar pressure. During deposition the substrate is rotated at 20 revolutions per minute. This ensures a more homogeneous distribution of material. The Ar inside the chamber is controlled automatically by the turbo throttle valve, see fig. 3.2. After each gun has been cleaned, the first sample holder is transferred back to the loadlock and at this point the machine is ready for deposition onto each substrate.

3.3 X-Ray Diffraction

X-ray diffraction (XRD) was used to characterize the structure of the deposited films, specifically, the lattice constant, crystal orientation, film thickness and film texture. The

measurements were performed using a PANanalytical X'Pert PRO MRD x-ray diffraction system with Cu-K_α radiation of monochromatic wavelength $\lambda_{\mathrm{CuK}\alpha} = 1.5418$ Å.

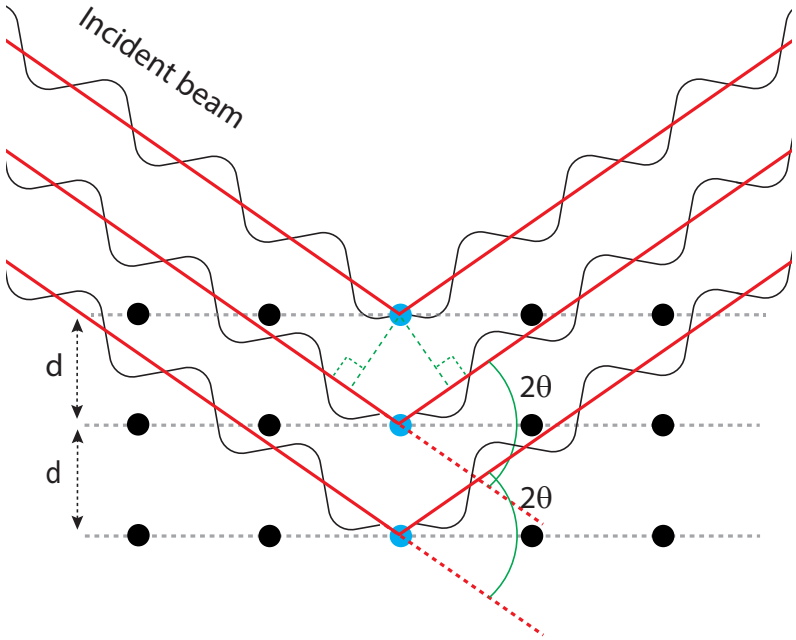

Figure 3.3: Illustration of the Bragg condition incident and reflected beams from lattice points. Constructive interference occurs when eq. (3.2) is satisfied.

XRD measurements rely on Thompson scattering, which is the elastic scattering of electromagnetic radiation with free, charged particles. The scattering is elastic due to the large difference in the energy of incoming photons and the rest-mass energy of the electron. X-ray photons, incident on the atoms of the crystal, accelerate the electrons causing them to re-emit the radiation at the same frequency as the source. Electromagnetic waves, re-emitted from electrons in the illuminated lattice, interfere at the detector. A peak intensity is measured at the detector when the scattered waves interfere constructively.

For crystalline materials, the scattering profile results in a extremely sharp peaks due to the periodicity of the structure. For a crystal structure with a periodic lattice spacing d, the constructive interference is given by Bragg's Law

$$2d\sin\theta = n\lambda_{\mathrm{CuK}\alpha}, \tag{3.2}$$

where n is an integer and θ is the angle between the incident and the diffracted x-ray beam. This relationship can be derived geometrically (see fig. 3.3). The scattering angle and vector are related through $q = 4\pi\sin(\theta)/\lambda$ and the scattering peak occurs at $q = 2\pi/d\ n$. Therefore the lattice spacing is given by $d = 2\pi/q$.

The lattice spacing of the planes parallel to the surface of the structures was determined with a $\theta - 2\theta$ type of measurement. In this configuration the x-ray beam incident angle, ω,

is half of the diffraction angle, 2θ, see fig. 3.4. In this situation the incident beam and the reflected beam are both at θ with respect to the sample surface. At some angle θ the beams interfere constructively, resulting in a peak intensity of the reflected beam. The lattice plane spacing of many materials is well tabulated in the literature which allows one to use the measured lattice spacing to determine the crystal structure and orientation of the deposited sample. The structures of the materials used in this thesis (Ta, Fe, Pt, Au, Co, NiFe) are very well established.

In some cases the spacing of the lattice planes parallel to the surface is not enough to uniquely identify the crystal structure of the material, one has to also probe the lattice spacing of planes perpendicular to the surface. This type of XRD measurement can be performed by orienting the x-ray source, sample surface and detector all in the same plane. In practice the sample is rotated such that the incident beam is at a grazing angle of 0.5°. The low incident angle results in a smaller penetration depth and higher surface structure sensitivity; this technique is advantageous for thin films and surface measurements. This type of measurement will be referred to as in-plane XRD. Due to the textured polycrystaline nature of the studied samples, the grains are generally randomly oriented within the sample plane.

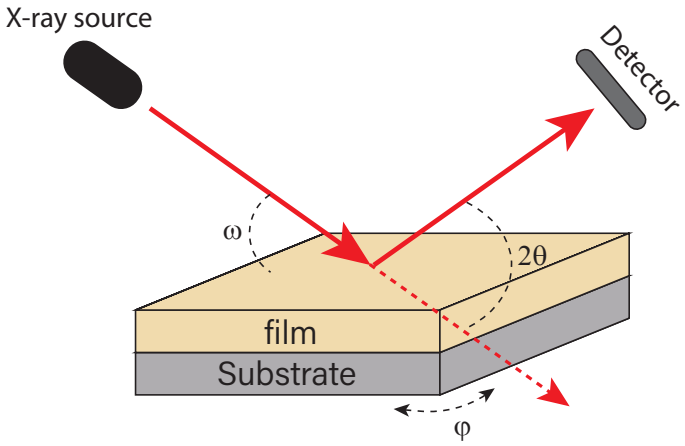

Figure 3.4: Geometry of the XRD measurement for the $\omega - 2\theta$ scan. In our measurements $\omega = \theta$.

One important parameter to gauge the quality of the deposited sample is the texture. As mentioned, the structures studied in this thesis are textured polycrystalline samples. In a highly textured sample, all the grains will be well aligned with respect to each other. The quality of the texture depends on the deposition conditions as well as the seed layers. A rocking curve type of measurement allows one to characterize the sample texture. The setup starts at the same geometry as the $\theta - 2\theta$ measurement but at an angle 2θ which results in a peak intensity on the detector. The sample is then repeatedly rotated between $-\delta\omega$ to $\delta\omega$ while 2θ is kept at a fixed value. The rocking curve captures the distribution of grain

orientations, see fig. 3.5. A poorly textured sample will have large spread of orientations and therefore will result in a much broader diffraction peak, see fig. 3.5(b). The full-width-half-maximum (FWHM) can be used as parameter to quantify the texture of a film.

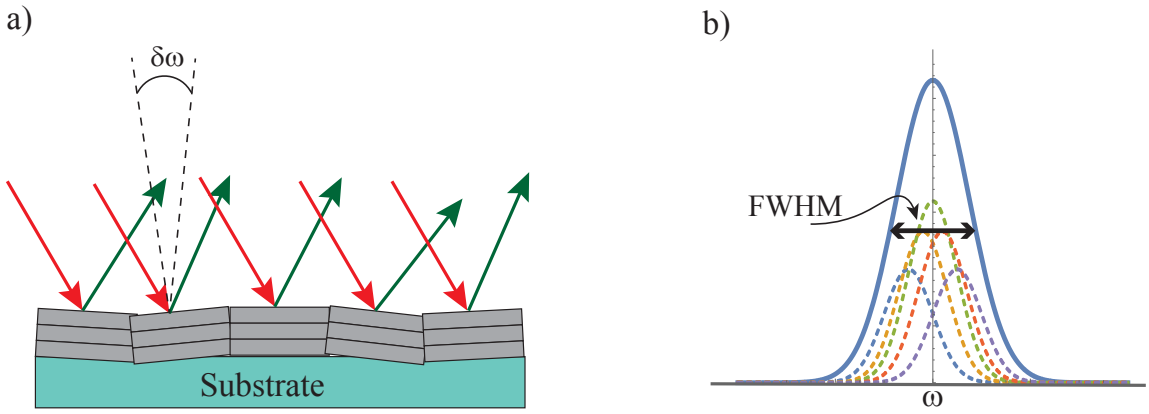

Figure 3.5: a) Illustration of the rocking curve measurement of a polycrystalline sample composed of many grains which are preferentially oriented normal to the film surface. Due to a distribution of deviations of orientations, net measured signal (b) is a sum from each individual grain and is therefore broadened by the distribution of orientations. The dashed lines in (b) represent the individual signals of each grain and the the solid is their sum.

3.4 X-Ray Reflectivity (XRR)

Low angle x-ray reflectivity (XRR) measurements were used to the determine the film thickness and calibrate the deposition rate of sputter deposition. The geometry is the same as the $\theta - 2\theta$ but at low angles ($\theta < 0.8°$). For thin films this measurement results in an exponentially decreasing oscillatory signal, known as the Kiessig fringes. A beam incident on the sample will experience a partial reflection at the interface of the film due to the change in a refractive index. Constructively interfering beams will result in peaks of the signal while destructively interfering beams will result in valleys leading to the oscillatory behaviour. It can be shown that the position of the maxima of the intensity is given by [48]

$$\frac{m\lambda_{\mathrm{CuK}\alpha}}{2} = d\sqrt{\sin^2(\theta_m) - \sin^2(\theta_c)}, \tag{3.3}$$

where θ_c is the angle at which the intensity is at half maximum, θ_m is the angle of the m_{th} fringe and d is the film thickness.

3.5 SQUID Magnetometer

A magnetometer with a superconducting quantum interference device (SQUID) is one of the most sensitive methods for measuring a magnetic moment. The SQUID magnetometer used

in the studies presented in this thesis was a commercial machine (MPMS XL from Quantum Design) which consisted of a large superconducting electromagnet and superconducting detection coils connected to a SQUID (fig. 3.6).

The measurements were performed by moving a magnetic sample through the detection coils, resulting in a change of magnetic flux and an induced electric current. The detection coils consist of a single piece of a superconducting wire wound into four coils (fig. 3.6). The upper and lower coils are wound in the opposite direction to the two center coils. The flux change in the two central coils is exactly canceled by the flux change of the top and bottom coils in the absence of sample. The top and bottom coils are just compensating the ambient magnetic field noise. In fact, this geometry is only sensitive to the second derivative of the external field. This configuration improves the signal to noise by reducing the noise from the fluctuations of the external magnetic field.

The DC SQUID is inductively coupled to the detection coils and the measurement is done with the flux-locked-loop configuration. A bias current is passed through the SQUID and a voltage is measured across the two ends of the SQUID. A measurable voltage develops when the bias current is larger than twice the critical current of each branch of the SQUID. An external magnetic field results in a screening current inside the SQUID which influences the critical current in each branch of the SQUID. Since the flux enclosed by the superconducting loop in the SQUID must be an integer number of flux quanta, the critical current will be periodic with magnetic field. Flux-locked-loop refers to the configuration in which the resulting voltage from the SQUID is used to drive another superconducting coil which opposes the flux generated by the SQUID. The SQUID should remain at zero magnetic flux condition and one only needs to the measure the current going through the flux-locked-loop to determine the magnitude of the unknown magnetic flux [49, 50].

3.6 Resistivity Measurements

Resistivity of the deposited materials was measured by using the four point probe method. This method allows one to measure the resistivity of an arbitrary shape thin film sample with constant thickness. Four electrical contacts are placed on the edges of the sample. The resistance can be determined by applying a current between contacts A and B and measuring the voltage between contacts D and C resulting in $R_A = V_{BC}/I_{AD}$ and $R_B = V_{BD}/I_{AC}$, where the I and V represent the current and voltage between the respective contacts. It was observed that a more consistent resistivity measurement could be obtained if the probes were placed along the center of the sample, see fig. 3.7(b). In this configuration the resistances are $R_A = V_{BC}/I_{AD}$, $R_B = V_{BD}/I_{AC}$, and $R_C = V_{CD}/I_{AB}$ [51]. The measurement was performed by an AC resistance bridge (Lakeshore Model 370 AC resistance bridge).

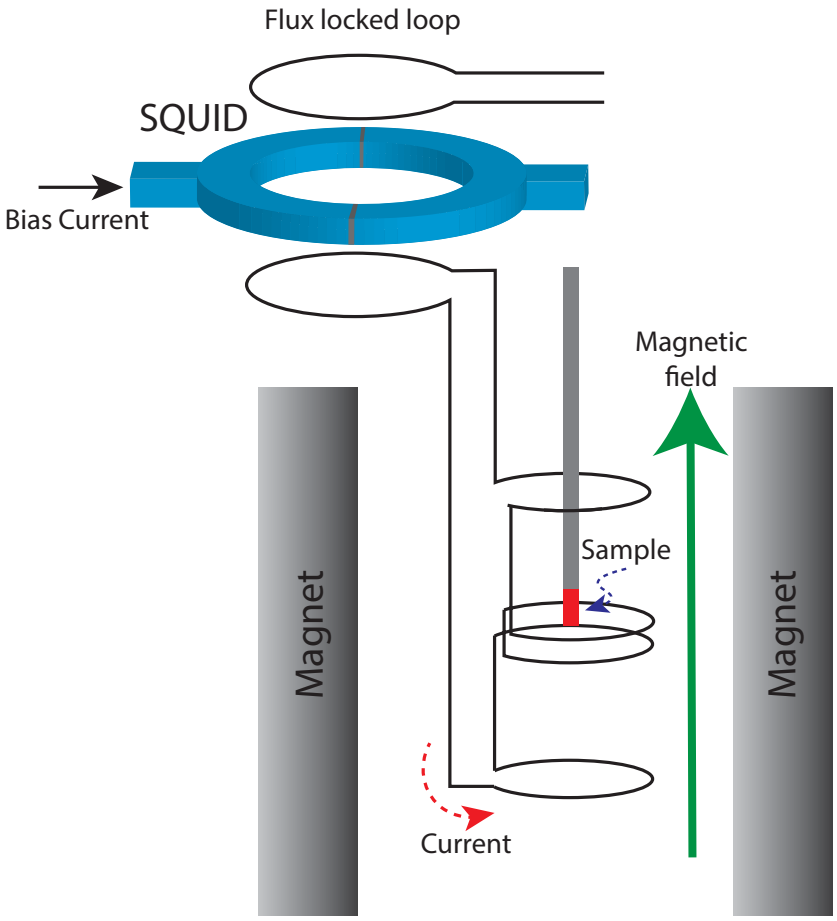

Figure 3.6: Illustration of the SQUID magnetometer.

R_A, R_B, and R_C must satisfy the following two relations, [52]

$$\exp\left(-\frac{2\pi R_A d}{\rho}\right) + \exp\left(-\frac{2\pi R_C d}{\rho}\right) = 1 \tag{3.4}$$

and

$$\exp\left(\frac{2\pi R_A d}{\rho}\right) - \exp\left(\frac{2\pi R_B d}{\rho}\right) = 1, \tag{3.5}$$

where ρ is the resistivity and d is the thickness of the film. The two equations should yield the same value for ρ within measurement error, therefore, to improve the accuracy one can average the ρ as determined from both eq. (3.4) and eq. (3.5).

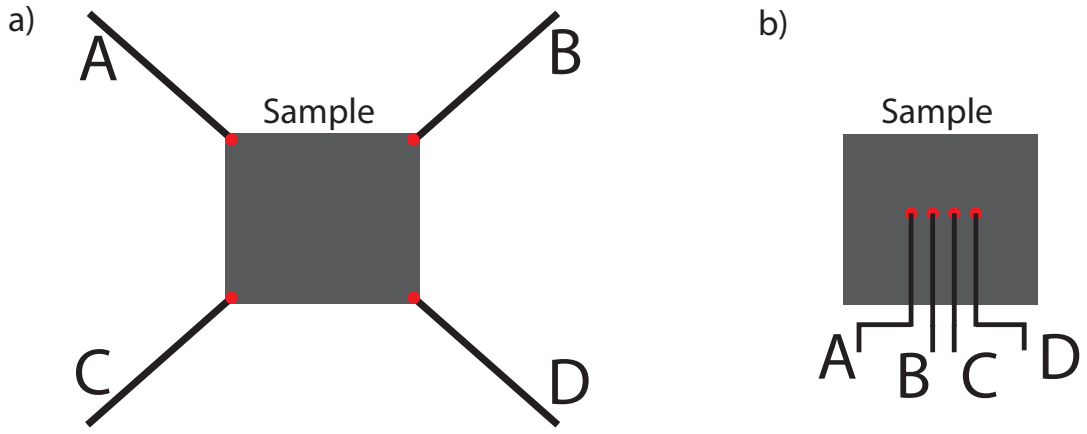

Figure 3.7: Van der Pauw measurement configuration for (a) a conventional geometry in which the probes are connected to the edges of the sample and (b) the four point probe geometry in which the probes are placed in a line along the axis of symmetry of the sample.

For the resistivity measurements the structures were deposited on glass instead of Si due to its large resistance. Importantly, during the deposition process the samples are held in place by the edges, this results in a smaller amount of material deposited on the edges than the rest of the sample. To rectify this, the edges of the samples were cut off before the resistivity measurements. The AC resistance bridge was connected to a PC via GPIB. LABVIEW code allowed for the automation of the measurement, which helped improve the signal to noise ratio.

3.7 Broadband Ferromagnetic Resonance Spectrometry

Ferromagnetic resonance spectrometry is a widely used experimental technique to study both static and dynamic magnetic properties of magnetic materials. The work presented in this thesis focuses on characterizing spin-pumping into various metals and developing a self-consistent interpretation of the experimental results. FMR is one of the few tools which allows one to accurately study the magnetic damping and therefore can be used to

determine the spin-pumping induced damping. In this thesis FMR was extensively made use of to study the magnetic properties of thin film metallic ferromagnets. This section explains the design of the FMR setup, and the equations used for the interpretation of the data; the theoretical origins of FMR are presented in section 2.3.

3.7.1 Experimental Setup

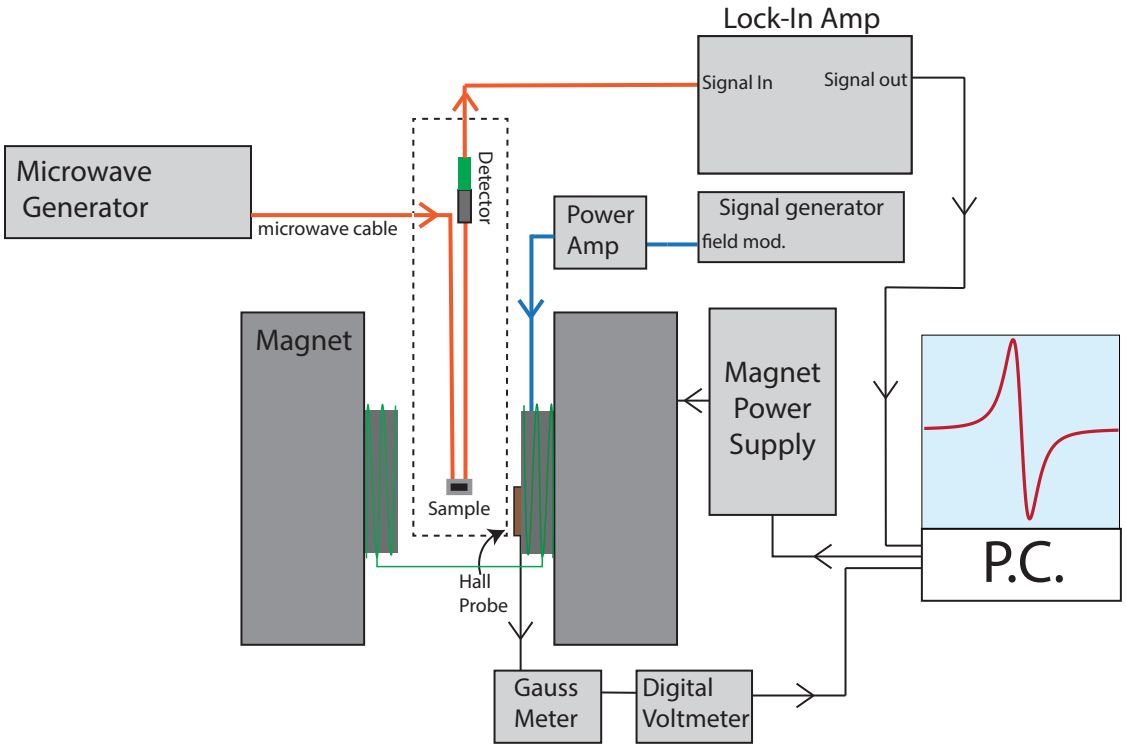

Figure 3.8: Schematic of the FMR setup using the coplannar waveguide setup. The sample is mounted at the end of the waveguide and the measured signal is proportional to the absorbed microwave power. The red lines carry high-frequency microwave signal (2-70 GHz), the blue wires carry the modulating signal (100 Hz).

The schematic of the FMR setup is presented in fig. 3.8. The signal originates from the Anritsu MG3696B microwave generator (2 to 70 GHz) and follows the microwave cable into the coplanar waveguide (CPW), fig. 3.9. The CPW is mounted in the center between the two pole pieces of a Varian 3800 electromagnet. As the signal travels through the CPW, some power may be absorbed by the sample (if in or near resonance). The resonance will be defined by the sample properties and depends on the driving frequency and the external magnetic field, see more details below. The signal coming out of the CPW then propagates into a diode detector. The diode is connected to a Stanford Research Systems SR830 DSP Lock-In Amplifier to measure the modulated signal.

The lock-in amplifier allows one to increase the signal-to-noise ratio of the FMR response. The lock-in technique requires the modulation of some parameter in the system such that signal can be measured at the same frequency as the modulation. In this FMR H_{DC} is modulated by an additional pair of coils centered around the pole-pieces of the electromagnet, fig. 3.8. The modulation is aligned in the same direction as H_{DC} but its magnitude is significantly lower. In a typical measurement H_{DC} is swept over some range and the rf driving frequency is set to a constant value. The generated external magnetic field is measured by a Hall probe which is positioned directly on the pole-pieces. As the field sweeps through the resonance of the sample, a portion of the transmitted power will be absorbed by the sample which results in a decrease in the transmitted signal. However, since the measured signal is actually modulated in field, the measured response is proportional to the field derivative of the actual transmitted signal.

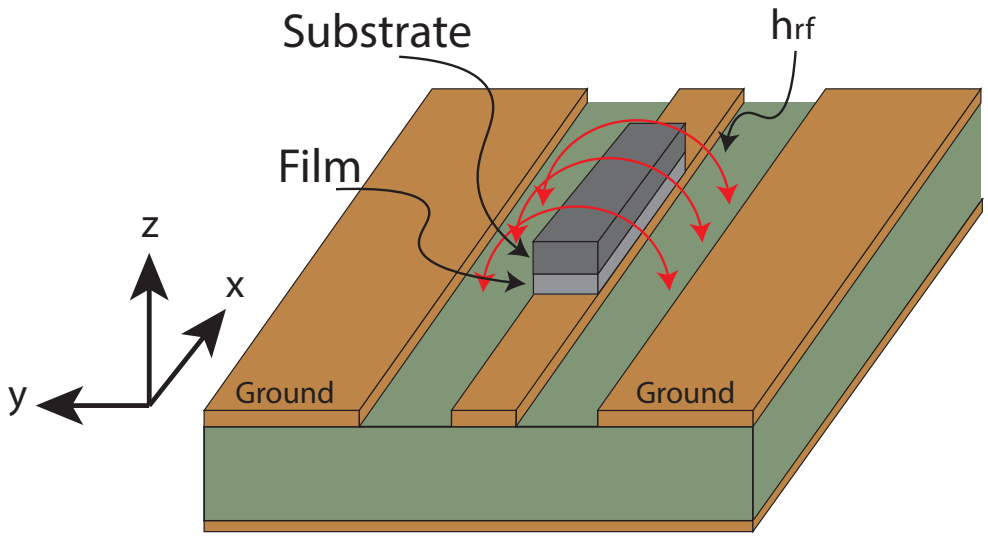

Figure 3.9: Illustration of the coplanar waveguide. The sample is mounted on the central conductor with the film side facing the conductor. The natural oxide on the conductor prevents any charge from the coplanar waveguide from leaking into the sample.

Within the CPW the sample is mounted directly on top of the central conductor with the film side facing the waveguide. The sample has to be electrically isolated from the CPW. The traveling electromagnetic wave creates an oscillatory rf magnetic field, h_{rf}, which is approximately parallel to the surface of the sample. In the presence of an external magnetic field the sample can be driven into FMR. As discussed in the section 2.3, the external field, H_{DC}, must be perpendicular to the driving field, therefore either along the x or z directions, fig. 3.9. If H_{DC} is along the x direction, then this corresponds to the in-plane measurement setup, section 2.3.1. Sample alignment is performed by adjusting the position and angle of the CPW and looking for the largest resonant field of the sample for a given frequency.

For the perpendicular-to-plane alignment, see section 2.3.2, the CPW is rotated such that the surface normal of the sample is parallel with H_{DC}. In this situation H_{DC} is along the z direction and the rf-field remains in the same y direction fig. 3.9. In order to achieve resonance in the perpendicular-to-plane geometry one needs to first overcome the effective demagnetizing field of the sample (~ 10 kOe for $Ni_{80}Fe_{20}$ or ~ 21 kOe for iron). Often the limiting resource in perpendicular-to-plane alignment is the external field, the maximum field achievable by the Varian 3800 electromagnet is 25 kOe.

A typical FMR setup uses a waveguide to propogate the rf power to the sample and the sample is situated inside of a resonance cavity at the end of the waveguide to increase the signal. This setup is beneficial for very weak signals, however it also has some practical drawbacks. To perform a frequency dependent measurement one needs to swap to a new cavity for each new measurement, re-align the sample and finally setup the measurement. This is a time consuming procedure which requires the attention of the operator. The CPW setup results in a weaker response, however, for the samples studied in this work the response is more than enough to perform a quantitative analysis, see fig. 4.4. The advantage of the CPW setup is the ability to measure the response for a large span of frequencies (2 GHz - 30 GHz) without having to adjust the setup between each measurement. This advantage allows for the capability of automation of the FMR to perform several measurements of a given sample without the operators attention. This was done in the LABVIEW code which is responsible for the data gathering. For most of the studies in this thesis the CPW is sufficient to allow quantitative analysis of the data, however, in some cases it may be important to go to higher frequencies. In the study discussed in chapter 6 it was necessary to measure up to 70 GHz in order to extract a meaningful value for the coupling strength between two ferromagnetic films. The CPW struggles to propagate any signal above 30 GHz, for such high frequency measurements it was important to use a terminated waveguide setup.

The terminated waveguide setup is very similar to the CPW. The difference being that the microwave cables and the CPW are replaced with a waveguide and directional coupler, see fig. 3.10. The sample is mounted at the end of the waveguide in the area between the pole-pieces. The elecromagnetic wave travels through the WR15 waveguide, reflects off the sample and returns into the detector. The power of the reflected signal will depend on the energy absorbed by the sample. The WR15 waveguide supports frequencies between 50-75 GHz, allowing the user to measure FMR at frequencies above CPW. Similarly to the CPW, the terminated waveguide setup allows for the measurement of multiple frequencies without any adjustment from the user which makes it applicable for automation of the measurement for multiple frequencies.

3.7.2 FMR Example Data and Analysis

In an FMR experiment the response signal is proportional to the rf magnetic susceptibility, χ_{rf}, in the direction of the applied field. The response is typically a mixture of the real and

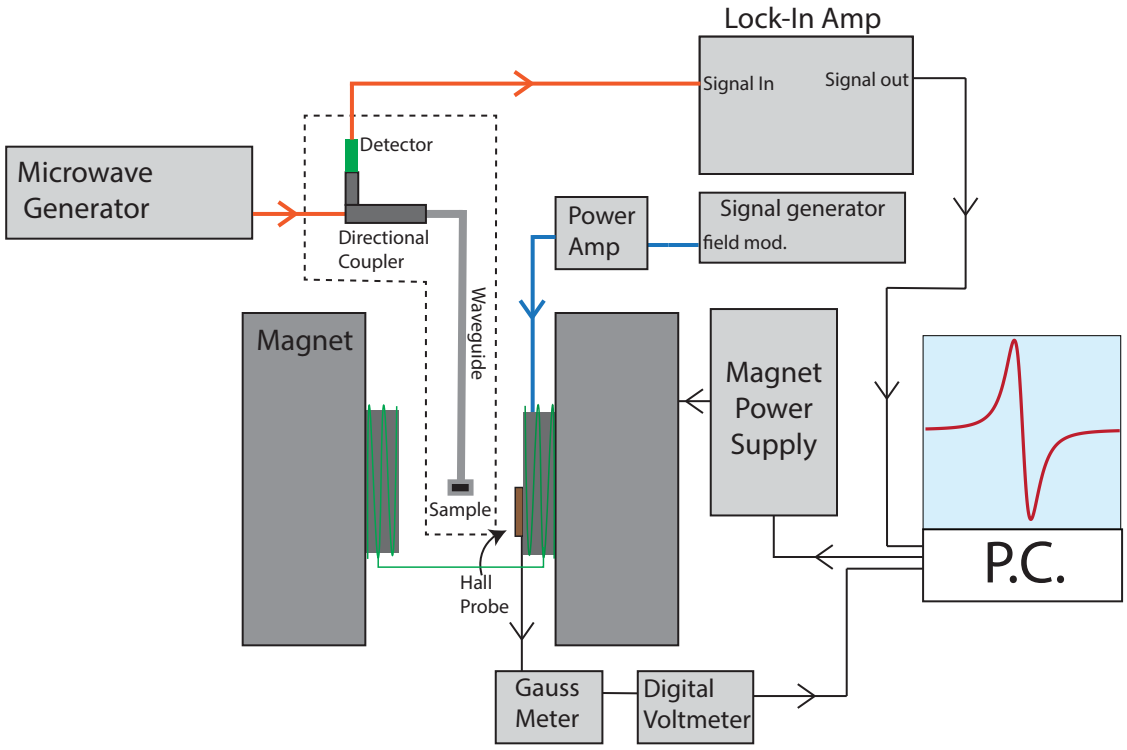

Figure 3.10: Schematic of the FMR setup using the rectangular waveguide setup. The sample is mounted at the end of the waveguide and the measured signal is proportional to the reflected microwave power. For the coplannar setup the structure outlines in the dashed line is replaced with microwave cables to carry the signal and a coplanner waveguide to excite FMR in the sample. The red lines carry high-frequency microwave signal (2-70 GHz), the blue wires carry the modulating signal (100 Hz).

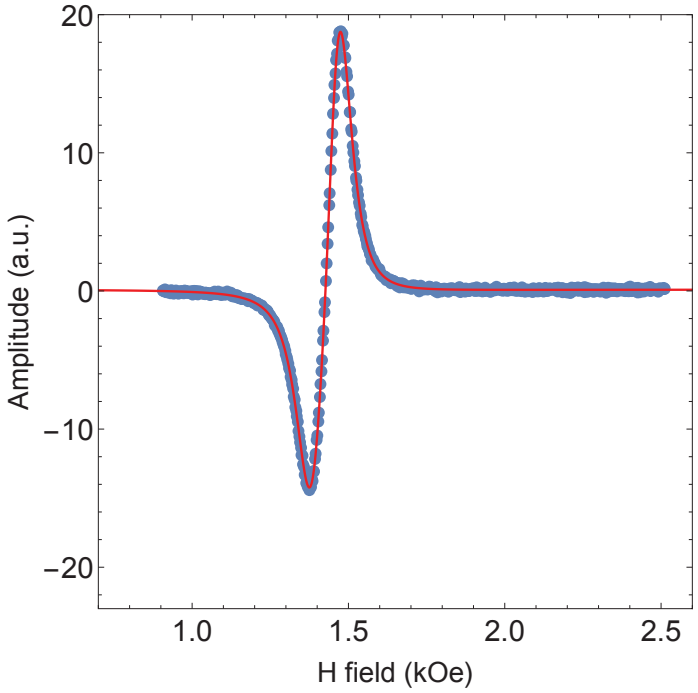

Figure 3.11: Example FMR data for Si/Py(6)/Pt(2) sample where the numbers are thicknesses in nm. The fit is performed using eq. (3.7), the relevant fitting parameters are ΔH = 72 Oe and H_{res} = 1430 Oe.

imaginary parts of χ_{rf}, which can be expressed as [21],

$$\epsilon^{\text{mix}}_{\chi_{\text{rf}}} = \epsilon_{\chi'} \sin(\phi) + \epsilon_{\chi''} \cos(\phi), \tag{3.6}$$

where $\epsilon_{\chi'}$ and $\epsilon_{\chi''}$ are proportional to the real and imaginary parts of the rf susceptibilities, ($\epsilon_{\chi'} \propto \chi'$, $\epsilon_{\chi''} \propto \chi''$), see section 2.3. ϕ is the phase used to describe the mixing of the two components. Due to the field modulation of the FMR setup described above, the measured response is proportional to the derivative of the mixed signal with respect to the field,

$$\epsilon'_{\chi_{\text{rf}}} = \frac{d(\epsilon^{\text{mix}}_{\chi_{\text{rf}}})}{dH}. \tag{3.7}$$

This equation has 4 fitting parameters: A (amplitude of the response), ϕ, H_{res} and ΔH. For the works presented in this thesis the relevant parameters are H_{res} and ΔH. In principle the proportionality constant can be used to determine the M_s of the sample however this is a much more involved process [53]. A typical FMR response and its fit by eq. (3.7) are shown in fig. 3.11

Chapter 4

Structural and magnetic studies of Py|Fe bilayers

4.0.1 Motivation

The typical spin-pumping experiments rely on a magnetic damping measurement of a ferromagnetic/ferrimagnetic material. Therefore it is important to have magnetic materials which can maximize the signal to noise of the measurement without sacrificing the reproducibility and accuracy of the experiment. To understand how one can optimize magnetic structures for a spin-pumping experiment it is useful to look at the equation of magnetic damping due to spin-pumping for a single magnetic layer structure, FM/NM (see section 2.5.4 for derivation of this equation),

$$\alpha_{\mathrm{sp}}^{\mathrm{SL}} = \frac{g\mu_{\mathrm{B}}}{4\pi M_s}\frac{\tilde{g}_{\uparrow\downarrow}}{d_{\mathrm{FM}}}\left[1+\frac{\tilde{g}_{\uparrow\downarrow}\mathcal{R}}{\tanh\left(\frac{d_{\mathrm{NM}}}{\lambda_{\mathrm{sd}}}\right)}\right]^{-1}, \tag{4.1}$$

where

$$\mathcal{R} = \frac{\rho_{\uparrow}e^2}{2\pi\hbar}\lambda_{\mathrm{sd}}. \tag{4.2}$$

e is the fundamental charge and $\rho_{\uparrow}$ is the bulk, single spin, electrical resistivity [7]. The parameters relevant to the NM are the resistivity and the spin diffusion length, $\rho_{\uparrow}$ and λ_{sd} respectively. The FM/NM interface is characterized by the spin-mixing conductivity, $\tilde{g}_{\uparrow\downarrow}$, this and the previous parameters are the targets of research. However, since spin-pumping is an interface effect, it strongly influences the adjacent FM. And as any interface effect it decreases as 1/(thickness of the ferromagnet). In our case the studies are done on thin films so the area is identical for all structures and therefore can be divided out of the equations. Therefore, the magnetic properties of the FM in eq. (4.1) depend on the g, M_s and d_{FM} as follows;

$$\alpha_{\mathrm{sp}}^{\mathrm{SL}} \propto \frac{g}{M_s d_{\mathrm{FM}}}. \tag{4.3}$$

There are effectively two important parameters which strongly influence the measured magnetic damping, the thickness of the ferromagnet (d_{FM}) and the saturation magnetization of the ferromagnet (M_s). The Lande g-factor is also involved however this is much more difficult to adjust with material properties. Therefore, it seems obvious that to get a large spin-pumping induced damping one simply needs to choose a FM with small M_s and deposit it very thinly to minimize d_{FM}. Experimentally, however, there are many other limiting factors which dictate the FM suitable for a spin-pumping experiment, such as the intrinsic damping of the FM, other possible contributions to enhancements in damping (two magnon scattering, interface roughness...) and the quality and reproduciblility of the films. In addition to these limitations for the experiments performed in this research, it was important to have structures such as FM1/NM/FM2, where the two FM1 and FM2 achieve FMR at different external magnetic fields but have very similar interfaces with the NM. This section outlines the choice of such FM materials and their subsequent optimization and characterization for the following spin-pumping experiments.

As mentioned, to increase the sensitivity of the spin-pumping experiment it seems that a good choice would be a material with low $4\pi M_s$ like the ferrimagnetic insulator yttrium iron garnet (YIG) $Y_3Fe_5O_{12}$, with $4\pi M_{s,\mathrm{YIG}} \sim 1700$ G. The additional benefit of YIG is its low intrinsic magnetic damping. Since the experimental measurement measures the total damping,

$$\alpha = \alpha_{\mathrm{sp}} + \alpha_{\mathrm{intrisic}} + \alpha_{\mathrm{other}}, \tag{4.4}$$

for a high precision measurement it is important that $\alpha_{\mathrm{intrisic}}$ is reasonably small, for thin film YIG this can be as low as $\alpha_{\mathrm{intrisic}} \sim 10^{-4}$. The benefit of the low magnetic damping of YIG is that it allows for a higher signal to noise of its FMR spectra since the width of the resonance is proportional to the magnetic damping and the extremely narrow FMR lines of YIG can be measured very precisely. It is for this reason that YIG is occasionally used in some spin-pumping studies (in addition to it being a ferrimagnetic insulator) ever since the first observation of spin-pumping from YIG [9]. The only issue with YIG is its unreliability in deposition of reproducible thin film YIG samples [54]. Since the typical spin-pumping studies focus on measuring the spin-pumping contribution to the magnetic damping of a set of structure, it is important the underling intrinsic damping of each deposited sample be highly reproducible. In fact the variation of the intrinsic damping from sample to sample is the dominating experimental uncertainty. In this regard sputter deposited Py ($Ni_{80}Fe_{20}$) provides a FM for spin-pumping studies since its magnetic properties are very consistent from sample to sample. In the studies presented in this thesis this consistency was achieved by the careful/consistent sample and sputter machine preparation (discussed in section 3.2.1). In this regard Py ($Ni_{80}Fe_{20}$) serves as a good choice and is often selected for spin-pumping studies in sputter deposited samples [55, 56, 57, 58, 59].

As will be shown, spin-pumping studies require another ferromagnet in order to obtain a unique interpretation of the results. One must simultaneously fit the magnetic damping data of both the FM1/NM and FM1/NM/FM2 structures in order to extract a unique set of parameters. A naive solution is to choose FM1=Py ($Ni_{80}Fe_{20}$) and FM2=Fe, however, as shown in this chapter, the quality of the deposited Fe films strongly depends on the underlying layers. An additional issue is that the NM in Py/NM/Fe would have an asymmetric interface with respect to spin-transport and therefore complicate the analysis. Choosing Py for both FM1 and FM2 would solve this issue, however, for interlayer exchange coupling measurements (chapter 6) it is useful that the two ferromagnetic materials have different demagnetizing fields such that they become easily distinguishable in an FMR measurement. The simplest solution is to choose a ferromagnet which consists of a bilayer of two magnetic materials [Py/Fe]. A thin layer of Py ensures that the interface with the NM is symmetric, while the Fe deposited directly on top of the Py increases the effective demagnetizing field of the direct exchange coupled [Py/Fe] structure. The interface is provided by the Py however the net magnetic moment is given by the average of the Py and Fe and therefore its FMR response is shifted away from that of Py.

This chapter presents structural and magnetic studies of [Py/Fe] structures deposited on Ta. The main goal of this study was to gain a clear understanding of the magnetic properties of Py, Fe and [Py/Fe] in order to use them in the subsequent spin-pumping/spin-transport studies.

4.0.2 Deposition and Structure Characterization

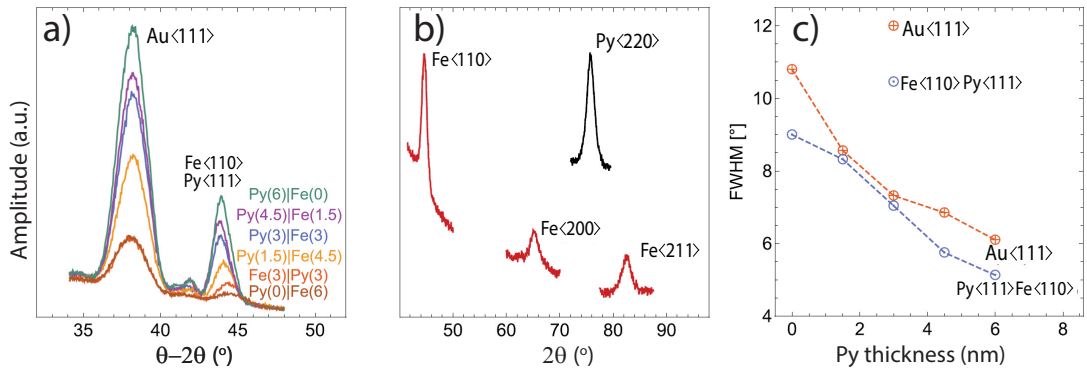

Figure 4.1: a) Out-of-plane XRD $\theta - 2\theta$ scan for Py|Fe and Fe|Py bilayers deposited on Ta and capped with Au. Layer thickness in nm are labeled in parenthesis. The peak at 38.1° is from ⟨1 1 1⟩ Au protective layer and the peak between 44.0 – 44.4° is from both ⟨1 1 1⟩ Py (bulk at 44.0°) and ⟨1 1 0⟩ Fe (bulk at 44.4°). b) In-plane XRD at 0.5° grazing incidence angle of Ta (3)|Py(1.5)|Fe(10.5)|Ta (3) (bottom peaks) and Ta (3)|Py(12)|Ta (3) (top peak). c) FWHM of XRD rocking curve of ⊕ Au and ⊙ Py|Fe peaks of Ta (3)|Py(d_{Py})|Fe($6 - d_{Py}$), dashed lines are guide for the eye.

On the cleaned Si substrate (see section 3.2.1 for cleaning procedure) an initial seed layer of 3 nm of Ta (Ta (3)) was deposited first. The Ta (3) has a mostly amorphous structure with beginnings of crystallization (see fig. 5.2) [23]. This allows for a $\langle 1\,1\,1\rangle$ growth orientation of the subsequent Py($Ni_{80}Fe_{20}$) deposited on top of amorphous Ta, see below. All structures were covered with ~ 3.6 nm of Au (Au(3.6)) to protect the rest of the film from oxidation. The full sample structures were Si|Ta (3)|Py(d_{Py})|Fe($6 - d_{Py}$)|Au (3.6) , where the numbers in parenthesis refer to the layer thicknesses in nm. The Py layer thickness is given as d_{Py}, and the total thickness of the magnetic bilayer was kept constant at 6 nm. For comparison additional structures with reversed stack order of the Py and Fe were deposited (Fe/Py).

Out-of-plane, X-ray diffraction (XRD) measurements were performed on Si|Ta (3)|Py(d_{Py})|Fe($6 - d_{Py}$)|Au (3.6) film structures for d_{Py} = 0, 1.5, 3.0, 4.5, 6.0 nm, see fig. 4.1 a). Due to the very similar lattice spacings of $\langle 1\,1\,1\rangle$ Py (bulk at 44.0°) and $\langle 1\,1\,0\rangle$ Fe (bulk at 44.4°), the XRD peaks are overlapping. As the ratio of Py is increased in comparison to Fe, the XRD peak shifts to a lower diffraction angle, consistent with a slight difference in the lattice spacings. Additionally, the intensity of the peaks increases as the ratio of Py is increased, this suggests an improvement in the texture of the structure. XRD rocking curves of the Au $\langle 1\,1\,1\rangle$ and Py $\langle 1\,1\,1\rangle$|Fe $\langle 1\,1\,0\rangle$ peaks for the Ta (3)|Py(d_{Py})|Fe($6 - d_{Py}$)|Au (3.6) and Ta (3)|Fe(3)|Py(3)|Au (3.6) samples are plotted as a function of Py thickness in fig. 4.1c).

The full width at half maximum (FWHM) of the XRD rocking curves of the Au $\langle 1\,1\,1\rangle$ and Py $\langle 1\,1\,1\rangle$|Fe $\langle 1\,1\,0\rangle$ peaks for the Ta (3)|Py(d_{Py})|Fe($6 - d_{Py}$)|Au (3.6) and Ta (3)|Fe(3)|Py(3)|Au (3.6) samples are plotted as a function of Py thickness in fig. 4.1c). The figure shows that there is indeed an increase in the texture of both Au and Py|Fe layers with increasing thickness of Py. If Fe is grown directly on top of Ta the film texture deteriorates. The increase in texture results in the increase of peak intensity in the out-of-plane XRD scans in fig. 4.1a). The texture of the Au capping layer is also improved as the result of the improved texture of Py|Fe film.

In-plane XRD of Si|Ta (3)|Py(1.5)|Fe(10.5)|Ta (3) and Si|Ta (3)|Py(12)|Ta (3) are displayed in fig. 4.1 b). The magnetic layer thicknesses for in-plane XRD were increased to improve instrument sensitivity. The in-plane XRD samples were capped with an amorphous Ta (3) [23] instead of Au (3.6) to avoid interference of the polycrystalline Au in XRD data. Both out-of-plane and in-plane measurements show that Py grows along the $\langle 1\,1\,1\rangle$ directions when deposited on Ta, the brackets represent a family of directions. In-plane XRD measurements show that Fe deposited on Py is textured along the $\langle 1\,1\,0\rangle$ crystallographic axis. For the rest of this chapter the Si|Ta (3)|Py(d_{Py})|Fe($6 - d_{Py}$)|Au (3.6) and Si|Ta (3)|Fe(3)|Py(3)|Au (3) structures are abbreviated as Py(d_{Py})|Fe($6 - d_{Py}$) and Fe(3)|Py(3) respectively, it should be assumed that there is a Ta (3) seed layer and a Au (3) capping layer unless otherwise stated.

4.0.3 Magnetic Characterization

SQUID

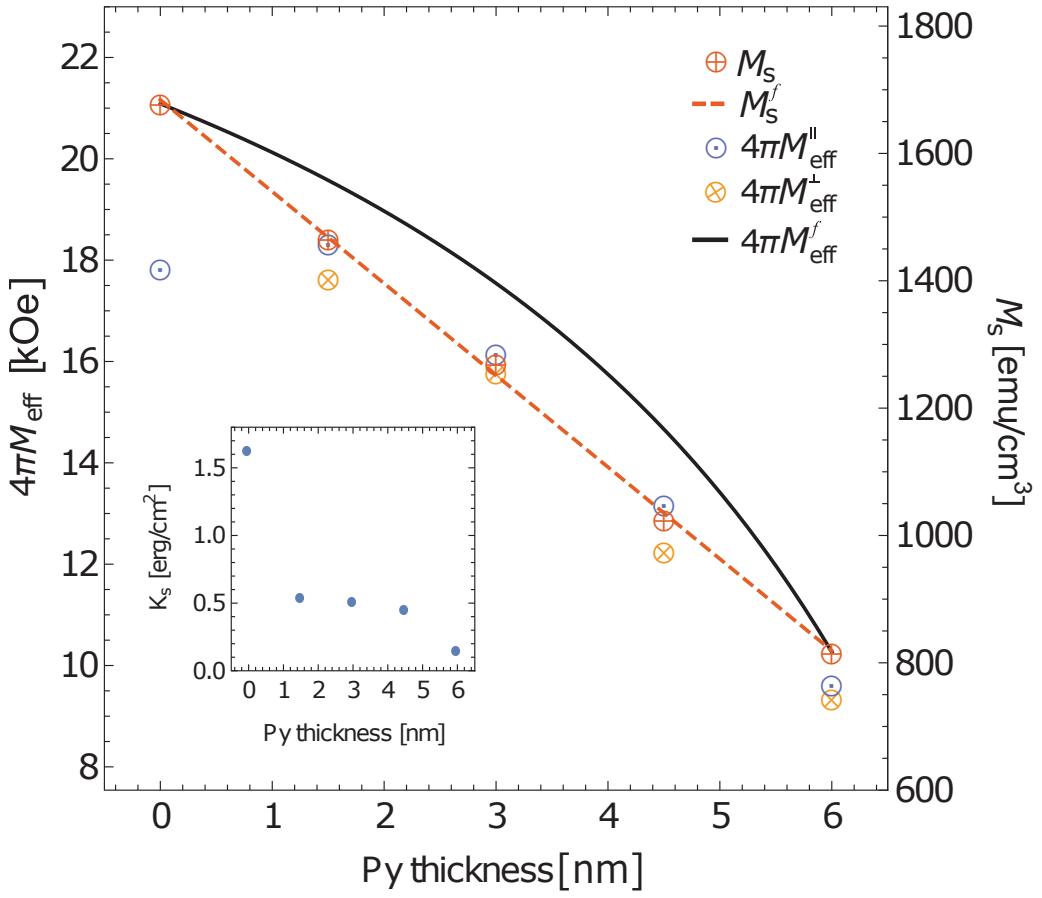

Figure 4.2: The saturation magnetization M_s as determined from SQUID measurements (right axis) and effective saturation induction $4\pi M_{\text{eff}}$ as determined by FMR (left axis) for the Py(d_{Py})|Fe(6–d_{Py}) structure. Left axis is scaled by 4π to right axis for direct comparison. The dashed line represents a linear fit to the M_{s} data using eq. (4.5) and the solid line is a plot of eq. (4.8) using M_{s}^{Py} = 817 emu/cm^3 and M_{s}^{Fe} = 1678 emu/cm^3. The interface anisotropy as extracted from eq. (4.9) is shown in the inset.

In-plane hysteresis measurements (−70 kOe to 70 kOe) were performed at 300 K to determine the magnetic moment of the studied structures using the SQUID magnetometer (see section 3.5). The samples were diced into several smaller sized pieces, adequate for the SQUID, (5x7 mm) and measured in an orientation such that the external field was parallel to the film surface. The areas of each sample were digitally determined from a magnified photograph of each sample. The thickness of the ferromagnetic films was determined from XRR calibration of the sputter deposition rate. Using the area and thickness of the film it is trivial to calculate the volume of the ferromagnetic material for each sample. The satura-

tion magnetization M_s for the samples was then determined by normalizing the measured moment by the total volume of ferromagnetic material (Py + Fe) in the sample.

The measured saturation magnetizations, M_s, of $\mathrm{Py}(d_{\mathrm{Py}})|\mathrm{Fe}(6{-}d_{\mathrm{Py}})$ is plotted in fig. 4.2. There is a linear decrease in M_s with an increasing ratio of Py to Fe. One can calculate the expected trend of M_s as a function of Py to Fe ratio by weighting the individual magnetizations by the corresponding thicknesses of each material,

$$M_s^f = \frac{M_{\mathrm{s}}^{\mathrm{Py}} d_{\mathrm{Py}}}{d_{\mathrm{Py}} + d_{\mathrm{Fe}}} + \frac{M_{\mathrm{s}}^{\mathrm{Fe}} d_{\mathrm{Fe}}}{d_{\mathrm{Py}} + d_{\mathrm{Fe}}}. \tag{4.5}$$

where $M_{\mathrm{s}}^{\mathrm{Py}}$ and $M_{\mathrm{s}}^{\mathrm{Fe}}$ are the saturation magnetization of Py and Fe, respectively, and d_{Py} and d_{Fe} are the thicknesses of Py and Fe layers, respectively. The measured magnetization values for Py (at $d_{\mathrm{Py}} = 6$ nm) is $M_{\mathrm{s}}^{\mathrm{Py}} = 817 \pm 7$ emu/cm^3 for Fe (at $d_{\mathrm{Py}} = 0$ nm) is $M_{\mathrm{s}}^{\mathrm{Fe}} = 1678 \pm 7$ emu/cm^3. One can plot the expected dependence of the average saturation of magnetization with an increasing ratio of Py to Fe, eq. (4.5), see red, dashed line on fig. 4.2. As observed, the SQUID measurements overlap with the expected average saturation of magnetization M_s^f which indicates a high quality of the sputtered films. Any defects which would reduce the measured M_s, such as a film interface oxidation, appear not to be present in the structures.

FMR - Demagnetizing Field

As discussed in the theory section, the FMR resonance condition for a textured, thin film, with zero in-plane anisotropy, in the in-plane geometry, is given by

$$\left(\frac{\omega}{\gamma}\right)^2 = (H_{\mathrm{FMR}})\left(H_{\mathrm{FMR}} + 4\pi M_{\mathrm{eff}}^{\parallel}\right), \tag{4.6}$$

where ω is the microwave frequency, $\gamma = g\mu_B/\hbar$, g is the Landé g-factor, μ_B is the Bohr magneton, $\hbar$ is the reduced Planck constant, H_{FMR} is the resonance field, $4\pi M_{\mathrm{eff}}^{\parallel} = 4\pi M_s - 2K_{\mathrm{u}}^{\perp}/M_s$ and $K_{\mathrm{u}}^{\perp}$ is the perpendicular-to-plane uniaxial anisotropy. Due to the polycrystalline nature of the samples, the in-plane magnetocrystalline anisotropy is averaged out and therefore not observed in the in-plane FMR measurements.

For perpendicular-to-plane FMR, resonance condition is given by

$$\frac{\omega}{\gamma} = H_{\mathrm{FMR}} + 4\pi M_{\mathrm{eff}}^{\perp}. \tag{4.7}$$

where $4\pi M_{\mathrm{eff}}^{\perp} = 4\pi M_s - 2K_{\mathrm{u}}^{\perp}/M_s - K_4/M_s$. For perpendicular-to-plane FMR one can measure an additional anisotropy term not observed in the in-plane measurements.

In-plane and perpendicular-to-plane FMR measurements were carried out on a coplanar waveguide for a frequency range of $6 - 36$ GHz. In-plane FMR was also performed on a terminated rectangular waveguide for a frequency range of $50 - 67$ GHz, see fig. 4.4(a), as

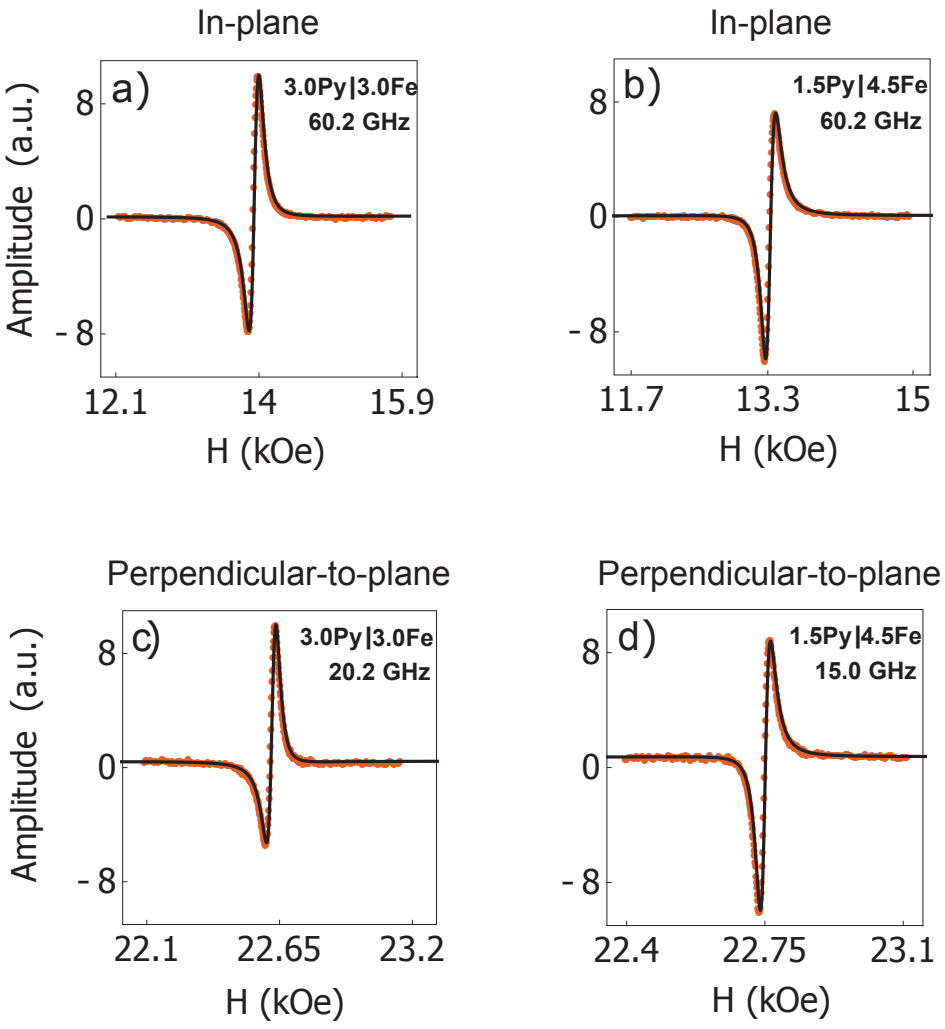

Figure 4.3: FMR spectra of a) Py(3)|Fe(3) in-plane at 20.2 GHz, b) Py(3)|Fe(3) perpendicular-to-plane at 60.2 GHz, c) Py(1.5)|Fe(4.5) in-plane at 15 GHz, and d) Py(1.5)|Fe(4.5) perpendicular-to-plane at 60.2 GHz. The solid line is a perfect fit to the signal by assuming an admixture of the out-of-phase and in-phase components of RF susceptibility, see section 3.7.2, this is a common procedure for measurements on transmission line and terminated waveguides.

detailed in section 3.7. The quality of the data for the high and low frequency measurements is shown in fig. 4.3. Fits of the resonance spectra were done using eq. (3.7), see solid black lines on section 3.7, which yielded a resonance field (H_{FMR}) and a linewidth (ΔH) for each frequency. Note, there was no observable trend in the residuals of the fits suggesting that the [Py/Fe] are indeed behaving as predicted for a strongly coupled magnetic system.

The frequency dependent resonance field measurements were interpreted by using eq. (4.6). Fitting of the in-plane and perpendicular-to-plane FMR data was performed using eq. (4.6) and eq. (4.7). During the fitting the g–factor was constrained between $g = 2.09 - 2.10$ in order to be consistent with reported literature values: $g_{\mathrm{Fe}} = 2.09$ [60, 61] and $g_{\mathrm{Py}} = 2.10$ [62, 63, 64]. Examples of the fits are presented in fig. 4.4.

For a single magnetic layer structure, without any magnetic anisotropy, the demagnetizing field is given by $4\pi M_s$. However, most real structures will have some measure of perpendicular magnetic anisotropy which is aligned with the demagnetizing field and from the point of view of an FMR measurement is indistinguishable from the demagnetizing field. Therefore one typically measures the effective demagnetizing field $4\pi M_{\mathrm{eff}}$ which is a sum of the anistropy and the demagnetizing field. The effective demagnetizing field of a bilayer system, assuming no anisotropy is given by [34],

$$4\pi M_{\mathrm{eff}}^{f} = 4\pi \frac{\left(M_{\mathrm{s}}^{\mathrm{Py}}\right)^2 d_{\mathrm{Py}}}{M_{\mathrm{s}}^{\mathrm{Py}} d_{\mathrm{Py}} + M_{\mathrm{s}}^{\mathrm{Fe}} d_{\mathrm{Fe}}} + 4\pi \frac{\left(M_{\mathrm{s}}^{\mathrm{Fe}}\right)^2 d_{\mathrm{Fe}}}{M_{\mathrm{s}}^{\mathrm{Py}} d_{\mathrm{Py}} + M_{\mathrm{s}}^{\mathrm{Fe}} d_{\mathrm{Fe}}}. \tag{4.8}$$

The plot of eq. (4.8) using $M_{\mathrm{s}}^{\mathrm{Py}}$ and $M_{\mathrm{s}}^{\mathrm{Fe}}$ from SQUID measurements is shown as a black solid line on fig. 4.2. Clearly this does not overlap with the experimental measurements for either $4\pi M_{\mathrm{eff}}^{\perp}$ or $4\pi M_{\mathrm{eff}}^{\parallel}$ and suggests that there is in fact some measurable anisotropy.

The anisotropy of the Py(d_{Py})|Fe($6 - d_{\mathrm{Py}}$) and Fe(3)|Py(3) can be determined by comparing the measured $4\pi M_{\mathrm{eff}}$ to the expected values calculated from eq. (4.8), the black solid line in fig. 4.2. All the measured values are lower than what is expected from anisotropy free structures, indicating a positive uniaxial anisotropy perpendicular to the film surface. The origin of the anisotropy can be from multiple sources: surface roughness, interface anisotropy and magnetocrystalline anisotropy. The measured in-plane effective saturation $4\pi M_{\mathrm{eff}}^{\perp}$ is lower than $4\pi M_{\mathrm{eff}}^{\parallel}$ for all samples. $4\pi M_{\mathrm{eff}}$ can be different for the in-plane and perpendicular FMR. Magnetic anisotropy perpendicular to the film surface for thin films has two parts, one is a typical uniaxial anisotropy proportional to square of $\cos^2(\theta)$ and the second is proportional to $\cos^4(\theta)$. The forth power plays no role for the in-plane FMR, but it fully contributes as a dc field for the perpendicular FMR. In-plane 4-fold anisotropy is 3^{rd} power in the effective field so in the linear approximation it is negligible. Therefore the in-plane measurements can be used to extract information about the interface anisotropies

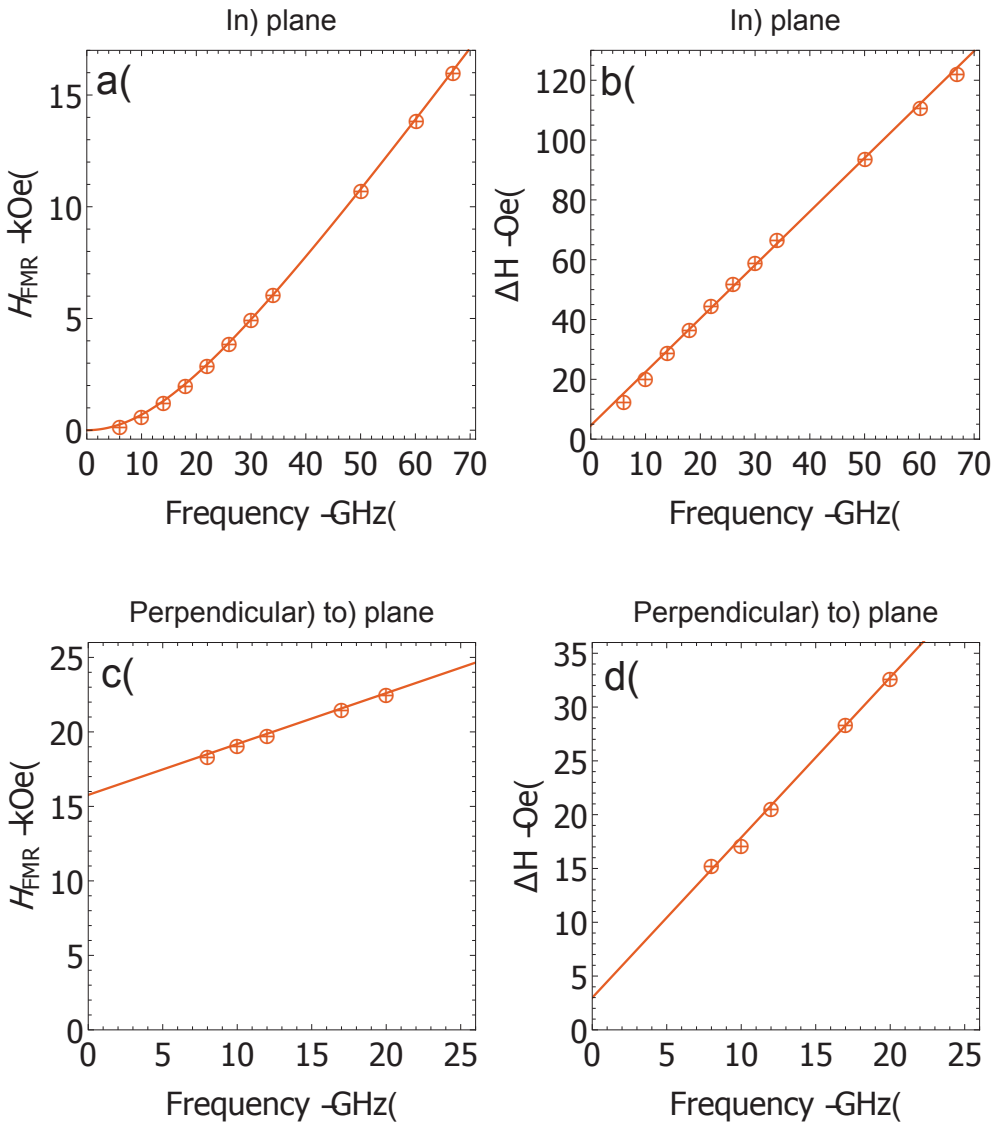

Figure 4.4: Examples of FMR data for in-plane and perpendicular-to-plane measurements of Py(3)|Fe(3) sample. The resonance fields, H_{FMR}, and the resonance peak broadening, ΔH, as a function of frequency for a), b), in-plane, and c), d), perpendicular-to-plane external field configurations.

(see inset in fig. 4.2) by using,

$$K_s = \frac{(d_{\mathrm{Py}} M_{\mathrm{s}}^{\mathrm{Py}} + d_{\mathrm{Fe}} M_{\mathrm{s}}^{\mathrm{Fe}})}{2}(4\pi M_{\mathrm{eff}}^{f} - 4\pi M_{\mathrm{eff}}^{\parallel}). \tag{4.9}$$

As expected, the interface anisotropy for the Py(6) sample is small. For the Py(4.5)|Fe(1.5), Py(3)|Fe(3) and Py(1.5)|Fe(4.5) samples the anisotropy constant increases to $K_s \sim 0.5$ erg/cm^2, similar in value to the reported interface anisotropy of $\langle 1\,1\,0\rangle$Fe|Au [65]. For the Fe(6) sample, the interface anisotropy jumps to $K_s \sim 1.6$ erg/cm^2 due to the presence of both Ta|Fe and Fe|Au interfaces.

4.0.4 Magnetic Damping and Spin-Pumping

Measurements of the magnetic damping were determined from the linewidth of the FMR response. The linewidth is well described by Gilbert-like damping,

$$\Delta H(\omega) = \alpha \frac{\omega}{\gamma} + \Delta H(0), \tag{4.10}$$

where $\Delta H(0)$ is the zero-frequency line broadening due to magnetic inhomogeneity [34, 66, 67] and the slope determines the effective damping parameter α. As before, g–factor was constrained between $g = 2.09 - 2.10$ for the fits for $\Delta H(0)$ and α [62, 63, 64].

Measurements of the in-plane and perpendicular-to-plane magnetic damping values are displayed in fig. 4.5. In-plane FMR measurements of Fe sputtered directly on Ta yields a high value for both $\Delta H(0) = 96$ Oe and $\alpha^{\parallel}_{\mathrm{Fe(6)}} = 11.5 \times 10^{-3}$. This could be improved if Py was deposited on top of Fe as in the Fe(3)|Py(3) sample resulting in $\Delta H(0) = 20$ Oe and $\alpha^{\parallel}_{\mathrm{Fe(3)|Py(3)}} = 8.7 \times 10^{-3}$. However, a more dramatic improvement in the measured damping is observed if Py is deposited before Fe. For the Py(1.5)|Fe(4.5) structure, this results in a reduction of magnetic damping by up to a factor of 3 leading to $\alpha^{\parallel}_{\mathrm{Py(1.5)|Fe(4.5)}} = 4.6 \times 10^{-3}$ and $\Delta H(0) = 7$ Oe. This is nearly two times lower than the damping of the pure Py sample, Py(6), $\alpha^{\parallel}_{\mathrm{Py(6)}} = 7.9 \times 10^{-3}$. The measured damping of the Py(6) sample is the same as that reported for bulk Py [68, 69]. Importantly, depositing Py before the Fe also leads to a large reduction in $\Delta H(0)$ with the insertion which be attributed to exchange narrowing [70]. Fe deposited before Py (directly on Ta) leads to larger grains in Fe which have a greater spread in their distribution, this is consistent with the decrease in film texture of Fe/Py samples (see fig. 4.1 c)). A distribution of grains orientations, will lead to a distribution of resonant fields leading to a large magnetic inhomogeneity. As the grains become small enough, and more textured, the exchange field will decrease the variations of internal fields by the exchange narrowing effect [70]. Depositing Py before Fe sets up the grow of the subsequent Fe and allows it to grow more textured with smaller grains.

Perpendicular-to-plane FMR measurements, the solid blue line in fig. 4.5, yield a damping consistently lower than the in-plane, solid red line in fig. 4.5, by $\Delta\alpha = \alpha^{\parallel} - \alpha^{\perp} = 0.7 \times 10^{-3}$.

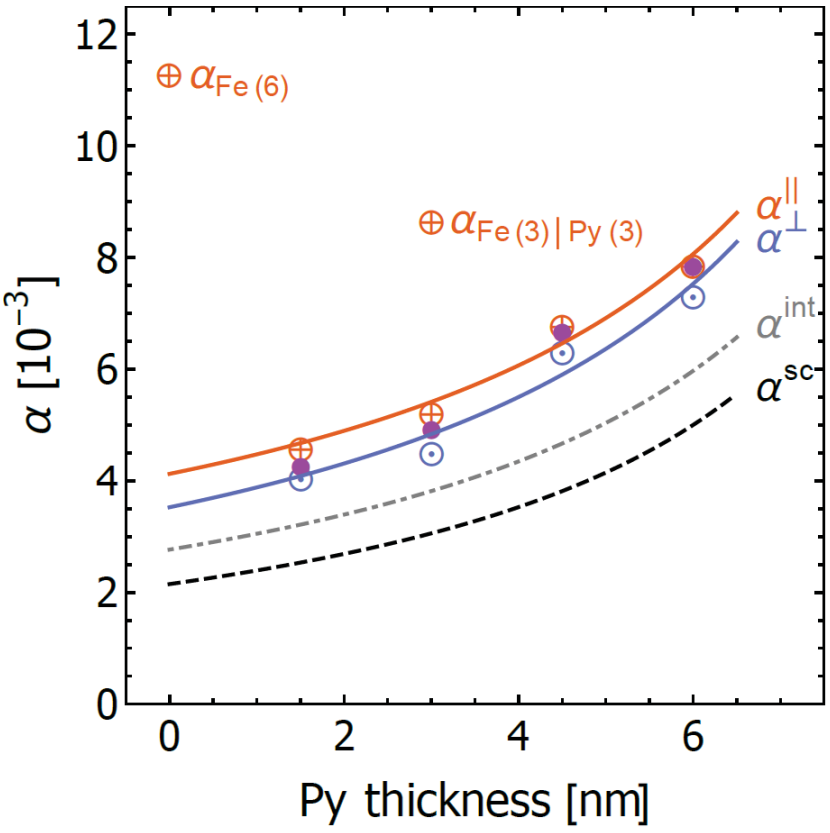

Figure 4.5: Gilbert damping as function of Py thickness (d_{Py} = 0, 1.5, 3.0, 4.5, and 6.0 nm) in magnetic bilayer Py(d_{Py})|Fe(6 − d_{Py}). Data is shown for all in-plane frequencies (⊕), high in-plane frequencies 50-67 GHz (●), and perpendicular-to-plane (⊙) FMR configurations. The solid lines, $\alpha^{\perp}$ and $\alpha^{\parallel}$, are fits to the data using eq. (4.11). The two outlier points show very large enhancement in damping for samples where Fe was deposited before Py. α_{int} is the fit of the perpendicular-to-plane damping using eq. (4.11), with the contribution due to spin-pumping in Ta subtracted off (see chapter 5 for determination of spin-pumping contribution). The fitting parameters are $\alpha_{\mathrm{int,Py}} = \alpha^{\perp}_{\mathrm{Py}} - \alpha_{\mathrm{sp,Py}} = 6.0(4) \times 10^{-3}$ and $\alpha_{\mathrm{int,Fe}} = 2.8(4) \times 10^{-3}$. α^{sc} is an estimate of the damping for a bulk single-crystal structure of Py|Fe from eq. (4.11).

One possibility is that the discrepancy is from to two-magnon scattering in the in-plane FMR [71]. The origin of two-magnon scattering is due the presence of spin-wave modes degenerate with the FMR mode. In the perpendicular-to-plane orientation there are no magnons degenerate with FMR modes and therefore two-magnon scattering does not contribute to the measured damping [34]. Evidence of two-magnon contribution is present in the dependence of in-plane ΔH in fig. 4.4b), which shows a slight deviation from linear behaviour at low frequencies, < 15 GHz, consistent with two-magnon behaviour [71]. The lowest total measured damping is $\alpha^{\perp} = 4.1 \times 10^{-3}$ for the Py(1.5)|Fe(4.5) structure. Since the two-magnon scattering contribution saturates at higher frequencies, we extracted the in-plane damping for the high frequency (50 - 67 GHz) and low frequency (6 - 14 GHz) measurements separately using eq. (4.10). The low frequency fits yield larger damping, $\alpha^{\parallel}_{\text{LowFreq.}} = 5.7 \times 10^{-3}$ and $\Delta H = 1.4$ Oe for the Py(1.5)|Fe(4.5) sample. The high frequency data yield lower damping, $\alpha^{\parallel}_{\text{HighFreq.}} = 4.3{\times}10^{-3}$, and $\Delta H = 12$ Oe for Py(1.5)|Fe(4.5). For this sample the $\alpha^{\parallel}_{\text{HighFreq.}}$ and $\alpha^{\perp}$ are very similar, suggesting that the discrepancy is mostly due to two-magnon scattering. However, for the thicker Py samples the difference between $\alpha^{\parallel}_{\text{HighFreq.}}$ and $\alpha^{\perp}$ increases, see fig. 4.5. In fact, for the Py(6) sample there is no evidence for two-magnon behaviour in the measured frequency range, $\alpha^{\parallel}_{\text{HighFreq.}} = \alpha^{\parallel}_{\text{LowFreq.}}$. The discrepancy between $\alpha^{\perp}$ and $\alpha^{\parallel}$ for the thicker Py samples could be because two-magnon scattering saturates at a much higher frequency. Alternatively, it could be due to the difference in intrinsic damping of the two orientations, not uncommon for thin film structures.

The damping measured by FMR is the total damping of the entire bilayer structure, averaged by the relative magnetic moment of each layer. Given that the damping of Py is relatively high, it must mean that the damping of the Fe layer deposited on top of Py is quite low. A quantitative analysis of damping can be done by assuming strong coupling between Py and Fe [34],

$$\alpha_{\text{Py|Fe}} = \alpha_{\text{Py}} \frac{d_{\text{Py}} M_{\text{s}}^{\text{Py}}}{d_{\text{Py}} M_{\text{s}}^{\text{Py}} + d_{\text{Fe}} M_{\text{s}}^{\text{Fe}}} + \alpha_{\text{Fe}} \frac{d_{\text{Fe}} M_{\text{s}}^{\text{Fe}}}{d_{\text{Py}} M_{\text{s}}^{\text{Py}} + d_{\text{Fe}} M_{\text{s}}^{\text{Fe}}}. \tag{4.11}$$

Results of fitting the in-plane damping data using the above equation are: $\alpha^{\parallel}_{\text{Py}} = 8.1(3){\times}10^{-3}$ and $\alpha^{\parallel}_{\text{Fe}} = 4.1(3) \times 10^{-3}$, see red solid line in fig. 4.5. Fitting the perpendicular-to-plane damping data leads to: $\alpha^{\perp}_{\text{Py}} = 7.5(4) \times 10^{-3}$ and $\alpha^{\perp}_{\text{Fe}} = 3.5(4) \times 10^{-3}$, see blue line in fig. 4.5.

Finally, it is interesting to determine and compare the intrinsic damping of the polycrystalline structure to the expected values from an equivalent bilayer of single crystal materials. The total damping is the sum of the intrinsic and extrinsic dampings, where the extrinsic arises from the spin-pumping of Py|Fe into the seed Ta layer, $\alpha = \alpha_{\text{int}} + \alpha_{\text{sp}}$. The enhancement in damping due to spin-pumping is given by [7]

$$\alpha_{\mathrm{sp}}^{\mathrm{SL}} = \frac{g\mu_{\mathrm{B}}}{4\pi M_s}\frac{\tilde{g}_{\uparrow\downarrow}}{d_{\mathrm{FM}}}\left[1+\frac{\tilde{g}_{\uparrow\downarrow}\mathcal{R}}{\tanh\left(\frac{d_{\mathrm{Ta}}}{\lambda_{\mathrm{sd}}}\right)}\right]^{-1}. \tag{4.12}$$

where $\mathcal{R} = \frac{\rho e^2}{2\pi\hbar}\lambda_{\mathrm{sd}}$, e is the fundamental charge and ρ is the single spin resistivity, d_{FM} is the thickness of the ferromagnet ($d_{\mathrm{Py}} + d_{\mathrm{Fe}}$), $\tilde{g}_{\uparrow\downarrow}$ is the renormalized spin mixing conductance which determines the efficiency of spin-pumping and depends on the Ta|Py interface, M_s is the average in Ta. Using the parameters from Montoya *et al.* [23] (see next chapter for determination of these parameters) of $\lambda_{\mathrm{sd}} = 1.0$ nm, $\rho = 300$ $\mu\Omega$cm , and $\tilde{g}_{\uparrow\downarrow} = 1.5\times10^{15}$ cm^{-2} as well as M_s from SQUID measurements in fig. 4.2, one can determine the spin-pumping into Ta for any Py(d_{Py})|Fe($6 - d_{\mathrm{Py}}$) structure. The intrinsic damping, α_{int}, is obtained by subtracting the spin-pumping contribution, α_{sp}, from perpendicular-to-plane damping obtained from fitting using eq. (4.11), the dashed gray line in fig. 4.5. For Py(1.5)|Fe(4.5), the perpendicular-to-plane damping, $\alpha^{\perp}$, without spin-pumping, is $\alpha_{\mathrm{int}} = \alpha - \alpha_{\mathrm{sp}} = 3.0\times10^{-3}$, approaching the damping for perfect single crystal Fe [60], $\alpha_{\mathrm{Fe}} \sim 2.1\times10^{-3}$. One can also estimate the intrinsic damping for an equivalent single crystal Py|Fe structure, α^{sc}, by using bulk single crystal damping parameters of Py ($\alpha_{\mathrm{Py}}^{\mathrm{sc}} = 5\times10^{-3}$) [72] and Fe ($\alpha_{\mathrm{Fe}}^{\mathrm{sc}} = 2.1\times10^{-3}$) [60] in eq. (4.11) assuming $\alpha_{\mathrm{sp}} = 0$, see black bottom dashed line in fig. 4.5.

Additional samples, Si|Ta|Py(1.5)|Fe(4.5)|Ta (3), where we covered the Fe layer with Ta instead of Au were deposited in order to test if the large increase in α of the Fe(6) structure vs. the Py(1.5)|Fe(4.5) structure is due to spin-orbit coupling at the interface of Ta|Fe. In this case the Fe layer shares an interface with the Ta layer, similar to the Fe(6)|Au (3.6) structure. It was observed that for the Si|Ta|Py(1.5)|Fe(4.5)|Ta (3) structure the $4\pi M_{\mathrm{eff}}$ is equal to that of Si|Ta|Py(1.5)|Fe(4.5)|Au (3.6). A small increase of α in Si|Ta|Py(1.5)|Fe(4.5)|Ta (3) in comparison Si|Ta|Py(1.5)|Fe(4.5)|Au (3.6) can be attributed to additional spin-pumping at the second Fe|Ta interface. This suggests that spin-orbit coupling at the Ta|Fe interface plays a minimal role in increasing the damping, however, this interpretation has a possible flaw. The Fe deposited on amorphous Ta [23] is poorly textured, see fig. 4.1a) and c). In this case where Fe initially grows on Ta, the Fe layer may have grains oriented in different directions and after some thickness Fe grains that do not grow along the ⟨1 1 0⟩ crystal orientation get annihilated. As a result the two interfaces, Ta|Fe and Fe|Ta, are different. The Ta|Fe interface may be an ensemble of the different orientations of Fe grains on Ta such as: Ta|Fe⟨1 1 0⟩ and Ta|Fe⟨1 0 0⟩, while Fe|Ta almost entirely consists of Fe⟨1 1 0⟩|Ta grains. Peng *at el.* [73] have shown that there is a large perpendicular interface anisotropy at the Ta|FeCo ⟨1 0 0⟩ interface. Since the Ta|Fe interface is a combination of Fe grains with different crystallographic orientation, a large difference in the interface anisotropy of the Ta|Fe⟨1 0 0⟩ and Ta|Fe⟨1 1 0⟩ would result in magnetic homogeneity throughout the Ta|Fe interface. This is consistent with the observed large zero frequency offset for the Fe(6) sample. The large inhomogeneity, in turn, leads to an enhancement in damping due

to non-uniform magnetization precession [74, 75]. Additionally, each orientation may have different damping, as was calculated for Co|Pd system [76]. Therefore, we concluded that the large damping in the Fe(6) and Fe(3)|Py(3) structures is the result of variation of the Ta|Fe interface anisotropy caused by initial, poorly-textured growth of Fe on Ta that led to variation of the Ta|Fe interface anisotropy.

Chapter 5

Spin-Pumping/Spin-Diffusion into Ta

Ta is widely used as a seed or adhesion layer for magnetic thin film structures [77, 78, 79, 80]. In all of the sputter deposited structures studied in this thesis, Ta was used a seed layer to promote textured deposition of Py. Like any other metal adjacent to a precessing ferromagnet (in our case Py) Ta will also absorb spin-current due to spin-pumping from Py. In this regard it was important to study the influence of Ta on the spin-pumping and damping of the precessing Py. Unlike most other studied spin-pumping materials such as Cu, Al, Ag, Au (whose spin diffusion lengths are 35 - 600 nm) the spin-diffusion length in Ta is very short. Despite the wide use of Ta in thin films and magnetic structures, the reported values of spin diffusion length range from 1.2 nm [81] to 2.5 nm [82] up to 10 nm [83]. This chapter presents a spin-pumping study of Ta into order to determine the spin-diffusion length in Ta. It will be shown the spin-diffusion length cannot be uniquely determined from a single thickness dependence study of Ta. In fact, one needs to consider both spin source and spin-sink structures in order to extract a self consistent spin-diffusion length. Furthermore, simultaneously fitting the two data sets allowed us to rule out alternative models for spin transport in Ta.

In this section I outline our work on on spin-pumping and spin transport studies using magnetic single layer (SL) and double layer (DL) heterostructures, where SL =FM1|NM and DL =FM1|NM|FM2. In these studies, FM1 is 3.5 nm Py ($= Ni_{80}Fe_{20}$), NM is Ta, and FM2= [Py|Fe] is an effective ferromagnetic layer composed of 1.5 nm Py followed by a 4.5 nm Fe. Therefore the studied structures are Py(3.5)|Ta(d_{Ta})|[Py(1.5)|Fe(4.5)] where the numbers indicate the thicknesses in nm and $0.4 < d_{Ta} < 20$ nm. The choice of FM2 was such that FM1 and FM2 have widely separated resonance fields for a given frequency. This will be shown to be very useful as it allows one to study spin transport in Ta using both spin-pump and spin-sink effects.

The structure of thin film Ta (0.4 - 20 nm) was investigated by x-ray diffraction (XRD) and transmission electron microscopy (TEM). Clear evolution of atomic structure is ob-

served over the full thickness range; Ta initially grows as amorphous or nano-crystalline solid up to ~ 2 nm, transitioning through the *bcc* structure and eventually establishing larger, well defined grains of β–Ta for $d_{\mathrm{Ta}} \gtrsim 10$ nm. Additionally, thickness-dependent resistivity measurements of Ta were made with the four-point-probe technique.

5.0.1 Sample preparation

RF magnetron sputtering was used to deposit $\mathrm{Ta}\,(3)\,|\mathrm{Py}\,(3.5)\,|\mathrm{Ta}\,(d_{\mathrm{Ta}})\,|\mathrm{Au}\,(3.6)$ and $\mathrm{Ta}\,(3)\,|\mathrm{Py}\,(3.5)\,|\mathrm{Ta}\,(d_{\mathrm{Ta}})\,|\mathrm{Py}\,(1.5)\,|\mathrm{Fe}\,(4.5)\,|\mathrm{Au}\,(3.6)$ films at room temperature on oxidized Si, where the numbers in parenthesis indicate the layer thicknesses in nm. A 3 nm thick Ta seed layer was used to establish the [1 1 1] growth orientation of Py. The thickness of the Ta overlayer was varied, with d_{Ta} = 0, 0.3, 0.6, 0.8, 1.2, 2.0, 3.1, and 10.0 nm. A thin gold capping layer was used to protect from formation of oxide. Additionally, Ta films were deposited on glass substrates for use in resistivity measurements. Layer thicknesses were inferred from fitting x-ray reflectivity measurements, allowing for a calibration of the growth rates.

5.0.2 Resistivity Measurements

Ex-situ resistivity measurements were done on sputter-grown glass/Ta(d_{Ta}), for $1 < d_{\mathrm{Ta}} < 23$ nm. Glass was used instead of Si due to its large resistance. When exposed to air Ta rapidly oxidizes which reduces the effective thickness of the metallic Ta. To prevent this its possible to cover the sample with a protect the film of Au, this dramatically reduced the sensitivity of our resistivity measurements since even a 1 nm layer of Au was an order of magnitude more conductive than Ta (literature values for sputter deposited Ta are ~ 200 $\mu\Omega$ cm as compared to ~ 8 $\mu\Omega$ cm for sputter deposited Au). Therefore for the resistivity it was decided to deposit the structures without a capping layer and allow the naturally formed surface oxide ($\approx$ 2 nm) to serve as a protective layer; its resistivity is expected to have negligible contribution due the oxide layer and Ta being in parallel with respect to the resistivity measurement. The thickness of the Ta metal and the Ta oxide was determined from fitting the x-ray reflectivity measurements of each glass/Ta(d_{Ta}) sample by PANalytical X'pert Reflectivity software.

Resistivity measurements were made in a collinear four point probe alignment along the symmetry axis on 12×12 mm samples, see section 3.6 for more details.

Due to limitations of the measurement, the thinnest measured Ta sample was 1.0 nm. A fit was done to extrapolate/interpolate for any $\rho(d_{\mathrm{Ta}})$ required for the α_{sp} analysis. The fitting model does not include the effects of an evolving atomic structure, amorphous/nano-crystalline $\Rightarrow$ *bcc* $\Rightarrow$ β, or the increase of grain size with film thickness. To interpret the resistivity data, a variation of the commonly used Fuchs–Sondheimer [84, 85] model was

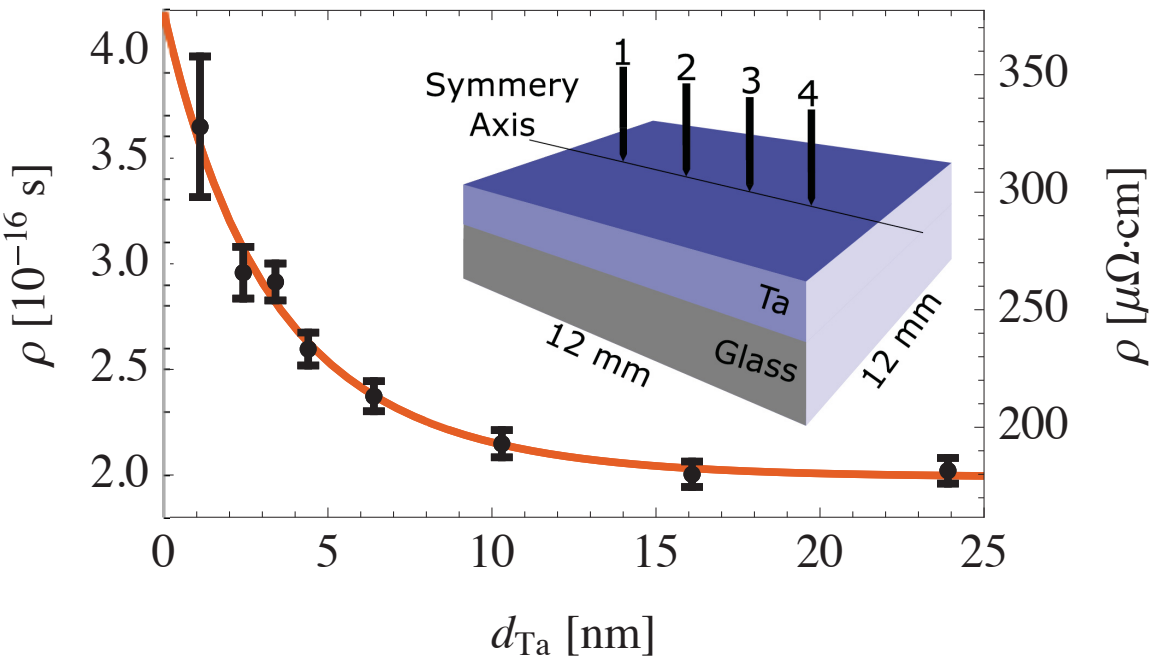

Figure 5.1: Resistivity as a function of Ta film thickness grown on glass substrate. The inset show the geometry and labeling scheme for the 4 point probe measurements.

used. This model includes scattering from both film surfaces and grain boundaries [86]

$$\rho = \rho_\infty \left[1 - \left(\frac{1}{2} + \frac{3}{4}\frac{\lambda_m}{d_{\mathrm{Ta}}}\right)(1 - e^{-\zeta d_{\mathrm{Ta}}/\lambda_m})e^{-d_{\mathrm{Ta}}/\lambda_m}\right]^{-1}, \tag{5.1}$$

where $\lambda_m = v_{\mathrm{F}}\tau_m^{Bulk} = 4.7(8)$ nm is the electron mean free path, $\rho_\infty = 179(4)$ $\mu\Omega$ cm is the bulk resistivity, and $\zeta = 0.70(7)$ is a parameter governed by the number of electrons scattered by the grain boundaries. The bulk resistivity approaches the values for β–Ta reported the in literature, $\rho_{\beta\text{–Ta}} = 170 - 220$ $\mu\Omega$ cm [87]. The inferred mean free path for our deposited Ta is an order of magnitude larger than the reported values for β–Ta, $0.3 - 0.5$ nm [88, 82].

5.0.3 XRD and Transmission electron microscopy

Out-of-plane x-ray diffraction (XRD) measurements using Cu K_α radiation were performed on Si/Ta(3)/Py(3.5)/Ta(20.1)/Au(3.6) film structures, see fig. 5.2 (a). As observed before, the deposited Py on top of Ta is oriented along the (111) directions. The large Si peak, originating from the substrate and the [1 1 1] Au peak, overlap with the β–Ta peak and *bcc*–Ta peak, therefore additional structures were deposited using a glass substrate, glass/Ta(20.1) see blue line on fig. 5.2 (a),(b). The spin-diffusion length in Ta is ~ 1 nm, therefore the interest is in the structure of Ta in that thickness range. Below $d_{\mathrm{Ta}} = 6$ nm there is no measurable signal from the out-of-plane XRD, see fig. 5.2 (b). With increasing d_{Ta} diffraction

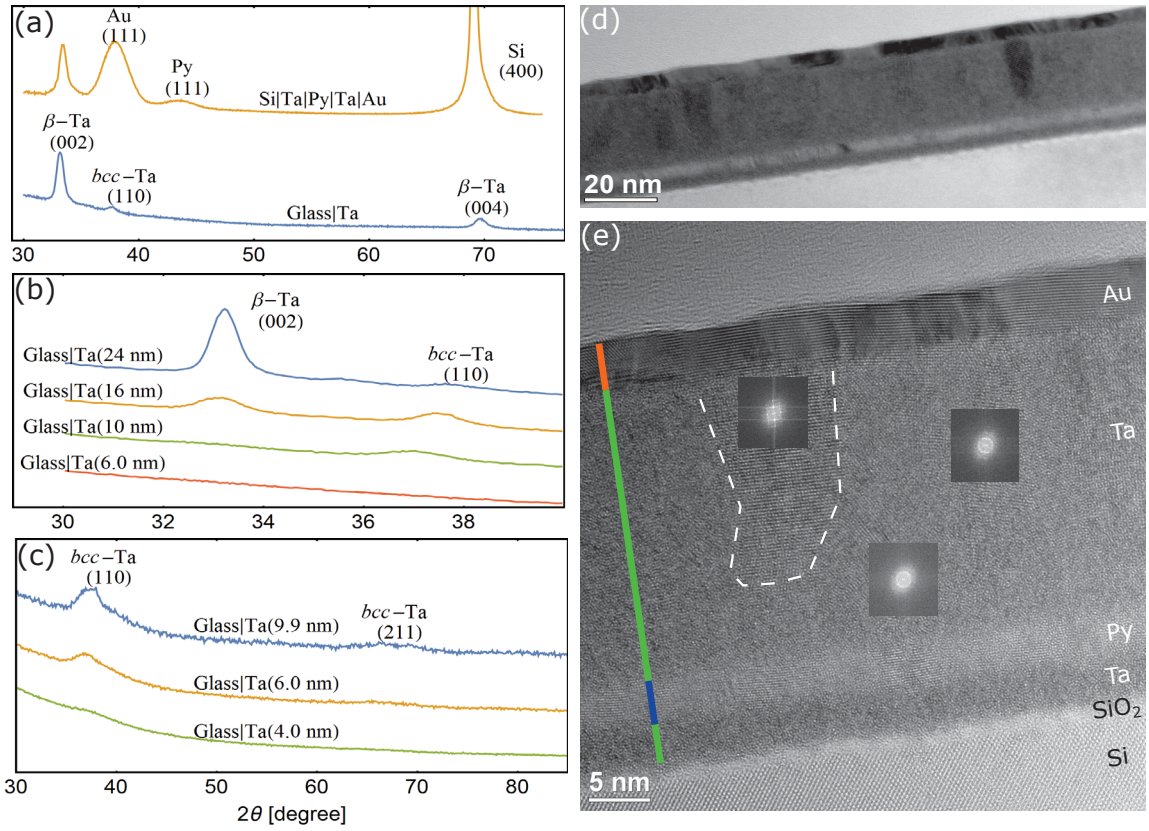

Figure 5.2: Out-of-plane $\theta - 2\theta$ XRD scan of **(a)** Si/Ta (3) |Py (3.5) |Ta (20.1) |Au (3.6), glass/Ta (20.1) and of **(b)** glass/Ta(d_{Ta}). **(c)** In-plane XRD scan at a 0.5 degree grazing incidence angle of glass/Ta(d_{Ta}). **(d)** Cross-sectional bright-field TEM and **(e)** High resolution TEM micrographs of the Si/Ta(3)/Py(3.5)/Ta(20)/Au(3.6) structure. The FFTs of three different regions in the Ta(20) layer are displayed in the corresponding square insets. A dashed white line is drawn around the β–Ta grain to outline its edges.

peaks begin to emerge, first the *bcc*−Ta peak at d_{Ta} = 10 nm and then the β−Ta peak at 16 nm. For even thicker Ta layers the β−Ta structure appears to dominate.

In-plane XRD was performed on glass/Ta(d_{Ta}) at a grazing incidence angle of 0.5 degrees, see fig. 5.2 (*c*). Note, the low incident angle of the in-plane XRD results in a much shallower penetration of the beam and therefore higher surface sensitivity of the sample. A much clearer XRD peak is observed for the glass/Ta(6) as compared to the out-of-plane measurement, however, below d_{Ta} = 6 nm the peak disappears entirely. The results of the out-of-plane and in-plane XRD measurements suggest that there is a lack of ordering in the structure of Ta in the very thin limit. This is not characteristic of other materials, as can be observed, both the Au(3.6) and Py(3.6) layers have very clear diffraction peaks, see fig. 5.2 (a).

To get a clearer picture of the the Ta structure below 4 nm thickness, Si/Ta(3)/Py(3.5)/Ta(20)/Au(3.6) samples were sent out for transmission electron microscopy (TEM) measurements by Dr. Rene Huebner in the Institute of Ion Beam Physics and Materials Research, Helmholtz-Zentrum Dresden-Rossendorf, Dresden, Germany. Analysis of a Si/Ta(3)/Py(3.5)/Ta(20)/Au(3.6) cross section was performed using an image C_s-corrected Titan 80-300 microscope (FEI) operated at an accelerating voltage of 300 kV. A bright-field TEM overview image of the layer structure is shown in fig. 5.2(d), while a corresponding HRTEM micrograph is presented below it. On fig. 5.2(e) one can observe a thin layer silicon oxide between the Si substrate and the Ta(3) seed layer. Based on the uniform gray level in fig. 5.2(d) and the absence of lattice fringes in fig. 5.2(e), the Ta(3) deposited on Si appears to be characterized by an amorphous structure, whereas the overlying Py(3.5) layer has a clear crystalline structure. The Ta(20), deposited on Py, initially grows without any long range order. However, one cannot conclude unequivocally whether this region is amorphous or partially nano-crystalline with a grain size of 1-2 nm, and therefore this thickness region will be referred to as the *intermediate*-Ta region. Note, for the spin-pumping/spin-transport studies this is exactly the thickness limit one is interested in. Increasing Ta thickness results in the formation of larger β−Ta grains, as confirmed by Fast Fourier Transform (FFT) of the HRTEM image in fig. 5.2(e). The TEM results are consistent with the XRD measurements.

Importantly, there is a very large difference in resistivity of amorphous-Ta ~ 270 – 2000 $\mu\Omega$cm as compared to *bcc*−Ta ~ 27 $\mu\Omega$cm and β−Ta ~ 200 $\mu\Omega$cm [89]. Given that one of the fitting parameters for spin-pumping damping is the resistivity of the material, eq. (2.83), it follows that the Ta structure should play a significant role in spin-pumping/spin-transport. Futhermore, the evolution of Ta structure with increasing thickness should contribute to the thickness-dependent Ta resistivity shown in fig. 5.1. In general, for applications involving spin-transport, one would require materials with a low resistivity since this allows for a larger spin-diffusion length. However, achievement high crystalline thin-film Ta (>3 nm) is non-trivial for sputter deposition, therefore for most devices the Ta layer will be amorphous.

5.0.4 FMR

FMR measurements of the Ta (3) |Py (3.5) |Ta (d_{Ta}) |Au (3.6) and Ta (3) |Py (3.5) |Ta (d_{Ta}) |Py (1.5) |Fe (4.5) |Au (3.6) were performed on the coplanar waveguide setup in the 6-36 GHz frequency range (see fig. 5.3). The resonance modes of the two magnetic layers (Py and [Py/Fe]) were well separated for all frequencies. The linewidth vs. frequency dependence of Py showed a linear trend for all measured samples. As before the linewidth frequency dependence was interpreted using,

$$\Delta H(\omega) = \alpha \frac{\omega}{\gamma} + \Delta H(0), \tag{5.2}$$

The zero-frequency offset due to inhomogeneity broadening was $\Delta H(0) < 5$ Oe for all samples.

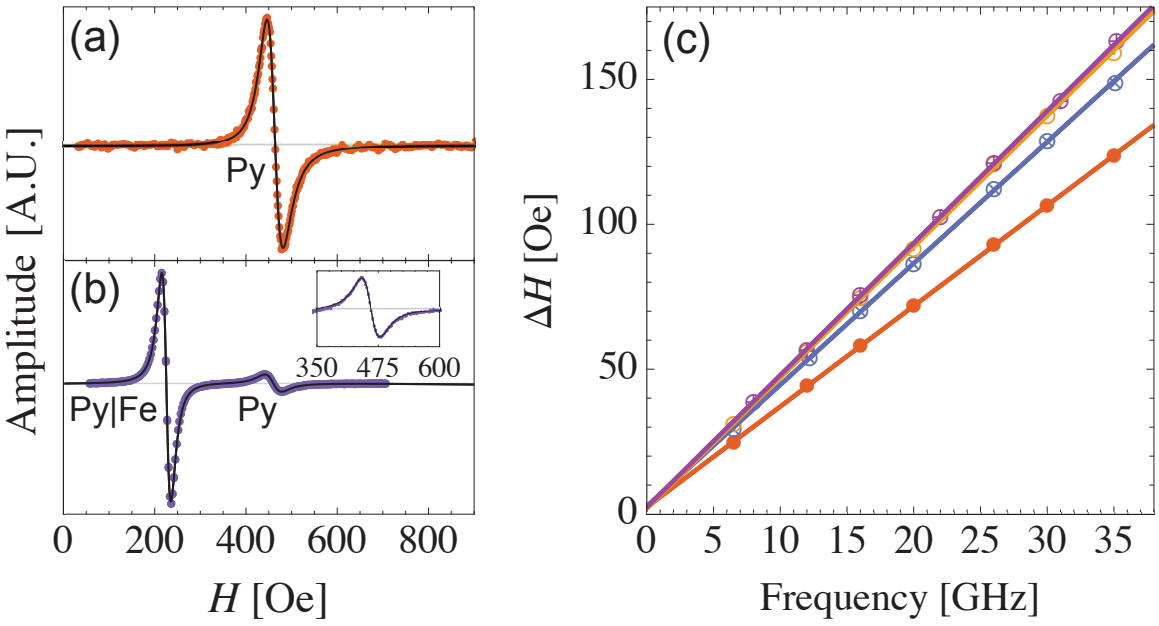

Figure 5.3: Example 6.5 GHz FMR spectra for **(a)** SL (FM1= Py) and **(b)** DL (FM1= Py, FM2= [Py/Fe]) samples with d_{Ta} = 1.0 nm. Inset of (b) is an expanded view of the FM1= Py resonance line. **(c)** FMR linewidth as a function of frequency. SL samples with d_{Ta} = (•) 0 nm (⊗) 0.8 nm, and (⊙) 10 nm with α = 10.2, 12.4, and 13.3 $\times 10^{-3}$, respectively. DL sample with d_{Ta} = (⊕) 0.8 nm and $\alpha = 13.2 \times 10^{-3}$.

5.0.5 Magnetic damping and spin-pumping in Ta

In the SL and DL structures, there are three main contributions to the measured damping of the Py layer. First is the bulk damping of the Py layer α_{bulk}. Second is the spin-pumping-induced damping due to the Ta(3) seed layer $\alpha_{\mathrm{sp,seed}}$. And third is the damping due to spin pumping into the Ta(d_{Ta}) overlayer α_{sp}. This is the quantity of interest. Therefore the total

damping is the sum of the three contributions

$$\alpha = \alpha_{\text{bulk}} + \alpha_{\text{sp,seed}} + \alpha_{\text{sp}}. \tag{5.3}$$

Since both the Py layer and Ta seed layer were held at constant thicknesses for all studied structures, their contribution to the total damping should also remain constant and will be referred to as

$$\alpha_{\text{ref}} = \alpha_{\text{bulk}} + \alpha_{\text{sp,seed}}. \tag{5.4}$$

$\alpha_{\text{ref}} = 10.4(\pm 0.2) \times 10^{-3}$ was determined by measuring FMR on five samples of Ta (3) |Py (3.5) |Au (3.6). Note the spin-diffusion length of the Au capping layer is much larger than its thickness therefore its contribution to the total spin-pumping-induced damping is minimal [90].

In a classical spin-pumping experiment, the spin-transport in the NM is investigated by monitoring the damping of the FM while increasing the thickness of the NM, in the FM/NM structure. In this study the α_{sp} of both the SL and the DL structures was monitored with increasing d_{Ta}, where

$$\alpha_{\text{sp}} = \alpha - \alpha_{\text{ref}}. \tag{5.5}$$

As discussed in section 2.5.2, the additional damping due to spin-pumping (some times referred to as spin-pumping induced damping) in the FM1 for a single magnetic layer structure (SL), Py/NM, can be shown to be

$$\alpha_{\text{sp}}^{\text{SL}} = \frac{g\mu_{\text{B}}}{4\pi M_s} \frac{\tilde{g}_{\uparrow\downarrow}}{d_{\text{Py}}} \left[1 + \frac{\tilde{g}_{\uparrow\downarrow}\mathcal{R}}{\tanh\left(\frac{d_{\text{Ta}}}{\lambda_{\text{sd}}}\right)} \right]^{-1}, \tag{5.6}$$

and

$$\mathcal{R} = \frac{\rho e^2}{2\pi\hbar} \lambda_{\text{sd}} \tag{5.7}$$

Where e is the fundamental charge, $\rho^{-1} = D\mathcal{N}e^2$ is resistivity determined from the Einstein relation, $\mathcal{N}$ is the density of states at the Fermi level and D is the diffusion constant.

For a double magnetic layer structure (DL), Py/NM/[Py/Fe], the damping dependence is given by

$$\alpha_{\text{sp}}^{\text{DL}} = \frac{g\mu_{\text{B}}}{4\pi M_s} \frac{\tilde{g}_{\uparrow\downarrow}}{d_{\text{Py}}} \left[1 + \tilde{g}_{\uparrow\downarrow}\mathcal{R} \left(\frac{1 + \tilde{g}_{\uparrow\downarrow}\mathcal{R} \tanh\left(\frac{d_{\text{Ta}}}{\lambda_{\text{sd}}}\right)}{\tanh\left(\frac{d_{\text{Ta}}}{\lambda_{\text{sd}}}\right) + \tilde{g}_{\uparrow\downarrow}\mathcal{R}} \right) \right]^{-1}. \tag{5.8}$$

The α_{sp} dependence on d_{Ta} of the Py(FM1) layer in both the SL and DL structures is shown in fig. 5.4. The parameters used for the interpretation are g-factor= 2.1 as determined by FMR measurements, $M_s = 817$ emu/cm^3 as determined by SQUID measurements, and ρ determined by 4 point probe resistivity measurements. The only free fitting parameters in eq. (5.6) and eq. (5.8) are $\tilde{g}_{\uparrow\downarrow}$ and λ_{sd}. As discussed, it is not clear what is the appropriate

value of ρ required to make a self-consistent fit, especially since it is thickness dependent. To investigate the most appropriate ρ the data was fit with a few different models with respect to the choices of the parameters λ_{sd} and ρ. Since both eq. (5.6) and eq. (5.8) share the same fitting parameters, it is possible to fit both SL and DL data sets simultaneously with the two respective equations.

- *Model 1: $\tilde{g}_{\uparrow\downarrow}$, ρ, and λ_{sd} are free parameters.* This model fits for an average ρ and λ_{sd} and is mostly sensitive to the d_{Ta} range where α_{sp} is changing.
- *Model 2: $\tilde{g}_{\uparrow\downarrow}$ and λ_{sd} are free parameters, while a constant ρ is taken from resistivity measurements.* Assuming a the bulk value of ρ is the most common approach found in literature.
- *Model 3: $\tilde{g}_{\uparrow\downarrow}$ is a free parameter, $\rho\,(d_{\mathrm{Ta}})$ is taken from resistivity measurements, and λ_{sd} is fitting parameter restricted to be inversely proportional to $\rho\,(d_{\mathrm{Ta}})$.*
- *Model 4: $\tilde{g}_{\uparrow\downarrow}$ is a free parameter, $\rho\,(d_{\mathrm{Ta}})$ is taken from resistivity measurements, and λ_{sd} is thickness independent fitting parameter. This model was proposed in ref. [91].*

Model 1 described both the SL and DL data well, see solid lines in fig. 5.4 (a). The fit parameters were $\tilde{g}_{\uparrow\downarrow} = 1.7(3) \times 10^{15}$ cm^{-2}, $\lambda_{\mathrm{sd}} = 1.0\,(1)$ nm, $\rho = 360(50)$ $\mu\Omega$ cm. The value of ρ is on the higher end of the measured resistivity values fig. 5.1.

Model 2 can be interpreted in ways, **(a)** using the bulk resistivity $\rho = 179(4)$ $\mu\Omega$ cm and **(b)** using the ρ value measured in the region where spin-currents are being absorbed ($\sim d_{\mathrm{Ta}} < 1$ nm). A simultaneous fit with model 2a showed that the SL data could be qualitatively described by this model while the DL data could not, see fig. 5.4 (b). To get more insight on where this model fails it is convenient to fit the SL and DL individually and then plot the expected behaviour for the DL and SL models assuming the same fitting parameters. The resulting fits are shown as solid lines in fig. 5.4 (c) and (d) for the individual fits of SL and DL respectively, the dashed lines correspond to the plots of the DL and SL assuming the extracted fitting parameters. There is disagreement in the fitting parameters of the individual fits of SL and DL using model 2a, see table 5.1. In Model 2b the resistivity value of $\rho = 325$ $\mu\Omega$ cm was used, which corresponds to the $d_{\mathrm{Ta}} = 1.1$ nm sample, see fig. 5.5(a), notes this fits overlaps the Model 1 fit nearly perfectly. The motivation is that the region where α_{sp} shows a large dependence on d_{Ta}, i.e. where there is significant spin-transport, is the *intermediate*-Ta region, where four point probe measurement showed the large resistivity. This model describes both the SL and DL data well, and the individual and simultaneous fits agree within error as shown in table 5.1. The simultaneous fit is shown by the solid lines in fig. 5.4 (b). The simultaneous fit parameters are $\tilde{g}_{\uparrow\downarrow} = 1.53 \times 10^{15}\,(8)$ cm^{-2} and $\lambda_{\mathrm{sd}} = 1.03\,(3)$ nm. These values are consistent with Model 1.

Model 3 is similar to the Elliot–Yafet type of scattering mechanism [45, 44], the spin-flip time is proportional to the electron scattering time, $\tau_{\mathrm{sf}} \propto \tau_{\mathrm{m}}$. In this model the spin-diffusion

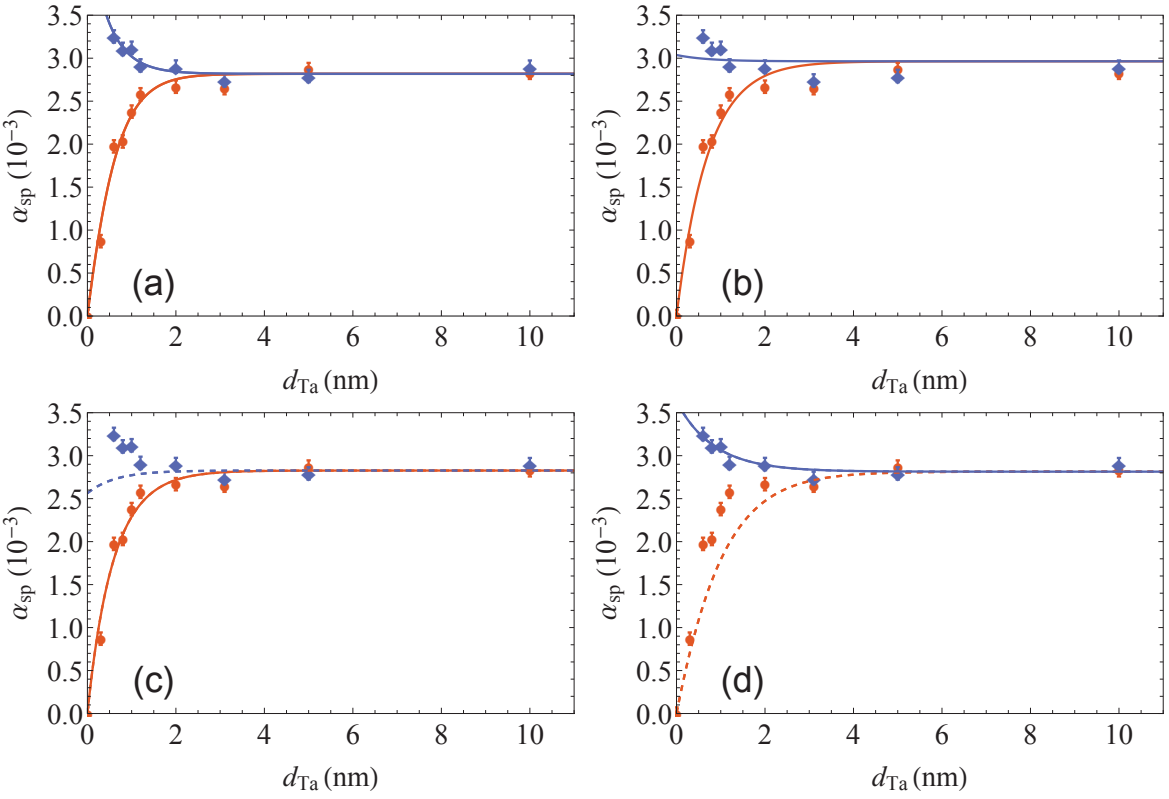

Figure 5.4: Damping due to spin-pumping into the Ta overlayer as a function of d_{Ta} for SL (•) and DL (⧫) samples. **(a)** Simultaneous fits to the two data sets using model 1 and models 2b, note the fits overlap nearly perfectly. **(b)** Simultaneous fits using model 2a. **(c)** Solid line is the individual fit of the SL (•) samples using model 2a and the dashed line is a plot of model 2a for the DL structure using the individual fit parameters as extracted from the SL fit. **(d)** Solid line is the individual fit of the DL (⧫) samples using model 2a and the dashed line is a plot of model 2a for the SL model using the individual fit parameters as extracted from the DL fit.

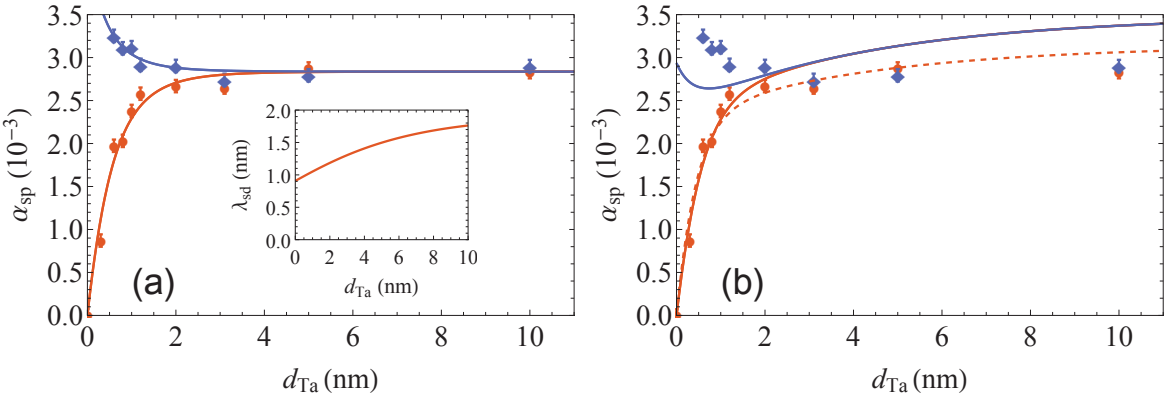

Figure 5.5: Damping due to spin-pumping into the Ta overlayer as a function of d_{Ta} for SL (•) and DL (⧫) samples. **(a)** Simultaneous fits using Model 3, inset shows the thickness dependent spin-diffusion length as determined from eq. (5.9). **(b)** solid lines are the simultaneous fits using Model 4, and the individual fit to SL is the dashed line.

length is dependence on the resistivity,

$$\lambda_{\mathrm{sd}}\left(d_{\mathrm{Ta}}\right) = \lambda_{\mathrm{sd}}^{\mathrm{bulk}} \frac{\rho_{\infty}}{\rho\left(d_{\mathrm{Ta}}\right)}, \tag{5.9}$$

where $\lambda_{\mathrm{sd}}^{\mathrm{bulk}}$ is the thick film limit of the spin diffusion length. The fitted parameters are $\tilde{g}_{\uparrow\downarrow} = 1.57(8)\times10^{15}$ cm^{-2} and $\lambda_{\mathrm{sd}}^{\mathrm{bulk}} = 1.91(5)$ nm. This model results in a good fit to both the SL and DL data in both individual and simultaneous fits, see table 5.1. The simultaneous fit is shown by the solid lines in fig. 5.5 (a). In this model the spin-diffusion length becomes thickness dependent as given by eq. (5.9), its dependence is plotted in the insert of fig. 5.4 (a). The fit value of the spin mixing conductance is in good agreement with both Models 1 and 2(b), however, $\lambda_{\mathrm{sd}}^{\mathrm{bulk}}$ is nearly twice as large as λ_{sd} in Models 1 and 2(b).

Model 4 was proposed in ref. [91] in order described the experimental spin-pumping data of Ta/Py/Pt, Ta/Py/Cu/Pt, Ta/Py/Pd, and Ta/Py/Cu/Pd heterostructures. This model was motivated by the Dykanov-Perel type of scattering mechanism which requires $\tau_{\mathrm{sf}} \propto 1/\tau_{\mathrm{m}}$. It was not possible to simultaneous fit both the SL and DL data with this model, see solid lines in fig. 5.5 (b). However, the model is able to describe the SL data as an individual fit, see red dashed line fig. 5.5 (b). The DL data could not be described by this model, attempts to fit the DL results in a curve similar to the blue (top) fit in fig. 5.5 (b). *It is worth highlighting the value of this result, if only the SL data is used in the models (which is typically the case for most spin-pumping studies) then any of the above models would be able to fit the data. In order to get a unique set of free fitting parameters and to be able to distinguish between competing models it is important to perform analyses of both the SL and DL data sets.*

It is worth comparing the models which result in good fits. In Model 1, the fit is essentially for an average value of λ_{sd} and ρ in the region where α_{sp} is still thickness dependent. The fitted ρ is consistent with the ρ measured by 4-point probe in the thickness range where α_{sp} has large dependence on d_{Ta}. Model 3 results in a $\tilde{g}_{\uparrow\downarrow}$ value which is consistent with Models 1 and 2b. However the fitted $\lambda_{\mathrm{sd}}^{\mathrm{bulk}}$ is nearly twice the value of λ_{sd} as compared to Model 1 or Model 2b. One can estimate an average spin diffusion length from Model 3 in the first 3 nm of Ta as $\simeq 1.1$ nm. This compares well to the λ_{sd} extracted from Model 1 or Model 2b.

Models 2a and 4 cannot describe the SL and DL data simultaneously, but both can be used to describe the SL data. While model 2a can fit SL and DL separately, fitting the single layer data with model 2a requires less efficient spin-pumping (smaller $\tilde{g}_{\uparrow\downarrow}$) and more efficient spin absorption in Ta (smaller λ_{sd}) than fitting the DL data. Using the SL fit parameters to calculate DL damping, eq. (5.8), model 2a yields an increase of α_{sp} with increasing Ta thickness, indicating that Ta is a more efficient spin absorber than spin sink. In other words, this model requires that spin absorption is occurring faster than in the diffusive limit, which is a mathematically achievable dependence that lacks physical meaning. Using the DL fit

Table 5.1: Spin diffusion model fit parameters. SL and DL refer to individual fits of the magnetic single layer and double layer data, respectively, otherwise fits are a simultaneous fit to both data sets shown in fig. 5.4 and fig. 5.5.

Model	$\tilde{g}_{\uparrow\downarrow}$ $\left[10^{15}\ \mathrm{cm}^{-2}\right]$	λ_{sd} [nm]	$\rho\,[\mu\Omega\mathrm{cm}]$
1	1.7(3)	1.0 (1)	370
2a	1.09(4)	1.39 (4)	179
2a - SL	0.92(6)	1.27 (6)	179
2a - DL	1.31(6)	1.7 (1)	179
2b	1.53(8)	1.03 (3)	323
2b - SL	1.4(2)	1.00 (5)	323
2b - DL	1.6(1)	1.03 (6)	323
3	1.57(8)	1.91 (5)	$\rho\,(d_{\mathrm{Ta}})$
3 - SL	1.6(2)	1.90 (8)	$\rho\,(d_{\mathrm{Ta}})$
3 - DL	1.6(1)	1.9 (1)	$\rho\,(d_{\mathrm{Ta}})$
4 - SL	0.9(5)	0.86 (4)	$\rho\,(d_{\mathrm{Ta}})$

parameters in the SL model underestimates the damping in the first 2 nm of Ta, see fig. 5.4 (c). The simultaneous fit is an average of these limits, which leads the nearly flat dependence of the DL. Model 4 fails for the DL for a similar reason.

A note to the reader: the interpretation of spin-pumping in this section uses the full resistivity of Ta. This is consistent with typical spin-pumping studies but in principle is incorrect since the derivation (see section 2.5.4) requires the single spin resistivity. It is important to point out that the main conclusions made in this sections remain true even if one uses the single spin resistivity, however the fitting parameters would change. In the following chapters, spin-pumping studies in Pt, the single spin resistivity is correctly used for all the spin-pumping interpretations.

5.0.6 Summary

An investigation of spin-transport in Ta within (SL = Py/Ta) and magnetic double layer (DL = Py/Ta/ [Py/Fe]) heterostructures was performed by means of spin-pumping. It was observed that the most common method for interpreting the spin-pumping induced data (bulk-like resistivity value of Ta) failed to fit the two data sets. Importantly, this interpretation could be applied to the (SL = Py/Ta) resulting in seemingly reasonable fitting parameters (within the span of reported values found in literature). This result points out the potential flaw of attempting to extract some meaningful spin-transport values from the single magnetic layer structure.

The origin of the problem appears to be coming from the fact that the Ta structure evolves with increasing thickness which results in a thickness dependent resistivity. Therefore the ρ_∞ is inconsistent with the data is because structure of Ta in the region of spin-pumping is not bulk-Ta. TEM studies show that initially Ta grows without long range order for upto

~ 2 nm, this is approximately the thickness range over which the spin-current can propagate over. For thicker Ta films, there begins to emerge some measurable structure as observed by XRD studies which show both β–Ta and *bcc*–Ta for $d_{\mathrm{Ta}} > 10$ nm.

The interpretations which fit both data set well require much larger resistivity values than the bulk-like value. Using the resistivity value as measured in the $d_{\mathrm{Ta}} = 1$ nm, $\rho = 323$ $\mu\Omega$cm, the spin diffusion model can describe $\alpha_{\mathrm{sp}}(d_{\mathrm{Ta}})$ for both SLs and DLs yielding a $\tilde{g}_{\uparrow\downarrow} = 1.53(8) \times 10^{15}$ cm^{-2} and $\lambda_{\mathrm{sd}} = 1.0(1)$ nm. Allowing ρ to be a free parameter in a simultaneous fit both data sets results in a fitted resistivity value of $\rho = 370$ $\mu\Omega$cm as well as $\tilde{g}_{\uparrow\downarrow}\left(1.7\,(3) \times 10^{15}\ \mathrm{cm}^{-2}\right)$ and $\lambda_{\mathrm{sd}}\,(= 1.03(3)$ nm). Since the resistivity of Ta is thickness dependent it is natural to simply incorporate into the model, $\alpha_{\mathrm{sp}}(d_{\mathrm{Ta}})$. This requires that $\lambda_{\mathrm{sd}} \propto \rho^{-1}$ (equivalent to $\tau_{\mathrm{sf}} \propto \tau_{\mathrm{m}}$) and results in a good fit to both the SL and DL data yielding $\tilde{g}_{\uparrow\downarrow} = 1.53(8) \times 10^{15}$ cm^{-2} and $\lambda_{\mathrm{sd}}(d_{\mathrm{Ta}} = \infty) = 1.91(5)$ nm. The average value of λ_{sd} in the *intermediate*-Ta region where spin-currents are propagating agrees well with the above (non-bulk resistivity) models. Finally, a model assuming a constant λ_{sd} and thickness-dependent ρ (equivalent to $\tau_{\mathrm{sf}} \propto 1/\tau_{\mathrm{m}}$) could be used to describe the single layer data alone, but could not describe the double layer data. The resulting spin diffusion parameters for the single layer fit, $\tilde{g}_{\uparrow\downarrow} = 0.9(5) \times 10^{15}$ cm^{-2} and $\lambda_{\mathrm{sd}} = 0.86(4)$ nm, did not agree with the other models.

Chapter 6

Experiment: Interlayer exchange coupling Pt

6.1 Motivation

The goal of this study was to determine the strength of the interlayer exchange coupling mediated by Pt and its influence on the FMR data. As was demonstrated in the previous chapters (spin-pumping into Ta) to uniquely determine the fitting parameters within the spin-pumping model one needs to do both an experiment with a single magnetic layer (FM/Pt) and a double magnetic layer structure (FM1/Pt/FM2). For Ta this worked out well since the static interlayer exchange coupling through Ta was negligible for the thickness range of interest. In contrast, Pt mediates static interlayer exchange coupling between two ferromagnets up to ~ 1 nm, this is within the thickness range over which spin transport occurs in Pt due to its short spin diffusion length (~ 1 nm as measured in spin-pumping experiments). Therefore to properly determine the magnetic damping data of (FM1/Pt/FM2) one needs to first understand the behaviour of the static interlayer exchange coupling which is mediated by Pt. In this section I outline my experimental studies of interlayer exchange coupling through Pt in Py(6)/Pt(d_{Pt})/[Py(1.5)/Fe(4.5)] by means of FMR.

6.2 Proximity Polarization of Pt Background

Proximity polarization is the effect by which a nonmagnetic metal (NM) acquires a magnetic moment due to its proximity to a ferromagnetic metal (FM). Is it accepted that the origin of the proximity induced moment (PIM) is a consequence of the hybridization of the electron orbitals of the two species and exchange coupling across the interface [92, 93, 94]. Typically PIM in a NM is very short range, localized to the FM/NM interface. The penetration depth of PIM is a property of the NM and depends on the magnetic susceptibility, χ, and the exchange coupling strength in the normal metal. The magnetic susceptibility of Stoner enhanced metals is larger as compared to normal metals (Au, Ag, Cu, Al...), and this can be significantly more pronounced in thin-films. In ref. [95] it was shown that the

magnetic susceptibility of thin film Pd can be enhanced by ~ 500 due to lattice strain from the adjacent Au layers. Fullerton *et al.* [96] observed an induced magnetic moment of Pd in Fe/Pd structures which was shown to be a consequence of the lattice strain. Therefore, Stoner enhanced metals can result in large [97] proximity polarization which can be the dominating coupling mechanism for thin films.

The nature of interlayer exchange coupling between two ferromagnetic layers is highly dependent on the properties of the spacer layer. Long range oscillatory coupling has been observed in many spacer layers (Cu [98, 99, 100, 98, 34], Au [101] Ag [102], Ru [103] and Cr [1, 104]) and has been well described theoretically [105]. RKKY-like interlayer coupling is dominant in systems with small Stoner enhancement factor. Oscillations in interlayer coupling arise as from the quantum well states of NM electrons pass through the Fermi surface with increasing spacer thickness. The strength of these contributions is significantly diminished by interface roughness. In fact, interface roughness can induce biquadratic coupling, resulting in non-collinear coupling between two ferromagnets. For Stoner enhanced materials, it has been argued that the electron-electron correlation effects lead to a suppression of the oscillatory dependence and an enhancement of the exponential decaying term [106]. Exactly this behaviour was observed for Fe/Pd/Fe by Fullerton *et al.* [96] where the authors observed a predominantly exponential dependence of the coupling strength with the spacer layer thickness for high quality MBE deposited samples. It was determined that the lattice expansion of Pd on top of Fe lead to a large enhancement in an induced magnetic moment. The dominating exponential dependence could be reproduced by including exchange enhancement in the paramagnetic susceptibility of Pd. These calculations start with the Yafet [40] approach of the FM/Pd/FM structure represented by an electron gas in-between two sheets of localized spins (the FMs) and include the exchange enhancement the random phase approximation [107, 108].

Induced proximity magnetization in Pt has its origin in quantum mechanics. Spin-polarized band-structure calculations show that Pt atoms attain a magnetic moment due to hybridization of the 3d orbital of Co and the 5d orbitals of Pt [109]. Experimentally, many XMCD studies have shown that interface Pt can have substantial polarization [97], up to 0.68 μ_B/atom for Co/Pt at 10 K [110] or 0.61 μ_B/atom for Co/Pt at room temperature [111]. Importantly, the induced magnetic moment is not solely localized at the interface, but extends into the Pt layer (~1 nm) [112]. Therefore, if the Pt spacer layer in the FM/Pt/FM is thin enough, it is natural to expect that the entire Pt has a magnetic moment (with some thickness dependence) which then in turn can mediate coupling between the two FM layers. The coupling strength is then dependent on the ability of Pt to mediate magnetic coupling.

Metals with a large Stoner enhancement, such as Pt and Pd, are of great interest to the recording media industry. Their proximity to magnetic films can induce large anisotropy perpendicular to film surface, especially for Co/Pt [113] or Co/Pd [114] films. Additionally, both Pt and Pd are magnetically polarizable materials [115, 116, 58], exhibiting induced

magnetic moment and allowing for strong coupling between magnetic films. This property is used in Co/Pt or Co/Pd multilayers where the role of (Pt, Pd) films is both to couple Co layers and induce large perpendicular magnetic anisotropy. In particular $[Co/Pt]_n$ multilayers can be found in many applications and their properties have been extensively studies over the past two decades [117, 118, 119, 113]. Surprisingly, however, there are few studies on the exchange coupling strength through Pt. The existing studies focus on Pt thicknesses much larger than those employed in $[Co/Pt]_n$ multilayer stacks [120, 121], $d_{Pt} \gtrsim 2$ nm. The reason is the larger ferromagnetic coupling between magnetic layers across sub-nanometre thick Pt, which is non-trivial to measure. Measurements of the exchange coupling strength through Pt are important for optimizing the fabrication of any $[FM/Pt]_n$ related device, where FM is a ferromagnet.

6.3 Experiment

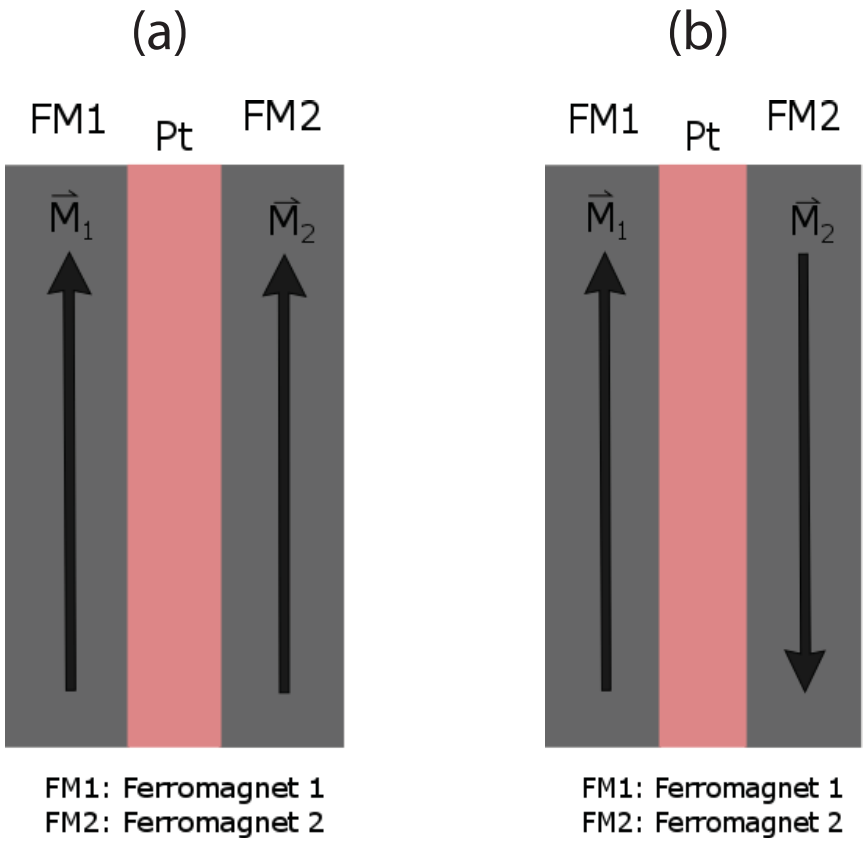

Figure 6.1: (a) Ferromagnetic and (b) antiferromagnetic coupling alignment of the magnetic moments in two magnetic thin films separated by a Pt spacer layer. In our experiment FM1 = Py and FM2 = [Py/Fe].

As mentioned the goal of this study is to determine the interlayer exchange coupling between two ferromagnets due to a Pt spacer. For two ferromagnetic thin films coupled antiferromagnetically fig. 6.1(b) (their magnetic moments are anti-aligned), one can determine the coupling strength from magnetometry studies by measuring the saturation magnetization as a function of external magnetic field. However, for two ferromagnetic thin films coupled ferromagnetically fig. 6.1(a) (their magnetic moments are aligned in the same direction), the saturation magnetization does not change with external field since the lowest energy state is already achieved with both ferromagnets aligned along the field. In order to measure ferromagnetic coupling strength with conventional magnetometry it is necessary to design a structure with a pinned layer [122] in order to force one of the FM1 or FM2 to be anti-aligned with the external applied field. This puts a limit on the coupling strength one can measure which must not exceed the exchange bias or the coercivity field of the pinned layer. The advantage, however, is that this method can be very sensitive to weak coupling strengths. An alternative technique is to use FMR and extract the coupling strength from the difference in resonance fields of the acoustic (in-phase) and optical (out-of-phase) modes. With this method one can measure the coupling of FM/Pt/FM without any modification to the structure required to pin one of layers. Additionally, the coupling strength measured by FMR is limited by the sensitivity and bandwidth of the FMR machine. With a high quality FMR setup one can measure significantly stronger ferromagnetic coupling strengths as compared to magnetometer with a pinned layer.

In this study broadband (8 - 67 GHz) FMR was used to measure the coupling strength through a variable thickness of Pt ($0.5 < d_{\mathrm{Pt}} < 2.2$ nm) surrounded by Py ($Ni_{80}Fe_{20}$) interfaces. Lower frequency points (8 - 36 GHz) were measured in an in-plane, field swept, coplanar wave-guide setup while the higher frequency points (50 - 69 GHz) were measured on a terminated, rectangular waveguide. The measured structure was
Si/Ta(3)/Py(6)|Pt(d_{Pt})[Py(1.5)|Fe(4.5)]/Ta(3), where the numbers are thicknesses in nm. As before, the Ta(3) was the seed layer for the structure and will be omitted in further discussion. Additionally, a Ta(3) layer was used as a capping layer to prevent oxidation of the top Fe. For ferromagnetic coupling strength measurements by FMR, it is required that the two magnetic layers have different resonances field [34]. The higher effective demagnetizing fields in [Py(1.5)|Fe(4.5)] compared to Py(6) results in a large separation of their resonance fields even for the lower frequencies [123], see chapter 4. Examples of the FMR data are shown in fig. 6.2.

Similarly to the previous sections, the FMR data was interpreted by an admixture of the in-phase and out-of-phase components of the rf susceptibility

$$\varepsilon^{mix} \propto -\sin(\phi)\chi' + \cos(\phi)\chi'', \tag{6.1}$$

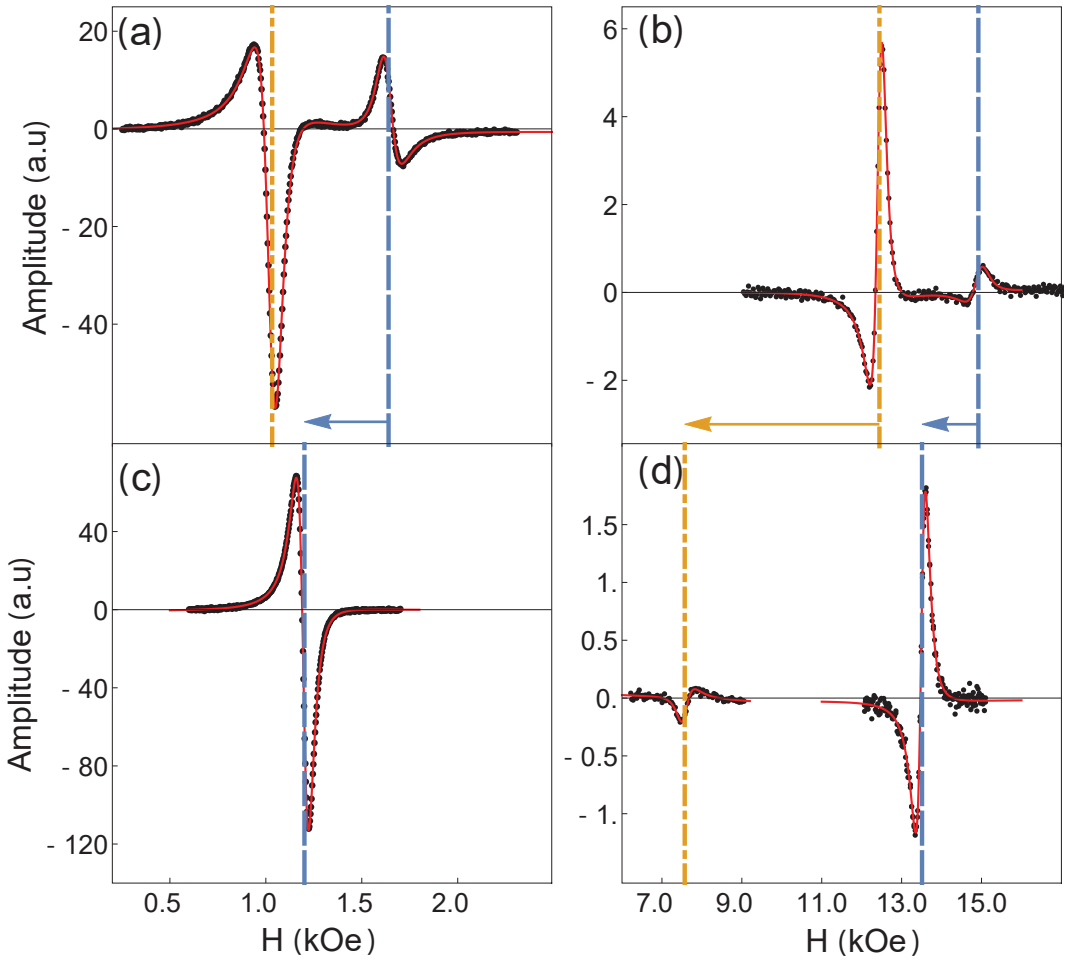

Figure 6.2: Examples of FMR spectra of the Py (higher field) and [Py/Fe] (lower field) resonance for (a) Py(6)/Pt(d_{Pt} = 2.2)/[Py(1.5)/Fe(4.5)] sample with J = 0.0 erg/cm^2 measured at 13 GHz and (b) Py(6)/Pt(d_{Pt} = 2.2)/[Py(1.5)/Fe(4.5)] sample with J = 0.0 erg/cm^2 measured at 57 GHz. For $J \neq 0$ the two resonance modes are now referred to as the acoustic (higher field) and optical (lower field) modes. c) Py(6)/Pt(d_{Pt} = 0.7)/[Py(1.5)/Fe(4.5)] sample with J = 1.9 erg/cm^2 measured at 13 GHz and d) Py(6)/Pt(d_{Pt} = 0.7)/[Py(1.5)/Fe(4.5)] sample with J = 1.9 erg/cm^2 measured at 57 GHz. The vertical yellow dashed and blue dot-dashed lines intersect the resonance position for the acoustic mode (or Py for J = 0) and optical mode (or [Py/Fe] for J = 0) , respectively. The direction and magnitude of the arrows indicate the direction and magnitude of the shifts of the acoustic and optical modes with increasing coupling strength.

where χ' and χ'' are the real and imaginary parts of the rf transverse susceptibility given by

$$\begin{aligned}\chi' &= A\left(\frac{H_{\mathrm{DC}} - H_{\mathrm{res}}}{\Delta H^2 + (H_{\mathrm{DC}} - H_{\mathrm{res}})^2}\right),\\ \chi'' &= A\left(\frac{\Delta H}{\Delta H^2 + (H_{\mathrm{DC}} - H_{\mathrm{res}})^2}\right).\end{aligned} \tag{6.2}$$

6.4 Coupling Model

The phenomenological free energy density of Pt is taken to be the following [120]

$$f(x) = \frac{\beta}{2}\boldsymbol{M}^2 + \frac{\zeta}{2}\left(\frac{d\boldsymbol{M}}{dx}\right)^2 - \boldsymbol{M}\cdot\boldsymbol{H}, \tag{6.3}$$

where β is the inverse susceptibility and ζ is the exchange stiffness of Pt. The first term on the RHS of eq. (6.3) is the increase in energy of the Pt layer as a result of proximity polarization from an adjacent ferromagnet. The first term on the RHS of describes the energy cost of the induced magnetic moment to decay to zero. It is assumed that the Zeeman term is small in comparison to the other energy terms. At the interface the exchange field is significantly larger than any external applied field.

We make the small angle approximation, assuming that the magnetization vector of the the two ferromagnets are nearly parallel. In this case the coordinate system can always be oriented such that $M_x = M_y = 0$ and $M_z = M$. Therefore the total energy can we written as

$$F = \int_{-d/2}^{d/2}\left[\frac{\beta}{2}M^2 + \frac{\zeta}{2}\left(\frac{dM}{dx}\right)^2\right]dx. \tag{6.4}$$

The intergral is performed over the entire thickness of the of Pt, d. It is convenient to position the coordinate system in the middle the Pt layer, see fig. 6.3. The minimum energy, F_{min}, occurs at some $M(x) = g(x)$, $F_{min} = F(g(x))$. The variation around the minimum energy is given by

$$F\left[g + \epsilon\delta M\right] = \int\left[\frac{\beta}{2}\left(g + \epsilon\delta M\right)^2 + \frac{\zeta}{2}\left(\frac{d}{dx}g + \frac{d}{dx}\epsilon\delta M\right)^2\right]dx, \tag{6.5}$$

expanding and dropping the $O(\epsilon^2)$ terms

$$F\left[g + \epsilon\delta M\right] = \int\left[\frac{\beta}{2}g^2 + \frac{\zeta}{2}\left(\frac{d}{dx}g\right)^2 + \beta g\delta M\epsilon + \zeta\frac{d}{dx}g\frac{d}{dx}\delta M\epsilon\right]dx, \tag{6.6}$$

This function has a minimum at $\epsilon = 0$, therefore $\frac{dF[g+\delta M\epsilon]}{d\epsilon}|_{\epsilon=0} = 0$ and

$$0 = \int\left[\beta g\delta M + \zeta\frac{d}{dx}g\frac{d}{dx}\delta M\right]dx, \tag{6.7}$$

Using integration by parts on the last term,

$$0 = \int \left[\beta g - \zeta \frac{d^2}{dx^2} g\right] \delta M dx + \left[\frac{d}{dx}(g)\delta M.\right]_{x=-d/2}^{x=d/2} \tag{6.8}$$

The last term is zero if one assumes a variation that does not contribute at the start and end of the path, $\delta M(d/2) = \delta M(-d/2) = 0$. This is a consequence of assuming that the magnetization is fixed at the boundaries due to the surrounding ferromagnetic layers. Since this integral must vanish for all δM, the integrand must be zero for all x

$$0 = \beta M(x) - \zeta \frac{d^2}{dx^2} M(x). \tag{6.9}$$

For convenience, the energy minimizing path g has been replaced with $M(x)$. This is the differential equation governing the magnetization inside the Pt layer. The general solution takes the form of two exponentials,

$$M(x) = A\mathrm{Exp}\left(-\frac{x}{\xi}\right) + B\mathrm{Exp}\left(\frac{x}{\xi}\right), \tag{6.10}$$

where $\xi = \sqrt{\beta/\zeta}$ and the two constants A and B are determined by the boundary conditions.

For the single layer structure, FM|Pt, the boundary conditions are

$$\begin{aligned} M(x) &= M_0 \Big|_{x=-d/2}, \\ \frac{dM(x)}{dx} &= 0 \Big|_{x=d/2}. \end{aligned} \tag{6.11}$$

The solution is

$$M(x) = M_0 \frac{\mathrm{Exp}\left(\frac{d}{2\xi} - \frac{x}{\xi}\right) + \mathrm{Exp}\left(\frac{x}{\xi} - \frac{d}{2\xi}\right)}{\mathrm{Exp}\left(-\frac{d}{\xi}\right) + \mathrm{Exp}\left(\frac{d}{\xi}\right)}. \tag{6.12}$$

For the double layer structure, FM1/Pt/FM2, in which the magnetic moments in both ferromagnetic layers are parallel (fig. 6.1(a)) the boundary conditions are

$$\begin{aligned} M(x) &= M_0 \Big|_{x=-d/2}, \\ M(x) &= M_0 \Big|_{x=d/2}, \end{aligned} \tag{6.13}$$

and the solution is

$$M(x)_{\mathrm{P}} = M_0 \frac{\mathrm{Exp}\left(x/\xi\right) + \mathrm{Exp}\left(-x/\xi\right)}{\mathrm{Exp}\left(d/2\xi\right) + \mathrm{Exp}\left(-d/2\xi\right)}. \tag{6.14}$$

Alternatively this can rewritten as

$$M(x)_{\mathrm{P}} = M_0 \frac{\cosh(x/\xi)}{\cosh(d/2\xi)}. \tag{6.15}$$

If, however, the magnetic moments are polarized in opposite directions (fig. 6.1(a)) it is easy to show that,

$$M(x)_{\mathrm{AP}} = M_0 \frac{\sinh(x/\xi)}{\sinh(d/2\xi)}. \tag{6.16}$$

The thickness dependence of the induced magnetic moment in Pt will have a thickness dependence as displayed in fig. 6.3.

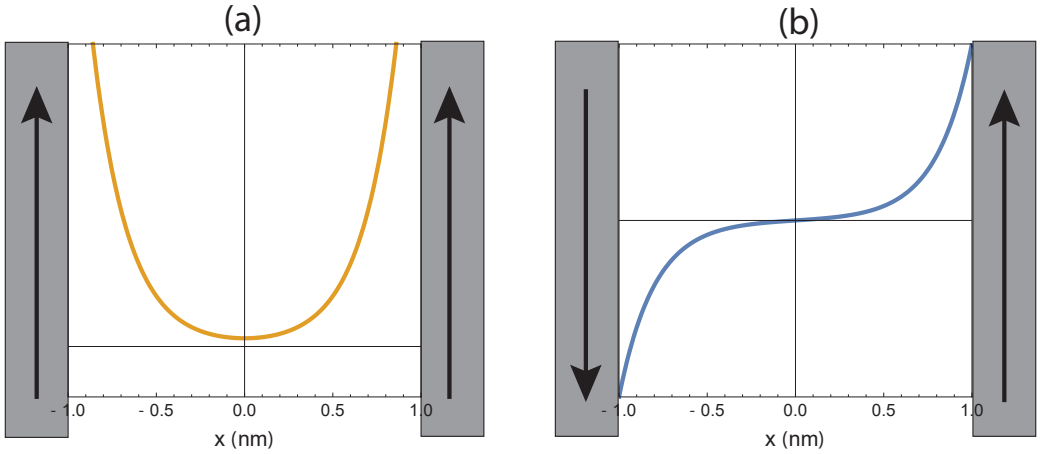

Figure 6.3: Examples of induced magnetic moment inside of Pt in FM/Pt/FM if both magnetic moments are parallel (a) from eq. (6.15) or antiparallel (b) from eq. (6.16). In this example $\xi = 0.2$ nm, $d_{\mathrm{Pt}} = 2$ nm, and $M_0 = 1$.

Finally, this can related to the coupling strength by determining the difference in energy for the parallel and anti-parallel configurations. By plugging eq. (6.15) and eq. (6.16) into eq. (6.4) and taking their difference it follows that the energy difference between the two configurations is

$$\Delta F = 2 \frac{M_0^2 \beta \xi}{\sinh(d/2\xi)}. \tag{6.17}$$

The difference in coupling from parallel to anti-parallel is given by $2J$, therefore it is simple to show that the exchange coupling strength is given

$$J(d_{\mathrm{Pt}}) = \frac{M_0^2 \beta \xi}{\sinh(d/2\xi)}. \tag{6.18}$$

6.5 Coupling Data Interpretation

The coupling strength J can be determined from the shifts in the resonance position of the optical and acoustic modes. In the structures studied in this section the ferromagnetic

coupling of FM1 and FM2 across Pt results in the resonance line of the Py(6) = FM1 to evolve into the acoustic mode and the resonance line of [Py(1.5)/Fe(4.5)] = FM2 evolve into the optical mode. As shown in chapter 4, the of FMR the [Py(1.5)/Fe(4.5)] bilayer behave like a single magnetic layer with a low intrinsic damping ($\alpha = 3 \times 10^{-3}$) and an effective demagnetizing field of $4\pi M_{\text{eff}}^{[Py/Fe]} = 18350 \pm 30$ Oe, as measured for the uncoupled sample, $d_{\text{Pt}} = 2.2$ nm. The difference in $4\pi M_{\text{eff}}^{[Py/Fe]}$ and $4\pi M_{\text{eff}}^{Py} = 10680 \pm 30$ Oe is enough to clearly distinguish the two resonances. Interlayer exchange coupling is an interface effect, so an additional advantage of [Py/Fe] is that Pt is only interfacing Py on both sides. This simplified the analysis since it was assumed that the structure had perfectly symmetric interfaces.

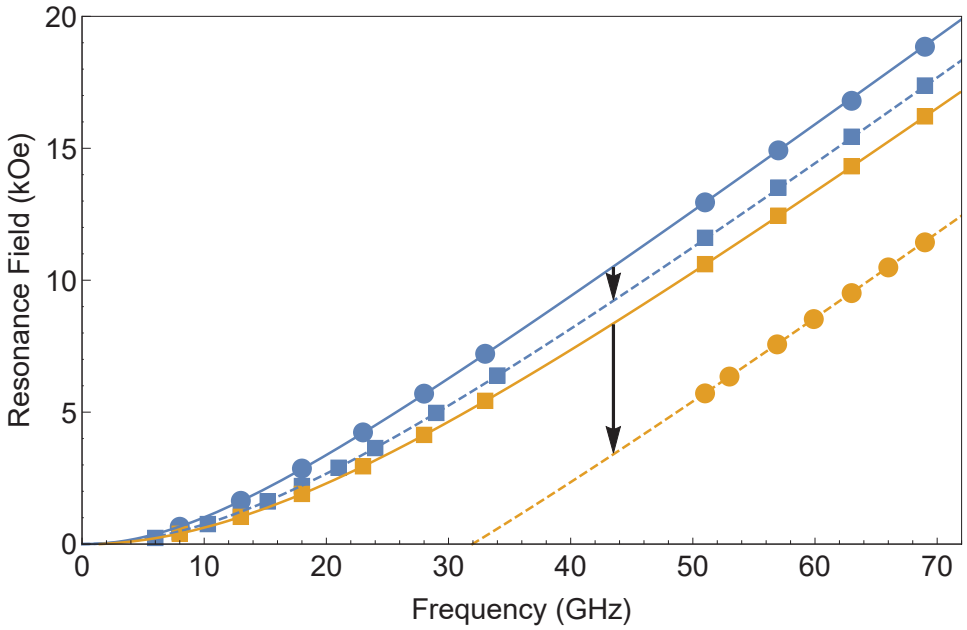

Figure 6.4: Examples of in-plane FMR data of the optical and acoustic modes for weakly and strongly coupled systems. The acoustic and optical modes are represented by the filled circles and squares, respectively. The yellow and blue colors correspond to the Py(6)/Pt(2.2)/[Py(1.5)/Fe(4.5)] ($J = 0.0$ erg/cm^2) and Py(6)/Pt(0.7)/[Py(1.5)/Fe(4.5)] ($J = 1.9$ erg/cm^2) structures. The solid lines are fits using solution to eq. (2.36).

The resonance position data, fig. 6.4, was interpreted with eq. (2.36). g-factor values were taken to be $g = 2.09$ [123] for both Py and [Py/Fe], consistent the with literature, $g_{Fe} = 2.09$ [124, 61] and $g_{Py} = 2.10$ [62, 63, 64]. $4\pi M_{\text{eff}}^{Py} = 10680 \pm 30$ Oe and $4\pi M_{\text{eff}}^{[Py/Fe]} = 18350 \pm 30$ Oe were determined by fitting the resonance position vs. frequency data of the uncoupled sample, $d_{\text{Pt}} = 2.2$ nm. The error margins were estimated from measurements of multiple, identical samples. For the rest of analysis the demagnetizing field was fixed at $4\pi M_{\text{eff}}^{Py}$ and $4\pi M_{\text{eff}}^{[Py/Fe]}$ to be constant for all d_{Pt}. Given these parameters, simultaneous fits to the acoustic and optical resonance positions vs. frequency using eq. (2.36) were made, where

the only free fitting parameter was J, see solid lines in fig. 6.4. All fits showed very good agreement with the data. Note, allowing g_i and g_j to be free fitting parameters yielded g_i and g_j values between 2.08 and 2.10 but did not change the value of J.

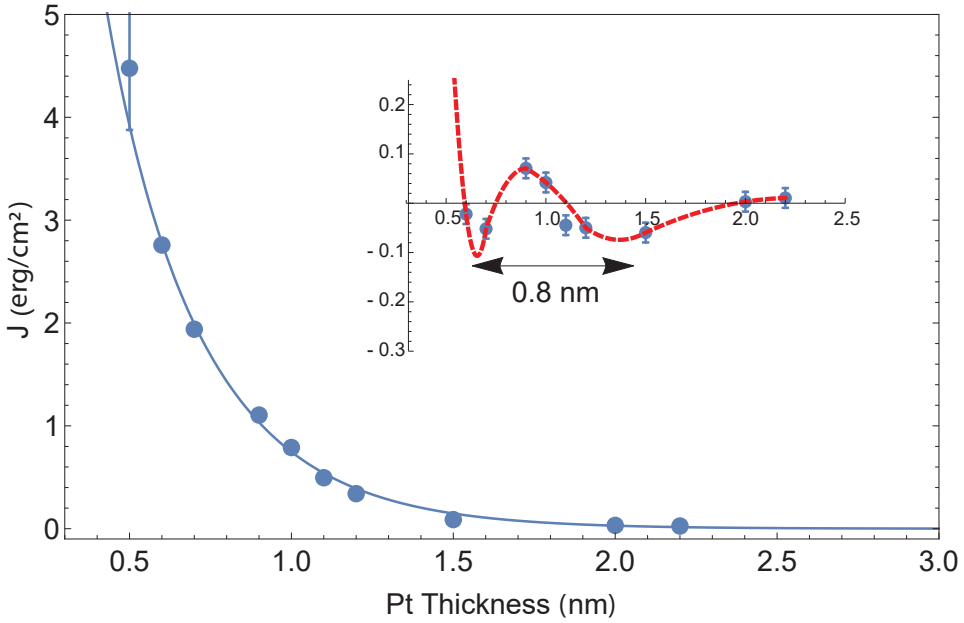

Figure 6.5: Interlayer exchange coupling strength J as a function of Pt thickness for Py(6)/Pt(d_{Pt})/[Py(1.5)/Fe(4.5)] structures. The solid line is a fit using eq. (6.18) yielding $\xi = 0.31 \pm 0.01$ nm. Residuals are plotted in the inset with dashed line used to guide the eye.

The main result of this study, the interlayer exchange coupling strength J, as a function of Pt thickness is displayed in fig. 6.5. Ferromagnetic coupling was observed for all thicknesses of Pt. For $d_{\mathrm{Pt}} \lesssim 1.5$ nm the coupling strength was monotonically and rapidly increasing with decreasing d_{Pt}. The maximum measured coupling strength was $J = 4.5 \pm 0.7$ erg/cm^2 for $d_{\mathrm{Pt}} = 0.5$ nm; the large error on this point is due to the very weak signal of the optical mode. For $d_{\mathrm{Pt}} < 0.5$ nm no optical mode was observed and therefore coupling strength could not be measured below this thickness.

It was assumed that the coupling of the two ferromagnetic layers is dominated by the proximity magnetism of Pt. This model has been proposed for a study of temperature dependence on coupling strength in Py/Pt(d_{Pt})/Py, where $d_{\mathrm{Pt}} > 2$ nm [120]; see section 6.4 for a detailed derivation. In [120] the coupling strength was measured for larger thicknesses of Pt, $2 \leq d_{\mathrm{Pt}} \leq 3.5$ nm. The coupling strengths were $J \lesssim 0.06$ erg/cm^2 at room temperature or $J \lesssim 0.35$ erg/cm^2 at cryogenic temperatures at $d_{\mathrm{Pt}} = 2$ nm. In our samples we measure $J = 0.03 \pm 0.02$ erg/cm^2 for $d_{\mathrm{Pt}} = 2$ nm. The lower coupling strength of our samples could be attributed to different growth conditions of our structures. Additionally, in the work

of [120], the exchange coupling measurements were done by employing the giant magneto resistance effect in a spin-valve structure, Py(8)/Pt(d_{Pt})/Py(3)Ir20Mn80(8)/Ta(1.5).

Fitting the experimental data with eq. (6.18) resulted in a good fit yielding ξ = 0.31±0.01 nm fig. 6.5, this values is close that observed in [120], ξ^{Lim} = 0.26 nm.

Ref. [120] observed a large temperature dependence of susceptibility, which was well described by Curie-Weiss law up to liquid nitrogen temperatures, clearly proving that the possible penetration of Py through Pt was not caused by the pinhole effect (thermally stable ferromagnetic bridges through Pt). The observed temperature dependence of susceptibility can be caused by thermally fluctuating clusters of magnetic moments in Pt (paramagnons). This was observed in ref. [95] where they observed a large temperature dependence of χ_m^{Pd} enhanced due to induced strain at the Au/Pd interface. It is expected that the presence of the proximity effect induced by the Py/Pt interface leads to the presence of paramagnons in our Py/Pt/Py structures. However, one cannot exclude some interdiffusion of Py into the Pt layer. This would further enhance the presence of paramagnons and would effectively increase the measured susceptibility of the Pt layer. Consequently, this would increase the penetration depth of the magnetic moment into Pt resulting in a larger ξ. These two cannot be distinguished, however, it does not change the model used for interpretation of the data.

The residuals of the fit resemble the characteristics of Ruderman-Kittel-Kasuya-Yosida (RKKY) [125] type of interlayer exchange coupling with a period of ≈ 0.8 nm and maximum amplitude of ≈ 0.1 erg/cm^2. This can be compared to an experimental study of interlayer exchange coupling of the MBE deposited single crystal Fe/Pd/Fe system [96]. The authors observed oscillations with a period of ≈ 0.6 nm and maximum amplitude ≈ 0.1 erg/cm^2 for thickness of Pd of 1.6 nm. The amplitude of oscillations from experiment is significantly lower than what is expected from first principles density functional theory, which reports oscillations with an amplitude of ≈ 10 erg/cm^2 in a Fe/Pd/Fe system [126] carried out for T=0. However, in our experiment the sputter deposited textured structures and fluctuating paramagnetic clusters in Pt at room temperature, both not included in theory, may also play a significant role in suppressing the oscillatory behaviour in exchange coupling.

With ξ determined, one can find the thickness dependent magnetization in Pt from eq. (6.12), see fig. 6.6. Using the results of an XMCD study of Py(6)/Pt(1) [58], the authors report an average magnetic moment for 1nm Pt of $\langle M \rangle$ = 0.27 μ_B/atom. To convert this to magnetization recall that $\mu_B = 9.274 \times 10^{-21}$ erg/G and fcc-Pt has 4 atoms per unit cell with a lattice constant of 3.9 Å. Equating this to the single layer solution, eq. (6.12), integrated over 1 nm results in M_0 = 650 erg/cm^3. The plots of the magnetization of the single layer and the double layer are shown in fig. 6.6. The decaying behaviour of the magnetization is very similar to that determined from first principle calculations for Pd, see fig. 9 in ref. [96].

Finally, with ξ and M_0 determined one can find the magnetic susceptibility of Pt from eq. (6.18), $\beta^{-1} = \chi^{Pt} = 1.6 \times 10^{-2} \pm 0.2 \times 10^{-2}$ (or $\chi_m^{Pt} = 1.4 \times 10^{-7} \pm 0.2 \times 10^{-7}$ m^3/mol). This is ~ 100 times larger than for bulk Pt ~ 10^{-9} m^3/mol [127]. Such a large enhancement is not

unreasonable if considering the work of [95] in which the authors observed an enhancement of χ_m^{Pd} by ~ 500 times due to induced strain at the Au/Pd interface.

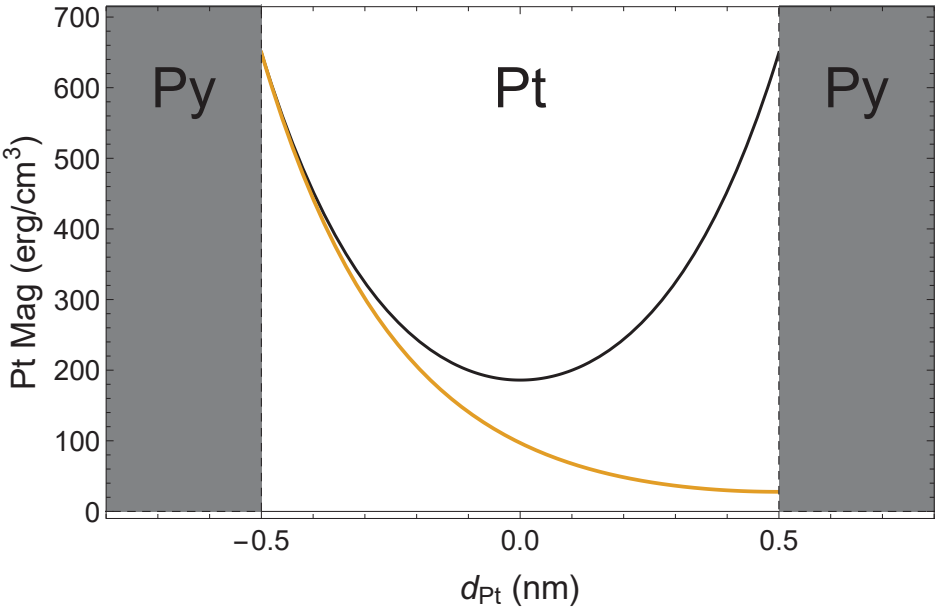

Figure 6.6: Simulated magnetization inside of 1 nm thick Pt. The black line is the magnetization of the Py/Pt(1)/Py as determined from eq. (6.14)(a). The yellow line is the magnetization of the Py/Pt(1) structure as determined from eq. (6.12)(b). The interface magnetization was determined using results from [58], see details in text.

6.6 Orange-Peel Coupling

An additional possible contribution to the measured coupling could originate from orange-peel coupling, which is a consequence of in plane film roughness [30, 31]. This is a form of dipolar coupling between the corrugation peaks in the film surface. Its contribution can be estimated from [128]

$$J_{op} = 4\pi M_{s1} M_{s2} \frac{\delta^2}{L} \mathrm{Exp}\left(\frac{-2\pi d_{\mathrm{Pt}}}{L}\right), \tag{6.19}$$

where δ is the amplitude of roughness oscillations and L is the lateral period of roughness. Note, in eq. (6.19), $J_{op} = J_{op}(L)$ is not a monotonic function, and has a maximum at $L = 2\pi d_{\mathrm{Pt}}$, therefore it is possible to estimate the upper limit of the coupling strength. Atomic force microscopy was performed on Py/Pt(1) samples of 500×500 nm sized. The root-mean-square roughness and standard deviation were measured to be $\sigma_{SD} = \delta_{\mathrm{RMS}} = 0.13$ nm, and the maximum to minimum depth is ~ 0.7 nm. Given that 95% of the sample is within $\pm 2\sigma_{SD}$, one can estimate the contribution due to orange peel coupling using the amplitude of roughness oscillations $\delta = 0.26$ nm. The coupling is between two Py interfaces, therefore taking $4\pi M_{s1} = 4\pi M_{s2} = 4\pi M_s^{Py} = 10.27$ kOe and $d_{\mathrm{Pt}} = 0.5$ nm (the thinnest

sample), it was found that eq. (6.19) has a maximum of $J_{op} = 0.003$ erg/cm^2 at $L = 3.1$ nm. This is within the measurement uncertainty of J as determined from FMR. Therefore orange-peel cannot be resposible for the observed interlayer exchange coupling.

6.7 Magnetic Damping

The measured effective damping of the acoustic mode (Py layer) is shown in fig. 6.8 (a) and the zero-frequency offset in fig. 6.8 (b). As before, the damping and zero frequency offset were both determined from fitting the line-width with,

$$\Delta H(\omega) = \alpha \frac{\omega}{\gamma} + \Delta H(0). \tag{6.20}$$

The high frequency measurements had much smaller amplitude and therefore required much longer scan times to get to similar statistical significance as lower frequency measurements, fig. 6.2. The optical mode (lower field peak in fig. 6.2) rapidly decreases in amplitude with increasing J and requires an unreasonable amount of time to extract a meaningful line-width. Therefore for the damping analysis the focus was on the acoustic modes within the frequency range of $8 < f < 34$ GHz, see fig. 6.7(a).

Qualitatively the damping behaviour of α vs d_{Pt} can be separated into three regions. For $0 < d_{\mathrm{Pt}} < 0.9$ nm, α_{eff} shows a linear increase with increasing d_{Pt}. The second region, $0.9 < d_{\mathrm{Pt}} < 1.5$ nm, shows a more rapid but still linear increase of α_{eff} with increasing d_{Pt}. In the third region, $1.5 < d_{\mathrm{Pt}} < 2.2$ nm, when $J \sim 0$, the α_{eff} saturates to 1.7×10^{-2}; in this case the acoustic mode is the normal resonance peak of the Py layer. The zero-frequency offset shows a non-linear dependence on d_{Pt}, fig. 6.8 (b).

The total extracted damping and zero-frequency offset can be considered as a sum of several contributions. First are the individual dampings of the Py and [Py/Fe] layers, α_{Py} and $\alpha_{[\mathrm{Py/Fe}]}$ respectively. In order to characterize the dampings of the individual layers two additional structures were deposited and their linewidth vs. frequency dependence was measured up to 69 GHz, see fig. 6.8(b). The Py(6) layer has a linear $\Delta H(0)$ frequency dependence, fitting it with eq. (4.10) yields $\alpha_{\mathrm{Py}} = 7.9 \times 10^{-3} \pm 0.1$ and $\Delta H(0)_{\mathrm{Py}} = 1.9 \pm 0.4$ Oe. However, the [Py(1.5)/Fe(4.5)] is non-linear, as was also observed in chapter 4. This non-linearity was attributed to two-magnon scattering which is the scattering of $k = 0$ (uniform precession) to $k \neq 0$ states within the ferromagnetic system. The effect of two-magnon scattering on the linewidth of the FMR resonance has been extensively studied and manifests itself as a non-linearity in the line-width vs. frequency dependence [129, 130]. Two-magnon scattering saturates above a high enough frequency and the linewidth again becomes linear in frequency [131]. To fit the contribution of two-magnon scattering to the

linewidth, one can use [129]

$$\Delta H(\omega) = \alpha\frac{\omega}{\gamma} + \frac{2\Gamma}{\pi}\sin^{-1}\sqrt{\frac{\sqrt{\omega^2+(\omega_0/2)^2}-\omega_0/2}{\sqrt{\omega^2+(\omega_0/2)^2}+\omega_0/2}}, \tag{6.21}$$

where Γ characterizes the strength of the two-magnon contribution to damping in units of Oe and ω_0 is the frequency on which the two-magnon contribution approaches saturation. The fit resulted in $\alpha_{[\mathrm{Py/Fe}]} = 3.5 \pm 0.1$, $\Gamma = 54.0$ Oe and $f_0 = \omega_0/2\pi = 59.2$ GHz for the Ta(3)/[Py(1.5)/Fe(4.5)]/Au(3.6) structure, fig. 6.7.

With the damping value of the two magnetic structures determined it is convenient to separate out the other contribution to the magnetic damping.

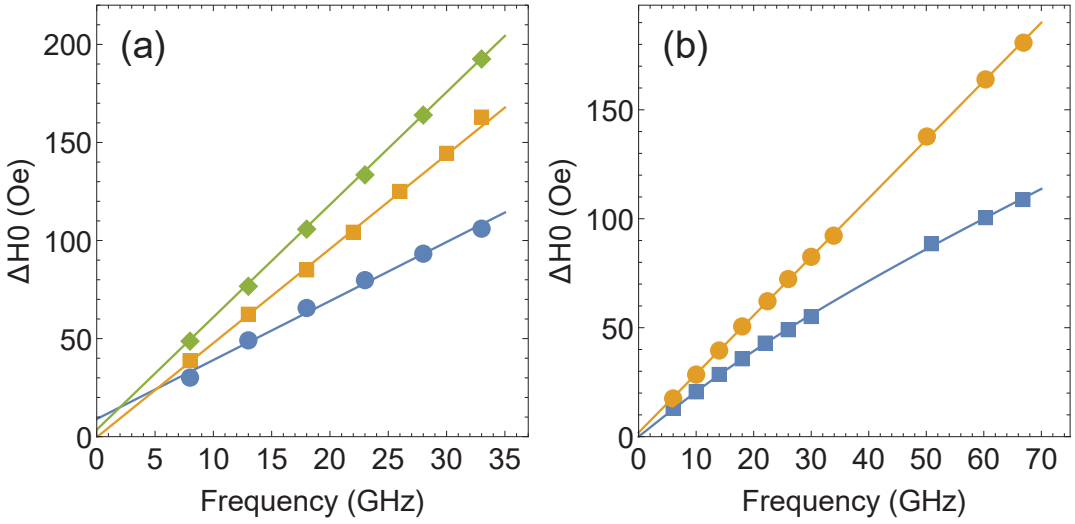

Figure 6.7: (a) Sample linewidth data of the acoustic mode for Ta(3)/Py(6)/**Pt(0.5)**/Py(1.5)/Fe(4.5)/Ta(3 (blue circle), Ta(3)/Py(6)/**Pt(1.1)**/Py(1.5)/Fe(4.5)/Ta(3) (yellow square) and Ta(3)/Py(6)/**Pt(2.2)**/Py(1.5)/Fe(4.5)/Ta(3) (green diamond), the solid lines are fits using eq. (6.20). (b) Linewidth data for Ta(3)/Py(6)/Au(3.6) (yellow circle) and Ta(3)/Py(1.5)/Fe(4.5)/Au(3.6) (blue square) with fits using eq. (6.20) and eq. (6.23).

With the damping value of the two magnetic structures determined it is convenient to separate out the other contribution to the magnetic damping

$$\begin{aligned} \alpha_{\mathrm{eff}} &= \alpha_J + \alpha_{sp} \\ \alpha_J &= \alpha_J\left(J, \alpha_{\mathrm{Py}}, \alpha_{[\mathrm{Py/Fe}]}\right). \end{aligned} \tag{6.22}$$

$\boldsymbol{\alpha_J}$: the damping contributions due to coupling of the two magnetic layers. The acoustic mode is the in-phase precession of the two magnetic layers and therefore the acoustic resonance has to have some damping corresponding to an average of the two magnetic layers. Given the damping of individual Py and [Py/Fe] layers and the exchange coupling

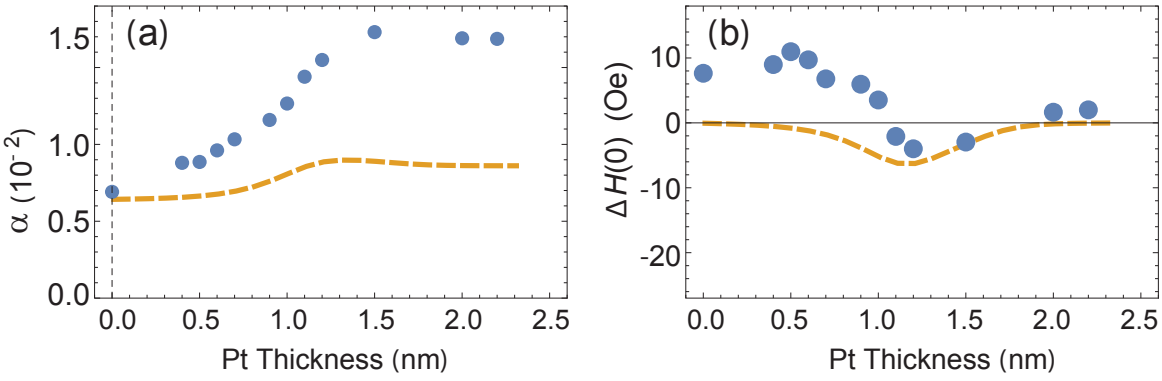

Figure 6.8: The measured effective damping (a) and zero-frequency offset (b) of the acoustic mode as a function of Pt thickness as determined from eq. (4.10). The dashed lines represent the simulations of α_{eff} (a) and $\Delta H(0)$ (b) including various contributions, see eq. (6.22).

constant, J, one should be able to determine the effect of the exchange coupling on the line-width. Note that since the line-width frequency dependence of the [Py/Fe] is nonlinear, it is expected that the resulting frequency dependence of the acoustic mode should also be non-linear with strong enough coupling.

$\boldsymbol{\alpha_{sp}}$: this is the spin-pumping contribution to magnetic damping of the acoustic mode. Currently there is no consensus on what is the appropriate spin-pumping model for the limit of thin Pt in proximity to a ferromagnet. Studies on spin diffusion length in Pt by means of (inverse spin hall effect)ISHE agree that there must spin loss at the ferromagnet/Pt interface [17, 132] to account for the large discrepancy in measured diffusion lengths from Gilbert damping vs. ISHE experiments [133]. These works focus on the thicker limit of Pt(~ 1 - 20 nm) in order to capture the full thickness dependence of ISHE-voltage, which does not saturate until ~ 15 nm for Pt. Theoretically, the effect of spin loss on the Gilbert damping measurements is to cause a large, and immediate, increase in the damping with the introduction of even the thinnest Pt adjacent to the ferromagnet [18]. This is contrary to what is observed in Gilbert damping studies for the thin limit (~ 0 - 3 nm) of Pt [58, 134, 91], where a steep approach to saturation is observed from 0 to ~ 2 nm. Experimental results presented here also do not show any abrupt increase in damping, but an approach to saturation, see fig. 6.8(a).

With the above contributions influencing the line-width it becomes a challenging problem to disentangle them with such limited data (only acoustic mode and only for lower frequencies). Therefore we decided to redesign the experiment in order to simplify the analysis (minimizing the two-magnon contribution). Before moving on it was interesting to at least attempt to address the effect of coupling strength on the damping and zero-frequency offset. This was done by simulating the FMR resonances for the structure Py/Pt/[Py/Fe] structure and comparing the results to the experimental data.

Simulation Procedure: For a given excitation frequency the entire FMR spectra of the coupled Py and [Py/Fe] system was simulated using solutions to eq. (2.35). The simulation parameters were: M_s^{Py} = 817 emu/cm^3, $M_s^{[Py/Fe]}$ = 1468 emu/cm^3, g-factor= 2.09, $4\pi M_{\text{eff}}^{Py}$ = 10680 Oe and $4\pi M_{\text{eff}}^{[Py/Fe]}$ = 18347 Oe. The damping of Py layer was taken to be $\alpha_{\text{Py}} = 7.9$ and for the [Py/Fe] layer a frequency dependent damping was used in order to include the two-magnon contribution,

$$\alpha_{[Py/Fe]}^{\text{TM}} = \alpha_{[\text{Py/Fe}]} + \frac{\gamma}{\omega}\frac{2\Gamma}{\pi}\sin^{-1}\sqrt{\frac{\sqrt{\omega^2 + (\omega_0/2)^2} - \omega_0/2}{\sqrt{\omega^2 + (\omega_0/2)^2} + \omega_0/2}}, \tag{6.23}$$

$\alpha_{[\text{Py/Fe}]} = 3.5 \pm 0.1$, Γ = 54.0 Oe and f_0 = 59.2 GHz as determined from the Ta(3)/[Py(1.5)/Fe(4.5)]/Au(3.6) structure. The effect of magnetic inhomogeneity, $\Delta H(0)_{\text{Py}}$ or $\Delta H(0)_{[\text{Py/Fe}]}$, was not included in the simulation in anyway. The simulated FMR spectra was repeated for the same frequencies as the experimental measurements, $8 < f < 33$ GHz, and the line-width of the acoustic mode was extracted for each frequency. Then the extracted line-width frequency dependence was fit with eq. (6.20) yielding values of α and $\Delta H(0)$ for the simulated acoustic mode. The above procedure was repeated for $0 < J < \infty$ erg/cm^2 where J is related to d_{Pt} through fig. 6.5. Results of the simulated damping and zero-frequency offset are displayed in fig. 6.8 as dashed lines. With this approach the experimental FMR data and the simulated FMR spectra was analyzed in the same way.

Qualitatively the simulated α_J reproduces most of the features of the experimental data. The damping is constant for $d_{\text{Pt}} \lesssim 1.5$ nm with rapid decrease at $d_{\text{Pt}} \sim 1.1$ nm, which corresponds to $J \sim 1$ erg/cm^2. However, at the very thin limit $d_{\text{Pt}} \lesssim 0.9$ nm, the experimental data show a continuous decrease in damping, while the simulation shows a saturation of damping below this thickness. However, there is a very large thickness dependent offset between the simulated data and the experimental results. This offset can be attributed to spin-pumping, but it's worth remembering that this is not the type of spin-pumping as expected in a simple FM/NM system. In this exchange coupled system both ferromagnetic layers are precessing and therefore spin-pumping at varying degrees depending on the strength of the exchange coupling.

It is interesting that the simulated linewidth data has a non-zero $\Delta H(0)$ even though no intrinsic $\Delta H(0)$ was taken into account during the simulation. This suggests that the exchange coupling of the two magnetic layers (one of which has a non-linear dependence of the linewidth vs frequency) results in an non-linear linewidth vs frequency. Fitting non-linear data with a straight line, eq. (6.20), results in a non-zero offset. Surprisingly the simulated zero-frequency offset, takes on a negative values for $d_{\text{Pt}} \sim 1.2$ nm, see fig. 6.8(b). Qualitatively this trend is also observed in the experimental data.

Chapter 7

Spin-Pumping in Pt From Optical and Acoustic Resonance modes

7.1 Motivation

At present the mechanism of spin-transport and spin-pumping into Pt is not well understood. Experimental studies of of spin-pumping induced damping into Pt show variety of thickness dependence, ranging from linear [58] to discontinuous [134] and the more conventional exponential [135, 136]. The interpretation of experimental results are complicated by the potential spin-memory loss at the FM/Pt interface [17, 132, 137], originating from the interface Rashba effect [18] Furthermore, the influence of magnetic proximity [138] on the spin-pumping and spin-transport remains a topic of debate. Spin-diffusion length measurements by inverse spin Hall effect (ISHE)[139, 140] observe a much longer length scale as compared to spin-pumping studies. Lastly, given the strong proximity polarization of Pt it is not clear if the conventional spin-pumping theory [7] applies to the ferromagnet/Pt interface. As observed in the previous section, the effective magnetic moment in Pt at the FM/Pt interface extends some distance into Pt [112, 32]. A simple approach to avoid proximity polarization is to separate the FM and Pt (or Pd) with a spacer layer, however such studies observe an oscillatory spin-pumping damping dependence (Cu [141] or Au [21]) which is clearly outside the conventional spin-pumping description and is likely related to the Cu/Pt or Au/Pt interface, see chapter 9.

One of the main difficulties in studying spin-pumping into Pt lies in experimentally separating out the various contributions which may influence the measured damping. As was shown in chapter 4, in order to make a unique interpretation of spin-pumping from magnetic damping measurements, it is necessary to study both the FM1/NM structure and the spin sink structures FM1/NM/FM2. In section 6.7 an attempt was made to interpret the magnetic damping measurement of the Py/Pt(d_{Pt})/[Py/Fe] structure. However, a large portion of the measured damping was associated with the difference in intrinsic dampings of the Py and the [Py/Fe] (which is averaged depending on the coupling strength) as well as

the two-magnon scattering of the [Py/Fe]. These contributions complicate the analysis and make it difficult to make a clear statement about the validity of the spin-pumping model in Pt. In order to simply the analysis the experimental structures were slightly altered to Py/Pt(d_{Pt})/Py which resulted in a much cleaner spin-pumping experiment.

7.2 Experimental Details

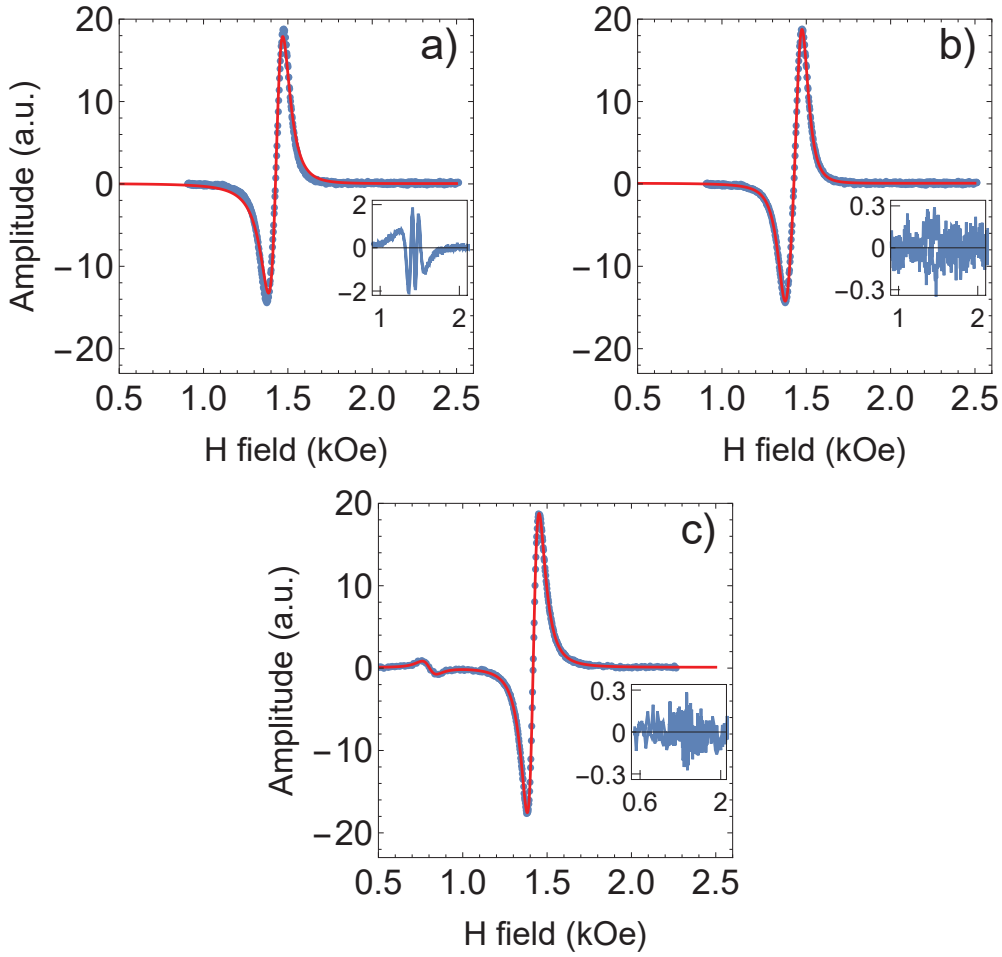

Figure 7.1: FMR response of the Py/Pt(3.5)/Py (a,b) and the Py/Pt(1.2)/Py (c) structures for rf driving at 12 GHz. a) is a fit with a single Lorentzian (eq. (6.1)) with ΔH = 70 Oe and H_{res} = 1436 Oe. b) is fit with two Lorentzians with ΔH_1 = 68 Oe, ΔH_2 = 72 Oe, H_{res1} = 1450 Oe and H_{res2} = 1395 Oe. For (c) the fitting parameters are $\Delta H^{\mathrm{Optical}}$ = 72 Oe, $\Delta H^{\mathrm{Acoustic}}$ = 60 Oe, $H_{\mathrm{res}}^{\mathrm{Optical}}$ = 800 Oe and $H_{\mathrm{res}}^{\mathrm{Acoustic}}$ = 1419 Oe. The insets represent the residuals of the resulting fits.

As in the previous chapters, the thin films were sputter deposited on a Si substrate, see section 3.2 for more details. The deposited structures were Ta(3)|Py(6)|Pt(d_{Pt})|Py(6)|Ta(3) and Ta(3)|Py(6)|Pt(d_{Pt}). The bottom Ta(3) was the seed layer and the top Ta(3) layer was

a protective layer for Py. Since the spin-pumping was determined from the damping of both the Py layers, it was important for both of them to have very similar damping in order to extract meaningful spin-pumping parameters. This is made clear in section 6.7 where the two ferromagnetic layers have different damping values which were averaged by the exchange coupling strength, resulting in a very complicated damping dependence. Having Ta(3) interfacing both the Py layers serves the purpose of making both Py have the same damping, since at it was observed in chapter 5 that there can be substantial spin-pumping damping into Ta. The spin-diffusion length of Ta is 1 nm, therefore a 3 nm thick Ta layer should already be in the saturated limit of spin-pumping, resulting in negligible variations of spin-pumping into Ta due to small variations in the thickness of Ta.

The magnetic damping of the system was determined from broadband, in-plane FMR as described in section 2.3.2. FMR data examples of the Ta(3)|Py(6)|Pt(d_{Pt})|Py(6)|Ta(3) structures with fits given by eq. (6.1) are presented in fig. 7.1. For very weak magnetic coupling ($J \sim 0$ at $d_{\mathrm{Pt}} = 3.5$ nm) there are two, slightly offset, overlapping FMR responses corresponding to the two Py layers of Ta(3)|Py(6)|Pt(d_{Pt})|Py(6)|Ta(3). The offset is a result of the small difference in their magnetic properties, this is not surprising considering that the two Py layers were deposited on different interfaces: the bottom one is on top of Ta, while the top one is on top of Pt. Visually this offset cannot be observed, see fig. 7.1(a), however fitting the data, assuming a single FMR response results in an obvious field dependent trend in the residuals, see inset of fig. 7.1(a) inset. This type of residual is not typical to fits of single layered magnetic structures. Refitting the same data with FMR resonances results in much larger residuals, without any observable trend (see inset of fig. 7.1 (b)) and yields two separate values for ΔH and H_{res} corresponding to the two magnetic Py layers. The extracted resonance field of one of the Py layers is always slightly larger than the other Py layer, $H_{\mathrm{res1}} > H_{\mathrm{res2}}$ with corresponding ΔH_1 and ΔH_2, see fig. 8.1 (a) and (b). Note for the purpose of this experiment it was important that the two resonance are nearly perfectly overlapping for zero coupling strength since this suggest that their magnetic properties are very similar. From the point of view of the analysis of the spin-pumping data the exact values of the two damping are not important, in fact they are treated as having identical damping values at $J \sim 0$ at $d_{\mathrm{Pt}} = 3.5$ nm.

Thinner Pt layers result in non-negligible exchange coupling ($d_{\mathrm{Pt}} = 1.2$ nm corresponding to $J = 0.3$ erg/cm^2) and the two resonance modes become well separated, see fig. 7.1 (c). The relative amplitude of the two resonances modes is quite small even for $J = 0.3$ erg/cm^2, much smaller than what was observed in chapter 6. For comparison see fig. 6.2(d) where the relative amplitude is smaller for a much larger coupling strength ($J = 1.9$ erg/cm^2). This is consequence of the two Py layers having very similar resonance fields at zero coupling. As discussed in chapter 6, the purpose of choosing two very different ferromagnetic layers was in order to be able to measure strong coupling strengths. Additionally, in the coplannar waveguide setup the magnetic field is not uniform in the measured structure (as compared

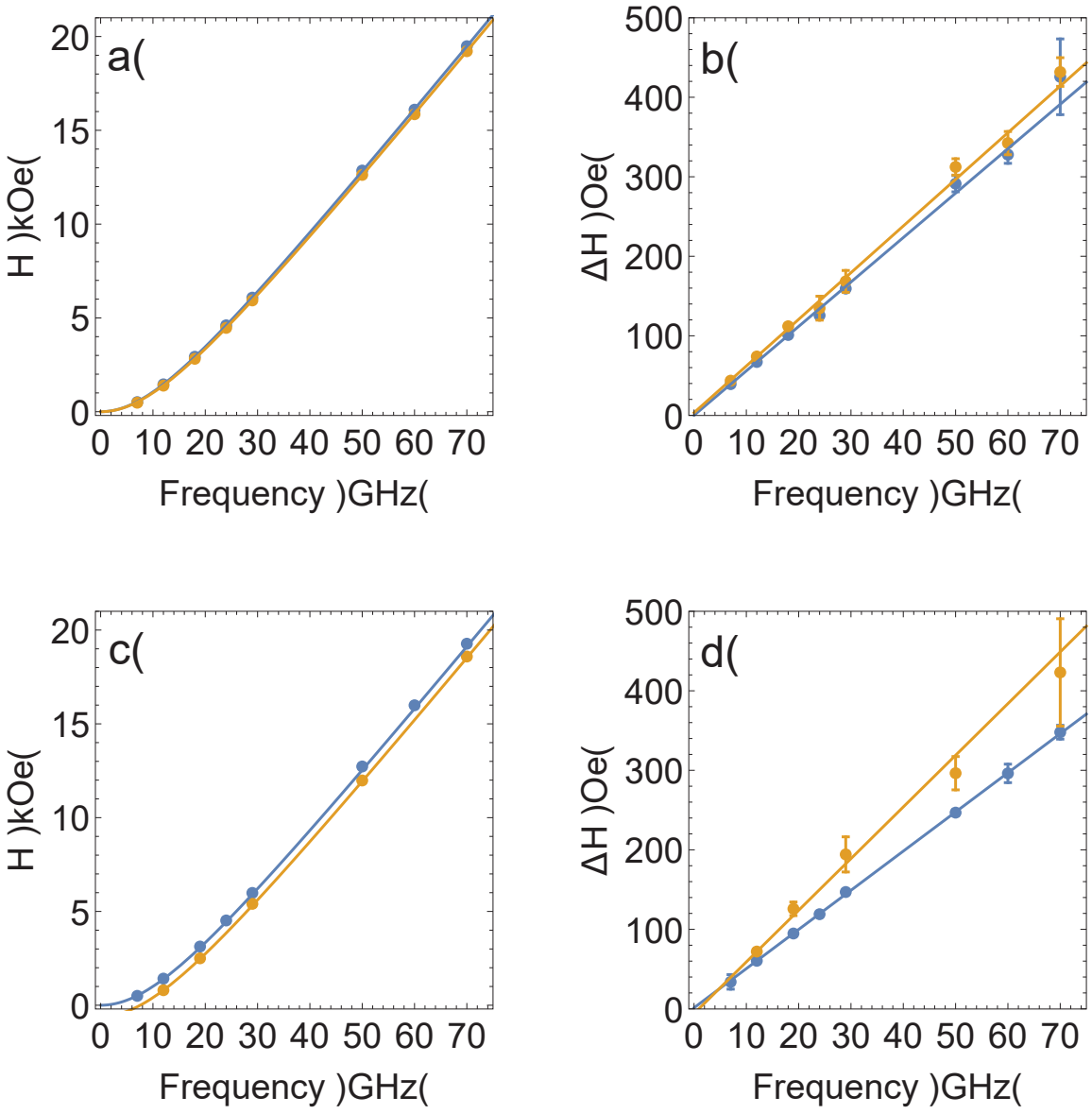

Figure 7.2: (a) and (c) are the resonance field of the acoustic (blue) and optical (yellow) modes for the Py/Pt(3.5)/Py and Py/Pt(1.2)/Py, respectively. The solid lines are fits using the solution to eq. (2.16) (see eq. (6) and eq. (7) in supplemental material of [15]) yielding $4\pi M_{\text{eff},1} = 10.2 \pm 0.1$ kOe and $4\pi M_{\text{eff},2} = 10.6 \pm 0.1$ kOe for fits in (a). (b) and (d) are the linewidth of the acoustic (blue) and optical (yellow) modes for the Py/Pt(3.5)/Py and Py/Pt(1.2)/Py, respectively.

to a cavity setup). This results in a difference in driving strength for each magnetic layer, i.e. the bottom layer is driven more strongly than the top layer and therefore there is a difference in the relative amplitude of the resonance modes. In principle this effect should also enhance the ability to measure the coupling strength for nearly identical magnetic layers.

7.3 Theory: Spin-pumping in an exchange coupled system

The magnetization dynamics of two interlayer exchange coupled, ferromagnetic films, under the influence of static external and internal fields and an oscillating rf-field, $\boldsymbol{h}_{rf}$, is described by the Landau-Lifshitz-Gilbert (LLG) equation, written in the form of effective torques,

$$\frac{1}{\gamma_1}\frac{\partial \boldsymbol{M}_1}{\partial t} = -\boldsymbol{M}_1 \times \left[\boldsymbol{H}_{\text{eff},1} + \frac{J\boldsymbol{n}_2}{d_1 M_{\text{s},1}}\right] + \alpha_1 \left[\boldsymbol{n}_1 \times \frac{1}{\gamma_1}\frac{\partial \boldsymbol{M}_1}{\partial t}\right] \tag{7.1a}$$

$$\frac{1}{\gamma_2}\frac{\partial \boldsymbol{M}_2}{\partial t} = -\boldsymbol{M}_2 \times \left[\boldsymbol{H}_{\text{eff},2} + \frac{J\boldsymbol{n}_1}{d_2 M_{\text{s},2}}\right] + \alpha_2 \left[\boldsymbol{n}_2 \times \frac{1}{\gamma_1}\frac{\partial \boldsymbol{M}_2}{\partial t}\right], \tag{7.1b}$$

where $\boldsymbol{M}_1$ and $\boldsymbol{M}_2$ are the instantaneous magnetization vectors with magnitudes $M_{\text{s},1}$, $M_{\text{s},2}$ and $\boldsymbol{n}_1$ and $\boldsymbol{n}_1$ are the unit vectors parallel to $\boldsymbol{M}_1$ and $\boldsymbol{M}_2$, respectively. $\boldsymbol{H}_{\text{eff},1}$ and $\boldsymbol{H}_{\text{eff},2}$ are the sum of internal and external H-fields, α_1 and α_2 are the dimensionless Gilbert damping parameters, J (in erg/cm^2) is the interlayer exchange coupling strength, d_1 and d_2 are the thicknesses of each ferromagnet, and $\gamma_1 = g_1\mu_B/\hbar$ and $\gamma_2 = g_2\mu_B/\hbar$ are the absolute values of gyromagnetic ratios, where g_1 and g_2 are the Landé g-factor, μ_B is the Bohr magneton and, $\hbar$ is the reduced Planck constant. The resonance conditions can be determined from the solution of eq. (7.1), see section 2.4 for more details.

For a structure consisting of two ferromagnetic films separated by a non-magnetic film, FM1/NM/FM2, the magnetic layers can act as either spin-current sources or as perfect spin-sinks [7] to the spin-current backflows at the FM1/NM and NM/FM2 interfaces. In these type of studies FM1 would be treated as the source of spin-current, while FM2 as the absorber. This is the situation when the resonance fields of FM1 and FM2 are far enough apart, such that they are not simultaneously driven the same rf field, this was the case in the previous chapter, section 6.7. If the two magnetic structures have different in-plane anisotropies then it is possible to bring the two FMR resonance fields to crossover. This clever experiment was performed on MBE deposited Fe/Au/Fe heterostructure where the two magnetic layers had a different angular dependence of in-plane anisotropies and therefore their resonance fields could be adjusted simply with the angle of the external applied magnetic field.[142] At crossover (the resonances fields of both layers over lap) which results in a simultaneous spin-pumping of both layer. The structures studied in my work do no have any in-plane anisotropies due to the random orientation of the grain in the plane of the film. However, it is possible to take advantage of a similar effect by depositing two struc-

tures with nearly identical magnetic properties. In the experiment presented in this section the two magnetic layer are nearly identical in their magnetic properties and are therefore always simultaneously driven. However, in these studies the spacer layer for FM1 and FM2 was Pt, and as it was observed in the previous chapter, Pt mediates interlayer exchange coupling [32]. For non-zero coupling the observed resonances are no longer independent and correspond to an in out-of-phase (optical mode) and in-phase (acoustic mode) types of precession. In this case both of the magnetic layers simultaneously act as sources of spin-currents and spin-sinks. The different phase of rf magnetization precession fundamentally changes their contribution of spin-pumping to the FMR linewidth for the acoustic and optical mode, see below. As it was discussed in section 2.5.1 spin-pumping can be derived from a time retarded response of the interlayer exchange coupling [24]. Presented below is detailed theoretical treatment is for spin-pumping in an interlayer exchange coupled FM1/NM/FM2 structure.

As discussed in section 2.5.2, spin-pumping in a FM1/NM structure leads to a non-equilibrium chemical potential imbalance of the spins in NM, $\boldsymbol{\mu}_s$ [7] which results in an accumulated spin density in the NM at the FM1|NM interface. The thickness dependence of $\boldsymbol{\mu}_s$ inside the NM is described by spin diffusion [143]

$$\frac{\partial^2 \boldsymbol{\mu}_s}{\partial x^2} = \frac{\boldsymbol{\mu}_s}{\lambda_{\mathrm{sd}}^2}, \tag{7.2}$$

where λ_{sd} is the spin diffusion length which represents the characteristic length scale over which the loss of accumulated spin density occurs in NM and x is the position along the coordinate perpendicular to the FM|NM interface. The general solution to this equation takes the form

$$\boldsymbol{\mu}_s = \boldsymbol{A} e^{-\kappa x} + \boldsymbol{B} e^{\kappa x}, \tag{7.3}$$

where $\boldsymbol{A}$ and $\boldsymbol{B}$ are constant vectors to be determined from the boundary conditions and $\kappa = 1/\lambda_{\mathrm{sd}}$. For the systems discussed in section 2.5.2, the boundary conditions would either be absorption or reflection of the spin-current at the NM/ambient or NM/FM2 interfaces, respectively. However, for the situation where both the ferromagnets are simultaneously put into precession, both the FM1/NM and NM/FM2 act as a spin-source and spin-sink at the same time. This can be described by the boundary conditions for the FM1|NM and NM|FM2 interfaces as given by the sum of all the spin-current lost and gained by the FM1 and FM2 at their respective interfaces with NM,

$$\begin{aligned} x = 0; \quad & -\frac{\hbar}{2\rho_{\uparrow} e^2} \frac{\partial \boldsymbol{\mu}_s}{\partial x} = \boldsymbol{I}_{\mathrm{sp1}} - \frac{\tilde{g}_{\uparrow\downarrow,1}}{4\pi} \boldsymbol{\mu}_s \Big|_{x=0}, \\ x = d_{\mathrm{NM}}; \quad & -\frac{\hbar}{2\rho_{\uparrow} e^2} \frac{\partial \boldsymbol{\mu}_s}{\partial x} = -\boldsymbol{I}_{\mathrm{sp2}} + \frac{\tilde{g}_{\uparrow\downarrow,2}}{4\pi} \boldsymbol{\mu}_s \Big|_{x=d_{\mathrm{NM}}}, \end{aligned} \tag{7.4}$$

$\boldsymbol{I}_{\rm sp1}$ and $\boldsymbol{I}_{\rm sp2}$ are the measures of spin-pumping due to the precession of FM1 and FM2; these are the sources of the spin-current in the NM spacer. The second terms on the right hand side of eq. (7.4) are the backflow terms which account for the spin-current reabsorbed back into the ferromagnet. In the conventional FM/NM spin-pumping experiment the backflow is a consequence of the spin-pumping form the FM. It can be thought of reabsorbtion of half the spin-accumulation which was developed by the spin-pumping process. However, for a system where spin-pumping is happening from both ends of the NM, the spin-accumulation depends on both the sources of the spin-current and therefore the backflow must include the contribution from both precessing ferromagnets. Given the boundary conditions, eq. (7.4), and the general solution, eq. (7.3), it is then possible to solve for the chemical potential imbalance inside the spacer layer, $\boldsymbol{\mu}_s$, in terms of $\boldsymbol{I}_{\rm sp1}$ and $\boldsymbol{I}_{\rm sp2}$.

Using eq. (7.3), the boundary condition equation are given by,

$$\begin{aligned}\frac{\hbar}{2\rho_\uparrow e^2}(\boldsymbol{A}k-\boldsymbol{B}k) &= \boldsymbol{I}_{\rm sp1}-\frac{\tilde{g}_{\uparrow\downarrow,1}}{4\pi}(\boldsymbol{A}+\boldsymbol{B})\\ \frac{\hbar}{2\rho_\uparrow e^2}(\boldsymbol{A}ke^{kd_{\rm NM}}-\boldsymbol{B}ke^{-kd_{\rm NM}}) &= -\boldsymbol{I}_{\rm sp2}+\frac{\tilde{g}_{\uparrow\downarrow,2}}{4\pi}(\boldsymbol{A}e^{kd_{\rm NM}}+\boldsymbol{B}e^{-kd_{\rm NM}})\end{aligned} \tag{7.5}$$

For convenience the spin currents can be rewritten as,

$$\begin{aligned}\boldsymbol{I}_{\rm sp1} &= \boldsymbol{A}\ \Omega_{A1}+\boldsymbol{B}\ \Omega_{B1},\\ \boldsymbol{I}_{\rm sp2} &= \boldsymbol{A}\ \Omega_{A2}+\boldsymbol{B}\ \Omega_{B2},\end{aligned} \tag{7.6}$$

where Ω_{A1}, Ω_{A2}, Ω_{B1} and Ω_{B2} are constants which can be easily obtained from eq. (7.5) and will depend on k, $d_{\rm NM}$, $\rho_\uparrow$, $\tilde{g}_{\uparrow\downarrow,1}$ and $\tilde{g}_{\uparrow\downarrow,2}$. By subtracting the two equations in eq. (7.6) it can be shown that to $\boldsymbol{A}$ and $\boldsymbol{B}$ are proportional to some linear combinations of $\boldsymbol{I}_{\rm sp1}$ and $\boldsymbol{I}_{\rm sp2}$. Therefore, the general solution to the non-equilibrium chemical potential imbalance, eq. (7.3), can be written as,

$$\boldsymbol{\mu}_s(x) = \boldsymbol{I}_{\rm sp1}\ \Omega_1(x)+\boldsymbol{I}_{\rm sp2}\ \Omega_2(x). \tag{7.7}$$

Note there is only a single chemical potential established by the two precessing ferromagnets. In principle one can solve for the chemical potential established by each ferromagnet and then take their sum to get the net chemical potential, this leads to the same solution. Also, recall that $\boldsymbol{I}_{\rm sp1}$ and $\boldsymbol{I}_{\rm sp2}$ are vectors which depend on the precession of the respective ferromagnetic layers,

$$\begin{aligned}\boldsymbol{I}_{\rm sp1} &= \tilde{g}_{\uparrow\downarrow}\frac{\hbar}{4\pi}\left(\boldsymbol{n_1}\times\frac{\partial\boldsymbol{n_1}}{\partial t}\right)\\ \boldsymbol{I}_{\rm sp2} &= \tilde{g}_{\uparrow\downarrow}\frac{\hbar}{4\pi}\left(\boldsymbol{n_2}\times\frac{\partial\boldsymbol{n_2}}{\partial t}\right).\end{aligned} \tag{7.8}$$

The unit vectors representing the direction of the magnetic moment of each FM ($\boldsymbol{n_1}$ and $\boldsymbol{n_2}$) do not need to be parallel, see more discussion below. The functions $\Omega_1(x)$ and $\Omega_2(x)$

can be thought of as spin accumulations in the NM spacer established by FM1 and FM2, respectively. If either of $\boldsymbol{I}_{\mathrm{sp1}}$ $\boldsymbol{I}_{\mathrm{sp2}}$ are zero in eq. (7.7) then the solution reduces to the previously derived solution for the FM/NM/spin-sink structure, eq. (5.8).

With the form of $\boldsymbol{\mu}_s(x)$ worked out, the next step is to relate the magnetic damping of each ferromagnet to the effect of spin-pumping. Assuming conservation of angular momentum, any spin-current ejected from a FM into a NM results in a torque on FM. Mathematically this can be expressed as

$$\boldsymbol{\tau}_1 = \left[\frac{1}{d_1}\left(\boldsymbol{I}_{\mathrm{sp1}} - \frac{\tilde{g}_{\uparrow\downarrow,1}\boldsymbol{\mu}_s}{4\pi}\right)\right]\Bigg|_{x=0}, \tag{7.9a}$$

$$\boldsymbol{\tau}_2 = \left[\frac{1}{d_2}\left(\boldsymbol{I}_{\mathrm{sp2}} - \frac{\tilde{g}_{\uparrow\downarrow,2}\boldsymbol{\mu}_s}{4\pi}\right)\right]\Bigg|_{x=d_{\mathrm{NM}}}. \tag{7.9b}$$

The left-hand sides of these equations are the torques acting on each ferromagnet due to spin-pumping from both ferromagnets. These torques are interface effects therefore they must scale as the inverse thickness of the ferromagnet. This inverse thickness dependence has been observed for FM(d_{FM})/Pt structures [144], as evidence that *spin-pumping at the proximity polarized Pt is still generated at the FM/Pt interface.*

It is useful to see a more explicit form of eq. (7.9) by including eq. (7.7) in eq. (7.9) which leads to the relationship between interface damping torque and spin-pumping,

$$\boldsymbol{\tau}_1 = \frac{1}{d_1}\left(\boldsymbol{I}_{\mathrm{sp1}} - \frac{\tilde{g}_{\uparrow\downarrow,1}}{4\pi}\left[\boldsymbol{I}_{\mathrm{sp1}}\Omega_1(0) + \boldsymbol{I}_{\mathrm{sp2}}\Omega_2(0)\right]\right), \tag{7.10a}$$

$$\boldsymbol{\tau}_2 = \frac{1}{d_2}\left(\boldsymbol{I}_{\mathrm{sp2}} - \frac{\tilde{g}_{\uparrow\downarrow,2}}{4\pi}\left[\boldsymbol{I}_{\mathrm{sp1}}\Omega_1(d_{\mathrm{NM}}) + \boldsymbol{I}_{\mathrm{sp2}}\Omega_2(d_{\mathrm{NM}})\right]\right). \tag{7.10b}$$

As mentioned, the vectors $\boldsymbol{I}_{\mathrm{sp1}}$ and $\boldsymbol{I}_{\mathrm{sp2}}$ do not need to be parallel. This results in a phase difference between the two precessing magnetic moments. If the two magnetic moments precess perfectly in-phase or out-of-phase, given by a phase difference of $\Delta\phi = 0$ or $\Delta\phi = \pi$, then $\boldsymbol{I}_{\mathrm{sp1}}$ and $\boldsymbol{I}_{\mathrm{sp2}}$ are always either parallel or antiparallel, see fig. 7.3. In this case the torques $\boldsymbol{\tau}_1$ and $\boldsymbol{\tau}_2$ will be aligned with damping torque. However, if $\Delta\phi \neq \pi$ and $\Delta\phi \neq 0$, then the torques are not aligned with the damping torques and can therefore be viewed as additional rf driving contributions (they do not need to be aligned with the driving exerted by the FMR system).

The work presented in this chapter focuses on spin-pumping of an interlayer coupled magnetic double layer structure, FM1/NM/FM2. The optical and acoustic modes of the system correspond to in-phase and out-of-phase precession of the two ferromagnets, see fig. 7.3(a) and (b), which are $\Delta\phi = 0$ or $\Delta\phi = \pi$. Therefore the two vectors, $\boldsymbol{I}_{\mathrm{sp1}}$ and $\boldsymbol{I}_{\mathrm{sp2}}$, are either antiparallel or parallel. This implies that the torques are aligned with the magnetic

damping and eq. (7.10) can be rewritten as

$$\begin{aligned}\alpha_{\mathrm{sp1}}\left(\boldsymbol{n_1}\times\frac{1}{\gamma_1}\frac{\partial \boldsymbol{M}_1}{\partial t}\right) &= \frac{1}{d_1}\left(\boldsymbol{I}_{\mathrm{sp1}}-\frac{\tilde{g}_{\uparrow\downarrow,1}}{4\pi}\left[\boldsymbol{I}_{\mathrm{sp1}}\Omega_1(0)+\boldsymbol{I}_{\mathrm{sp2}}\Omega_2(0)\right]\right)\\ \alpha_{\mathrm{sp2}}\left(\boldsymbol{n_2}\times\frac{1}{\gamma_2}\frac{\partial \boldsymbol{M}_2}{\partial t}\right), &= \frac{1}{d_2}\left(\boldsymbol{I}_{\mathrm{sp2}}-\frac{\tilde{g}_{\uparrow\downarrow,2}}{4\pi}\left[\boldsymbol{I}_{\mathrm{sp1}}\Omega_1(d_{\mathrm{NM}})+\boldsymbol{I}_{\mathrm{sp2}}\Omega_2(d_{\mathrm{NM}})\right]\right).\end{aligned} \tag{7.11}$$

The right-hand sides of eq. (7.11) are the torques exerted on each ferromagnet due to spin-pumping of both ferromagnets. The left hand side of eq. (7.11) must be a vector which is parallel or anti-parallel to $\boldsymbol{I}_{\mathrm{sp1}}$ and $\boldsymbol{I}_{\mathrm{sp2}}$. Since these vectors are indistinguishable from damping-like-torques, it is convenient to parameterize these terms by dimensionless constants α_{sp1} and α_{sp2} corresponding to the damping-like-torques exerted on FM1 and FM2, respectively. In this manner spin-pumping can be correlated to a measurable quantity, the magnetic damping. It is worth pointing out that this is only true for the case of perfectly in-phase and out-of-phase precession of the two magnetic layers, which is potentially not true for weak interlayer exchange coupling.

In the limit of two identical ferromagnetic layers with very strong coupling, eq. (7.11) can be further reduced to a much simpler, analytic, form

$$\alpha_{\mathrm{sp}}^{\mathrm{Acoustic}} = \frac{g\mu_{\mathrm{B}}}{4\pi M_s}\frac{\tilde{g}_{\uparrow\downarrow}}{d_{\mathrm{FM}}}\left[1+\frac{\tilde{g}_{\uparrow\downarrow}\mathcal{R}}{\tanh\left(\frac{d_{\mathrm{NM}}}{2\lambda_{\mathrm{sd}}}\right)}\right]^{-1}, \tag{7.12a}$$

$$\alpha_{\mathrm{sp}}^{\mathrm{Optical}} = \frac{g\mu_{\mathrm{B}}}{4\pi M_s}\frac{\tilde{g}_{\uparrow\downarrow}}{d_{\mathrm{FM}}}\left[1+\frac{\tilde{g}_{\uparrow\downarrow}\mathcal{R}}{\coth\left(\frac{d_{\mathrm{NM}}}{2\lambda_{\mathrm{sd}}}\right)}\right]^{-1}, \tag{7.12b}$$

where $\mathcal{R} = \frac{\rho_\uparrow e^2}{2\pi\hbar}\lambda_{\mathrm{sd}}$ and d_{FM} is the thickness of FM. It is assumed that the magnetic properties of the two magnetic layer are identical: $M_s = M_{s1} = M_{s2}$, $g = g_1 = g_2$ and $\tilde{g}_{\uparrow\downarrow} = \tilde{g}_{\uparrow\downarrow,1} = \tilde{g}_{\uparrow\downarrow,2}$.

It is interesting to compare these results to the spin-pumping damping of FM in a single magnetic layer system, FM/NM, structure [23],

$$\alpha_{\mathrm{sp}}^{\mathrm{SL}} = \frac{g\mu_{\mathrm{B}}}{4\pi M_s}\frac{\tilde{g}_{\uparrow\downarrow}}{d_{\mathrm{FM}}}\left[1+\frac{\tilde{g}_{\uparrow\downarrow}\mathcal{R}}{\tanh\left(\frac{d_{\mathrm{NM}}}{\lambda_{\mathrm{sd}}}\right)}\right]^{-1}, \tag{7.13}$$

Clearly eq. (7.13) is very similar to eq. (7.12a) with the only difference being an extra factor of 1/2 in the hyperbolic tangent term. Therefore one can expect that spin-pumping damping of an exchange coupled FM/NM/FM system should have the same dependence as for the FM/NM system but reach saturation twice as slowly. The optical mode damping of a FM/NM/FM, eq. (7.12b), once again appears very similar to eq. (7.13) but the tanh is

replaced by a coth which results in a different thickness dependence; its damping increases with decreasing $d_{\rm NM}$ on a length scale of $2d_{\rm NM}/\lambda_{\rm sd}$.

This thickness dependences can be understood from eq. (7.11). During the in-phase of the acoustic mode, see fig. 7.3(a), the two vectors $\boldsymbol{I}_{\rm sp1}$ and $\boldsymbol{I}_{\rm sp2}$ are parallel to each other, and assuming small angle of precession. This results in a increases of the backflow current (the term proportional to $\tilde{g}_{\uparrow\downarrow}$) on the right hand side of eq. (7.11) with decreasing spacer $d_{\rm NM}$. Both $\boldsymbol{I}_{\rm sp1}$ and $\boldsymbol{I}_{\rm sp2}$ are parallel vectors so they sum up. This is a consequence of the fact that during in-phase precession, the two magnetic layers compensate each other's loss due to spin-pumping. The magnetic moment lost by the first FM is reabsorbed by the second FM and vice-versa, see fig. 7.3(a). This compensation results in a reduction of spin-pumping induced damping. A similar effect was observed in Heinrich *et al.* [142] due to an accidental crossover of resonance fields observed in a Fe/Au/Fe structure, however since the thickness of Au was small in comparison to its spin-diffusion length (~ 30 nm), the role of spin-flip relaxation was insignificant. In out-of-phase precession, the $\boldsymbol{I}_{\rm sp1}$ and $\boldsymbol{I}_{\rm sp2}$ are anti-parallel to each other which results in spin-pumping of spin-currents with opposite polarization, see fig. 7.3(b). Therefore, the two vectors will have the opposite sign and result in a reduced backflow on the right-hand-side of eq. (7.11). As in the previous case both ferromagnets are absorbing the spin-current of their counter part, however in out-of-phase presession these currents are of opposite polarization and therefore lead to additional damping-like torque. Qualitative evidence of this was also observed in antiferromagnetically coupled Py/Ru/Py structures. In this case the spin-pumping damping in the antisymmetric mode of precession, in the canted magnetic moments of Py/Ru/Py, was higher than in the symmetric mode [144]. In the limit of a very large spin-diffusion length, $d_{\rm Pt} \ll \lambda_{\rm sp}$, i.e. the spin-current is unaffected by the relaxation of the spin momentum to the lattice, the spin-pumping contribution in the optical mode would reach its absolute maximum; *it is given by the full value of renormalized spin-pumping parameter* $\tilde{g}_{\uparrow\downarrow}$.

In the above discussion it is assumed that the precession of the two magnetic layer is either in-phase or out-of-phase for all values of $d_{\rm NM}$ as a result of strong enough coupling J. For NM = Pt this is not true since J decreases exponentially with increasing $d_{\rm NM}$ and $J \sim 0$ at $d_{\rm NM} \sim 2.5$ nm [120, 32]. In order to include the role of the coupling strength in the spin-pumping of the acoustic and optical modes one needs to solve the full LLG equations of motion, eq. (2.16), with eq. (7.10) as additional torque terms and simulate the full magnetization response in order to extract an effective damping parameter. The method of extracting an effective damping parameter is described in the Results and Discussion section. However, it was found that eq. (7.12) is in good agreement with the simulation for $J \gtrsim 0.07$ erg/cm^2 corresponding to a Pt thickness of $d_{\rm Pt} \lesssim 1.8$ nm. This is not surprising considering that the ferromagnetic layers in this experiment had almost identical magnetic properties and therefore the exchange coupling easily locks the precession of rf magnetic moments into the acoustic and optical modes. It is therefore instructive to use eq. (7.12)

as a tool to gain insight into the expected behaviour of spin-pumping due to in-phase and out-of-phase precession.

7.4 Results and Discussion

This study focused on the magnetic damping of the Ta/Py/Pt(d_{Pt}) structure and the damping of the optical and acoustic modes of the Ta/Py/Pt(d_{Pt})/Py/Ta structure as determined from broadband FMR. The Ta seed and capping layers were kept constant throughout the experiment. In further discussion of Ta/Py/Pt(d_{Pt}) the reference to Ta will be omitted.

(1) Py/Pt(d_{Pt}) structure:

The exponential thickness dependence of $\alpha(d_{\mathrm{Pt}})$ for the Py/Pt(d_{Pt}) structure, see blue solid points in fig. 7.4, is qualitatively in good agreement with previous spin-pumping in Pt studies [135, 136]. Single crystal studies of Fe/Pt(d_{Pt}) structures grown by MBE technique [135] report an exponential approach to saturation with a length-scale of ~ 1 nm. For a quantitative analysis the data in fig. 7.4 was fit with a eq. (7.13) assuming a bulk single spin resistivity [7] of Pt, $\rho^{\uparrow} = 2\rho_b = 34 \pm 1$ $\mu\Omega$cm, where ρ_b is the extracted bulk resistivity for both electrons spins. The resistivity measurements were performed by using a 4-point-probe technique, see chapter 4 for more details. However, it is not clear that the bulk resistivity is the appropriate value for this model. In chapter 5 it was found that the for a self consistent interpretation of spin-pumping into Ta it was necessary to use thin film resistivity, but this was the result of the thin film Ta being amorphous and therefore having a higher resistivity value. Pt is highly textured when deposited on top of Py and therefore one would not expect thickness dependent resistivity from the Pt itself. For thin films, interface scattering can be a significant contribution to the measured resistivity. In the original description of spin-pumping [7] the bulk, single spin resistivity is the appropriate value for the model, not including any interface scattering. In this study the bulk, single spin resistivity of Pt was used for all the interpretation of the data.

Fitting the Py/Pt(d_{Pt}) data with eq. (7.13) yields $\tilde{g}_{\uparrow\downarrow} = 4.3 \times 10^{15} \pm 0.4 \times 10^{15}$ cm^{-2} and $\lambda_{\mathrm{sd}} = 1.1 \pm 0.1$ nm, see solid line in fig. 7.4. These value are consistent with experimental studies which observe an exponential dependence of $\alpha(d_{\mathrm{Pt}})$ of FM/Pt(d_{Pt}) [135, 136]. The value for a single Py layer is shown as a black point in fig. 7.4. The 2 nm Au was a capping layer to prevent oxidation of Py. Some spin-pumping should also occur into the Au layer since it is also interfacing the Py. Its contribtuion can be estimated by using eq. (7.13), with $\tilde{g}^{\mathrm{Au}}_{\uparrow\downarrow} = 2.4 \times 10^{15}$ cm^{-2}, $\lambda^{\mathrm{Au}}_{\mathrm{sd}} = 31$ nm and $\rho = 3.96$ $\mu\Omega$cm [145, 146] resulting in additional damping of $\sim 0.3 \times 10^{-3}$. This is a small contribution which is roughly the size of the measurement error, it was considered to be negligible. Importantly, the solid line fits the experimental data for the entire thickness range, which indicates that there is no need to include any additional interface damping due to Pt interfacing Py.

(2) Py/Pt(d_{Pt})/Py structure:

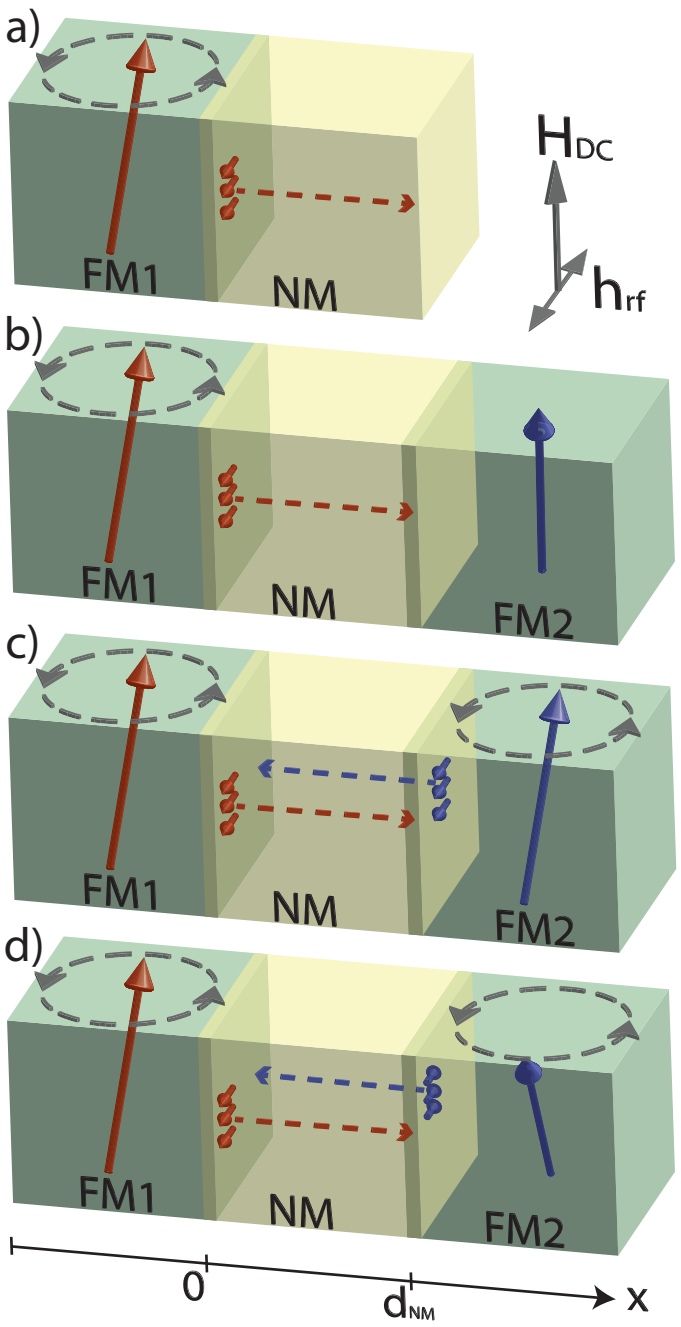

Figure 7.3: Schematic of magnetic precession and spin-pumping for (a) FM1/NM. In (b) the magnetic moment of FM1 is put into precession while FM2 is not, in this case FM2 is considered as a spin-sink. In (c) both magnetic layers precess in-phase (acoustic mode) and (d) are precessing out-of-phase (optical mode). Long red and blue arrows represent the magnetic moments of FM1 and FM2, respectively. The gray, dashed, circular arrows represent the direction of precession. The three red and three blue spins represent the ejected spin momentum by spin-pumping. The dashed red and blue arrows are the directions of spin-currents. H_{DC} and h_{rf} are the directions of the applied dc and rf magnetic fields, respectively.

Magnetic damping of the acoustic and optical modes for the Ta/Py/Pt(d_{Pt})/Py/Ta structure is shown in fig. 7.4. The thickness dependence of damping of the acoustic mode appears to approach saturation more slowly than in the Py/Pt(d_{Pt}) structure. This is consistent with the derivation for spin-pumping of the acoustic mode (in the limit of strong coupling) which showed that the approach to saturation should be a factor of two slower for the acoustic mode than for the single layer structure eq. (7.12). Once saturation is reached, at ~ 2 nm, the interlayer exchange coupling approaches zero and the damping of the two resonances modes are the independent damping of the two Py layers. By design the dampings of the two layers are very similar and therefore they are indistinguishable within the measurement error.

For the optical mode (out-of-phase precession), the damping increases with decreasing d_{Pt}, see orange points in fig. 7.4. As discussed, due to the out-of-phase precession of the optical mode the two magnetic layers pump spin-current with opposite polarization. Since they are both simultaneously acting as spin-sinks and are absorbing the others spin-current, this results in an enhancement in damping. *The enhancement of damping of the optical mode is very strong evidence for the fact that the two layers are communicating via spin-current.*

A comparison of the data to the spin-pumping model presented in fig. 6.5 was made by simulating the expected spin-pumping damping dependence of the optical and the acoustic modes given the spin-pumping parameters as determined from fitting the Py/Pt(d_{Pt}). These modes are a consequence of interlayer exchange coupling, therefore for the simulation the coupling strength was taken from measurements presented in chapter 5. The simulation procedure and mechanism for extracting damping values of the simulated data are presented below. Essentially the simulation procedure simulates the rf response of each of the magnetic layers from the LLG equation of motion (eqs. (7.1a) and (7.1b)) including the spin-pumping contribution as determined from the torque terms derived above. The simulated response is then treated in the same way as experimental data: it is fit with eq. (3.7) to extract a ΔH for each resonance mode, see more details below.

Simulation procedure: the torque induced due to spin-pumping (right hand sides of eqs. (7.10a) and (7.10b)) were added to the right hand sides of eqs. (7.1a) and (7.1b), respectively. These new coupled LLG equations represent the dynamics of each resonance mode and includes interlayer exchange coupling and spin-pumping. The rf-field is assumed to be directed along the $\hat{y}$ with a driving frequency of ω and the external H_{DC} along the $\hat{z}$ direction. The new LLG equations were solved for the $\hat{y}$ component of $\boldsymbol{M}_1$ and $\boldsymbol{M}_2$, assuming small angle of precession. For parameters related to spin-pumping, the values determined from the fit to the Py/Pt(d_{Pt}) structure were used, $\tilde{g}_{\uparrow\downarrow} = 4.3 \times 10^{15}$ cm^{-2} and $\lambda_{\mathrm{sd}} = 1.1 \pm 0.1$. The interlayer exchange coupling, $J(d_{\mathrm{Pt}})$, was assumed to have the same d_{Pt} thickness dependence as determined in chapter 6 [32]. The intrinsic dampings of both Py layers were taken to be $\alpha = 8.3 \times 10^{-3}$ (see black point in fig. 7.4); this includes contribution due to spin-pumping into an adjacent Ta layer. The $4\pi M_{\mathrm{eff}}$ for each two magnetic layers

taken to be, 10200 Oe and 10600 Oe, as measured from the uncoupled $d_{\mathrm{Pt}} = 3.5$ nm sample (see fig. 8.1 a)), and the $g - factor$ was fixed at 2.10, consistent with previous studies in Py [123]. All of the above parameters fully determine the new LLG equation and therefore one can simulated resulting in a sum of the magnetic susceptibilities, corresponding to the FMR responses of the each magnetic layer, $\chi^{rf} = \hat{y} \cdot (\boldsymbol{M}_1 + \boldsymbol{M}_2)/h_{rf}$. The simulated susceptibility was fit in the same manner as the experimental data, fig. 7.1, using two FMR lines, eq. (6.1), yielding $\Delta H_{\mathrm{sim}}^{\mathrm{Acoustic}}$ and $\Delta H_{\mathrm{sim}}^{\mathrm{Optical}}$. The above procedure was repeated for three frequencies (f = 8, 18, 38 GHz) and the resulting $\Delta H_{\mathrm{sim}}^{\mathrm{Acoustic}}$ and $\Delta H_{\mathrm{sim}}^{\mathrm{Optical}}$ vs. frequency dependence was fit by eq. (2.25) which yielded a $\alpha_{\mathrm{sim}}^{\mathrm{Acoustic}}(d_{\mathrm{Pt}})$ and $\alpha_{\mathrm{sim}}^{\mathrm{Optical}}(d_{\mathrm{Pt}})$. This was repeated for several values of d_{Pt} and the extracted damping of the simulated acoustic and optical modes is plotted as dashed lines in fig. 7.4.

The remarkable agreement between the standard spin-pumping model and the data for the Py/Pt and the acoustic and optic modes of Py/Pt/Py suggests that the model is representative of the physics governing spin-pumping in Py/Pt structures. Its important to point out that this is quite a rigorous test of the spin-pumping model considering it is sensitive to the phase of the spin-current. In this sense the extracted spin diffusion length is a meaningful parameter and is representative of the length over which the spin-current is attenuated. The short length scale, $\lambda_{\mathrm{sd}} = 1.1 \pm 0.1$ nm, can be explained by considering an analogy of spin-current propagating through a ferromagnet. It is well known that due to dephasing the penetration depth of a spin-current polarized transverse to the magnetic moment of a ferromagnet is given by $\lambda_{tr} \sim \pi/|k_f^{\uparrow} - k_f^{\downarrow}|$, where $k_f^{\uparrow}$ and $k_f^{\downarrow}$ are the Fermi wave vectors of the majority and the minority spins[147]; it is expected to be on the order of a few atomic layers. Experimentally it was found that for ferromagnetic materials such as Co and Py this length scale is indeed very short $\lambda_{tr}^{\mathrm{ex}} \sim 0.7$ nm [148]. Considering that Pt is strongly polarized at the interface with a ferromagnet [32], it is natural to argue that the transverse spin momentum of the spin-current can rapidly dephase in the proximity of polarized Pt. The dc inverse spin hall effect studies (ISHE) observe a much longer spin diffusion length, measured at $\lambda_{\mathrm{sd}} \sim 3.4$ nm [17] or even $\lambda_{\mathrm{sd}} \sim 8$ nm[140] for Pt. however, this measurement probes spin-current polarized longitudinal with respect to the induced moment in Pt. The internal molecular field of the polarized Pt is oriented in the same direction as the dc spin-current, and therefore it does not result in any rapid dephasing. The length scale over which the longitudinal spin-current is attenuated is governed by spin-flip scattering, which in analogy to ferromagnets can be substantially longer than the transverse spin-current, for Py it was calculated to be ~ 3 nm [149]. This is a natural argument, however, as it will be shown in next chapter, it cannot be true.

These results show no evidence of any significant interfacial spin memory loss (SML). Experimentally one would expect SML to result in an offset in the damping of all of the measured data except for the intrinsic damping of Py (see black point in fig. 7.4). It can be viewed as an additional contribution to the interface damping which does not lead

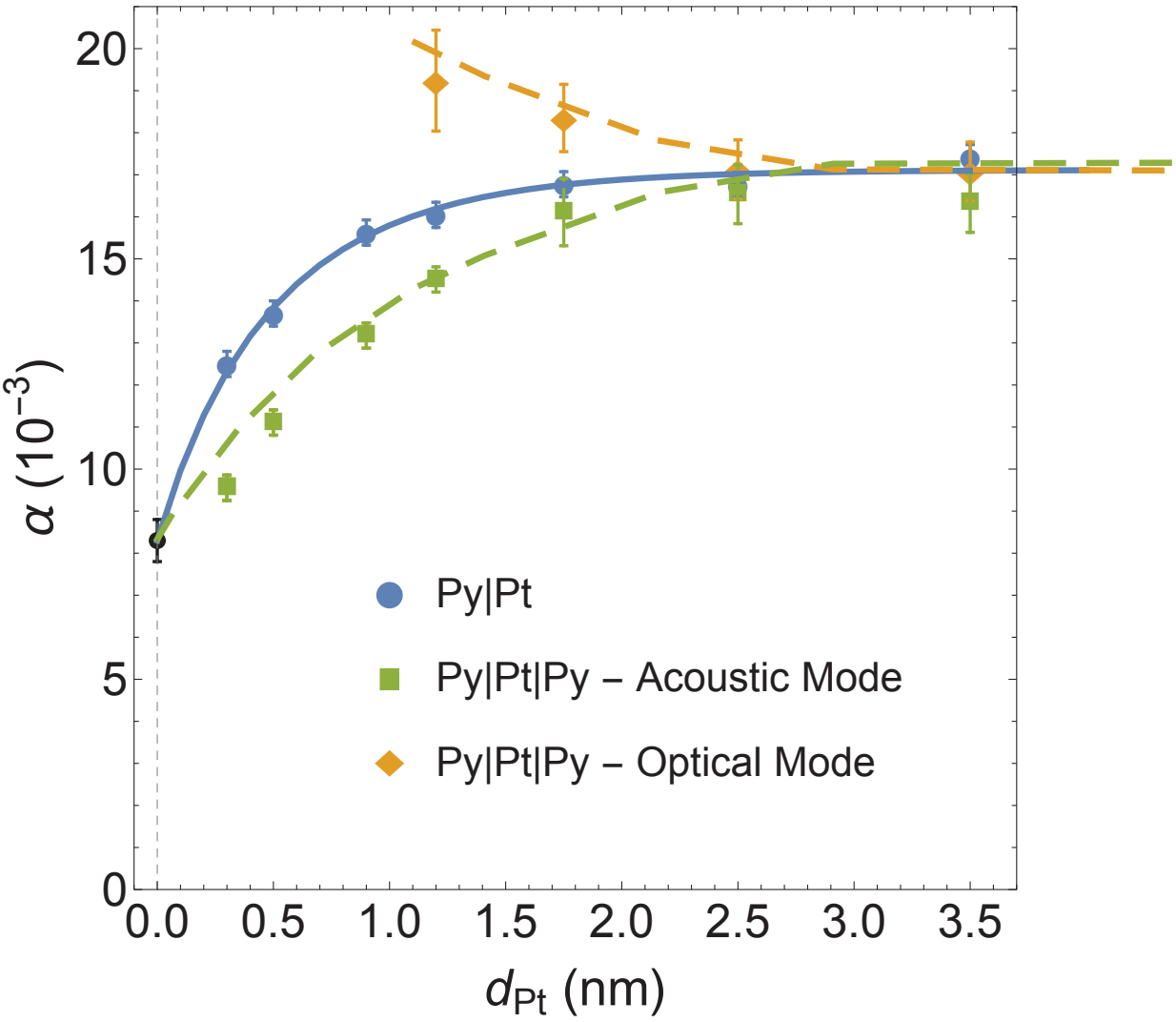

Figure 7.4: Damping with increasing thickness of Pt for the Py/Pt(d_{Pt}) (blue circles), the acoustic mode of Py/Pt(d_{Pt})/Py (green squares) and optical mode of Py/Pt(d_{Pt})/Py (yellow diamonds). The solid line is a fit to the Py/Pt(d_{Pt}) data using eq. (7.13). The dashed lines are simulations of the damping for the acoustic and optical modes using eqs. (2.16) and (7.11) with parameters taken from the resulting fit of the Py/Pt(d_{Pt}) data. The black point for $d_{\mathrm{Pt}} = 0$ is a Py/Au sample, where the 2 nm Au was used as protective capping layer. The contribution of Au to the magnetic damping of Py is estimated to be on the order of the measurement error.

to coherent spin-current in Pt. SML is generally attributed to spin orbit coupling at the interface of ferromagnet/Pt interface [18, 150], which results in dephasing of the spin-current at the interface. The fit and the simulations of the acoustic mode approach the intrinsic damping of Py (see black point in fig. 7.4) for $d_{\mathrm{Pt}} \to 0$ following the experimental data. *These results show no evidence of an offset.*

One can estimate the potential contribution of some interface damping corresponding to SML by repeating a fit to the Py/Pt using $\alpha_{\mathrm{Total}} = \alpha_{\mathrm{offset}} + \alpha_{\mathrm{sp}}^{\mathrm{SL}} + \alpha_{\mathrm{intrisic}}$ where α_{offset} is the offset due to some interfacial damping which does not lead to a spin-current in Pt, $\alpha_{\mathrm{sp}}^{\mathrm{SL}}$ is the spin-pumping contribution from eq. (7.13) and $\alpha_{\mathrm{intrisic}} = 8.3{\times}10^{-3}$ is the intrinsic damping of Py (including pumping into adjacent Ta). Then, refitting the data while excluding the first two data points ($d_{\mathrm{Pt}} = 0$ nm and $d_{\mathrm{Pt}} = 0.3$ nm) allows for the fit to choose an appropriate offset which would be consistent with the rest of the data points. The resulting fitting offset is $\alpha_{\mathrm{offset}} = 0.3 \times 10^{-3}$ which is small in comparison to the rest of the enhancement in damping suggesting that any thickness-independent offset in damping due to Pt is small in comparison to the thickness-dependent contribution. The values of the $\tilde{g}_{\uparrow\downarrow}$ and λ_{sd} are unchanged within the error bar.

The above results strongly suggest that the induced damping due to Pt is indeed a consequence of spin-pumping and that the generated spin-current results in a communication between the two magnetic layers. The meaningful length scale over which the spin-current can propagate across is the spin-diffusion length which was found to be $\lambda_{\mathrm{sd}} = 1.1$ nm. However, another important parameter in spin-pumping is the spin mixing conductance which determines the efficiency of spin-pumping, $\tilde{g}_{\uparrow\downarrow}$. The strength of spin-pumping depends on dynamic response of electrons in Pt spacer to the presence of interface magnetic interaction. Spin-pumping in systems with electron spin correlations is more complex than simple NM metals like Au, Ag and Cu. As presented in section 2.5.1 the enhanced electron spin correlations in a normal metal described by the Stoner factor lead to an increased susceptibility (increased spin fluctuations) and also to an enhanced spin mixing conductance[24], $\tilde{g}_{\uparrow\downarrow}$. This enhancement in susceptibility is very pronounced in Pt resulting in proximity effect in Py/Pt. Consequently, one can expect that electron spin correlations in Pt affect the strength of the interface pumping parameters. *Therefore the strong electron spin correlations in Pt do not require the introduction of a new set of spin-pumping parameters, but they play an essential part in determining their quantitative values.*

7.5 Summary

Magnetic damping measurements of the Py/Pt and Py/Pt/Py structures were performed by means of broadband ferromagnetic resonance. The enhancement in damping was analyzed using standard spin-pumping model extended to include interlayer exchange coupling in

the optical and acoustic modes of resonance for the Py/Pt/Py structure. There are several important conclusions one can draw from these results:

Spin-pumping in proximity polarized Pt is well described by the standard spin-pumping model. In fact, the spin-pumping model is robust enough to accurately describe all the observed damping for both the Py/Pt and acoustic and optical modes of Py/Pt/Py with a single set of parameters: $\tilde{g}_{\uparrow\downarrow} = 4.3 \times 10^{15}$ cm^{-2} and $\lambda_{sd} = 1.1$ nm. Spin dynamics studies in magnetic double layers, Py/Pt/Py, played an important role in testing the validity of the spin-pumping model in Pt. For the first time the role of phase in spin-pumping currents was demonstrated by analyzing the FMR linewidth for the optical and acoustic modes of precession thus providing a stringent test for the spin-pumping model in ferromagnet/Pt structures. There is no evidence for any additional strict interface loss mechanism.

The magnetic proximity mechanism, responsible for ferromagnetic coupling, does not play any explicit role in the mathematical interpretation of spin-pumping, but affects quantitatively the spin-pumping parameters $\tilde{g}_{\uparrow\downarrow}$ and λ_{sd}. The spin diffusion length, λ_{sd}, is reduced due to dephasing of spin-current in the presence of induced magnetic moment at the Py/Pt interface and the renormalized spin mixing conductance, $\tilde{g}_{\uparrow\downarrow}$, is affected by spin fluctuations due to electron spin correlations in Pt. In fact, spin-pumping with a very short spin diffusion length can be view as a spin loss mechanism which develops on the length scale of 1.1 nm.

Chapter 8

Spin Transport Across the Au/Pt interface

8.1 Motivation

Material properties determine the mechanism of spin transport within each layer, however interface properties determine spin transport in a multilayer system. There are relatively few spin-pumping experiments which focus on studying the effects of additional interfaces on spin transport. Most common experimental structure consists of a FM/NM where the only interface is that with a ferromagnet and influences the strength of spin-pumping. Often a fixed thickness spacer layer (FM/spacer/NM) is used to further investigate the effect of the ferromagnetic interface, [151, 58, 91] especially for the FM/Pt or FM/Pd interface since Pt and Pd are magnetically polarized by the FM. [115] For studies which include spin-transport across NM layers, NM/NM, the one can find two boundary conditions presented in literature which have been used to describe spin-transport across a NM/NM interface: the continuity of chemical potential across the interface, [91] or the continuity of spin-accumulation across the interface [152]. However, studies which focus on spin transport in multilayered structures stoner enhanced metals (FM/Au/Pd [21] and FM/Cu/Pt [22]) show oscillatory spin-pumping dependence with the thickness dependence of Cu or Au, this is outside of the conventional spin-diffusion description. It is not clear which boundary conditions are required to describe the spin transport across an interface of a normal metal and a stoner enhanced metal.

This chapter describes our experimental studies of spin-pumping in three structures: Py/Au/Pt, Py/Au/Pt/Co and Co/Pt. These structures fully characterize the spin-pumping at the Py/Au and Co/Pt interfaces, with the only remaining the boundary condition is at the Au/Pt interface. Both the continuity of chemical potential and continuity of spin accumulation are tested against the experimental data, neither of which were able to fit the data. A third boundary condition was presented which treats Pt as a partial spin-sink; it resulted in a remarkably good fit to all the data. Both the experimental observation and

the fitted model suggested that the spin-transport across the Au/Pt is asymmetric. Finally, a spin-memory-loss model at the Au/Pt interface was tested against the data resulting in unrealistic fitting parameters.

8.2 Structures and Experiment

The studied structures, Ta(3)|Py(6)|Au(3)|Pt(d_{Pt}), Ta(3)|Co(6)|Pt(d_{Pt}) and Ta(3)|Py(6)|Au(3)|Pt(d_{Pt})|Co(6)|Ta(3) were deposited on oxidized Si wafers by means of RF magnetron sputter deposition at room temperature, where Py = $Ni_{80}Fe_{20}$. d_{Pt} is the Pt thickness ($0 < d_{\mathrm{Pt}} < 3$ nm) and the numbers in parenthesis are thicknesses in nm. The substrate preparation and the deposition process is the same as discussed in the my previous studies, for more detail see section 3.2.1. For brevity these structures will be referred to as Py/Au/Pt(d_{Pt}), Co/Pt(d_{Pt}) and Py/Au/Pt(d_{Pt})/Co for the rest of this chapter.

In-plane FMR, measurements were carried out in a field-swept, field-modulated set-up in a frequency range of 6 - 28 GHz. The FMR signal, which is described by Lorentzian lineshape for rf susceptibilities, was interpreted as an admixture of the in-phase and out-of-phase components of rf susceptibility, for more detail see chapter 2.

The foci of the study are Co/Pt(d_{Pt}), Py/Au/Pt(d_{Pt}), Py/Au/Pt(d_{Pt})/Co structures. Since the Py/Au/Pt(d_{Pt})/Co has two separate ferromagnetic materials, it is possible to generate spin-pumping from either Py or Co (see fig. 8.2) resulting in two completely different data sets from the same structure. Unlike the study of Py/Pt/Py in the previous chapter, the FMR resonances of the two magnetic layer are well separated due to their different saturation magnetizations ($M_{\mathrm{s}}^{\mathrm{Co}}$ = 1250 [27] emu/cm^3 and $M_{\mathrm{s}}^{\mathrm{Py}}$ = 817 emu/cm^3) and therefore each layer can be put into resonance independently from the other, see fig. 8.1. In the case of spin-pumping from Py, the spin-current originates at the Py/Au interface and is transmitted across Au/Pt and finally absorbed by the Co layer. However, if spin-pumping from Co the spin-current originates at the Co/Pt interface and is transmitted through Pt/Au and finally absorbed by the Py layer. To clearly distinguish between the two data sets the following notation will be used: $\overrightarrow{\mathrm{Py}}$/Au/Pt($d_{\mathrm{Pt}}$)/Co and Py/Au/Pt($d_{\mathrm{Pt}}$)/$\overleftarrow{\mathrm{Co}}$, where the arrow above the ferromagnet signifies it as the source of the spin-current due to its precession, see fig. 8.2.

8.3 Results and Interpretation

The experimental results of the spin-pumping induced damping for $\overrightarrow{\mathrm{Py}}$/Au/Pt($d_{\mathrm{Pt}}$)/Co, $\overrightarrow{\mathrm{Py}}$/Au/Pt($d_{\mathrm{Pt}}$) and $\overrightarrow{\mathrm{Co}}$/Pt($d_{\mathrm{Pt}}$) are presented in fig. 8.3 (a, yellow points), fig. 8.3 (a, blue points) and fig. 8.3(b), respectively. The focus is the induced damping due to spin-pumping into the adjacent Au/Pt(d_{Pt}) or Pt(d_{Pt}) layers. The contribution to total damping which is due to the intrinsic damping of Py ($\alpha_{\mathrm{Py}} = 8.3 \times 10^{-3}$) or Co ($\alpha_{\mathrm{Co}} = 10.5 \times 10^{-3}$) can be

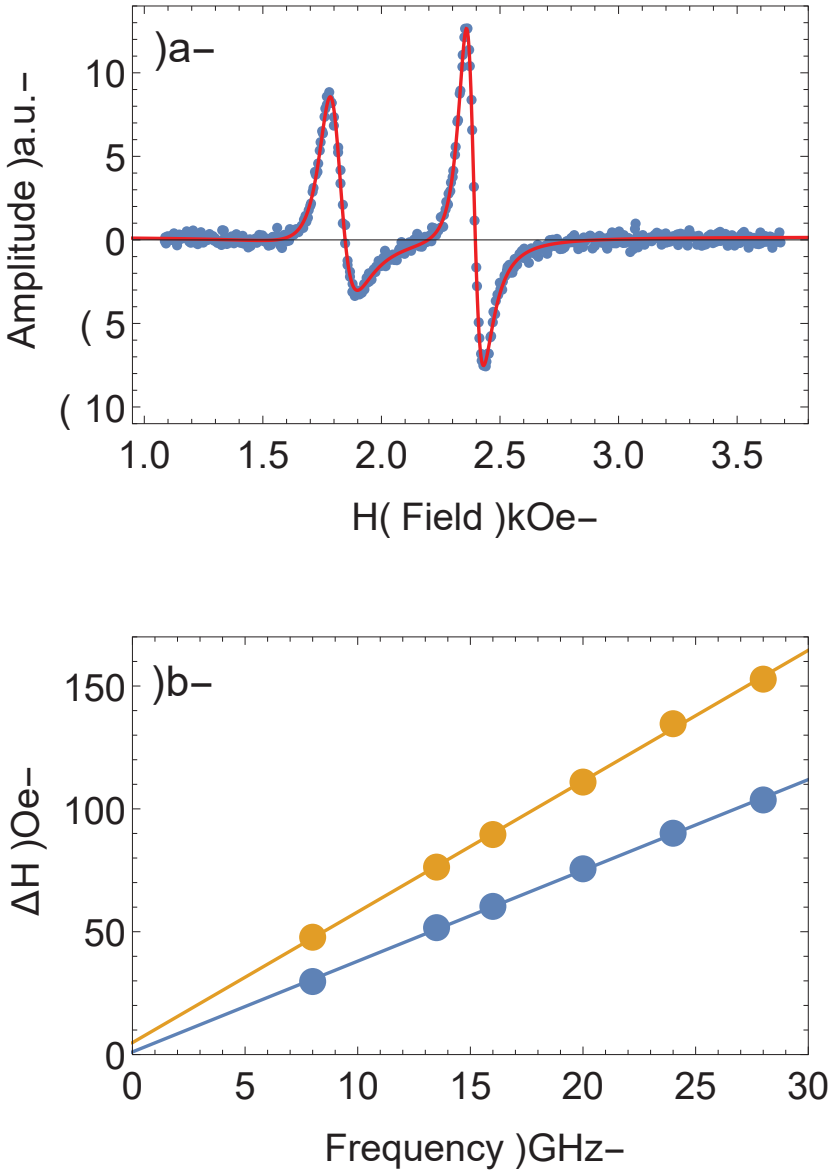

Figure 8.1: (a) FMR response at 16 GHz and (b) linewidth vs. frequency data of the Py/Au/Pt(2)/Co sample. The lower field peak in (a) is the Co resonance with fitting parameters ΔH = 90 Oe, H_{res} = 1807 Oe as determined from eq. (6.1). The higher field peak in (a) is the Py resonance with fitting parameters ΔH = 60 Oe, H_{res} = 2382 Oe as determined from eq. (6.1). Linewidth vs. frequency in (b) fit resulted in $\alpha = 16.1 \times 10^{-3}$ and $\Delta H(0)$ = 5 Oe for the Co resonances (yellow line) and $\alpha = 10.8 \times 10^{-3}$ and $\Delta H(0)$ = 1 Oe for the Py resonances (blue line).

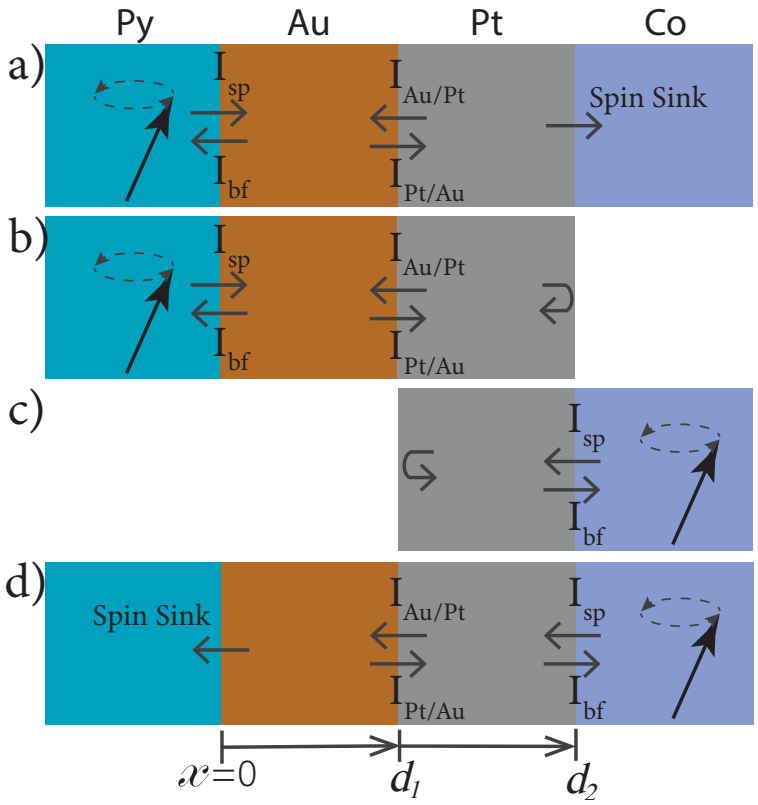

Figure 8.2: Schematic of the studied structures. Spin-current is ejected from the precessing ferromagnet (Py or Co) into the adjacent layer. At the Au/Pt interface a portion of the spin-current is reflected and transmitted. At the other end of the structure the spin-current is either absorbed by the second ferromagnet (spin-sink) or reflected at the metal/air boundary.

subtracted away since it is independent of the thickness of Pt. The remaining damping is due to spin-pumping into the adjacent Au/Pt(d_{Pt}) or Pt(d_{Pt}) layers.

For complete interpretation of the data it is required to know the spin-pumping/spin diffusion parameters into and through both Au and Pt. Spin-pumping into Au has been studied in great detail and shown to be well described by the conventional spin-pumping/spin diffusion model[142, 153, 146] with $\lambda_{\mathrm{sd,Au}}$ = 31 nm [3]. The single spin resistivity of Au was taken to be $\rho^{\uparrow}_{\mathrm{Au}}$ = 8 $\mu\Omega$cm [154]. However, the interface spin-mixing conductivity for Au was determined from the spin-pumping damping of the $\overrightarrow{\mathrm{Py}}$/Au/Pt($d_{\mathrm{Pt}}$=0) (first blue point on fig. 8.3(a)) and $\overrightarrow{\mathrm{Py}}$/Au/Pt($d_{\mathrm{Pt}}$=0)/Co (first yellow point on fig. 8.3(a)). The difference in damping of the two data points is

$$\alpha_{\mathrm{sp}}^{\mathrm{Py/Au/Co}} - \alpha_{\mathrm{sp}}^{\mathrm{Py/Au}} = 2.72 * 10^{-3}. \tag{8.1}$$

Using the single spin resistivity of Au, $\rho^{\uparrow}_{\mathrm{Au}}$ = 8 $\mu\Omega$cm[154] with $\lambda_{\mathrm{sd,Au}}$ = 31 nm[3], and using the relationship established in the theory section for conventional spin-pumping,

$$\alpha_{\mathrm{sp}}^{\mathrm{SL}} = \frac{g\mu_{\mathrm{B}}}{4\pi M s}\frac{\tilde{g}_{\uparrow\downarrow}}{d_{\mathrm{FM}}}\left[1 + \frac{\tilde{g}_{\uparrow\downarrow}\mathcal{R}}{\tanh\left(\frac{d_{\mathrm{NM}}}{\lambda_{\mathrm{sd}}}\right)}\right]^{-1}, \tag{8.2}$$

and

$$\alpha_{\mathrm{sp}}^{\mathrm{DL}} = \frac{g\mu_{\mathrm{B}}}{4\pi M_s}\frac{\tilde{g}_{\uparrow\downarrow}}{d_{\mathrm{FM}}}\left[1 + \tilde{g}_{\uparrow\downarrow}\mathcal{R}\frac{1 + \tilde{g}_{\uparrow\downarrow}\mathcal{R}\tanh\left(\frac{d_{\mathrm{NM}}}{\lambda_{\mathrm{sd}}}\right)}{\tanh\left(\frac{d_{\mathrm{NM}}}{\lambda_{\mathrm{sd}}}\right) + \tilde{g}_{\uparrow\downarrow}\mathcal{R}}\right]^{-1}, \tag{8.3}$$

it is simple to show that for these samples $\tilde{g}_{\uparrow\downarrow,\mathrm{Py/Au}} = 1.7\times10^{15}$ cm^{-2}. As before $\mathcal{R} = \frac{\rho_{\uparrow}e^2}{2\pi\hbar}\lambda_{\mathrm{sd}}$, M_s is the saturation magnetization, d_{FM} is the FM thickness (d_{Py}), d_{NM} is the NM thickness, $\mathcal{R} = \frac{\rho_{\uparrow}e^2}{2\pi\hbar}\lambda_{\mathrm{sd}}$, e is the fundamental charge and $\rho_{\uparrow}$ is the bulk, single spin, electrical resistivity [7].

The above characterizes the spin-pumping at the Py/Au interface and spin transport through the Au layer. The remaining fitting parameters will need to describe spin-pumping at the Co/Pt interface ($\tilde{g}_{\uparrow\downarrow,\mathrm{Pt/Co}}$), spin transport through Pt ($\lambda_{\mathrm{sd,Pt}}$ and $\rho^{\uparrow}_{\mathrm{Pt}}$) and the Au/Pt interface (this is determined by the model). In order to have unique fitting parameters it is important to simultaneously fit all data sets with the same fitting parameters [23]. As it was observed in chapter 5, any of the studied models were able to fit the SL structure with reasonable success but attempting to to also fit the DL data pointed out the flaw in this approach. In the study presented in this chapter the spin-sink structure is $\overrightarrow{\mathrm{Py}}$/Au/Pt($d_{\mathrm{Pt}}$)/Co. The 3 nm thick Au layer is used as a spacer layer to prevent interlayer exchange coupling between Py and Co which is mediated by proximity polarized Pt, as was observed in chapter 6 [32, 155]. Spin-current originating from Py passes through Au and Pt and gets absorbed by the Co layer. Since the diffusion length in Au is much larger than its thickness, the

spin-current is mostly unaffected by the Au spacer layer. However, this will still be taken into account within the model.

Before attempting to fit the data it is useful discuss it in a more qualitative manner. The spin-pumping damping of Py in $\overrightarrow{\text{Py}}$/Au/Pt($d_{\text{Pt}}$)/Co decreases with increasing Pt thickness, this is the expected thickness dependence of a FM/NM/spin-sink structure [23], see yellow points in fig. 8.3(a). The spin-pumping damping of $\overrightarrow{\text{Py}}$/Au/Pt($d_{\text{Pt}}$) increases with increasing Pt thickness, see blue points in fig. 8.3(a), consistent with expected behavior for a single FM/NM structure. In general the FM/NM and FM1/NM/FM2 are enough to uniquely fit the spin transport parameters of NM, however in this work the aim was to also determine the effect of the spacer Au layer on the spin transport. Therefore the Co/Pt(d_{Pt}) structures allows to more accurately determine $\tilde{g}_{\uparrow\downarrow,\text{Pt/Co}}$, $\lambda_{\text{sd,Pt}}$, $\rho^{\uparrow}_{\text{Pt}}$ parameters. The magnetic damping of the Co/Pt(d_{Pt}), see fig. 8.3(b), shows a rapid approach to saturation with a diffusion length of $\lambda_{\text{sd}} \sim 1$ nm. Similar results have been observed in single crystal structures [135] and textured structures [155]. This thickness dependence is very similar to that of Py/Pt in fig. 7.4.

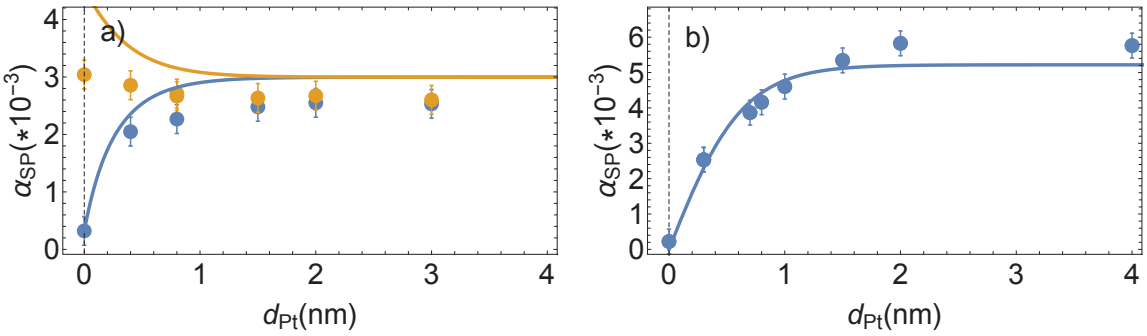

Figure 8.3: (a) Spin-pumping induced damping data for the $\overrightarrow{\text{Py}}$/Au/Pt($d_{\text{Pt}}$)/Co (yellow) and $\overrightarrow{\text{Py}}$/Au/Pt($d_{\text{Pt}}$) (blue) structures. Solid lines are fits by eq. (8.9) with conventional spin-pumping theory extended to include Au/Pt interface with eq. (8.4) and eq. (8.5) boundary conditions. (b) Spin-pumping damping data for $\overrightarrow{\text{Co}}$/Pt($d_{\text{Pt}}$) fit by with conventional spin-pumping theory using eq. (8.2). All fits were performed simultaneously yielding the following fitting parameters: $\tilde{g}_{\uparrow\downarrow,\text{Pt/Co}} = 40 \times 10^{15}$ cm^{-2}, $\lambda_{\text{sd,Pt}} = 0.6$ nm, $\rho_{\text{Pt}} = 174$ $\mu\Omega$cm.

8.3.1 Continuity of Chemical Potential or Continuity of Spin Accumulation

At this point it is instructive to attempt to fit the experimental with the spin-pumping model. Unlike the previous spin-pumping experiments presented in this thesis, where there is effectively only one NM present in the structure, in this experiment there are two NMs (Au and Pt) both of which strongly influence the spin-transport. The propagation of spin-current will still be modeled by the spin-diffusion theory, however one must also include the transport of spin-current across the Au/Pt interface. As mentioned, there are two existing

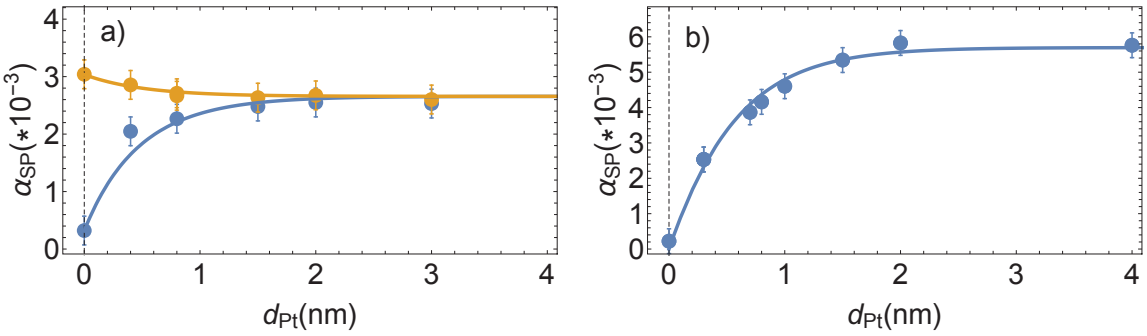

Figure 8.4: (a) Spin-pumping induced damping data for the $\overrightarrow{\text{Py}}$/Au/Pt($d_{\text{Pt}}$)/Co (yellow) and $\overrightarrow{\text{Py}}$/Au/Pt($d_{\text{Pt}}$) (blue) structures. Solid lines are fits with eq. (8.9) with conventional spin-pumping theory extended to include Au/Pt interface with eq. (8.6) and eq. (8.7) boundary conditions. (b) Spin-pumping damping data for $\overrightarrow{\text{Co}}$/Pt($d_{\text{Pt}}$) fit with conventional spin-pumping theory using eq. (8.2). All fits were performed simultaneously yielding the following fitting parameters: $\tilde{g}_{\uparrow\downarrow,\text{Pt/Co}} = 6.2 \times 10^{15}$ cm^{-2}, $\lambda_{\text{sd,Pt}} = 1.0$ nm, $\rho_{\text{Pt}} = 56$ $\mu\Omega$cm and $\mathcal{N}^{\text{Pt}}/\mathcal{N}^{\text{Au}} = 2.9$.

models in the literature, the continuity of chemical potential and the continuity of spin accumulation.

Continuity of chemical potential at the Au/Pt interface implies the following,

$$x = d_1; \qquad \boldsymbol{\mu}_{\text{s}}^{\text{Au}} = \boldsymbol{\mu}_{\text{s}}^{\text{Pt}}\Big|_{x=d_1}. \tag{8.4}$$

Also spin current across the interface is still assumed to be and continuous,

$$x = d_1; \quad -\frac{\hbar}{2\rho_{\text{Au}}^{\uparrow}e^2}\frac{\partial \boldsymbol{\mu}_{\text{s}}^{\text{Au}}}{\partial x} = -\frac{\hbar}{2\rho_{\text{Pt}}^{\uparrow}e^2}\frac{\partial \boldsymbol{\mu}_{\text{s}}^{\text{Pt}}}{\partial x}\Big|_{x=d_1}. \tag{8.5}$$

Continuity of spin accumulation is the second approach to model spin transport across the Au/Pt structure and it is given by

$$x = d_1; \quad \boldsymbol{\mu}_{\text{s}}^{\text{Au}}\mathcal{N}^{\text{Au}}(\text{E})_F = \boldsymbol{\mu}_{\text{s}}^{\text{Pt}}\mathcal{N}^{\text{Pt}}(\text{E})_F\Big|_{x=d_1}, \tag{8.6}$$

and continuity of spin-current,

$$x = d_1; \quad -\frac{\hbar}{2\rho_{\text{Au}}^{\uparrow}e^2}\frac{\partial \boldsymbol{\mu}_{\text{s}}^{\text{Au}}}{\partial x} = -\frac{\hbar}{2\rho_{\text{Pt}}^{\uparrow}e^2}\frac{\partial \boldsymbol{\mu}_{\text{s}}^{\text{Pt}}}{\partial x}\Big|_{x=d_1}, \tag{8.7}$$

where the spin accumulation is defined

$$\boldsymbol{s}_{\text{Au}} = \frac{\hbar}{2}\boldsymbol{\mu}_s^{\text{Au}}\mathcal{N}^{\text{Au}}(\text{E})_F \quad \text{and} \quad \boldsymbol{s}_{\text{Pt}} = \frac{\hbar}{2}\boldsymbol{\mu}_s^{\text{Pt}}\mathcal{N}^{\text{Pt}}(\text{E})_F \tag{8.8}$$

$\mathcal{N}(\mathrm{E})$ is the density of states at the Fermi energy.

Both models provide two additional boundary conditions which influence the solution of the spin diffusion equation and result in a different thickness dependence for the spin chemical potential and the spin-current. The aim is to solve for the spin chemical potential throughout the entire structure. As before, this is done by assuming a solution of the diffusion equation applied to the appropriate boundary conditions. At the Py/Au interface is the spin-pumping boundary condition and at the Pt/ambient or Pt/Co interface is a reflection or absorption (spin-sink) boundary condition, see section 2.5.2. The two remaining boundary conditions have to do with the Au/Pt interface. The solution of the spin chemical potential is then related to the magnetic damping by,

$$\alpha_{\mathrm{sp,Py}}\left(\boldsymbol{n}\times\frac{\partial\boldsymbol{n}}{\partial t}\right)=\frac{\gamma}{d_{\mathrm{Py}}}\left(\boldsymbol{I}_{sp}-\frac{\tilde{g}_{\uparrow\downarrow,\mathrm{Au}}}{4\pi}\boldsymbol{\mu}_{\mathrm{s}}^{\mathrm{Au}}\right)\Bigg|_{x=0}. \tag{8.9}$$

Continuity of chemical potential: In this approach it is assumed that the chemical potential at the Au/Pt interface follows the behavior described by eqs. (8.4) and (8.5). Including these into the spin-diffusion model for the SL ($\overrightarrow{\mathrm{Py}}$/Au/Pt($d_{\mathrm{Pt}}$)) structure and the DL ($\overrightarrow{\mathrm{Py}}$/Au/Pt($d_{\mathrm{Pt}}$)/Co) structure yields a solution for each structure. The two solutions share the same fitting parameters ($\lambda_{\mathrm{sd,Pt}}$, ρ_{Pt} and $\tilde{g}_{\uparrow\downarrow,\mathrm{Pt/Co}}$). Lastly, the Co/Pt($d_{\mathrm{Pt}}$) structure has a simple solution given by eq. (8.2) with the same fitting parameters. Therefore, the three data sets can all be simultaneously fit with the same set of parameters. Fits of the Co/Pt(d_{Pt}), $\overrightarrow{\mathrm{Py}}$/Au/Pt($d_{\mathrm{Pt}}$), $\overrightarrow{\mathrm{Py}}$/Au/Pt($d_{\mathrm{Pt}}$)/Co and data are plotted in fig. 8.3(b), fig. 8.3(a)(blue) and fig. 8.3(a)(yellow), respectively. The fitting parameters are $\tilde{g}_{\uparrow\downarrow,\mathrm{Pt/Co}} = 40\times10^{15}$ cm^{-2}, $\lambda_{\mathrm{sd,Pt}} = 0.6$ nm and $\rho_{\mathrm{Pt}} = 174$ $\mu\Omega$cm. This model fails to fit all the data and results in a fitted $\tilde{g}_{\uparrow\downarrow,\mathrm{Pt/Co}}$ which is far too large to be consistent with previous spin-pumping studies (normally between 1×10^{15} and 10×10^{15} cm^{-2}).

Continuity of spin accumulation: In this approach it is assumed that the spin accumulation at the Au/Pt interface follows the behavior described by eqs. (8.6) and (8.7). Note, this model has two additional parameters, the density of states at the Fermi level for Au and Pt. From the points of view of the fit the individual densities are not important, the ratio of the density of states is the unique fitting parameter. This ratio is allowed to be a free fitting parameter. Fits of the Co/Pt(d_{Pt}), $\overrightarrow{\mathrm{Py}}$/Au/Pt($d_{\mathrm{Pt}}$), $\overrightarrow{\mathrm{Py}}$/Au/Pt($d_{\mathrm{Pt}}$)/Co and data are plotted in fig. 8.4(b), fig. 8.4(a)(blue) and fig. 8.4(a)(yellow), respectively. This model fits the data much better yielding fitting parameters much closer to the expected range: $\tilde{g}_{\uparrow\downarrow,\mathrm{Pt/Co}} = 6.2\times10^{15}$ cm^{-2}, $\lambda_{\mathrm{sd,Pt}} = 1$ nm and $\rho_{\mathrm{Pt}} = 56$ $\mu\Omega$cm, see fig. 8.4. Therefore this model appears to be a better representation of spin transport across the Au/Pt interface.

However, there is a final dataset to test this model on, the Py/Au/Pt(d_{Pt})/$\overleftarrow{\mathrm{Co}}$. In this structure the spin-current is originating from the Co layer, propagating thorough the Au/Pt and being absorbed into the spin-sink Py. Since this is a spin-sink type of boundary condition, one would expect that the damping vs thickness dependence to increase with decreasing

d_{Pt}. However, the experimental result shows completely the opposite behavior, see fig. 8.5. To check if the continuity of spin accumulation model can reproduce this behavior, one can use the spin-pumping parameters as extracted from the *Continuity of spin accumulation* and plot the expected dependence for the Py/Au/Pt(d_{Pt})/$\overleftarrow{Co}$, see red line in fig. 8.5, clearly it fails to reproduce the data.

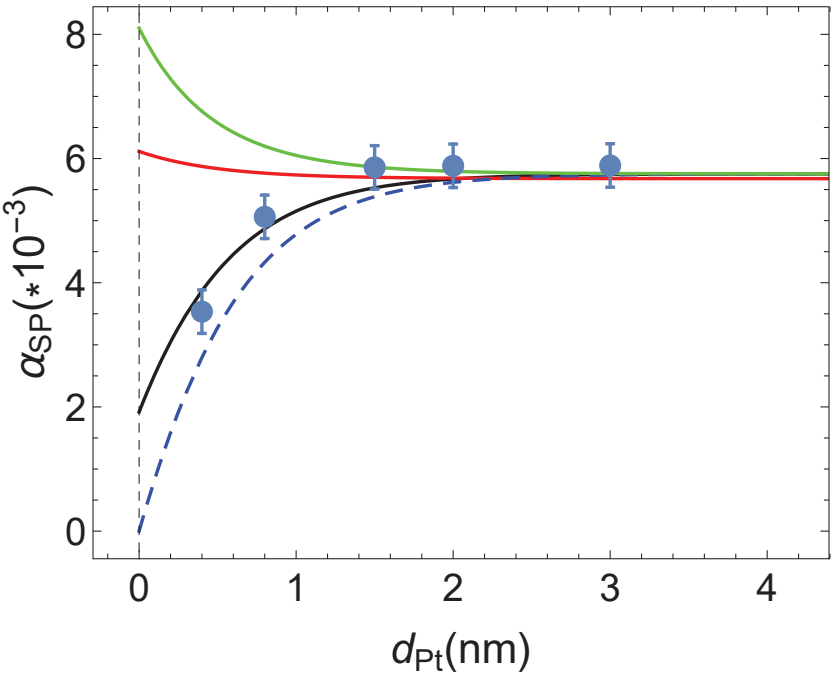

Figure 8.5: Spin-pumping induced damping for Py/Au/Pt(d_{Pt})/$\overleftarrow{Co}$, the spin-current is ejected from the Co layer. The black line is a fit with conventional spin-pumping theory extended to include Au/Pt interface with eq. (8.10) and eq. (8.11) boundary conditions. The red line is the simulated damping for Pt(d_{Pt})/$\overleftarrow{Co}$ structure assuming the same parameters as determined from the black line fit. The dashed blue line is the simulated damping for spin-sink/Pt(d_{Pt})/$\overleftarrow{Co}$ structure assuming the same parameters as determined from the black line fit.

In contrast to the $\overrightarrow{Py}$/Au/Pt(d_{Pt})/Co data, the spin-pumping damping of Py/Au/Pt(d_{Pt})/$\overleftarrow{Co}$ (fig. 8.5) does not have the typical spin-sink/NM/FM thickness dependence, in fact it is much more similar to the damping of $\overrightarrow{Co}$/Pt, for comparison this is plotted as the dashed blue line in fig. 8.5. This observation suggests that the Au/Pt interface is preventing a large portion of the spin-current from reaching the spin-sink (Py). Since such a behavior is not observed in $\overrightarrow{Py}$/Au/Pt(d_{Pt})/Co, it was concluded that the spin transparency of the Au/Pt structure depends on the direction of the spin-current.

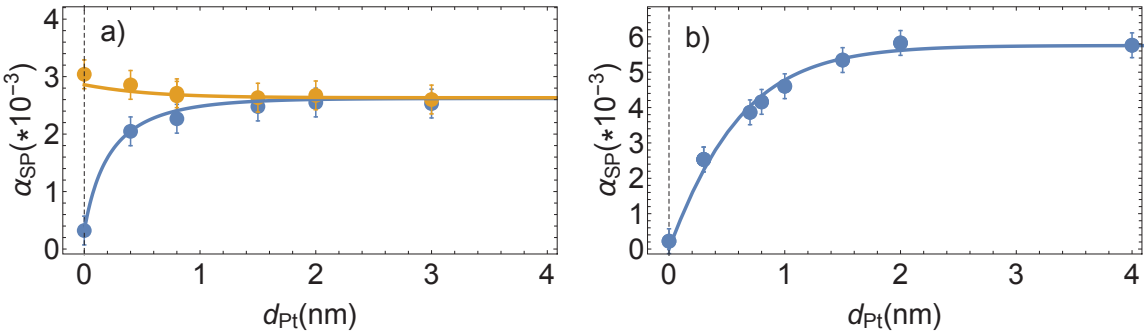

Figure 8.6: (a) Spin-pumping induced damping data for the $\overrightarrow{\text{Py}}$/Au/Pt($d_{\text{Pt}}$)/Co (yellow) and $\overrightarrow{\text{Py}}$/Au/Pt($d_{\text{Pt}}$) (blue) structures. Solid lines are fits by eq. (8.9) with conventional spin-pumping theory extended to include Au/Pt interface with eq. (8.10) and eq. (8.11) boundary conditions. (b) Spin-pumping damping data for $\overrightarrow{\text{Co}}$/Pt($d_{\text{Pt}}$) fit by with conventional spin-pumping theory. All fits were performed simultaneously yielding the following fitting parameters: $\tilde{g}_{\uparrow\downarrow,\text{Pt/Co}} = 7.6\times10^{15}$ cm^{-2}, $\lambda_{\text{sd,Pt}} = 1.0$ nm, $\rho_{\text{Pt}} = 61$ $\mu\Omega$cm and $\tilde{g}_{\uparrow\downarrow,\text{Au/Pt}} = 3.2\times10^{15}$ cm^{-2}.

8.3.2 Partial Spin Sink Model

In the literature Pt is often treated as a perfect spin-sink, however this is clearly not the case since there is a definite dependence of spin-pumping on the thickness of Pt. A perfect spin-sink is considered to immediately absorb any spin-current impinging on it and reflect nothing. In this scenario it would not lead to any thickness dependence or either spin-pumping or of the measured damping. Motivated by the idea of a spin-sink it is natural to attempt to treat the Pt layer as a partial spin-sink. Borrowing from the spin-sink boundary conditions, one assumes that all the spin-current impinging on Pt is then absorbed into it, the additional feature to this "partial spin-sink" effect is that due to the spin-accumulation within Pt, it is assumed that it results in some backflow back into the Au layer. Mathematically this can be expressed as,

$$-\frac{\hbar}{2\rho^{\uparrow}_{\text{Au}}e^2}\frac{\partial\boldsymbol{\mu}^s_{\text{Au}}}{\partial x} = \frac{\tilde{g}_{\uparrow\downarrow,\text{Au/Pt}}}{4\pi}\boldsymbol{\mu}^s_{\text{Au}} - \frac{\tilde{g}_{\uparrow\downarrow,\text{Pt/Au}}}{4\pi}\boldsymbol{\mu}^s_{\text{Pt}}\Big|_{x=d_1}, \tag{8.10}$$

$$-\frac{\hbar}{2\rho^{\uparrow}_{\text{Pt}}e^2}\frac{\partial\boldsymbol{\mu}^s_{\text{Pt}}}{\partial x} = -\frac{\tilde{g}_{\uparrow\downarrow,\text{Pt/Au}}}{4\pi}\boldsymbol{\mu}^s_{\text{Pt}} + \frac{\tilde{g}_{\uparrow\downarrow,\text{Au/Pt}}}{4\pi}\boldsymbol{\mu}^s_{\text{Au}}\Big|_{x=d_1}. \tag{8.11}$$

e is the fundamental charge and $\rho^{\uparrow}_{\text{Au}}(\rho^{\uparrow}_{\text{Pt}})$ is the single spin resistivity of Au(Pt). The efficiency of transfer of spin-current from Au into Pt or from Pt into Au, ($\tilde{g}_{\uparrow\downarrow,\text{Au/Pt}}$), is represented by a similar parameter as the spin-mixing conductivity at the interface FM/NM for spin-pumping. These boundary conditions are akin to those at FM/NM where the first term on the right hand side represents the spin-current injected from Au into Pt and the second term on the right hand side is the back-flow from Pt into Au due to spin accumulation in Pt. Conceptually the terms on the right hand side of eqs. (8.10) and (8.11) can be thought

of as the forward spin-current into the Au/Pt (first term) and the backward spin-current reflected at Au/Pt (second term). The left hand side is the net spin-current which makes it across the Au/Pt interface. Including these boundary conditions in the conventional spin-pumping model it is possible to simultaneously fit the $\overrightarrow{\text{Co}}$/Pt, $\overrightarrow{\text{Py}}$/Au/Pt($d_{\text{Pt}}$) and $\overrightarrow{\text{Py}}$/Au/Pt($d_{\text{Pt}}$)/Co data sets resulting in $\tilde{g}_{\uparrow\downarrow,\text{Pt/Co}} = 7.6\times10^{15}$ cm^{-2}, $\lambda_{\text{sd,Pt}} = 1.0$ nm, $\rho^{\uparrow}_{\text{Pt}} = 61$ $\mu\Omega$cm and $\tilde{g}_{\uparrow\downarrow,\text{Au/Pt}} = \tilde{g}_{\uparrow\downarrow,\text{Pt/Au}} = 3.2\times10^{15}$ cm^{-2}. These boundary condition results in a good fit to all the data sets, see fig. 8.6 for the fits.

The $\tilde{g}_{\uparrow\downarrow,\text{Pt/Co}} = 7.6\times10^{15}$ cm^{-2} is quite large in comparison to other materials, for example in this work the Py/Au interface is $\tilde{g}_{\uparrow\downarrow,\text{Py/Au}} = 1.7\times10^{15}$ cm^{-2}. However, it is well known that spin-pumping experiments yield a larger spin-mixing conductivity for Co/Pt structures usually $\tilde{g}_{\uparrow\downarrow,\text{Pt/Co}} \sim 4-9\times10^{15}$ cm^{-2} [17, 156, 157, 136]. The single spin resistivity extracted from the fit is $\rho^{\uparrow}_{\text{Pt}} = 61$ $\mu\Omega$cm, this is approximately twice the bulk single spin resistivity for Pt ~ 34 $\mu\Omega$cm [155]. The parameters $\tilde{g}_{\uparrow\downarrow,\text{Au/Pt}} = \tilde{g}_{\uparrow\downarrow,\text{Pt/Au}} = 3.2\times10^{15}$ cm^{-2} is describe the efficiency of spin transport across the Au/Pt from one of the other side of the interface. In principle these can have different values, however it was found that forcing $\tilde{g}_{\uparrow\downarrow,\text{Au/Pt}} = \tilde{g}_{\uparrow\downarrow,\text{Pt/Au}}$ still yields a good fit to the data.

With all the fitting parameters established it is possible to plot the expected thickness dependence of Py/Au/Pt(d_{Pt})/$\overleftarrow{\text{Co}}$ and compare this to the actual data of Py/Au/Pt(d_{Pt})/$\overleftarrow{\text{Co}}$, see black line in fig. 8.5. This model was found to reproduce the unexpected thickness dependence of the Py/Au/Pt(d_{Pt})/$\overleftarrow{\text{Co}}$ data set, see black line in fig. 8.5. As mentioned, this thickness dependence is very similar to $\overrightarrow{\text{Co}}$/Pt data, for comparison see the dashed blue line in fig. 8.5 which is the $\overrightarrow{\text{Co}}$/Pt fit. Importantly, at $d_{\text{Pt}} = 0$ the spin-pumping damping of this model does not start at zero but at a slightly larger (~2) value suggesting that there is some portion of the spin-current is making it through the Au/Pt interface and is not returning back to the Co layer. One can compare these results to the expected thickness dependence of a hypothetical spin-sink/Pt(d_{Pt})/$\overleftarrow{\text{Co}}$ structure assuming the same spin transport parameters, see green line in fig. 8.5. Clearly the observed experimental behaviour is nothing like that which would results from a spin-sink structure. Note, such a structure cannot be experimentally achieved since the Pt layer results in static interlayer exchange coupling between the Co and the sink [155], however, mathematically it is easy to model. This suggests that the Au/Pt interface is playing a very large role in the observed spin transport.

The portion of reflected and transmitted spin-current at Au/Pt can be determined from eq. (8.10) and eq. (8.11). The first term on the right hand side of eq. (8.10) is the spin-current flowing from Pt and transmitted across the Au/Pt interface. The second term is effectively the current reflected at the Au/Pt interface and flowing back into Pt. The only way the right hand side is not zero (some net current is transmitted) is if there is a difference in the chemical potentials across the Au/Pt interface ($\boldsymbol{\mu}^{s}_{\text{Au}} \neq \boldsymbol{\mu}^{s}_{\text{Pt}}$ at the interface). The ratio of the chemical potentials at the interface is therefore the ratio of the transmitted to reflected currents, $T_{\text{s}}/R_{\text{s}}$. Assuming the spin-pumping parameters as determined from the fits with

d_{Au} = 3 nm and d_{Pt} = 1 nm one can show that T_s/R_s = 1.5 ($\boldsymbol{\mu}^s_{Pt}/\boldsymbol{\mu}^s_{Au}$) for spin-pumping from the Co in Py/Au/Pt(d_{Pt})/$\overleftarrow{Co}$. Note, if T_s/R_s = 1 then the reflected current is perfectly compensated by the transmitted current and the net flow across is zero.

The spin-pumping data of the $\overrightarrow{Py}$/Au/Pt(d_{Pt})/Co and $\overrightarrow{Py}$/Au/Pt(d_{Pt}) structures (fig. 8.6(a)) does not show such a large reflection of spin-current at the Au/Pt interface. The $\overrightarrow{Py}$/Au/Pt(d_{Pt}=0)/Co data point on fig. 8.6(a) establishes the maximum spin-pumping achievable in the $\overrightarrow{Py}$/Au/Co structure due to Co acting as a spin-sink. Once again, taking the ratio of the chemical potentials at the Au/Pt interface to determine T_s/R_s for spin-pumping from the Au side to find T_s/R_s = 3.2 ($\boldsymbol{\mu}^s_{Au}/\boldsymbol{\mu}^s_{Pt}$). Therefore there is much less reflection when spin-pumping from the Au side as compared to when spin-pumping from the Pt side. However, there is still substantial reflection even when pumping from the Au side, this is in line with the experimental observations of quantum well state in the Fe/Au/Pd structure [21] or oscillatory spin-polarization of Pt in Py/Cu/Pt structures [141], both of which suggest a reflection of spin-current at the Au/Pd or Cu/Pt interface. The asymmetry in reflection of spin-current at Au/Pt interface can be thought of as acting similar to a spin-current diode, allowing more spin-current in one direction than the other.

8.3.3 Spin Memory Loss Model

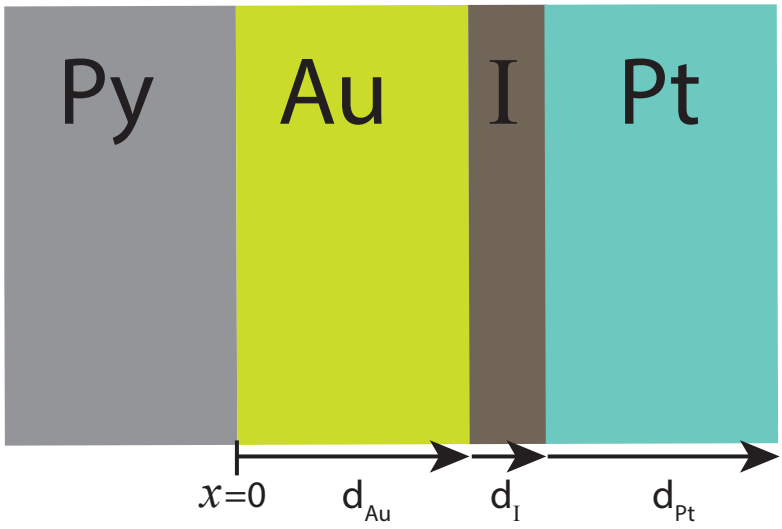

Figure 8.7: Schematic of the structure with a thin SML layer labeled as I.

It has been suggested that there is a rapid dephasing of the spin-current at the interface of a Au and a large spin-orbit coupling metal like Pt [20]. This dephasing should show up as nearly a discontinuity of spin-current at the Au/Pt interface. This effect can be introduced into our existing spin-pumping model by following the approach of Gupta *et al.* [20] in which an additional fictitious layer I is introduced in between the existing Au/Pt interface, see fig. 8.7. Therefore the structures now become $\overrightarrow{Py}$/Au/Pt → $\overrightarrow{Py}$/Au/I/Pt and $\overrightarrow{Py}$/Au/Pt/Co

$\rightarrow \overrightarrow{\text{Py}}$/Au/I/Pt/Co, where I is the spin memory loss (SML) layer. This layer is assumed to act as a typical normal metal whose spin-transport properties are given by its spin-diffusion length λ_{I} and resistivity ρ_{I}. The measure of the dephasing or SML is then dependent on the thickess of this layer, its λ_{I} and ρ_{I}. Since this is an interface layer, its thickness should be approaching zero and therefore the parameters relevant to the SML effect are

$$\delta_{\text{I}} = \lim_{d_{\text{I}} \to 0} \frac{d_{\text{I}}}{\lambda_{\text{I}}}, \tag{8.12}$$

and

$$AR_{\text{I}} = \lim_{d_{\text{I}} \to 0} \rho_{\text{I}} d_{\text{I}}. \tag{8.13}$$

The quantities δ_{I} and AR_{I} are to be determined experimentally or calculated from scattering theory. Note that $\delta_{\text{Au/Pt}} = 0$ would result in zero SML and $\delta_{\text{Au/Pt}} = 1$ would result in very large SML. Gupta *et al.* [20] calculate a $\delta_{\text{Au/Pt}} = 0.62$ and $AR_{\text{Au/Pt}} = 0.54$ fΩm^2 for atomically sharp interfaces at 300K. It is expected that such large values should result in significant SML at the I layer (Au/Pt interface). Since Gupta *et al.* [20] assume continuity of spin-accumulation, it is easy to include this SML layer into the conventional spin-pumping model. This can be done by simply adding another pair of "continuity of spin-accumulation" boundary conditions with some λ_{I} and ρ_{I} into the structure and forcing the I layer thickness to approach zero, see fig. 8.7. Importantly, this model requires three additional free fitting parameters, δ_{I}, AR_{I} and $\mathcal{N}_{\text{Pt}}(\text{E})_F/\mathcal{N}_{\text{Au}}(\text{E})_F$ for a total of 6 fitting parameters. Lastly, before fitting the data, it is important to recognize that the very first point (black point in fig. 8.8(a)) is the Py/Au structure with no Pt on top. This model would not anticipate any SML for this structure since there is no Au/Pt interface. All the subsequent points have some thickness of Pt deposited on top, so one would expect SML for the rest of the data. For this reason the Py/Au (black point in fig. 8.8(a)) is omitted during the fitting routine.

All the datasets (including the Py/Au/Pt(d_{Pt})/$\overleftarrow{\text{Co}}$ data) were fit simultaneously using the SML model, see fig. 8.8. This model appears to fit the data quite well. Surprisingly, it seems to also fit the Py/Au even though this was not included in the fit. A closer look at the resulting fitting parameters reveals the reason: $\rho_{\text{Pt}} = 58$ $\mu\Omega$cm, $\mathcal{N}_{\text{Pt}}(\text{E})_F/\mathcal{N}_{\text{Au}}(\text{E})_F = 1.0$, $\lambda_{\text{sd,Pt}} = 1.0$ nm, $\tilde{g}_{\uparrow\downarrow,\text{Pt/Co}} = 7.9 \times 10^{15}$ cm^{-2}, $\delta_{\text{Au/Pt}} = 9 \times 10^{-6}$ and $AR_{\text{Au/Pt}} = 1.17$ fΩm^2. This fit suggests that there is no SML at the Au/Pt layer. Also, this model forces the density of states of Au and Pt to be equal, this would be more inline with the continuity of chemical potential" as oppose to the continuity of spin-accumulation". Even though the model is able to fit the data quite well, the resulting fit parameters are not consistent with the calculated values from Gupta *et al.* [20], i.e. $\delta_{\text{Au/Pt}} = 0.62$.

Given this large calculated value of $\delta_{\text{Au/Pt}} = 0.62$ for the Au/Pt, it is interesting to observe the quality of the fit if the SML parameter is constrained to be $\delta^{\text{fit}}_{\text{Au/Pt}} = 0.5$, see fig. 8.9. This fit yields $\rho_{\text{Pt}} = 47\mu\Omega$cm, $\mathcal{N}_{\text{Pt}}(\text{E})_F/\mathcal{N}_{\text{Au}}(\text{E})_F = 1.0$, $\lambda_{\text{sd,Pt}} = 1.1$ nm, $\tilde{g}_{\uparrow\downarrow,\text{Pt/Co}} =$

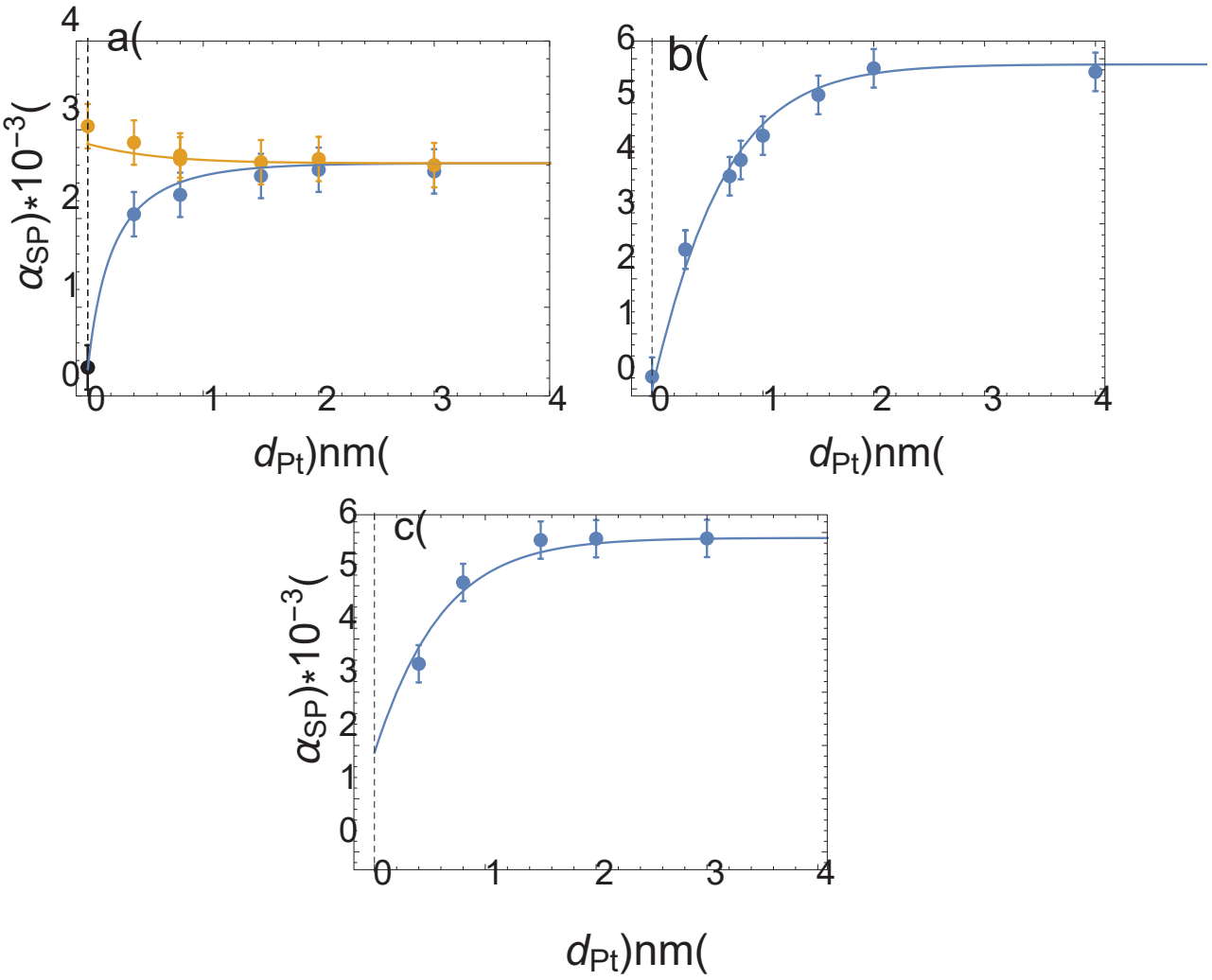

Figure 8.8: Spin-pumping induced damping data for the (a) $\overrightarrow{\text{Py}}$/Au/I/Pt (blue) and $\overrightarrow{\text{Py}}$/Au/I/Pt/Co (yellow), (b) $\overrightarrow{\text{Py}}$/Pt and (c) Py/Au/I/Pt/$\overrightarrow{\text{Co}}$. The black data point represents the the $\overrightarrow{\text{Py}}$/Au structure. All data was fit simultaneously assuming continuety of accumulation model with the additional interface SML layer as discussed in the text. The plots are done using the following parameters: $\tilde{g}_{\uparrow\downarrow,\text{Pt/Co}} = 7.9 \times 10^{15}$ cm^{-2}, $\lambda_{\text{sd,Pt}} = 1.0$ nm, $\rho_{\text{Pt}} = 58$ $\mu\Omega$cm $\mathcal{N}_{\text{Pt}}(\text{E})_F/\mathcal{N}_{\text{Au}}(\text{E})_F = 1.0$, $\delta_{\text{Au/Pt}} = 9 \times 10^{-6}$ and $AR_{\text{Au/Pt}} = 1.17$ fΩm^2.

6.5×10^{15} cm^{-2}, and $AR_{\mathrm{Au/Pt}} = 1.4$ fΩm^2. As before, the of density of states ratio is fitted to be 1, this result suggests that within this model the continuity of chemical potential, eq. (8.4), may be the more appropriate boundary condition as opposed to continuity of the density of spin accumulation, eq. (8.6). The quality of the fit clearly suffers for $\delta^{\mathrm{fit}}_{\mathrm{Au/Pt}} = 0.5$ especially for the $\overrightarrow{\mathrm{Py}}$/Au/Pt and $\overrightarrow{\mathrm{Py}}$/Au/Pt/Co data sets. Any further increase in $\delta_{\mathrm{Au/Pt}}$ deteriorates the fit quality even further. This model does introduce a discontinuity in the spin-current at the Au/Pt interface, this can observed by plotting the spin-current for the above parameters, see fig. 8.10

It is important to point out that the work of Gupta *et al.* [20] is aimed at interpreting polarized spin-current type of experiments (such as CPP-magnetoresistance experiment, GMR). Fundamentally, a spin-pumping experiment is different in two ways, first spin-pumping generates a spin-accumulation which is subsequently transported away from the interface by its gradient, it results in a pure-spin-current (no net charge). Second, spin-pumping injects a spin-current which is transverse to the magnetization of the ferromagnet. In contrast, a GMR type of experiment results in a charge current which is also spin-polarized in the direction of the ferromagnet. The spin-current is injected as a consequence of an electrical potential difference.

From the above fits it appears that the best approach is to assume zero SML at the Au/Pt but a large value for $AR_{\mathrm{Au/Pt}}$, see fig. 8.8. Given that this model yields a good fit with such parameters, it is interesting to determine the ratio of the transmitted and reflection spin-currents at the Au/Pt interface, similarly to what was done in the Partial Spin Sink Model. In this case it is a little more subtle what needs to be done in order to determine the reflected and the absorbed spin-currents. First, note that the net spin-current is always given by the derivative of the chemical potential times the diffusion constant. The chemical potential in every layer is fully characterized from the six fitted parameters, $\rho_{\mathrm{Pt}} = 58\mu\Omega$cm, $\mathcal{N}_{\mathrm{Pt}}(\mathrm{E})_F/\mathcal{N}_{\mathrm{Au}}(\mathrm{E})_F = 1.0$, $\lambda_{\mathrm{sd,Pt}} = 1.0$ nm, $\tilde{g}_{\uparrow\downarrow,\mathrm{Pt/Co}} = 7.9 \times 10^{15}$ cm^{-2}, $\delta_{\mathrm{Au/Pt}} = 9 \times 10^{-6}$ and $AR_{\mathrm{Au/Pt}} = 1.17$ fΩm^2. Therefore the net current, coming from the Au side into the Au/I interface is

$$I_{\mathrm{net}} = -\frac{\hbar}{2\rho^{\uparrow}_{\mathrm{Au}} e^2} \frac{\partial \boldsymbol{\mu}^{\mathrm{Au}}_{\mathrm{s}}}{\partial x}\bigg|_{x=d_1}. \tag{8.14}$$

For the $\overrightarrow{\mathrm{Py}}$/Au/Pt structure the net current is given by eq. (8.14) and is the sum of both the forward and reflected currents. In order to determine the reflected current, one needs to compare I_{net} to a structure which does not have reflected spin-current i.e. to the $\overrightarrow{\mathrm{Py}}$/Au/sink structure.

In the $\overrightarrow{\mathrm{Py}}$/Au/sink there exists only forward current since in this case the sink acts as perfect absorber of the spin-current and therefore does not result in any reflection. Therefore,

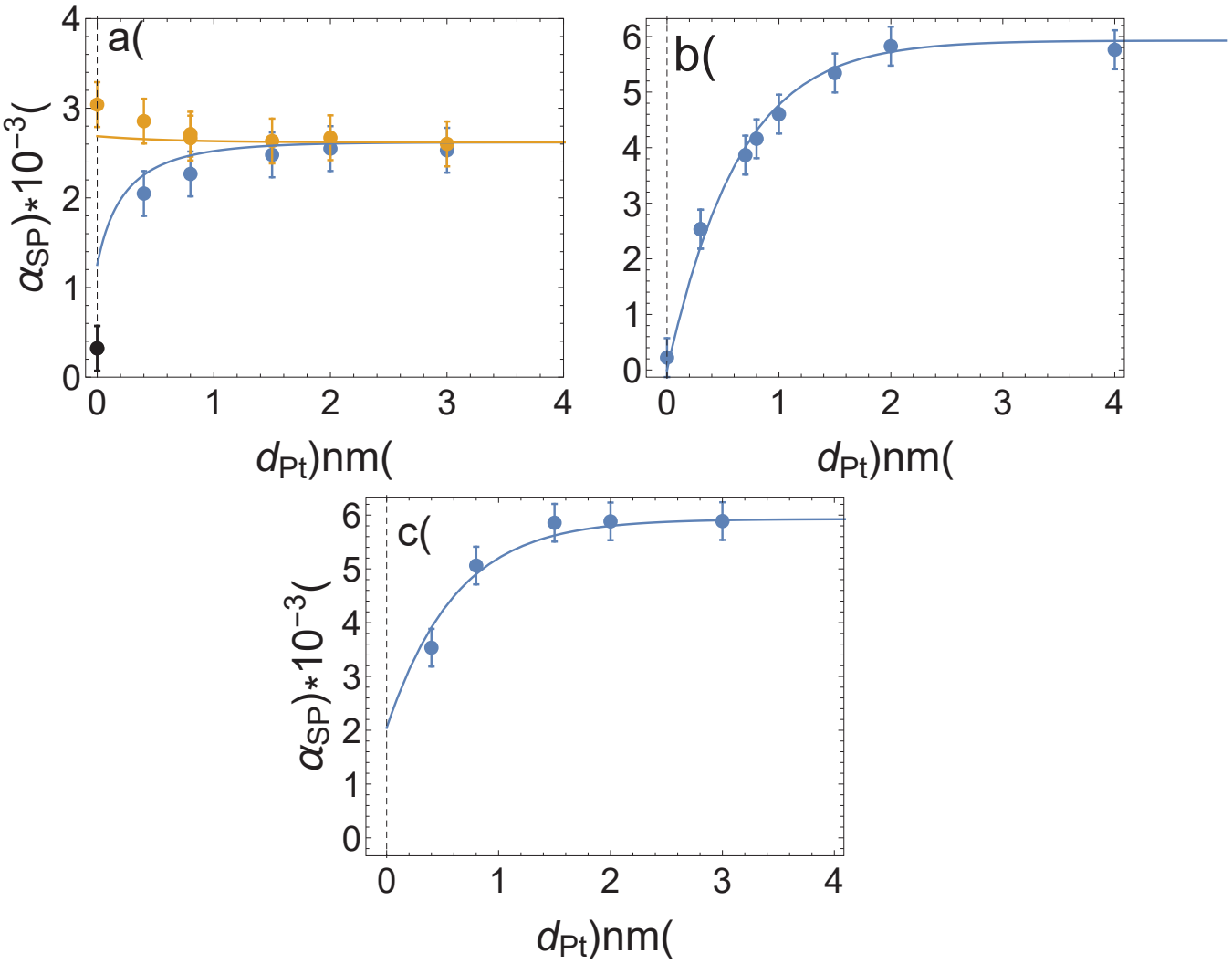

Figure 8.9: Spin-pumping induced damping data for the (a) $\overrightarrow{\text{Py}}$/Au/I/Pt (blue) and $\overrightarrow{\text{Py}}$/Au/I/Pt/Co (yellow), (b) $\overrightarrow{\text{Py}}$/Pt and (c) Py/Au/I/Pt/$\overrightarrow{\text{Co}}$. The black data point represents the the $\overrightarrow{\text{Py}}$/Au structure. All data was fit simultaneously assuming continuity of accumulation model with the additional interface SML layer as discussed in the text. The fitting parameters are $\tilde{g}_{\uparrow\downarrow,\text{Pt/Co}} = 6.5 \times 10^{15}$ cm^{-2}, $\lambda_{\text{sd,Pt}} = 1.1$ nm, $\rho_{\text{Pt}} = 47$ $\mu\Omega$cm and $\mathcal{N}_{\text{Pt}}(\text{E})_F/\mathcal{N}_{\text{Au}}(\text{E})_F = 1.0$, $AR_{\text{Au/Pt}} = 1.4$ fΩm^2 and $\delta_{\text{Au/Pt}}$ was constrained to be $\delta_{\text{Au/Pt}} = 0.5$.

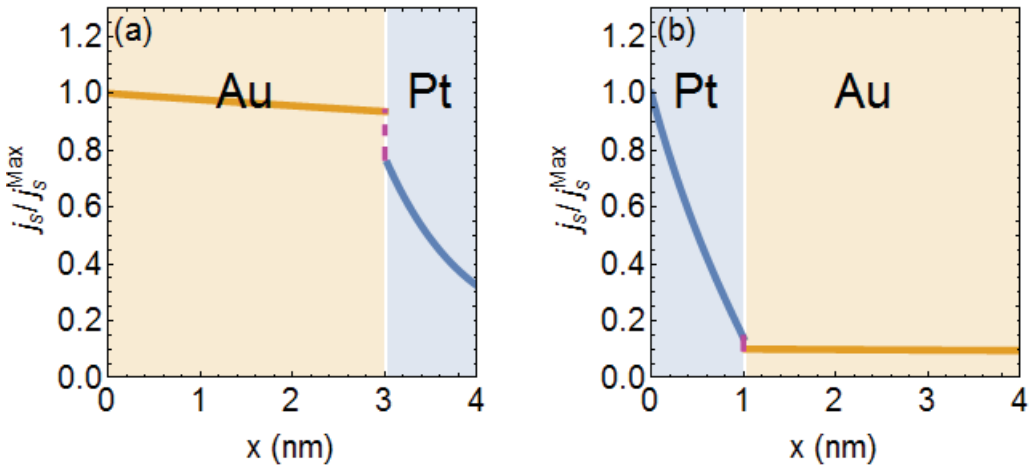

Figure 8.10: Spin-current normalized by its maximum value plotted for entire thickness of the (a) $\overrightarrow{\text{Py}}$/Au/Pt(1)/Co and (b) Py/Au/Pt(1)/$\overleftarrow{\text{Co}}$ structures for the spin-memory loss model assuming $\rho_{\text{Pt}} = 47\mu\Omega\text{cm}$, $\mathcal{N}_{\text{Pt}}(\text{E})_F/\mathcal{N}_{\text{Au}}(\text{E})_F = 1.0$, $\lambda_{\text{sd,Pt}} = 1.1$ nm, $\tilde{g}_{\uparrow\downarrow,\text{Pt/Co}} = 6.5 \times 10^{15}$ cm^{-2}, $AR_{\text{Au/Pt}} = 1.4$ fΩm^2 and $\delta_{\text{Au/Pt}} = 0.5$.

the net current at the Au/sink interface is the forward current and is given by,

$$I_{\text{forward}} = -\frac{\hbar}{2\rho^{\uparrow}_{\text{Au}} e^2} \frac{\partial \boldsymbol{\mu}_{\text{s}}^{\text{Au}}}{\partial x}\bigg|_{x=d_1}, \tag{8.15}$$

where the established chemical potential is still determined by the same constants ($\rho_{\text{Pt}} = 58\mu\Omega\text{cm}$, $N_{Au}(\text{E})_F/N_{Pt}(\text{E})_F = 1.0$, $\lambda_{\text{sd,Pt}} = 1.0$ nm, $\tilde{g}_{\uparrow\downarrow,\text{Pt/Co}} = 7.9 \times 10^{15}$ cm^{-2}, $\delta_{\text{Au/Pt}} = 9 \times 10^{-6}$ and $AR_{\text{Au/Pt}} = 1.17$ fΩm^2) but only for the $\overrightarrow{\text{Py}}$/Au/sink structure. Taking the difference of I_{net} and I_{forward} for the $\overrightarrow{\text{Py}}$/Au/Pt and $\overrightarrow{\text{Py}}$/Au/sink structures results in 11% of the spin-current reflected at the Au/Pt interface if the current is coming from the Au side. Since this picture assumes zero SML, the spin-current is continuous across the interface and therefore 89% of the spin-current is transmitted.

This approach can be repeated for the case in which the spin-current is coming the Pt side into the I/Pt interface, with the same fitting parameters, which results in 75% of the spin-current being reflected and 25% being transmitted.

Therefore, one can conclude that even the spin-memory loss model requires that the transmission of the spin-current be asymmetric at the Au/Pt interface. This is in line with conclusions from the partial spin-sink model (eqs. (8.10) and (8.11)) which also suggest an asymmetric transmission of the spin-current at Au/Pt interface.

8.4 Summary

Spin-transport across the Au/Pt interface was studied by mean of spin-pumping in Py/Au/Pt(d_{Pt})/Co, Py/Au/Pt(d_{Pt}) and Co/Pt(d_{Pt}) structures deposited by sputter deposition. The spin-pumping

induced damping of the Py/Au/Pt(d_{Pt})/Co and Py/Au/Pt(d_{Pt}) structures, when pumping from the Py layer, shows the characteristic spin-source and spin-sink type of thickness dependencies. Additionally, the Co/Pt(d_{Pt}) samples also shows the expected thickness dependence for spin-pumping into Pt i.e. a rapid increase in spin-pumping damping reaching a saturation on a length scale of 1 nm. However, the spin-pumping induced damping when pumping from the Co layer in Py/Au/Pt(d_{Pt})/Co shows a very unexpected d_{Pt} thickness dependence. Qualitatively the data suggests that there is a large reflection of spin-current is the pumping is originating from the Co layer. This is not observed if the pumping is originating from the Py layer. Two models are used to interpret the observed data, continuity of spin-accumulation and continuity of chemical potential a at the Au/Pt interface. Both models fail to fit all the data sets. A new model is presented, which treats Pt as a partial-sink. This model provides a good fit to all the data sets with a single set of fitting parameters. It also suggests that there is an asymmetric reflection of the spin-current at the Au/Pt interface which depends on the direction of propagation of the spin-current. Finally, an attempt is made to analyze the damping data using the spin memory loss model (this is an extension of the continuity of spin accumulation assuming that spin is not conserved at the interface). This model is able to fit that data as well but yields unrealistic fitting parameters.

Chapter 9

Summary

Spin-transport in Pt was studied by means of spin-pumping in a variety of magnetic multilayered heterostructures. It was identified that in order to make a clear interpretation of spin-pumping into Pt one needs to study both the single and double magnetic layer structures. Py is often used as the ferromagnet of choice for the single magnetic layer structure spin-pumping studies. The double magnetic layer structure requires an additional ferromagnet, one which would allow for a symmetric interface but still have a distinguishable FMR resonance. It was found that a direct exchange coupled bilayer of [Py/Fe] satisfies both of these properties. Chapter 4 presents magnetic and structural studies of Py and [Py/Fe]. It was found that the underling Py serves as a good seed layer for Fe, improving the texture of the growth and reducing the magnetic damping. In chapter 5 both Py and [Py/Fe] were used in the single and double magnetic layer structure in order to determine the spin-transport into Ta. It was found that the structure of Ta evolves with increasing thickness, first starting out as amorphous, then *bcc*-Ta and finally dominated by β-Ta. Since each structure has very different resistivity values, the thickness dependent resistivity of Ta is in part a consequence of the evolving crystal structure. The length scale of spin-pumping into Ta is very short, 1 nm, this is in the amorphous thickness region. The interpretation of the spin-pumping damping into Ta is complicated by the rapidly changing resistivity, it is not clear which resistivity value is appropriate for the correct interpretation. However, by simultaneously interpreting the single and double magnetic layer spin-pumping induced damping data it becomes clear which models are not appropriate. It was found that the data can only fit if the resistivity is that approximately the value of the amorphous Ta. Additionally, by using the the single and double magnetic layer, it was shown that the Dyakonov-Perel like interpretation of spin-transport in Ta does not fit the data.

Having characterized the properties of each ferromagnet (Py and [Py/Fe]) and of the Ta seed layer, the next step was to perform an analogous experiment with Pt, using the single and double magnetic layer structures. However, due to the property of Pt to become proximity polarized by the adjacent magnetic layers, it results that the double magnetic layer structure experiences interlayer exchange coupling. Therefore it was required to study

the interlayer exchange coupling mediated by Pt in the double magnetic layer structure in order to quantify the spin-pumping induced damping in the double magnetic layer structure. Chapter 6 presents a study of interlayer exchange coupling by means of broadband FMR. It was found that the exchange coupling is of ferromagnetic nature and is monotonically increasing with decreasing Pt thickness. Due to the exchange coupling the resonances of each magnetic layers were no longer independent and resulted in either in-phase or out-of-phase precession of the two magnetic moments. An attempt was made to interpret the damping of the in-phase and out-of-phase resonance modes, however the interpretation was overwhelmingly complicated by the presence of two-magnon scattering of the [Py/Fe] layer which was averaged over the two ferromagnetic layers due to the thickness dependent interlayer exchange coupling.

In order to avoid the problems due to the averaging of the two-magnon scattering by the exchange coupling, a new set of magnetic structures were deposited such that both the ferromagnetic materials had very similar magnetic damping without any contribution from two-magnon scattering. This significantly simplified the interpretation of the double magnetic layer structure. However, the exchange coupling was still present which again resulted in the in-phase and out-of-phase resonance modes. The spin-pumping model had to be extended to account for simultaneous spin-pumping from both of the ferromagnetic layers. For the case of the in-phase precession, the experimental results showed an increase in damping with increasing Pt thickness. For the out-of-phase precession, the damping decreased with increasing thickness. Simply changing the mode of precession led to a very large effect on the measured magnetic damping. This is a very unique result since it suggests that there is indeed communication of the spin-current between the two magnetic layers. These observations cannot be explained by some other form of interface related damping mechanism, such as spin-memory-loss. The data was interpreted by modeling the expected behaviour of the in-phase and out-of-phase resonance modes damping using the spin-pumping parameters as extracted from the single layer structure. There was very good agreement between the data and the simulated model.

To further understand the spin-pumping behaviour into Pt the above study was repeated in a similar structure however the interlayer exchange coupling was broken by the addition of a thin Au layer into the deposited structure: Py/Au/Pt/Co. In these studies Co was used as the second ferromagnetic layer. The Au decouples the Py and Co and allows one to measure their independent spin-pumping contributions. Surprisingly, it was observed that there was a very large asymmetry in spin-pumping from Py as compared to Co. An attempt was made to interpret the data by two models commonly used in literature to model the transport of spin-current across a NM/NM interface: continuity of spin-accumulation and continuity of chemical potential. Both models failed to fit the data, therefore a third model was presented which treats Pt as a partial spin-sink. This model was able to fit all the studied data sets and even showed that it has predictive power since it was able to reproduce the

unexpected damping dependence when spin-pumping from the Co layer. Futhermore, this model suggested that there is indeed an asymmetry in the transport of spin-current across the Au/Pt which depends on the direction of the spin-current. Lastly, data was analyzed with the spin memory loss model the results of which suggested that there is spin loss at the interface. This model also suggested that the spin-transport across the Au/Pt interface is asymmetric.

Bibliography

[1] P. Grünberg, R. Schreiber, Y. Pang, M. B. Brodsky, and H. Sowers, Phys. Rev. Lett. **57**, 2442 (1986).

[2] B. Kardasz and B. Heinrich, Phys. Rev. B **81**, 094409 (2010).

[3] G. Woltersdorf, O. Mosendz, B. Heinrich, and C. H. Back, Phys. Rev. Lett. **99**, 246603 (2007).

[4] B. Kardasz, O. Mosendz, B. Heinrich, Z. Liu, and M. Freeman, Journal of Applied Physics **103**, 07C509 (2008), https://doi.org/10.1063/1.2834399 .

[5] T. Gerrits, M. L. Schneider, and T. J. Silva, Journal of Applied Physics **99**, 023901 (2006), https://doi.org/10.1063/1.2159076 .

[6] S. Mizukami, Y. Ando, and T. Miyazaki, Phys. Rev. B **66**, 104413 (2002).

[7] Y. Tserkovnyak, A. Brataas, G. E. W. Bauer, and B. I. Halperin, Reviews of Modern Physics **77**, 1375 (2005).

[8] C. W. Sandweg, Y. Kajiwara, K. Ando, E. Saitoh, and B. Hillebrands, Applied Physics Letters **97**, 252504 (2010).

[9] B. Heinrich, C. Burrowes, E. Montoya, B. Kardasz, E. Girt, Y.-Y. Song, Y. Sun, and M. Wu, Phys. Rev. Lett. **107**, 066604 (2011).

[10] A. Kapelrud and A. Brataas, Physical Review Letters **111**, 097602 (2013).

[11] P. Vaidya, S. A. Morley, J. van Tol, Y. Liu, R. Cheng, A. Brataas, D. Lederman, and E. del Barco, Science **368**, 160–165 (2020).

[12] H. Wang, C. Du, P. C. Hammel, and F. Yang, Phys. Rev. Lett. **113**, 097202 (2014).

[13] C. Hahn, G. de Loubens, V. V. Naletov, J. B. Youssef, O. Klein, and M. Viret, EPL (Europhysics Letters) **108**, 57005 (2014).

[14] T. Moriyama, S. Takei, M. Nagata, Y. Yoshimura, N. Matsuzaki, T. Terashima, Y. Tserkovnyak, and T. Ono, Applied Physics Letters **106**, 162406 (2015), https://doi.org/10.1063/1.4918990 .

[15] S. Watanabe, K. Ando, K. Kang, S. Mooser, Y. Vaynzof, H. Kurebayashi, E. Saitoh, and H. Sirringhaus, Nature Physics **10**, 308–313 (2014).

[16] D. Sun, K. J. van Schooten, M. Kavand, H. Malissa, C. Zhang, M. Groesbeck, C. Boehme, and Z. Valy Vardeny, Nature Materials **15**, 863–869 (2016).

[17] J.-C. Rojas-Sánchez, N. Reyren, P. Laczkowski, W. Savero, J.-P. Attané, C. Deranlot, M. Jamet, J.-M. George, L. Vila, and H. Jaffrès, Phys. Rev. Lett. **112**, 106602 (2014).

[18] K. Chen and S. Zhang, Phys. Rev. Lett. **114**, 126602 (2015).

[19] X. Tao, Q. Liu, B. Miao, R. Yu, Z. Feng, L. Sun, B. You, J. Du, K. Chen, S. Zhang, L. Zhang, Z. Yuan, D. Wu, and H. Ding, Science Advances **4** (2018), 10.1126/sciadv.aat1670, http://advances.sciencemag.org/content/4/6/eaat1670.full.pdf .

[20] K. Gupta, R. J. H. Wesselink, R. Liu, Z. Yuan, and P. J. Kelly, Phys. Rev. Lett. **124**, 087702 (2020).

[21] E. Montoya, B. Heinrich, and E. Girt, Phys. Rev. Lett. **113**, 136601 (2014).

[22] A. M. Gonçalves, F. Garcia, H. K. Lee, A. Smith, P. R. Soledade, C. A. C. Passos, M. Costa, N. M. Souza-Neto, I. N. Krivorotov, L. C. Sampaio, and I. Barsukov, Scientific Reports **8**, 2318 (2018).

[23] E. Montoya, P. Omelchenko, C. Coutts, N. R. Lee-Hone, R. Hübner, D. Broun, B. Heinrich, and E. Girt, Phys. Rev. B **94**, 054416 (2016).

[24] E. Šimánek and B. Heinrich, Phys. Rev. B **67**, 144418 (2003).

[25] E. Šimánek, Physical Review B **68**, 224403 (2003).

[26] B. Heinrich and Cochran, Advances in Physics **42**, 523 (1993).

[27] C. Eyrich, A. Zamani, W. Huttema, M. Arora, D. Harrison, F. Rashidi, D. Broun, B. Heinrich, O. Mryasov, M. Ahlberg, O. Karis, P. E. Jönsson, M. From, X. Zhu, and E. Girt, Phys. Rev. B **90**, 235408 (2014).

[28] G. T. L. and K. J. M., Conf. Magnetism and Magnetic Materials , 253 (1955).

[29] Z. Celinski, K. Urquhart, and B. Heinrich, Journal of Magnetism and Magnetic Materials **166**, 6 (1997).

[30] L. Neél, C. R. Hebd. Seances Acad. Sci. **255**, 1545 (1962).

[31] L. Neél, C. R. Hebd. Seances Acad. Sci. **255**, 1676 (1962).

[32] P. Omelchenko, B. Heinrich, and E. Girt, Applied Physics Letters **113**, 142401 (2018), https://doi.org/10.1063/1.5050935 .

[33] P. Bruno, Phys. Rev. B **52**, 411 (1995).

[34] B. Heinrich and J. Cochran, Advances in Physics **42**, 523 (1993).

[35] M. Sparks, *Ferromagnetic-Relaxation Theory* (New York: McGraw-Hill, 1964).

[36] Y. Tserkovnyak, A. Brataas, and G. E. W. Bauer, Physical Review Letters **88**, 117601 (2002).

[37] P. Brouwer, Physical Review B **58**, R10135 (1998).

[38] M. D. Stiles, in *Ultrathin Magnetic Structures III*, edited by J. A. C. Bland and B. Heinrich (Springer-Verlag, Berlin/Heidelberg, 2005) Chap. 4, pp. 99–140.

[39] N. Zubarev, Soviet Physics Uspechi **3**, 320 (1960).

[40] Y. Yafet, Phys. Rev. B **36**, 3948 (1987).

[41] M. Zwierzycki, Y. Tserkovnyak, P. Kelly, A. Brataas, and G. E. Bauer, Physical Review B **71**, 064420 (2005).

[42] K. M. Schep, J. B. A. N. van Hoof, P. J. Kelly, G. E. W. Bauer, and J. E. Inglesfield, Phys. Rev. B **56**, 10805 (1997).

[43] M. A. Gijs and G. E. Bauer, Advances in Physics **46**, 285 (1997), https://doi.org/10.1080/00018739700101518 .

[44] R. Elliott, Physical Review **96**, 266 (1954).

[45] Y. Yafet, Physical Review **85**, 478 (1952).

[46] M. Dyakonov and V. Perel, Sov. Phys. Solid State **13**, 3023 (1972).

[47] I. M. Dyakonov and I. V. Perel, Sov. Phys. JETP **33**, 1053 (1971).

[48] Y. M., The Rigaku Journal **2** (2010).

[49] J. Lenz and S. Edelstein, IEEE Sensors Journal **6**, 631 (2006).

[50] Y. S. Shaikh, *Electron spin resonance in low-dimensional spin chains and metals*, Dissertation, University of Stuttgart (2008).

[51] L. J. van der Pauw, Philips Technical Review **26**, 220 (2010).

[52] S. Thorsteinsson, F. Wang, D. H. Petersen, T. M. Hansen, D. Kjær, R. Lin, J.-Y. Kim, P. F. Nielsen, and O. Hansen, Review of Scientific Instruments **80**, 053902 (2009).

[53] Z. Celinski, K. Urquhart, and B. Heinrich, Journal of Magnetism and Magnetic Materials **166**, 6 (1997).

[54] J. Ding, C. Liu, Y. Zhang, U. Erugu, Z. Quan, R. Yu, E. McCollum, S. Mo, S. Yang, H. Ding, X. Xu, J. Tang, X. Yang, and M. Wu, Phys. Rev. Applied **14**, 014017 (2020).

[55] P. Deorani and H. Yang, Applied Physics Letters **103**, 232408 (2013), https://doi.org/10.1063/1.4839475 .

[56] R. Bansal, N. Chowdhury, and P. K. Muduli, Applied Physics Letters **112**, 262403 (2018), https://doi.org/10.1063/1.5033418 .

[57] W. Cao, L. Yang, S. Auffret, and W. E. Bailey, Phys. Rev. B **99**, 094406 (2019).

[58] H. Yang, Y. Li, and W. E. Bailey, Applied Physics Letters **108**, 242404 (2016), https://doi.org/10.1063/1.4953622 .

[59] S. Azzawi, A. Ganguly, M. Tokaç, R. M. Rowan-Robinson, J. Sinha, A. T. Hindmarch, A. Barman, and D. Atkinson, Phys. Rev. B **93**, 054402 (2016).

[60] D. Fraitová, in *Front. Magn. Reduc. Dimens. Syst*, Vol. III, edited by V. G. Bar'yakthar, P. E. Wigen, and N. A. Lesnik (Springer Netherlands, Dordrecht, 1998) Chap. 4, p. 121–152.

[61] B. Kardasz, E. A. Montoya, C. Eyrich, E. Girt, and B. Heinrich, Journal of Applied Physics **109**, 7 (2011).

[62] D. Bastian and E. Biller, Physica Status Solidi (a) **35**, 465 (1976).

[63] J. M. Shaw, H. T. Nembach, and T. J. Silva, Applied Physics Letters **99**, 012503 (2011).

[64] J. M. Shaw, H. T. Nembach, T. J. Silva, and C. T. Boone, Journal of Applied Physics **114** (2013), 10.1063/1.4852415.

[65] M. Johnson, P. Bloemen, F. Broeder, den, and J. de Vries, Reports on Progress in Physics **59**, 1409 (1996).

[66] B. Heinrich, in *Ultrathin Magnetic Structures*, Vol. III, edited by J. A. C. Bland and B. Heinrich (Springer, Berlin, 2005) Chap. 5, pp. 143–206.

[67] R. D. Mcmichael, D. J. Twisselmann, and A. Kunz, Physical Review Letters **90**, 227601 (2003).

[68] Y. Zhao, Q. Song, S.-h. Yang, T. Su, W. Yuan, and S. S. P. Parkin, Scientific Reports **6**, 22890 (2016).

[69] S. Mizukami, T. Kubota, X. Zhang, H. Naganuma, M. Oogane, Y. Ando, and T. Miyazaki, Japanese Journal of Applied Physics **50**, 103003 (2011).

[70] B. Heinrich, T. Monchesky, and R. Urban, Journal of Magnetism and Magnetic Materials **236**, 339 (2001).

[71] K. Zakeri, J. Lindner, I. Barsukov, R. Meckenstock, M. Farle, H. Wende, W. Keune, J. Rocker, S. S. Kalarickal, K. Lenz, W. Kuch, K. Baberschke, and Z. Frait, Physical Review B **76**, 104416 (2007).

[72] K. Kobayashi, N. Inaba, N. Fujita, Y. Sudo, T. Tanaka, M. Ohtake, M. Futamoto, and F. Kirino, IEEE Transactions on Magnetics **45**, 2541 (2009).

[73] S. Peng, M. Wang, H. Yang, L. Zeng, J. Nan, J. Zhou, Y. Zhang, A. Hallal, M. Chshiev, K. L. Wang, Q. Zhang, and W. Zhao, Scientific Reports **5**, 18173 (2015).

[74] Y. Tserkovnyak, E. M. Hankiewicz, and G. Vignale, Phys. Rev. B **79**, 094415 (2009).

[75] H. T. Nembach, J. M. Shaw, C. T. Boone, and T. J. Silva, **117201**, 1 (2013).

[76] T. Qu and R. H. Victora, **224426**, 1 (2016).

[77] S. N. Piramanayagam, C. S. Mah, C. Y. Ong, J. Z. Shi, J. A. Dumaya, T. Onoue, and S. Ishibashi, Journal of Applied Physics **101** (2007), 10.1063/1.2735398.

[78] S. N. Piramanayagam, Journal of Applied Physics **102** (2007), 10.1063/1.2750414.

[79] S. Ikeda, K. Miura, H. Yamamoto, K. Mizunuma, H. D. Gan, M. Endo, S. Kanai, J. Hayakawa, F. Matsukura, and H. Ohno, Nature materials **9**, 721 (2010).

[80] S. Mangin, D. Ravelosona, J. A. Katine, and E. E. Fullerton, INTERMAG 2006 - IEEE International Magnetics Conference **5**, 5 (2006).

[81] J. H. Kwon, P. Deorani, J. Yoon, M. Hayashi, and H. Yang, Applied Physics Letters **107**, 022401 (2015).

[82] G. Allen, S. Manipatruni, D. E. Nikonov, M. Doczy, and I. A. Young, Physical Review B - Condensed Matter and Materials Physics **91**, 044004 (2015), arXiv:1411.0601 .

[83] O. Boulle, V. Cros, J. Grollier, L. G. Pereira, C. Deranlot, F. Petroff, G. Faini, J. Barnaś, and a. Fert, Nature Physics **3**, 492 (2007), arXiv:0704.0370 .

[84] K. Fuchs, Mathematical Proceedings of the Cambridge Philosophical Society **34**, 100 (1938).

[85] E. H. Sondheimer, Advances in Physics **1**, 1 (1952).

[86] P. Fan, K. Yi, J.-D. Shao, and Z.-X. Fan, Journal of Applied Physics **95**, 2527 (2004).

[87] N. O. Nnolim, T. a. Tyson, and L. Axe, Journal of Applied Physics **93**, 4543 (2003).

[88] N. O. Nnolim, *Understanding the origins of metastability in thin film growth; tantalum and the early group VB-VIB metals*, Dissertation, The New Jersey Institute of Technology (2003).

[89] K. Stella, D. Bürstel, S. Franzka, O. Posth, and D. Diesing, Journal of Physics D: Applied Physics **42**, 135417 (2009).

[90] O. Mosendz, G. Woltersdorf, B. Kardasz, B. Heinrich, and C. H. Back, Phys. Rev. B **79**, 224412 (2009).

[91] C. T. Boone, J. M. Shaw, H. T. Nembach, and T. J. Silva, Journal of Applied Physics **117**, 223910 (2015), https://doi.org/10.1063/1.4922581 .

[92] B. N. Cox, R. A. Tahir-Kheli, and R. J. Elliott, Phys. Rev. B **20**, 2864 (1979).

[93] G. J. Mata, E. Pestana, and M. Kiwi, Phys. Rev. B **26**, 3841 (1982).

[94] J. Tersoff and L. M. Falicov, Phys. Rev. B **25**, 2959 (1982).

[95] M. B. Brodsky and A. J. Freeman, Phys. Rev. Lett. **45**, 133 (1980).

[96] E. E. Fullerton, D. Stoeffler, K. Ounadjela, B. Heinrich, Z. Celinski, and J. A. C. Bland, Phys. Rev. B **51**, 6364 (1995).

[97] C. Klewe, T. Kuschel, J.-M. Schmalhorst, F. Bertram, O. Kuschel, J. Wollschläger, J. Strempfer, M. Meinert, and G. Reiss, Phys. Rev. B **93**, 214440 (2016).

[98] B. Heinrich, Z. Celinski, J. F. Cochran, W. B. Muir, J. Rudd, Q. M. Zhong, A. S. Arrott, K. Myrtle, and J. Kirschner, Phys. Rev. Lett. **64**, 673 (1990).

[99] S. S. P. Parkin, R. Bhadra, and K. P. Roche, Phys. Rev. Lett. **66**, 2152 (1991).

[100] W. F. Egelhoff and M. T. Kief, Phys. Rev. B **45**, 7795 (1992).

[101] Z. Celinski and B. Heinrich, Journal of Magnetism and Magnetic Materials **99**, L25 (1991).

[102] J. Unguris, R. J. Celotta, and D. T. Pierce, Journal of Applied Physics **75**, 6437 (1994), https://doi.org/10.1063/1.356954 .

[103] S. S. P. Parkin, N. More, and K. P. Roche, Phys. Rev. Lett. **64**, 2304 (1990).

[104] B. Heinrich, J. F. Cochran, T. Monchesky, and R. Urban, Phys. Rev. B **59**, 14520 (1999).

[105] M. D. Stiles, in *Ultrathin Magnetic Structures III*, Vol. III, edited by B. Heinrich and J. A. C. Bland (Springer-Verlag, Berlin, 2005) Chap. 4, pp. 99–142.

[106] R. Skomski, J. Zhang, V. Sessi, J. Honolka, K. Kern, and A. Enders, Journal of Applied Physics **103**, 07D519 (2008), https://doi.org/10.1063/1.2828594 .

[107] Y. Takahashi, Phys. Rev. B **56**, 8175 (1997).

[108] M. Noshiravani, A. Koohi, F. Ebrahimi, and M. M. Tehranchi, Phys. Rev. B **59**, 14461 (1999).

[109] A. Kootte, C. Haas, and R. A. de Groot, Journal of Physics: Condensed Matter **3**, 1133 (1991).

[110] F. Wilhelm, P. Poulopoulos, A. Scherz, H. Wende, K. Baberschke, M. Angelakeris, N. K. Flevaris, J. Goulon, and A. Rogalev, physica status solidi (a) **196**, 33 (2003), https://onlinelibrary.wiley.com/doi/pdf/10.1002/pssa.200306346 .

[111] M. Suzuki, H. Muraoka, Y. Inaba, H. Miyagawa, N. Kawamura, T. Shimatsu, H. Maruyama, N. Ishimatsu, Y. Isohama, and Y. Sonobe, Phys. Rev. B **72**, 054430 (2005).

[112] R. M. Rowan-Robinson, A. A. Stashkevich, Y. Roussigné, M. Belmeguenai, S.-M. Chérif, A. Thiaville, T. P. A. Hase, A. T. Hindmarch, and D. Atkinson, Scientific Reports **7**, 16835 (2017).

[113] Y. Liu, J. Qiu, S. T. Lim, S. L. Toh, Z. Zhu, G. Han, and K. Zhu, Applied Physics Express **10**, 013005 (2017).

[114] A. V. Davydenko, A. G. Kozlov, A. V. Ognev, M. E. Stebliy, A. S. Samardak, K. S. Ermakov, A. G. Kolesnikov, and L. A. Chebotkevich, Phys. Rev. B **95**, 064430 (2017).

[115] F. Wilhelm, P. Poulopoulos, G. Ceballos, H. Wende, K. Baberschke, P. Srivastava, D. Benea, H. Ebert, M. Angelakeris, N. K. Flevaris, D. Niarchos, A. Rogalev, and N. B. Brookes, Phys. Rev. Lett. **85**, 413 (2000).

[116] D.-O. Kim, K. M. Song, Y. Choi, B.-C. Min, J.-S. Kim, J. W. Choi, and D. R. Lee, Scientific Reports **6** (2016).

[117] T. Devolder, S. Couet, J. Swerts, and G. S. Kar, Journal of Physics D: Applied Physics **51**, 135002 (2018).

[118] C.-J. Lin, G. Gorman, C. Lee, R. Farrow, E. Marinero, H. Do, H. Notarys, and C. Chien, Journal of Magnetism and Magnetic Materials **93**, 194 (1991).

[119] K.-F. Huang, D.-S. Wang, H.-H. Lin, and C.-H. Lai, Applied Physics Letters **107**, 232407 (2015), https://doi.org/10.1063/1.4937443 .

[120] W. L. Lim, N. Ebrahim-Zadeh, J. C. Owens, H. G. E. Hentschel, and S. Urazhdin, Applied Physics Letters **102**, 162404 (2013), https://doi.org/10.1063/1.4802954 .

[121] L. Li, Y. Lu, Z. Liu, Y. Lv, Y. Zhang, S. Liu, C. Hao, and W. Lv, Journal of Magnetism and Magnetic Materials **325**, 117 (2013).

[122] E. Girt and H. J. Richter, IEEE Transactions on Magnetics **39**, 2306 (2003).

[123] P. Omelchenko, E. A. Montoya, C. Coutts, B. Heinrich, and E. Girt, Scientific Reports **7**, 4861 (2017).

[124] Z. Frait and D. Fraitova, in *Frontiers in Magnetism of Reduced Dimension Systems*, Vol. 49, edited by V. G. Baryakthar, W. E. Philip, and N. A. Lesnik (Springer, 1997) Chap. 4, p. 121.

[125] W. Baltensperger and J. S. Helman, Applied Physics Letters **57**, 2954 (1990), https://doi.org/10.1063/1.103737 .

[126] E. Holmström, L. Nordström, and A. M. N. Niklasson, Phys. Rev. B **67**, 184403 (2003).

[127] J. E. van Dam, P. C. M. Gubbens, and G. J. Van den Berg, Physica **70**, 520 (1973).

[128] B. Heinrich, in *Ultrathin Magnetic Structures III*, Vol. III, edited by B. Heinrich and J. A. C. Bland (Springer-Verlag, Berlin, 2005) Chap. 5.

[129] K. Lenz, H. Wende, W. Kuch, K. Baberschke, K. Nagy, and A. Jánossy, Phys. Rev. B **73**, 144424 (2006).

[130] B. Heinrich, "Spin Relaxation in Magnetic Metallic Layers and Multilayers," Chap. Spin Relaxation in Magnetic Metallic Layers and Multilayers, vol. III of [128] (2005).

[131] G. Woltersdorf and B. Heinrich, Phys. Rev. B **69**, 184417 (2004).

[132] Y. Liu, Z. Yuan, R. J. H. Wesselink, A. A. Starikov, and P. J. Kelly, Phys. Rev. Lett. **113**, 207202 (2014).

[133] Z. Feng, J. Hu, L. Sun, B. You, D. Wu, J. Du, W. Zhang, A. Hu, Y. Yang, D. M. Tang, B. S. Zhang, and H. F. Ding, Phys. Rev. B **85**, 214423 (2012).

[134] A. Conca, B. Heinz, M. R. Schweizer, S. Keller, E. T. Papaioannou, and B. Hillebrands, Phys. Rev. B **95**, 174426 (2017).

[135] S. Keller, L. Mihalceanu, M. R. Schweizer, P. Lang, B. Heinz, M. Geilen, T. Brächer, P. Pirro, T. Meyer, A. Conca, D. Karfaridis, G. Vourlias, T. Kehagias, B. Hillebrands, and E. T. Papaioannou, New Journal of Physics **20**, 053002 (2018).

[136] C. Swindells, A. T. Hindmarch, A. J. Gallant, and D. Atkinson, Phys. Rev. B **99**, 064406 (2019).

[137] A. J. Berger, E. R. J. Edwards, H. T. Nembach, O. Karis, M. Weiler, and T. J. Silva, Phys. Rev. B **98**, 024402 (2018).

[138] A. Conca, S. Keller, M. R. Schweizer, E. T. Papaioannou, and B. Hillebrands, Phys. Rev. B **98**, 214439 (2018).

[139] X. D. Tao, Z. Feng, B. F. Miao, L. Sun, B. You, D. Wu, J. Du, W. Zhang, and H. F. Ding, Journal of Applied Physics **115**, 17C504 (2014), https://doi.org/10.1063/1.4862215 .

[140] X. Tao, Q. Liu, B. Miao, R. Yu, Z. Feng, L. Sun, B. You, J. Du, K. Chen, S. Zhang, L. Zhang, Z. Yuan, D. Wu, and H. Ding, Science Advances **4** (2018), 10.1126/sciadv.aat1670, https://advances.sciencemag.org/content/4/6/eaat1670.full.pdf .

[141] A. M. Gonçalves, F. Garcia, H. K. Lee, A. Smith, P. R. Soledade, C. A. C. Passos, M. Costa, N. M. Souza-Neto, I. N. Krivorotov, L. C. Sampaio, and I. Barsukov, Scientific Reports **8**, 2318 (2018).

[142] B. Heinrich, Y. Tserkovnyak, G. Woltersdorf, A. Brataas, R. Urban, and G. E. W. Bauer, Physical Review Letters **90**, 187601 (2003).

[143] M. Johnson and R. H. Silsbee, Phys. Rev. B **37**, 5312 (1988).

[144] H. Yang, Y. Li, and W. E. Bailey, Applied Physics Letters **108**, 242404 (2016), https://doi.org/10.1063/1.4953622 .

[145] O. Mosendz, V. Vlaminck, J. E. Pearson, F. Y. Fradin, G. E. W. Bauer, S. D. Bader, and A. Hoffmann, Phys. Rev. B **82**, 214403 (2010).

[146] B. Kardasz, O. Mosendz, B. Heinrich, Z. Liu, and M. Freeman, Journal of Applied Physics **103**, 07C509 (2008), https://doi.org/10.1063/1.2834399 .

[147] M. Zwierzycki, Y. Tserkovnyak, P. J. Kelly, A. Brataas, and G. E. W. Bauer, Phys. Rev. B **71**, 064420 (2005).

[148] A. Ghosh, S. Auffret, U. Ebels, and W. E. Bailey, Phys. Rev. Lett. **109**, 127202 (2012).

[149] R. J. H. Wesselink, K. Gupta, Z. Yuan, and P. J. Kelly, Phys. Rev. B **99**, 144409 (2019).

[150] K. Dolui and B. K. Nikolić, Phys. Rev. B **96**, 220403 (2017).

[151] T. Nan, S. Emori, C. T. Boone, X. Wang, T. M. Oxholm, J. G. Jones, B. M. Howe, G. J. Brown, and N. X. Sun, Phys. Rev. B **91**, 214416 (2015).

[152] E. Montoya, *Spin pumping and spin transport in magnetic heterostructures*, Dissertation, Simon Fraser University (2016).

[153] E. Montoya, B. Kardasz, C. Burrowes, W. Huttema, E. Girt, and B. Heinrich, Journal of Applied Physics **111**, 07C512 (2012), https://doi.org/10.1063/1.3676026 .

[154] M. Isasa, E. Villamor, L. E. Hueso, M. Gradhand, and F. Casanova, Phys. Rev. B **91**, 024402 (2015).

[155] P. Omelchenko, E. Girt, and B. Heinrich, Phys. Rev. B **100**, 144418 (2019).

[156] W. Zhang, W. Han, X. Jiang, S.-H. Yang, and S. S. P. Parkin, Nature Physics **11**, 496 (2015).

[157] C.-F. Pai, Y. Ou, L. H. Vilela-Leão, D. C. Ralph, and R. A. Buhrman, Phys. Rev. B **92**, 064426 (2015).